High Integrity Carrier Phase Based Relative Positioning for Precision Landing using a Robust Nonlinear Filter

Master Thesis

Institute of
COMMUNICATION AND NAVIGATION
Univ.-Prof. Dr.-Ing. C. Günther
Fakultät für Elektrotechnik und Informationstechnik
Technische Universität München

by
Susanne Schlötzer

Supervisors:	Dipl.-Ing. Patrick Henkel (TUM)
	Dipl.-Ing. Markus Rippl (DLR)
Examiner:	Univ.-Prof. Dr.-Ing. Christoph Günther

Munich, February 2009

Affirmation

Hereby I declare that I have written this thesis entitled

High Integrity Carrier Phase Based Relative Positioning for Precision Landing using a Robust Nonlinear Filter

by myself without any assistance from third parties, that I have exclusively used the indicated literature and that I have marked literal quotations.

Munich, 2009-02-27

Susanne Schlötzer

Abstract

In this work a GNSS navigation filter is developed and procedures are derived in order to provide integrity of the navigation solution. The position solution has to meet high accuracy demands, for example those of zero-visibility precision approach. Therefore, low-noise carrier phase measurements are processed in addition to the GNSS pseudorange measurements. It is essential to resolve the ambiguities of the carrier phase measurements quickly and reliably in order to support high-accuracy real-time kinematic (RTK) positioning. Ambiguity resolution relies in this work on a geometry-based model. It is expected for the near future that the satellite geometry and the signal quality will improve, since GPS is planned to be modernized and GALILEO will be operational. Both factors are relevant for making progress in the domain of RTK carrier phase-based relative positioning. This study is restricted to the use of dual-frequency measurements in order to ensure compatibility with the requirements of civil aviation with respect to the Aeronautical Radio-Navigation Service (ARNS) bands. GPS's L1 and L5 signals or GALILEO's E1 and E5a signals are considered as measurement input to the filter. The user position and velocity vector, the ambiguities of the phase measurements and ionospheric terms are estimated by the filter. The performance of three different ionosphere models has been investigated. Although the estimation of ionospheric range errors is improved by processing measurements on two different frequencies, the results are only very good in absence of un-modeled biases. For example, if multiple measurements are biased by multipath it might happen that these un-modeled biases intrude into the ionosphere state estimation. The unknown states are only estimated reliably by the Extended Kalman Filter (EKF) if all un-modeled error sources were white Gaussian noise. Both multipath errors and residual tropospheric range errors after double-differencing are neglected in this filter approach. Alternatively to estimating the residual ionospheric errors it has also been considered to utilize ionosphere-free linear combinations. The user velocity vector is derived from instantaneous Doppler shift measurements. All measurements which are processed by the filter are double-differenced in order to keep the number of parameters to be estimated as small as possible. The disadvantage of double-differencing is that the measurement noise is amplified.

By implementing the standard equations of the EKF numeric stability cannot be assured. Numerical problems were avoided by choosing the Bierman-Thornton UD filter implementation for the problem at hand. Though, it is already sufficient to make the standard EKF equations more robust by implementing the Joseph form for the update of the covariance matrix of state estimation uncertainty. After introducing this measures in order to improve numeric robustness of the filter in presence of computer round-off errors, no further numerical problems where observed any longer in the succeeding simulation runs.

Because of the usage of an EKF it is difficult to derive the integrity risk analytically. The results depend on filter initialization and the concrete data sequence. However, a linear Kalman filter produces optimal state estimates by minimizing the sum of the mean-square errors. The integrity risk can be estimated for the nonlinear navigation filter solution by making some restrictive assumptions. Nevertheless, the effective integrity risk has to be determined by excessive simulations. Autonomous Filter-based fault Detection, Identification and model Adaptation (AFDIA) is proposed in order to detect model invalidations and to compensate them. So far only

single-channel biases can be detected and corrected, although the extension to multiple biases is possible, but complex. In the navigation algorithm tests all simulated cycle slips and code-outliers were detected successfully and the model was adapted properly afterwards. Protection levels are computed for both the user position estimates and the user velocity estimates. The derivation of the protection levels for the filter-based approach is restricted to two mutually exclusive hypotheses: normal operation of the filter in absence of biases and the fault mode if there is one bias in the measurement data. The non-Gaussian tails of the error distributions are accounted for by introducing inflation factors in the computation of the protection levels. This procedure is referred to as sigma-overbounding.

The performance of the navigation filter and the plausibility of the protection levels have been verified by Monte-Carlo simulations. In addition, real-signal tests of a precision approach have been carried out with a hardware simulator and a GALILEO receiver. The accuracy of the position estimates and the magnitude of the protection levels strongly depend on the availability of a carrier phase ambiguity-fixed solution. The float solution is already very accurate after the first hundred observation epochs because of the filter-based approach. In the Monte-Carlo simulations the carrier phase ambiguities could be typically fixed at a baseline length of 20 km between the user receiver and the reference receiver. The probability of wrong ambiguity fixing has been set to $1 \cdot 10^{-9}$. Successful carrier phase ambiguity resolution is demonstrated in the real-signal tests for a baseline length of 54 km, where the navigation filter has been started when the airplane was about 75 km away from the airport. The results of the real-signal tests are very good because of the availability of low-noise E5a pseudorange measurements. Furthermore, only ionospheric delays have been simulated with the hardware simulator. Tropospheric delays and multipath were neglected. The Vertical Protection Level (VPL) of the carrier phase ambiguity-fixed position solution is below 20 cm under the condition of good satellite geometry. The associated integrity risk is assumed to be at the order of $3 \cdot 10^{-9}$. If there are only few visible satellites, the VPL may be as large as 2 m although the ambiguities have already been fixed correctly. There is a great difference between the fault-mode protection level and the fault-free protection level. With respect to bad satellite geometry, the fault-mode protection level clearly dominates the overall protection level.

The performance results of the navigation filter are very promising with respect to the position accuracy and the magnitude of the protection levels which can be achieved. Since the actual integrity risk has to be assessed by simulations, it is rather difficult to proof that the integrity risk is indeed in the range of 10^{-9}, which is required for zero-visibility precision approach in civil aviation. The application of the navigation filter in domains where even higher position accuracy than in civil aviation is required, but where the specified integrity risk can still be verified by simulations, seems to be more likely. Several airport-related applications can be listed, for example automated cargo traffic, taxiing and coasting, but also precision approach in the military domain.

Zusammenfassung

Die vorliegende Arbeit, deren Ergebnisse hier gekürzt dargestellt sind, beschäftigt sich mit der Entwicklung eines GNSS Navigationsfilters und dem Herleiten von Mechanismen, um die Integrität der Navigationslösung sicherzustellen. Die Positionslösung soll hohen Genauigkeitsanforderungen gerecht werden, beispielsweise denen eines autonomen Landeanflugs. Aus diesem Grund werden neben GNSS Code-Messungen auch die wesentlich rauschärmeren Trägerphasenmessungen verarbeitet. Für hochgenaue und echtzeitkritische Positionierungsanwendungen ist es wichtig, dass die Mehrdeutigkeiten der Trägerphasenmessungen schnell und zuverlässig gelöst werden. Die Lösung der Mehrdeutigkeiten beruht in dieser Arbeit auf einem geometriebasierten Modell. Da sowohl eine Modernisierung von GPS geplant ist, als auch GALILEO operativ zur Verfügung stehen wird, kann zukünftig mit einer verbesserten Satellitengeometrie und mit höherer Signalqualität gerechnet werden. Beides sind relevante Faktoren, um Fortschritte im Bereich der echtzeitfähigen relativen Trägerphasenpositionierung zu machen. Die hier durchgeführte Studie beschränkt sich auf die Verwendung von Zweifrequenzmessungen, um mit den Anforderungen der zivilen Luftfahrt hinsichtlich der zugelassenen Frequenzbänder konform zu bleiben. Es werden GPS-Signale auf L1 und L5 oder alternativ GALILEO-Signale auf E1 und E5a berücksichtigt. Die Zustände, die mit dem Filter geschätzt werden, sind der Positionsvektor und der Geschwindigkeitsvektor des Nutzers, die Mehrdeutigkeiten der Phasenmessungen und ionosphärische Störgrößen. Drei verschiedene Ionosphärenmodelle sind hinsichtlich ihrer Effizienz untersucht worden. Obwohl die Schätzung von Ionosphärenfehlern durch die Verwendung von Messungen auf zwei verschiedenen Frequenzen verbessert wird, sind die Ergebnisse nur in Abwesenheit von nicht modellierten systematischen Fehlern sehr gut. Sind beispielsweise mehrere Messungen durch Mehrwegeausbreitung gestört, so fließen diese nicht modellierten Störgrößen gegebenenfalls fälschlicherweise in die Schätzung der Ionosphärenfehler mit ein. Der verwendete Extended Kalman Filter (EKF) Ansatz gewährleistet nur eine zuverlässige Schätzung der Zustände, insofern alle nicht modellierten Fehlerquellen durch weißes gaußsches Rauschen beschrieben werden können. Neben Mehrwegeausbreitung bleibt auch der troposphärische Restfehler nach der Doppelten Differenzbildung unberücksichtigt. Als Alternative zur Schätzung der ionosphärischen Restfehler wurde auch die Verwendung ionosphärenfreier Linearkombinationen in Betracht gezogen. Die Geschwindigkeit des Nutzers wird aus Messungen der Dopplerfrequenzverschiebung ermittelt. Um die Anzahl der zu schätzenden Parameter gering zu halten, werden Doppelte Differenzen aller Messgrößen gebildet, mit dem Nachteil eines verstärkten Messrauschens.

Die numerische Stabilität des EKF muss durch eine geeignete Implementierung sichergestellt werden, die sich nicht durch die Verwendung der Standardgleichungen erzielen lässt. Beispielsweise weißt der Bierman-Thornton UD Filteransatz für das vorliegende Problem keine numerischen Probleme auf. Es ist allerdings auch bereits ausreichend, die Standardgleichungen numerisch robuster zu gestalten, indem die Joseph-Form für die Aktualisierung der Kovarianzmatrix der Zustandsschätzungen gewählt wird. Nach diesen Stabilisierungsmaßnahmen konnte in keinem weiteren Simulationslauf ein numerisches Problem mehr nachgewiesen werden.

Ein analytischer Ansatz zur Bestimmung des Integritätsrisikos gestaltet sich auf Grund des verwendeten EKF als schwierig. Die Ergebnisse sind von der Filterinitialisierung sowie von der tatsächlichen Datensequenz abhängig. Ein lineares Kalman Filter ist hingegen ein optimaler Schätzer hinsichtlich der Minimierung der Summe aus den mittleren quadratischen Zustandsschätzfehlern. Mit gewissen Einschränkungen kann aber auch für den nichtlinearen Navigationsfilter, der hier entwickelt wurde, eine Abschätzung des Integritätsrisikos erstellt werden. Der tatsächliche Nachweis muss jedoch durch aufwändige Simulationen erbracht werden. Für die Erkennung, Identifizierung und Behebung von Modellfehlern wird die Verwendung von AFDIA (Autonomous Filter-based fault Detection, Identification and Model Adaptation) vorgeschlagen. Bisher wird nur die Identifizierung und Adaption für einzeln auftretende Fehler unterstützt. Alle simulierten Einzelfehler, beispielsweise Cycle Slips und Ausreißer der Code-Messungen, sind stets erfolgreich erkannt und kompensiert worden. Für die Positionslösung und für die Geschwindigkeitslösung werden Protection Levels berechnet. Das Herleiten der Protection Levels für den Filteransatz beschränkt sich auf zwei sich gegenseitig ausschließende Hypothesen: der Filter arbeitet im Normalbetrieb und es liegen keine systematischen Fehler vor oder es liegt genau ein systematischer Fehler vor. Durch Gewichtungsfaktoren, die größer eins sind, wird berücksichtigt, dass es in der Realität zu Abweichungen von den angenommenen Gaußverteilungen kommt. Man spricht in diesem Zusammenhang von Sigma-Verbreiterung zur Erfassung nicht-gaußscher Fehlerrandverteilungen.

Die Leistungsfähigkeit des Navigationsfilters und die Plausibilität der Protection Levels wurden durch Monte-Carlo Simulationen nachgewiesen. Zudem wurde mit einem Hardware-Simulator ein GALILEO-Szenario erzeugt und die Signale mit einem GALILEO-Empfänger für einen simulierten Landeanflug aufgezeichnet. Die Genauigkeit der Positionslösung, und dementsprechend auch die Größenordnung der Protection Levels, sind stark davon abhängig, ob die Trägerphasenmehrdeutigkeiten bereits gelöst wurden. Auf Grund des gewählten Filteransatzes werden allerdings auch schon für die Float-Lösung sehr hohe Genauigkeiten erzielt. In den Monte-Carlo Simulationen konnten die Trägerphasenmehrdeutigkeiten typischerweise ab einer Distanz von 20 km zur Referenzstation gelöst werden. Die Wahrscheinlichkeit, die Mehrdeutigkeiten falsch zu lösen, liegt dabei bei $1 \cdot 10^{-9}$. Bei der Auswertung der realen Empfängermessungen ließen sich die Trägerphasenmehrdeutigkeiten auf E1 bereits in einer Entfernung von 54 km zur Referenzstation erfolgreich lösen. Die sehr guten Ergebnisse bei den Tests mit den realen Signalmessungen ergeben sich durch die Verwendung der enorm rauscharmen Code-Messung auf E5a. Zudem wurden nur Ionosphärenfehler mit dem HW-Simulator simuliert, nicht aber Mehrwegeausbreitung und Troposphärenfehler. Der VPL (Vertical Protection Level) der Positionslösung nach erfolgreicher Trägerphasen-Mehrdeutigkeitslösung liegt unterhalb von 20 cm insofern eine gute Satellitengeometrie vorliegt. Das zugrunde liegende Integritätsrisiko wird dabei auf $3 \cdot 10^{-9}$ geschätzt. Sind nur sehr wenige Satelliten in Sicht, so kann sich auch ein VPL von knapp 2 m ergeben. Es stellt sich dann eine starke Abweichung zwischen dem Protection Level für den Fehlerfall und dem Protection Level für den Normalbetrieb ein, wobei das Protection Level für den Fehlerfall klar dominiert.

Die mit dem Filter erzielten Ergebnisse sind hinsichtlich der Positionsgenauigkeit und der dazugehörigen Protection Levels vielversprechend. Da der Nachweis des tatsächlichen Integritätsrisikos jedoch durch Simulationen erbracht werden muss, ist es entsprechend schwierig, in den Bereich von 10^{-9}, der in der zivilen Luftfahrt für die Landung ohne Sicht vorgesehen ist, vorzudringen. Anwendungen, bei denen noch höhere Genauigkeitsanforderungen als in der zivilen Luftfahrt bestehen, die aber ein größeres Integritätsrisiko zulassen, so dass der Nachweis durch Simulationen erfolgen kann, erscheinen geeigneter für den Einsatz des Navigationsfilters. Zu diesen flughafennahen Anwendungen gehören beispielsweise der automatisierte Frachtverkehr und Logistikaufgaben, aber auch der Einsatz für Landeanflüge im militärischen Bereich.

Acknowledgements

First, I would like to express my deep gratitude to my supervisors, Markus Rippl and Patrick Henkel, for their support, thoughtful comments and guidance throughout this study.

Very special thanks go to my examiner, Professor Dr.-Ing. Christoph Günther, for giving me the opportunity to work on this project. His lectures gave me a thorough insight into satellite navigation and I appreciate his vast knowledge.

Third, I would like to express my thanks to all my colleagues from the DLR and especially those from the integrity team for supporting me with this work. My special gratitude to Holmer Denks, who made it possible to carry out the real-signal tests with the Spirent hardware simulator.

Finally, I would like to thank my family and all my friends for their endless patience and continuous encouragement during the time of my master studies.

Table of Contents

I. List of Abbreviations

AFDIA	Autonomous Filter-based fault Detection, Identification and model Adaptation
ARNS	Aeronautical Radio-Navigation Service
BLUE	Best Linear Unbiased Estimator
CAR	Cascading Ambiguity Resolution
CP	Carrier Phase
DD	Double-Difference
DLR	Deutsche Luft- und Raumfahrtagentur
DOP	Dilution Of Precision
ECEF	Earth Centered Earth Fixed
EKF	Extended Kalman Filter
ENU	East-North-Up
FAA	Federal Aviation Administration
GBAS	Ground Based Augmentation System
GNSS	Global Navigation Satellite System
GPS	Global Positioning System
HAL	Horizontal Alert Limit
HMI	Hazardous Misleading Information
HPL	Horizontal Protection Level
IAB	Integer Aperture Bootstrapping
IB	Integer Bootstrapping
ILS	Instrument Landing System
INS	Inertial Navigation System
LAAS	Local Area Augmentation System
LAMBDA	Least Squares AMBiguity Decorrelation Adjustment
MDB	Minimum Detectable Bias
PDF	Probability Density Function
PRN	Pseudo Random Noise
RAIM	Receiver Autonomous Integrity Monitoring
RINEX	Receiver Independent Exchange format
RMS	Root Mean Square
RTK	Real-Time Kinematic

SBAS	Satellite Based Augmentation System
SF	Slant Factor
SIS	Signal-In-Space
SVID	Space Vehicle Identification number
TEC	Total Electron Content
TTA	Time To Alert
VAL	Vertical Alert Limit
VIG	Vertical Ionospheric Gradient
VPL	Vertical Protection Limit
VTEC	Vertical Total Electron Content
WAAS	Wide Area Augmentation System
WGS 84	World Geodetic System of 1984
WL	Widelane
WSSE	Weighted Sum of Squared Errors

II. List of Notation

Matrices and Vectors

A	Matrix A; matrices are represented by capital letters
$A_{(i,j)}$	Matrix element of A at the i^{th} row and j^{th} column
$\underline{A}$, $\underline{a}$	Vector $\underline{A}$ and vector $\underline{a}$; vectors are represented by an underscore
$\underline{A}_{(i)}$, $\underline{a}_{(i)}$	i^{th} entry of the vector $\underline{A}$ and $\underline{a}$
a	Scalar a; scalars are represented by lower case letters
$I_{(m)x(m)}$	Identity matrix of size (m)x(m)
$\|.\|_2$	Euclidean vector norm
$\circ$	Dot product

Kalman Filtering

H	Measurement sensitivity matrix
K	Kalman gain matrix
P	Covariance matrix of state estimation uncertainty
Q	Covariance matrix of process noise (in the system state dynamics)
R	Covariance matrix of measurement noise
$\underline{f}$	(Nonlinear) dynamic model functions
$\underline{h}$	(Nonlinear) measurement functions
$\underline{x}$	State vector
$\underline{y}$ / $\underline{z}$	Measurement vector
Φ	State transition matrix
$\underline{\upsilon}$	Measurement noise vector
$\underline{\omega}$	Process noise vector
(-)	A priori value
(+)	A posteriori value

Parameter Characterization

$D\{.\}$	Dispersion
$E\{.\}$	Expectation
$\chi^2(\upsilon,\lambda)$	Chi-square distributed with υ degrees of freedom and the noncentrality parameter λ
$F(\upsilon_1,\upsilon_2)$	F-distributed with υ_1 and υ_2 degrees of freedom
$N(\mu,\sigma^2)$	Normally distributed with mean μ and variance σ^2
$\tilde{\square}$	Randomness of a variable
$\hat{\square}$	(Float) Estimate of a parameter
$\breve{\square}$	(Integer) Estimate of a parameter

III. List of Figures

IV. List of Tables

1 Introduction

1.1 Requirements for Precision Approach and Landing

Real-time kinematic carrier phase techniques fulfill the highest accuracy requirements once the unknown carrier phase ambiguities have been resolved successfully. However, in the domain of safety-critical applications this is not yet sufficient: integrity, continuity and availability requirements have to be met as well. Many safety regulations for civil aviation are published by the Federal Aviation Administration (FAA) which belongs to the U.S. Department of Transportation. In this work the requirements for Category III precision instrument approach and landing are of special interest, since they are the most challenging for present-day technology. There is no decision height minimum assigned to Category III, e.g. it applies to the final phase of the flight (see Figure 1.1). The Instrument Landing System (ILS) category CAT III can be subdivided into three sub-classes: CAT IIIa requires a runway visual range of at least 700 feet, CAT IIIb requires a visual range of at least 150 feet and CAT IIIc finally applies to zero-visibility. The user-referenced position solution of the airplane has to be protected against severe position errors in order to prevent hazardous maneuvers due to wrong position information. Therefore a horizontal alert limit (HAL) and a vertical alert limit (VAL) are specified. The HAL is defined as the radius of a circle in the horizontal plane and the horizontal position estimate is required to be located within this circle with a specified probability as derived from the integrity risk [36]. The true horizontal position of the airplane is located in the center of this circle. Similarly, the VAL is defined as half the length of a segment on the vertical axis. The vertical position estimate is required to be located within this segment during the approach with a specified probability as derived from the integrity risk. The true vertical position of the airplane is located in the center of the segment. Concerning CAT IIIc precision approaches, the HAL is defined to be 15.5 m and the VAL is defined to be 5.3 m.

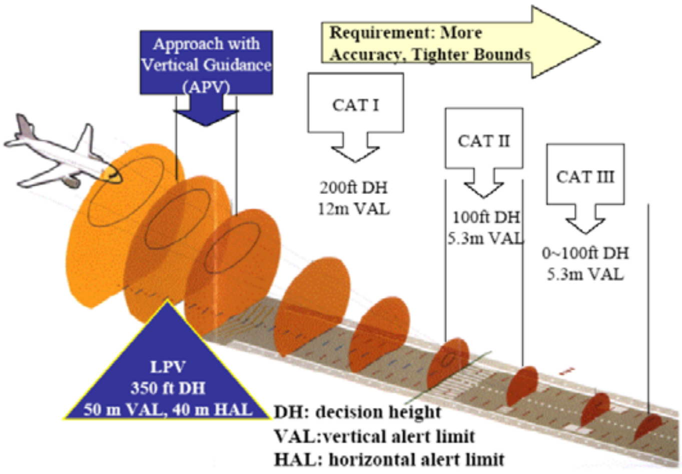

Figure 1.1: Requirements for precision approach and landing (Source FAA [8])

Recent research in the domain of GNSS (Global Navigation Satellite System) addresses to developing GNSS integrity architectures satisfying the requirements of civil aviation with regard to precision approach and even auto-landing. GNSS as primary source of navigation could replace ILS even during the most critical phases of flight if powerful integrity monitoring algorithms were available for high-accuracy relative positioning with GNSS. There are multiple GNSS-related navigation error sources, and only some of them are listed hereafter. The precision of the measurements may be deteriorated by multipath. Solar storms, unannounced satellite maneuvers, incorrect upload of the navigation message data, component failures as well as jumps of the satellite clock frequency or excessive clock drifts can cause severe degeneration of the position solution. Concerning carrier phase based positioning undetected cycle slips deteriorate the navigation performance and have to be accounted for as well.

The modernization of GPS and the introduction of GALILEO favor the research with regard to the use of carrier phase based techniques in safety-critical applications. It is expected that the availability of civil signals on multiple frequencies will improve the success rate of integer ambiguity resolution and shorten the time which is required in order to derive an ambiguity-fixed solution [37]. The GNSS frequencies considered for civil aviation have to reside in aeronautic radio-navigation service (ARNS) bands. The two ARNS bands which are of relevance for GNSS go from 960 – 1215 MHz and from 1559 – 1610 MHz. In case of modernized GPS, the L1 and L5 signals reside in an ARNS band. Concerning GALILEO, the E1 and E5 band are considered for civil aviation as they also reside in an ARNS band. The characteristics of the GNSS signals which are considered in this work are listed in Table 7.1 of Sect. 7.1.1.

The navigation filter which is derived here will always forward the best navigation solution that is presently available. This solution may either be a float solution or an ambiguity-fixed solution. As soon as the carrier phase ambiguities are resolved, the required accuracy for precision approach and landing will easily be met. Achieving the compliance with the integrity requirements of civil aviation will be more difficult part. Characteristic parameters of integrity are according to [23] the alert limit, the Time To Alert (TTA) and the integrity risk. The HAL and the VAL have been defined before. An alarm has to be raised if the user position error exceeds the alert limit. After the occurrence of an alarm condition the user has to be informed within the specified time to alert. Finally, the integrity risk is given by the probability of not informing the user-site of a position error that exceeds the alert limit within the specified TTA. Further important parameters are the continuity risk and the system availability. Preliminary numerical values for characteristic integrity parameters during precision approach and landing are indicated in the GNSS Evolutionary Architecture Study [9]. The system availability must be greater than 99% under all weather conditions. The continuity risk may not exceed $8x10^{-6}$ per 15 seconds for the duration of the airport approach. Finally, the integrity risk may not exceed $1x10^{-9}$ per approach if an autoland was to be performed.

Pervan et al. presented in [33] the requirements for military shipboard landings under zero-visibility conditions. A vertical alert limit of 1.1 m with an associated integrity risk of 10^{-7} and a system availability of at least 99.7% has been assessed. Compared to the requirements of civil aviation, the VAL is set even tighter, but the integrity risk is more relaxed. There are far more applications than precision approach and landing the navigation filter with integrated integrity monitoring features might address to. Among them are taxiing, coasting, automated cargo traffic and military aeronautical applications. All these applications require possibly even higher position accuracy than precision approach and landing in civil aviation, but are likely to be more relaxed with respect to the system availability and the continuity risk. Reliable carrier phase based relative positioning might therefore be even more appealing to airport-related traffic management and logistic if it turns out that ambiguity resolution on-the-fly does not meet the continuity and availability requirements of civil aviation.

1.2 Objectives and Outline of the Work

The main object of this work is to derive robust navigation filter algorithms for carrier phase based relative positioning and to investigate the integrity of the filter-based navigation solution. The derivation of an integrity concept requires basic knowledge in statistical test. In chapter 2 important parameter distributions, which are used when developing the protection levels for the navigation solution, are presented. Furthermore, the basics of hypothesis testing are introduced, which play a major role in GNSS model validation. Double-differenced pseudorange, carrier phase and Doppler shift measurements are processed by the navigation filter. The observation equations and the variance-covariance error propagation due to double-differencing are presented in chapter 3. This thesis is focused on processing dual-frequency measurement data from either GPS or GALILEO. The concept of forming inter-frequency combinations as well as its advantages and disadvantages are also depicted in chapter 3. The widelane phase measurement, which is generated by combining the E1 and E5a or L1 and L5 phase measurements, has a wavelength of 0.75 m. It is used as filter input with the expectation that the widelane integer ambiguities can be resolved faster than the carrier phase integer ambiguities. Furthermore, the utilization of ionosphere-free measurement combinations is considered as an alternative to estimating ionospheric delay terms. The navigation filter which is developed here relies on the theory of Kalman filtering. In chapter 4 the Kalman filter equations are introduced. Filter convergence and divergence are discussed as well as numerical stability of the Kalman filter equations. It has shown in the simulations in MATLAB® that numerical robustness due to computer round-off is indeed a problem with respect to the classical filter equations. Therefore, the Bierman-Thornton UD filter implementation is considered as well as further implementation aspects in order to improve numerical robustness. In chapter 5 the actual navigation filter architecture is presented in detail. An extended Kalman filter is used, where the linearization takes place about the filter's estimated trajectory. The underlying measurement model and state space model are depicted. Altogether three different ionosphere models are considered in order to estimate the ionospheric delay terms. The widelane and the carrier phase integer ambiguities are resolved in the filter by resorting to standard ambiguity resolution methods, e.g. the LAMBDA method or Integer Bootstrapping. The theoretical part of this thesis is completed with chapter 6. In this chapter a concept in order to monitor the integrity of the filter-based navigation solution is proposed. Autonomous Filter-based fault Detection, Identification and model Adaptation (AFDIA) is suggested for the overall model validation and the proceedings after an error has been detected. In addition, a procedure for computing the position and velocity solution protection levels for the fault-free mode and the fault-mode is derived. The navigation filter performance is evaluated by Monte-Carlo simulations and by real-signal tests, whose results are presented in chapter 7 and 8. It is verified whether AFDIA is capable of detecting and correcting single-channel biases. Finally, the results of this work are summarized in chapter 9.

2 Basics of Model Testing and Integrity

2.1 Important Distributions in Statistical Tests

2.1.1 Normal Distribution

Given the expectation $E\{N_{\mu,\sigma^2}\} = \mu$ and the dispersion $D\{N_{\mu,\sigma^2}\} = \sigma^2$ of a normally distributed random variable N_{μ,σ^2}, the general form of the normal distribution of N_{μ,σ^2} reads

$$F_{N,\mu,\sigma}(x) = P\left(N_{\mu,\sigma^2} \leq x\right) = \frac{1}{\sqrt{2\pi} \cdot \sigma} \int_{-\infty}^{x} \mathrm{e}^{-\frac{(t-\mu)^2}{2\cdot\sigma^2}} \mathrm{dt} \quad , \tag{2.1}$$

with the probability density function (PDF)

$$f_{N,\mu,\sigma}(x) = \frac{1}{\sqrt{2\pi} \cdot \sigma} \cdot \mathrm{e}^{-\frac{(t-\mu)^2}{2\cdot\sigma^2}} \quad . \tag{2.2}$$

The following notation is used in order to specify the normal distribution of an n-dimensional random vector $\underline{x}$:

$$\underline{x} \sim N\left(\underline{\mu}, \mathrm{Q}\right) \quad , \tag{2.3}$$

where $\underline{\mu}$ is the n-dimensional vector of expectation and Q is the (n)x(n) positive definite covariance matrix. The standardized normal distribution follows from the general normal distribution by setting $\mu = 0$ and $\sigma^2 = 1$:

$$\Phi(\mathrm{x}) = \mathrm{P}\left(N_{0,1} \leq \mathrm{x}\right) = \frac{1}{\sqrt{2\pi}} \cdot \int_{-\infty}^{\mathrm{x}} \mathrm{e}^{-\frac{t^2}{2}} \mathrm{dt} \tag{2.4}$$

2.1.2 Chi-Square Distribution

The χ^2-distribution belongs to the family of exponential distributions. Assuming that there are υ independently distributed samples $x_i \sim N(0,1)$, then the squared sum of the samples

$$\sum_{\mathrm{i}=1}^{\upsilon} \mathrm{x}_\mathrm{i}^2 \sim \chi^2(\upsilon) \quad , \quad \mathrm{x}_i \sim N(0,1) \tag{2.5}$$

is χ^2-distributed [27]. The central χ^2-PDF is given as

$$f_{\chi^2,\upsilon}(x) = \frac{e^{-\frac{x}{2}} \cdot x^{\frac{\upsilon}{2}-1}}{2^{\frac{\upsilon}{2}} \cdot \Gamma(\frac{\upsilon}{2})} \quad ,x > 0$$
$$f_{\chi^2,\upsilon}(x) = 0 \quad ,x \leq 0 \tag{2.6}$$

with υ degrees of freedom and the Gamma function

$$\Gamma(\mathrm{x}) = \int_0^\infty t^{x-1} \cdot e^{-t} dt \quad ,x > 0 \quad . \tag{2.7}$$

The run of the central χ^2-PDF for various degrees of freedom is illustrated in Figure 2.1.

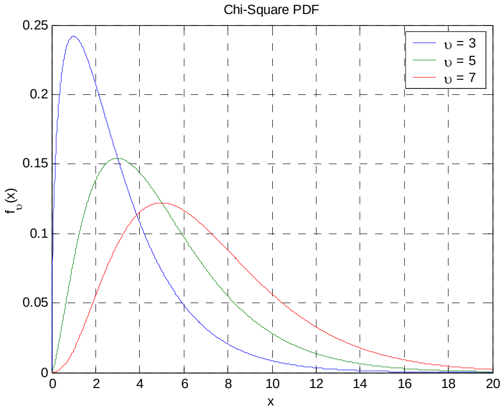

Figure 2.1: Central χ^2-PDF for three different degrees of freedom

The χ^2 cumulative distribution function is obtained from integrating the PDF of Eq. (2.6):

$$F_{\chi^2,\upsilon}(x) = P(\chi^2 \leq x) = \frac{1}{2^{\frac{\upsilon}{2}} \cdot \Gamma(\frac{\upsilon}{2})} \int_0^x e^{-\frac{t}{2}} \cdot t^{\frac{\upsilon}{2}-1} dt \quad ,(x > 0) \tag{2.8}$$

According to [3] it holds that $E\{\chi^2\} = \upsilon$ and $D\{\chi^2\} = 2 \cdot \upsilon$ in case of a central χ^2 distribution.

Now it is assumed that the υ samples are again independently normally distributed with unit variance, but arbitrary mean, e.g. $x_i \sim N(\mu_i, 1)$. Then the squared sum of samples

$$\sum_{\mathrm{i}=1}^{\upsilon} \mathrm{x}_\mathrm{i}^2 \sim \chi^2(\upsilon, \lambda) \quad , \quad \mathrm{x}_\mathrm{i} \sim N(\mu_\mathrm{i}, 1) \tag{2.9}$$

has a non-central χ^2 distribution with the noncentrality parameter λ, which follows from [27]:

$$\lambda = \sum_{\mathrm{i}=1}^{\upsilon} \mu_\mathrm{i}^2 \tag{2.10}$$

The non-central χ^2 probability density function with the noncentrality parameter λ is

$$
\begin{aligned}
f_{\chi^2,\upsilon,\lambda}(x) &= \frac{e^{-\frac{x+\lambda}{2}} \cdot x^{\frac{1}{2}\cdot(\upsilon-1)} \cdot \sqrt{\lambda}}{2 \cdot (\lambda \cdot x)^{\frac{\upsilon}{4}}} \cdot I_{\frac{\upsilon}{2}-1}\left(\sqrt{\lambda \cdot x}\right) \quad &, x > 0 \quad , \\
f_{\chi^2,\upsilon,\lambda}(x) &= 0 \quad &, x \leq 0 \quad ,
\end{aligned}
\tag{2.11}
$$

where $I_{\mathrm{k}}(z)$ is a modified Bessel function of the first kind

$$
I_{\mathrm{k}}(z) = \left(\frac{z}{2}\right)^{k} \cdot \sum_{i=0}^{\infty} \frac{\left(\frac{z}{2}\right)^{2\cdot i}}{i!\,\Gamma(k+i+1)} \quad . \tag{2.12}
$$

In case of a non-central χ^2 distribution it holds that $E\{\chi^2\} = \upsilon + \lambda$ and $D\{\chi^2\} = 2 \cdot \upsilon + 4 \cdot \lambda$. The non-central χ^2-PDF is plotted in Figure 2.2 for various degrees of freedom.

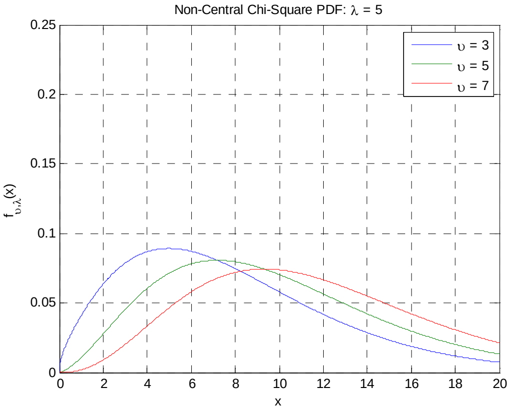

Figure 2.2: Non-central χ^2-PDF with λ=5 for three different degrees of freedom

2.1.3 F-Distribution

A random variable $F_{\upsilon_1,\upsilon_2}$ that is calculated from the ratio of two independent χ^2-distributed random variables X_1 and X_2 divided by their degrees of freedom υ_1 and υ_2,

$$
F_{\upsilon_1,\upsilon_2} = \frac{X_1 \cdot \upsilon_2}{\upsilon_1 \cdot X_2} \sim F(\upsilon_1, \upsilon_2) \quad , \quad X_1 \sim \chi^2(\upsilon_1) \quad \text{and} \quad X_2 \sim \chi^2(\upsilon_2) \quad , \tag{2.13}
$$

has an F-distribution with υ_1 and υ_2 degrees of freedom [3]. The central F-PDF with degrees of freedom υ_1 and υ_2 reads

$$
\begin{aligned}
f_{F,\upsilon_1,\upsilon_2}(x) &= \left(\frac{\upsilon_1}{\upsilon_2}\right)^{\frac{\upsilon_1}{2}} \cdot \frac{\Gamma\left[\frac{\upsilon_1+\upsilon_2}{2}\right] \cdot x^{\frac{\upsilon_1-2}{2}}}{\Gamma\left(\frac{\upsilon_1}{2}\right) \cdot \Gamma\left(\frac{\upsilon_2}{2}\right) \cdot \left[1 + \frac{\upsilon_1}{\upsilon_2} \cdot x\right]^{\frac{\upsilon_1+\upsilon_2}{2}}} \quad &, x > 0 \\
f_{F,\upsilon_1,\upsilon_2}(x) &= 0 \quad &, x \leq 0
\end{aligned}
\tag{2.14}
$$

and the cumulative F-distribution function is given by

$$F_{F,\upsilon_1,\upsilon_2}(x) = P\left(F_{\upsilon_1,\upsilon_2} \le x\right) = \int\limits_0^x f_{F,\upsilon_1,\upsilon_2}(t)dt \quad . \tag{2.15}$$

It holds that the expectation of $F_{\upsilon_1,\upsilon_2} \sim F(\upsilon_1, \upsilon_2)$ is $E\{F_{\upsilon_1,\upsilon_2}\} = \frac{\upsilon_2}{\upsilon_2 - 2}$ $(\upsilon_2 > 2)$ and its dispersion is $D\{F_{\upsilon_1,\upsilon_2}\} = \frac{2 \cdot \upsilon_2^2 \cdot (\upsilon_1 + \upsilon_2 - 2)}{\upsilon_1 \cdot (\upsilon_2 - 2)^2 \cdot (\upsilon_2 - 4)}$ $(\upsilon_2 > 4)$. The run of the central F-PDF is depicted in Figure 2.3, where the first degree of freedom υ_1 is set to a fixed value and second degree of freedom υ_2 is varied.

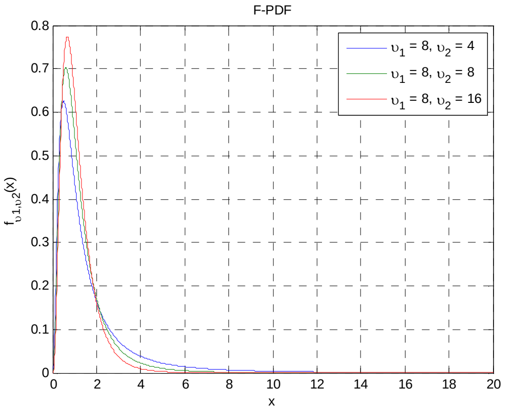

Figure 2.3: F-PDF in dependence of the degrees of freedom υ_1 and υ_2

In the following the more general case of two independently normally distributed random vectors with arbitrary expectation $\underline{\mu}$, $\underline{x}_1 \sim N\left(\underline{\mu}_1, Q_1\right)$ of length υ_1 and $\underline{x}_2 \sim N\left(\underline{\mu}_2, Q_2\right)$ of length υ_2, will be considered. The ratio

$$\frac{\underline{x}_1^T \cdot Q_1^{-1} \cdot \underline{x}_1 \cdot \upsilon_2}{\upsilon_1 \cdot \underline{x}_2^T \cdot Q_2^{-1} \cdot \underline{x}_2} \sim F(\upsilon_1, \upsilon_2, \lambda) \quad , \quad \underline{x}_1 \sim N\left(\underline{\mu}_1, Q_1\right) \quad \text{and} \quad \underline{x}_2 \sim N\left(\underline{\mu}_2, Q_2\right) \tag{2.16}$$

has a non-central F-distribution (see [47]) with the noncentrality parameter λ

$$\lambda = \underline{x}_1^T \cdot Q_1^{-1} \cdot \underline{x}_1 \quad . \tag{2.17}$$

Furthermore, the following notation is used in this work:

$$\frac{\underline{x}^T \cdot Q \cdot \underline{x}}{\upsilon} \sim F(\upsilon, \infty, \lambda) \quad , \quad \underbrace{\underline{x}}_{\upsilon \times 1} \sim N\left(\underline{\mu}, Q\right) \tag{2.18}$$

A further important relationship between F-distributed random variables and χ^2-distributed random variables in the context of statistical test, which is frequently used in this work, becomes obvious from Eq. (2.18): If $\underline{x} \sim N(\underline{\mu}, Q)$ is a vector of length υ with normally distributed random variables with mean $\underline{\mu}$ and the covariance matrix Q, then $\left(\underline{x}^T \cdot Q^{-1} \cdot \underline{x}\right) \sim \chi^2(\upsilon, \lambda)$ is χ^2-distributed with υ degrees of freedom and the noncentrality parameter $\lambda = \underline{\mu}^T \cdot Q^{-1} \cdot \underline{\mu}$. By dividing the weighted sum of squared entries $\underline{x}^T \cdot Q^{-1} \cdot \underline{x}$ by the number of degrees of freedom υ, then $\frac{\underline{x}^T \cdot Q^{-1} \cdot \underline{x}}{\upsilon} \sim F(\upsilon, \infty, \lambda)$ is F-distributed with υ and ∞ degrees of freedom.

2.2 Statistical Testing

2.2.1 Fundamentals of Statistical Test Theory

In hypothesis testing the problem of deciding whether a hypothesis that has been formulated is correct or false is solved by statistical means. Based on the test result the hypothesis is accepted or rejected. An introduction to statistical tests can be found in [18]. First, the parameter space θ is divided into two mutually exclusive and non-empty sub-sets θ_0 and θ_1:

$$\theta = \theta_0 \cup \theta_1 \tag{2.19}$$

The sub-set θ_0 is called the region of acceptance, and the subset θ_1 the critical region. A statistical test provides a decision rule for any realization x of the random variable X, which assesses whether the null hypothesis $H_0 \quad (\vartheta \in \theta_0)$ or the alternative hypothesis $H_1 \quad (\vartheta \in \theta_1)$ is accepted. In hypothesis testing the correct decision may be taken or one of two possible errors may be committed, see also Table 2.1. The error of the 1st kind denotes the case that the null hypothesis H_0 is wrongly rejected due to the test outcome. The probability of wrongly rejecting H_0 is given by α, which is also referred to as level of significance of the statistical test. The confidence level of the statistical test is given by $1\text{-}\alpha$. The error of the 2nd kind denotes the case that the null hypothesis H_0 is wrongly accepted due to the test outcome, but in truth it holds that $\vartheta \in \theta_1$. The probability of the error of the 2nd kind is β. Although it is desirable to keep both the probability of the error of the 1st kind and the probability of the error of the 2nd kind to a minimum, it is not possible to control both probabilities simultaneously for a given number of observations [27]. The power of the test is given by $1\text{-}\ \beta$, e.g. the probability of rejecting H_0 when it is indeed false.

Provided that it is known that the random variable under test is either normally-, χ^2- or F-distributed, the critical value k can be determined uniquely for a given level of significance α and for the concrete PDF at hand. The critical value k is also referred to as $(1\text{-}\alpha)$-quantile or decision threshold and follows from solving the cumulative normal PDF in Eq. (2.1), or the cumulative χ^2-PDF in Eq. (2.8), or cumulative F-PDF in Eq. (2.15), respectively, for the upper limit of the integral. The $(1\text{-}\alpha)$-quantiles are frequently computed in advance for the different levels of significance α which are of interest for the concrete application at hand, and for different degrees of freedom in case of the χ^2-distribution and the F-distribution. Then the pre-computed quantiles are saved in lookup-tables in order to reduce the real-time computational effort during operation.

Table 2.1: Hypothesis Testing

		Reality	
		$\vartheta \in \Theta_0$	**$\vartheta \in \Theta_1$**
Decision	**H_0**	Correct decision *(normal operation)*	Error of 2nd kind (β) *(missed detection)*
	H_1	Error of 1st kind (α) *(false alarm)*	Correct decision *(alarm)*

Statistical testing is applied in GNSS integrity monitoring algorithms. In safety-critical navigation tasks it has to be ensured that an alert is forwarded within the specified TTA with a probability close to 1 if the position error does exceed a critical value. Therefore, the probability of missed detection $P_{MD,[t,t+T_M]}$ is introduced. $P_{MD,[t,t+T_M]}$ is defined as the probability of not raising an alarm within the specified TTA after a critical event has occurred. A critical event occurs when the position estimate is outside of the admissible region for the position solution. In this work P_{MD} will only refer to the current observation epoch and therefore no time interval index is used in the notation. In the context of hypothesis testing, P_{MD} corresponds to the probability β of the error of the 2nd kind. Besides a very low probability of missed detection, high continuity of the system during the duration of a maneuver T_M shall be preserved. The probability of the continuity risk $P_{cr,[t,t+T_M]}$ can be approximated as [14]:

$$P_{cr,[t,t+T_M]} = P\left(A_{[t,t+T_M]} | E_{[t,t+T_M-TTA]}\right) + P_{FA,[t,t+T_M]} \quad , \tag{2.20}$$

with $P\left(A_{[t,t+T_M]} | E_{[t,t+T_M-TTA]}\right)$ is the probability of an alert A in the interval $[t, t+T_M]$ under the condition of a critical event E in the interval $[t, t+T_M-TTA]$. $P_{FA,[t,t+T_M]}$ is the probability of false alarm in the interval $[t, t+T_M]$, e.g. the probability of raising an alarm although no critical event has occurred. Hereafter, the probability of false alarm will only refer to the current observation epoch. Therefore, the notation P_{FA} is used in the following sections instead of $P_{FA,[t,t+T_M]}$. P_{FA} corresponds to the probability α of the error of the 1st kind in hypothesis testing. The procedure that is frequently used in GNSS integrity monitoring algorithms is to fix the probability of false alarm in order to derive the decision threshold, e.g. the (1-α)-quantile, for the test statistic.

2.2.2 Hypothesis Testing in GNSS Model Validation

Hypothesis testing is used in order to validate the stochastic and the functional GNSS model. The following considerations refer to parameter adjustment by least-squares estimation in batch mode. The randomness of variables is explicitly expressed by a tilde $\tilde{\square}$ above the variable name in this section. Let the functional model be

$$E\left\{\underline{\tilde{y}}\right\} = A \cdot \underline{x} \quad , \tag{2.21}$$

where $\underline{\tilde{y}}$ is the random vector of observables, A is the design matrix and $\underline{x}$ is the vector of unknown parameters. The stochastic model that reflects the measurement uncertainty is expressed by

$$D\left\{\underline{\tilde{y}}\right\} = R \quad , \tag{2.22}$$

where R is the covariance matrix of the observables. The definition of the functional and stochastic model is used in order to formulate the null hypothesis:

$$H_0: \quad E\left\{\underline{\tilde{y}}\right\} = A \cdot \underline{x} \quad , D\left\{\underline{\tilde{y}}\right\} = R \tag{2.23}$$

Furthermore, it is assumed that $\underline{\tilde{y}}$ is normally distributed, e.g. the null hypothesis is completely specified by:

$$H_0: \quad \underline{\tilde{y}} \sim N\left(A \cdot \underline{x}, R\right) \tag{2.24}$$

H_0 is tested against an alternative hypothesis, H_1, which reflects the presence of biased observables:

$$H_1:\quad E\left\{\underline{\tilde{y}}\right\} = A\cdot\underline{x} + E\cdot\underline{\varepsilon}\quad, D\left\{\underline{\tilde{y}}\right\} = R \tag{2.25}$$

E is a known design matrix of model errors and $\underline{\varepsilon}$ is an unknown q-dimensional vector of biases that have been assumed to be absent in the null hypothesis. An appropriate test statistic for the quality control of the functional model is given in Teunissen [44]:

$$\tilde{T} = \frac{1}{q}\cdot\underline{\hat{\tilde{v}}}^T\cdot R^{-1}\cdot E\cdot\left[E^T\cdot R^{-1}\cdot Q_{\underline{\hat{\tilde{v}}}}\cdot R^{-1}\cdot E\right]^{-1}\cdot E^T\cdot R^{-1}\cdot\underline{\hat{\tilde{v}}}\quad, \tag{2.26}$$

where $\underline{\hat{\tilde{v}}} = \underline{\tilde{y}} - \underline{\hat{\tilde{y}}}$ is the measurement residuals vector after the least-squares adjustment and $Q_{\underline{\hat{\tilde{v}}}}$ is the associated covariance matrix of measurement residuals. If H_0 is true, the test statistic has a central F-distribution with $\upsilon_1 = \mathrm{q}$ and $\upsilon_2 = \infty$ degrees of freedom:

$$H_0:\quad \tilde{T}\sim F(q,\infty) \tag{2.27}$$

Contrary, the distribution of the test statistic is non-central under H_1:

$$H_1:\quad \tilde{T}\sim F(q,\infty,\lambda\neq 0)\quad, \tag{2.28}$$

where the noncentrality parameter λ follows from

$$\lambda = \underline{\varepsilon}^T\cdot E^T\cdot R^{-1}\cdot Q_{\underline{\hat{\tilde{v}}}}\cdot R^{-1}\cdot E\cdot\underline{\varepsilon}\quad . \tag{2.29}$$

For a fixed level of significance α the hypothesis H_0 is only accepted if $\tilde{T} < D_\alpha$. The decision threshold D_α is chosen such that it fulfills $F_{F,\mathrm{q},\infty}(D_\alpha) = 1-\alpha$ according to Eq. (2.15). This ensures that the probability of falsely rejecting H_0 although it is indeed true, e.g. the error of the 1st kind, does not exceed a specified limit. The error of the 2nd kind implies that H_0 is accepted while it is indeed false. The probability of the error of the 2nd kind follows from:

$$\beta = \int_0^{D_\alpha} f_{F,\mathrm{q},\infty,\lambda\neq 0}(x)dx \tag{2.30}$$

In general, the model error $E\cdot\underline{\varepsilon}$ is not known. This implies that one cannot compute the noncentrality parameter λ from Eq. (2.29). However, if the probabilities α and β follow from the system specification, it is possible to determine λ from Eq. (2.30). Once the noncentrality parameter λ is known, it is possible to indicate the Minimum Detectable Bias (MDB). The MDB is the size of a model error that can still be detected with a probability of $1-\beta$. Restricting to the one-dimensional case where q=1 (e.g. $\underline{\varepsilon}$ is reduced to a scalar), and therefore E reduces to a vector $\underline{e}$, the MDB $|\varepsilon|$ can be calculated from [44]:

$$|\varepsilon| = \sqrt{\frac{\lambda}{\underline{e}^T\cdot R^{-1}\cdot Q_{\underline{\hat{\tilde{v}}}}\cdot R^{-1}\cdot\underline{e}}} \tag{2.31}$$

2.3 Basics of RAIM

Integrity monitoring is crucial during landing approaches since deviations of the estimated user position from the actual flight path lead to hazardous misinformation. There are several methods of GNSS integrity monitoring, e.g. RAIM which is an acronym for Receiver Autonomous Integrity Monitoring, SBAS (Satellite Based Augmentation System) and GBAS (Ground Based Augmentation System). The benefit of RAIM is that the integrity monitoring of the position solution is directly performed at the user-site. RAIM becomes even more important if GNSS is to be used as primary navigation system at the airplane. In order to allow for integrity checks it is required that redundant measurements are available. RAIM has originally been developed for standalone GPS. If only pseudorange measurements are used to derive the position solution, at least five visible satellites are required in order to detect hazardous position errors [23]. The measurement redundancy is one since there are five pseudorange measurements available, but only four system unknowns, e.g. the user position vector and the user receiver clock bias. Given that there are six or even more satellites in view, the faulty satellite can even be identified and excluded from the navigation solution. This is an important feature in order to reduce the continuity risk for airborne use of GNSS. RAIM algorithms aim at determining protection levels for the horizontal and vertical component of the position estimate. These levels restrict the maximum deviation of the position estimate from the true position without being detected with a specified probability of missed detection and a specified probability of false alert. The horizontal and vertical position errors are user-referenced. The horizontal position error comprises the error in the east and north component, while the vertical position error comprises the up-component. The probability of missed detection P_{MD} is derived from the integrity risk and the probability of false alert P_{FA} follows from the continuity risk according to the respective system specification.

The horizontal and vertical position errors are not directly observable. Other methods have to be found in order to derive appropriate test statistics. Three popular RAIM schemes that have already been developed in the late 1980s are:

- Range-Comparison Method [26]
- Least-Squares Residuals Method [31]
- Parity-Space Method [38]

The equivalence of the three RAIM schemes with regard to equal alarm rates is demonstrated in Brown [4]. Comparing the RAIM schemes under the aspect of implementation, the least-squares residuals method seems favorable. The test statistic is obtained by simply summing up the squared residuals of the least-squares solution. If a weighted least-squares approach is used in order to derive the position solution, Walter et al. [50] propose to compute the weighted sum of least-squares residuals. The weighting matrix is given by the inverse of the covariance matrix of measurement noise. The identification of biased measurements with the parity-space method is less computational expensive than the range-comparison method, which requires the computation of different permutations.

In the following the test statistic will be derived from the Weighted Sum of Squared Errors (WSSE). The WSSE has a chi-square distribution as the least-squares residuals vector $\underline{r}$ is normally distributed. The number of degrees of freedom of the chi-square distribution depends on the actual algorithm in use [55]:

$$WSSE = \underline{r}^T \cdot W \cdot \underline{r} \quad \sim \quad \begin{cases} \chi^2(n_{meas} - n_{states}, \lambda), & snapshot\ algorithm \\ \chi^2(n_{meas}, \lambda) \quad , & filter\ approach \end{cases} \tag{2.32}$$

Concerning snapshot RAIM algorithms, the size of the parity vector is given by the number of measurements n_{meas} reduced by the number of states n_{states} to be estimated. Thus, the WSSE is composed of only $v = n_{meas} - n_{states}$ independently normally distributed random variables. The number of states is four if only the user position vector and the receiver clock bias are to be estimated. In contrast to snapshot RAIM algorithms, the number of degrees of freedom of filter-based integrity monitoring algorithms is $v = n_{meas}$ as both present and past information is used to derive the navigation solution. The computation of the residual vector $\underline{r}$ and the weighting matrix W in Eq. (2.32) is also dependent on the concrete algorithm in use. If a measurement is biased, the noncentrality parameter λ of the chi-square PDF differs from zero. The hypothesis H_0 "no bias present" is tested against the alternative hypothesis H_1 "bias present". The formal representation of hypothesis testing has already been introduced in Sect. 2.2.1. The central chi-square PDF which corresponds to H_0 and the non-central chi-square PDF which corresponds to H_1 are depicted graphically in Figure 2.4. The graphic represents the case that the WSSE itself is taken as normalized test statistic. The degrees of freedom of the chi-square PDFs are given by the parameter υ.

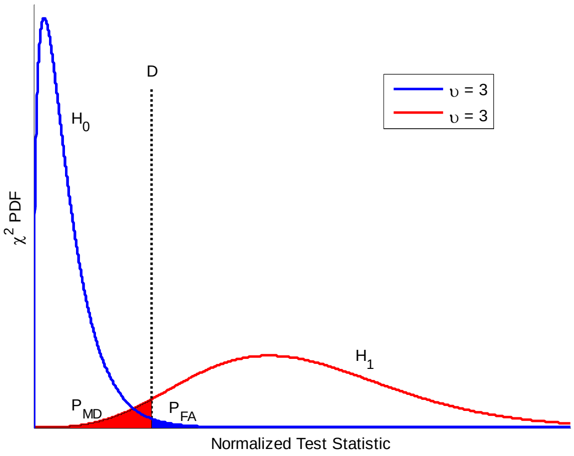

Figure 2.4: Relationship between the detection threshold, the probability of missed detection and the probability of false alert

If the probability of false alert P_{FA} is specified, the decision threshold D can be computed from:

$$1 - P_{FA} = \int_{0}^{D} f_{\chi^2,\upsilon}(x)dx \tag{2.33}$$

Many RAIM algorithms ([4], [10], [50]) take the square root of the WSSE as test statistic instead of the WSSE itself. Consequently, the new decision threshold follows from the square root of the decision threshold D indicated in Eq. (2.33). The navigation system is only declared available if the computed protection levels (HPL, VPL) are below the specified alert limits (HAL, VAL):

$$\left.\begin{array}{l} HPL < HAL \\ VPL < VAL \end{array}\right\} \; RAIM\ is\ available \tag{2.34}$$

If the inequalities indicated in Eq. (2.34) are not fulfilled, an alert flag has to be raised that indicates that the position solution may not be trusted.

Low availability of integrity monitoring is not tolerable in aeronautics. Especially during a landing approach high availability of RAIM is essential to support GNSS as primary means of navigation. It has to be investigated if a filter-based approach and the usage of low-noise carrier phase measurements for positioning do improve the availability of modified RAIM algorithms.

3 GNSS Observation Model

3.1 Single-Point, Differential and Relative Positioning

Both differential and relative positioning involve two or even more receivers in the system, while one receiver is sufficient for single-point positioning. However, single-point positioning is less accurate than differential or relative positioning. The following definition of single-point positioning assumes that no single-differences between different satellites (see Sect. 3.5) and no inter-frequency combinations of observations (see Sect. 3.4) are formed. Under these assumptions both the receiver antenna coordinates and the receiver clock error plus the receiver hardware biases have to be estimated in single-point positioning. Satellite-dependent nuisance parameters and atmospheric refraction are assumed to be absent. These assumptions are not justified where high precision of the position solution is required. Differential positioning aims at improving the precision of the position solution by applying extrapolated differential corrections to the measurements from the user receiver. The differential corrections are calculated at one or multiple reference receiver sites and provided to the user receiver via a data link. All further considerations are restricted to the use of two receivers in the system. One receiver serves as reference receiver whose coordinates are known precisely. The second receiver is the user receiver which may be mobile or static and whose coordinates are to be determined. In Figure 3.1 the constellation of a reference receiver A and a user receiver B as well as two satellites S1 and S2 is shown. The displacement between receiver A and B is denoted as baseline b_{AB}.

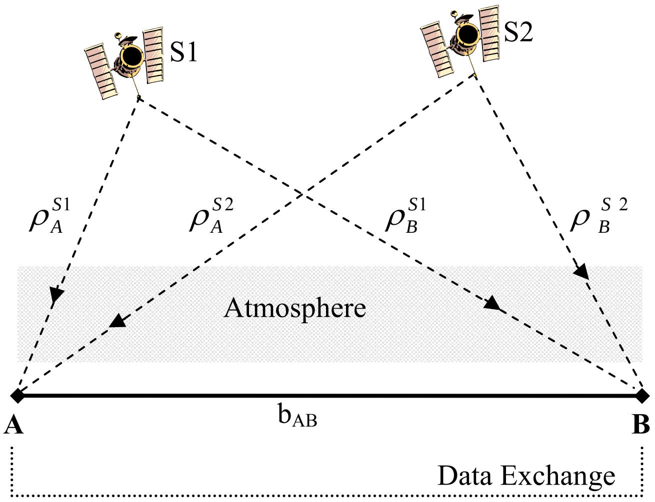

Figure 3.1: Differential and relative positioning

In case of differential positioning the knowledge of the reference receiver coordinates is exploited by computing the difference between the measured range and the true geometric range between the reference station and each satellite in view. From this information the differential corrections are derived. According to Hofmann-Wellenhof et al. [19], satellite-related and medium-related biases can be reduced significantly by applying the differential corrections at the user receiver site. Although the precision of differential positioning is already much better than the precision of single-point positioning, further improvement can be achieved by relative positioning. In case of relative positioning, the observations from the reference receiver are directly transferred to the user receiver instead of transferring extrapolated differential corrections. It is required that the reference receiver and the user receiver make their observations (almost) simultaneously to a sufficient number of the same satellites. Furthermore, there are stringent requirements on the data link with regard to delay times in order to support real-time kinematic (RTK) positioning. Therefore, the operational area of relative positioning is restricted given that there is not a whole network of reference receivers. However, relative positioning is well-suited for precision landing as the operational area is restricted to the vicinity of the airport. Nuisance parameters can be reduced to a great degree by applying differencing methods that are described in detail in Sect. 3.5. Integrity concepts for differential and relative positioning systems are more complex than those for single-point positioning since the reliability of data link and reference receiver related issues have to be considered as well. In this work the focus is on integrity monitoring at the user receiver site when using relative positioning techniques.

3.2 Coordinate Systems

The global Cartesian Earth-Centered Earth-Fixed (ECEF) coordinate system is chosen as reference system for relative positioning in this work. The origin of the ECEF coordinate system is identical with the origin of the World Geodetic System 1984 (WGS-84) ellipsoidal. Transformation equations for the conversion from ellipsoidal coordinates to Cartesian coordinates and vice versa can be found in textbooks on GNSS, for example in [13], [19] and [23].

Besides the two global coordinate systems, e.g. ECEF and WGS-84, also a local coordinate system is frequently used in this thesis. The first reason for referring to local coordinates is that the protection levels and alert limits of RAIM are in general indicated in a user-referenced coordinate system. The second reason is that in navigation it is often desirable to exclude satellites seen under low elevation angles at the receiver-site from the position solution. Signals from these satellites suffer from large atmospheric delay and are more likely subject to multipath. Therefore, satellites that are seen below a scalable receiver masking angle are either excluded from the position solution or they are scaled with less weight in a weighted position solution. In order to compare the satellite elevation angles at the receiver site with the receiver masking angle, a transformation from ECEF coordinates to local level coordinates, e.g. East-North-Up (ENU) coordinates, is performed. Then the elevation angle ϑ can be computed from the Cartesian ENU coordinates x_{east}, x_{north}, x_{up} by applying a conversion to spherical coordinates [3]:

$$\vartheta = \frac{\pi}{2} - tan^{-1}\left(\frac{\sqrt{x_{east}^2 + x_{north}^2}}{x_{up}}\right) = cot^{-1}\left(\frac{\sqrt{x_{east}^2 + x_{north}^2}}{x_{up}}\right) \tag{3.1}$$

However, initially the satellite and receiver coordinates are indicated in the global ECEF coordinate system and a conversion to ENU is required. After [19], the satellite ECEF coordinates can be transformed to ENU coordinates with the receiver antenna location in the origin of the local coordinate system by

$$\underline{X}_{ENU}^{S} = \begin{bmatrix} -\sin\lambda_R & \cos\lambda_R & 0 \\ -\sin\varphi_R\cos\lambda_R & -\sin\varphi_R\sin\lambda_R & \cos\varphi_R \\ \cos\varphi_R\cos\lambda_R & \cos\varphi_R\sin\lambda_R & \sin\varphi_R \end{bmatrix} \cdot \begin{bmatrix} x^S - x_R \\ y^S - y_R \\ z^S - z_R \end{bmatrix} \quad , \tag{3.2}$$

where:

$\underline{X}_R = (x_R \quad y_R \quad z_R)^T$: Receiver position in ECEF coordinates

$\underline{X}^S = (x^S \quad y^S \quad z^S)^T$: Satellite position in ECEF coordinates

$\underline{X}_{ENU}^{S} = \left(x_{east}^{S} \quad x_{north}^{S} \quad x_{up}^{S}\right)^T$: Satellite position in ENU coordinates

φ_R: WGS-84 ellipsoidal latitude of the receiver position

λ_R: WGS-84 ellipsoidal longitude of the receiver position

The geodetic latitude φ_R and longitude λ_R of the receiver position with respect to the WGS-84 ellipsoid can be derived from the receiver's ECEF coordinates $\underline{X}_R$ in closed-form. While λ_R follows immediately from

$$\lambda_R = \begin{cases} \tan^{-1}\left(\dfrac{y_R}{x_R}\right) & , \; x_R \geq 0 \\ \tan^{-1}\left(\dfrac{y_R}{x_R}\right) + \pi & , \; x_R < 0 \; and \; y_R \geq 0 \\ \tan^{-1}\left(\dfrac{y_R}{x_R}\right) - \pi & , \; x_R < 0 \; and \; y_R < 0 \end{cases} \tag{3.3}$$

a closed-form solution of φ_R is rather lengthy and can be found in [23]. Instead of applying a closed-form solution, the geodetic latitude and height can also be found iteratively as demonstrated in [19]. The geodetic latitude φ_R can be expressed as a function of the radius of curvature N in prime vertical and the geodetic height h_R:

$$\varphi_R = \tan^{-1}\left[\frac{z_R}{\sqrt{x_R^2 + y_R^2}} \cdot \left(1 - \frac{a^2 - b^2}{a^2} \cdot \frac{N}{N + h}\right)^{-1}\right] \quad , \tag{3.4}$$

where $a = 6378137.0\,m$ is the semi-major axis of the WGS-84 reference ellipsoid and $b = 6356752.314\,m$ is the semi-minor axis. The radius of curvature N in prime vertical is given by

$$N = \frac{a}{\sqrt{1 - \dfrac{a^2 - b^2}{a^2} \cdot sin^2\varphi_R}} \tag{3.5}$$

and the geodetic height h_R follows from

$$h_R = \frac{\sqrt{x_R^2 + y_R^2}}{cos\,\varphi_R} - N \quad . \tag{3.6}$$

In the positioning software Eq. (3.4) and Eq. (3.6) are solved iteratively.

3.3 Observation Equations

3.3.1 Pseudorange Observation

The notation pseudo-ranging has been introduced into the terminology of satellite navigation in order to indicate that the measured ranges differ from the true geometric ranges. The receiver measurements are biased by clock offsets since the receiver clocks are not perfectly synchronized to GPS/GALILEO system time. Besides the clock offset, there are far more error sources which deteriorate the pseudorange measurements and that have to be accounted for in order to derive an accurate position solution.

The following notation is used in this work: the subscript c indicates the dependency on the carrier frequency, the subscript R indicates the receiver and the superscript S indicates the satellite, respectively. The time-dependency of the parameters is not explicitly shown. Using this notation, the pseudorange measurement can be expressed by

$$\begin{aligned}\rho_{c,R}^{Sj} = r_R^{Sj} + c_0 \cdot \left(dt^{Sj} - dt_R\right) + d_{ion,R}^{Sj} \cdot \frac{f_{ion}^2}{f_c^2} + d_{orb}^{Sj} + d_{trop,R}^{Sj} + d_{m_{\rho,c},R}^{Sj} \\ + d_{b_c}^{Sj} + d_{b_c,R} + v_{\rho_c,R}^{Sj} \quad ,\end{aligned} \tag{3.7}$$

where:

$\rho_{c,R}^{Sj}$: Pseudorange measurement

r_R^{Sj}: True geometric range between the receiver R and the satellite S_j:

$$r_R^{Sj} = \sqrt{(x^{Sj} - x_R)^2 + (y^{Sj} - y_R)^2 + (z^{Sj} - z_R)^2}$$

c_0: Velocity of light

dt^{Sj}: Satellite clock error

dt_R: Receiver clock error

$d_{ion,R}^{Sj}$: Range error due to ionospheric refraction with respect to the frequency f_{ion}

f_c : Carrier frequency

d_{orb}^{Sj}: Orbital error

$d_{trop,R}^{Sj}$: Troposphere range error

$d_{m_{\rho,c},R}^{Sj}$: Multipath range error on the pseudorange

$d_{b_c}^{Sj}$: Satellite hardware bias

$d_{b_c,R}$: Receiver hardware bias

$v_{\rho_c,R}^{Sj}$: Pseudorange measurement noise

By expressing the range difference due to ionospheric refraction by $d_{ion,R}^{Sj} \cdot \frac{f_{ion}^2}{f_c^2}$, range errors which correspond to higher order terms of the ionospheric gradient are assumed to be negligible.

3.3.2 Carrier Phase Observation

The carrier phase observation is ambiguous in contrast to the pseudorange observation. Carrier phase measurements are obtained by comparing the phase of the carrier signal generated by the receiver at signal reception time with phases of the carrier signals generated by the satellites at signal transmission time. The ambiguity of the carrier phase measurement results from the periodicity of the phase with 2π. Only the fractional carrier phase can be measured, leaving an unknown number of integer cycles between the satellite and the receiver. However, only the initial integer ambiguities are unknown. With the help of a cycle counter all further inter cycles are recorded during continuous tracking as long as no cycle slip occurs. Carrier phase observations are of special importance for high-accuracy positioning. The receiver noise of the carrier phase measurement is frequently lower than 0.01 cycles, which corresponds to a measurement noise in the range domain of less than 2 mm at L1 or E1, respectively. Therefore, the key to RTK positioning with accuracies of the position solution in the centimeter range is fast carrier-cycle ambiguity resolution. The parameterization of the carrier phase observation can be written as

$$\begin{aligned}\phi_{c,R}^{Sj} = r_R^{Sj} + \lambda_c \cdot N_{c,R}^{Sj} + c_0 \cdot \left(dt^{Sj} - dt_R\right) - d_{ion,R}^{Sj} \cdot \frac{f_{ion}^2}{f_c^2} + d_{orb}^{Sj} + d_{trop,R}^{Sj} \\ + d_{m_{\phi,c},R}^{Sj} + d_{b_{\phi,c}}^{Sj} + d_{b_{\phi,c},R} + \upsilon_{\phi_c,R}^{Sj} \quad ,\end{aligned} \tag{3.8}$$

where:

$\phi_{c,R}^{Sj}$: Carrier phase measurement in units of meters

λ_c: Carrier wavelength

$N_{c,R}^{Sj}$: Initial carrier phase integer ambiguity in units of cycles

$d_{m_{\phi,c},R}^{Sj}$: Multipath range error on the carrier phase

$d_{b_{\phi,c}}^{Sj}$: Satellite hardware bias

$d_{b_{\phi,c},R}$: Receiver hardware bias

$\upsilon_{\phi_c,R}^{Sj}$: Carrier phase measurement noise in units of meters

Note that unlike the other parameters, the integer ambiguity $N_{c,R}^{Sj}$ is not time-varying as long as no cycle slip occurs. As mentioned before, GNSS receivers do not provide the carrier phase measurement in units of meters $\phi_{c,R}^{Sj}$ as indicated in Eq. (3.8), but the carrier phase measurement in units of cycles $\Phi_{c,R}^{Sj}$. The conversion is given as:

$$\lambda_c \cdot \Phi_{c,R}^{Sj} = \phi_{c,R}^{Sj} \tag{3.9}$$

From Eq. (3.7) and (3.8) follows that the carrier phase is advanced by the ionospheric refractivity, while the code (group) phase is delayed. The derivation of ionosphere-free linear combinations of code and carrier phase measurements is described in Sect. 3.4.

3.3.3 Instantaneous Doppler Measurement

The measurement of the Doppler frequency shift is a by-product of the carrier phase measurement. Nevertheless, Xu [54] states that the Doppler measurement is an independent observation, providing useful information about the instantaneous range rate. The Doppler frequency shifts are caused by relative motion of the satellites with respect to the receiver antenna. Both the velocity of the space vehicle travelling along its orbit and the receiver velocity in case of a mobile receiver contribute to observed relative range change. The Doppler frequency shift is expressed by

$$\Delta f_R^S = f_R^S - f_c^S = -f_c^S \cdot \frac{\underline{v}_{rel,R}^S \circ \dfrac{\underline{X}^S - \underline{X}_R}{r_R^S}}{c_0} \quad , \tag{3.10}$$

where:

Δf_R^S: Doppler frequency shift due to the relative motion between the satellite S and the receiver antenna R

f_R^S: Frequency of the satellite signal S received at the receiver antenna site R

f_c^S: Carrier frequency transmitted by the satellite S

$\underline{v}_{rel,R}^S$: Vector of the relative velocity between the satellite S and the receiver antenna R

$\frac{\underline{X}^S - \underline{X}_R}{r_R^S}$: Line-of-sight unit vector pointing from the receiver site R to the satellite S, also denoted as $\underline{1}_R^S$, where $r_R^S = \left\|\underline{X}^S - \underline{X}_R\right\|_2$ is the true geometric range between satellite S and receiver R

According to [23], Doppler frequency shifts typically range from ±4 kHz with respect to f_c^S=1575.42 MHz due to relative GPS satellite motion observed from an earth-fixed receiver. The relative velocity vector $\underline{v}_{rel,R}^S$ introduced in Eq. (3.10) can be rewritten in terms of the satellite velocity vector and the receiver velocity vector:

$$\underline{v}_{rel,R}^S = \underline{\dot{X}}^S - \underline{\dot{X}}_R = \begin{pmatrix} \dot{x}^S \\ \dot{y}^S \\ \dot{z}^S \end{pmatrix} - \begin{pmatrix} \dot{x}_R \\ \dot{y}_R \\ \dot{z}_R \end{pmatrix} \tag{3.11}$$

The determination of the satellite velocity vector $\underline{\dot{X}}^S$ from broadcast ephemeris data is shown in Appendix B. Following the parameterization of the Doppler equation in terms of known and unknown parameters given in [23], Eq. (3.10) can be rearranged as

$$\frac{\mathrm{c_0} \cdot \Delta \mathrm{f_R^S}}{\mathrm{f_c^S}} + \begin{pmatrix} \dot{\mathrm{x}}^\mathrm{S} \\ \dot{\mathrm{y}}^\mathrm{S} \\ \dot{\mathrm{z}}^\mathrm{S} \end{pmatrix} \circ \begin{pmatrix} \dfrac{\mathrm{x^S - x_R}}{\mathrm{r_R^S}} \\ \dfrac{\mathrm{y^S - y_R}}{\mathrm{r_R^S}} \\ \dfrac{\mathrm{z^S - z_R}}{\mathrm{r_R^S}} \end{pmatrix} = \begin{pmatrix} \dot{\mathrm{x}}_\mathrm{R} \\ \dot{\mathrm{y}}_\mathrm{R} \\ \dot{\mathrm{z}}_\mathrm{R} \end{pmatrix} \circ \begin{pmatrix} \dfrac{\mathrm{x^S - x_R}}{\mathrm{r_R^S}} \\ \dfrac{\mathrm{y^S - y_R}}{\mathrm{r_R^S}} \\ \dfrac{\mathrm{z^S - z_R}}{\mathrm{r_R^S}} \end{pmatrix} \quad . \tag{3.12}$$

From Eq. (3.12) follows that the instantaneous Doppler measurements provided by many GNSS receivers are well-suited in order to derive the velocity of the user receiver. In general, the transmitted frequency f_c^S is offset from the nominal carrier frequency, which has to be considered when working with measured quantities. However, according to Kaplan et al. [23]

the offset between the transmitted satellite signal frequency and the nominal carrier frequency is usually negligible. Also f_R^S is biased by a frequency offset compared to the theoretical receive signal frequency, which would be obtained if ideal clocks were available. The bias related to the receiver clock drift is in general not negligible. The following short notation of the measured Doppler frequency shift scaled to range rate will be used in the succeeding sections:

$$D_{c,R}^S = \frac{c_0 \cdot \Delta f_R^S}{f_c^S} = -\left(\underline{\dot{X}}^S - \underline{\dot{X}}_R\right) \circ \frac{\underline{X}^S - \underline{X}_R}{r_R^S} + c_0 \cdot \left(\dot{d}t^S - \dot{d}t_R\right) + \upsilon_{D_c,R}^S \quad , \tag{3.13}$$

where $\dot{d}t^S$ and $\dot{d}t_R$ denote the satellite and receiver clock drift and $\upsilon_{D_c,R}^S$ denotes the combined measurement noise. In Eq. (3.13), changes of the atmospheric refractivity during the measurement interval are incorporated in the combined noise term $\upsilon_{D_c,R}^S$.

3.4 Inter-frequency Combinations of Observations

3.4.1 Dual-frequency Carrier Phase Combination

With present high-end GPS receivers measurements on two different carrier frequencies can be taken. Depending on the specific task, various strategies have been developed to exploit the availability of dual-frequency measurements. In the near future, GALILEO and modernized GPS will provide signals on more than just two frequencies. Thus, there will be the possibility to form linear combinations of observations on three or even more frequencies. Nevertheless, in civil aeronautics there is the requirement that the GNSS frequencies have to reside in an ARNS band. For this reason most considerations on evolutionary GNSS techniques in the domain of civil aviation are restricted to the use of GPS's L1 and L5 band and GALILEO's E1 and E5 band. It is assumed here that a dual-frequency approach will more easily meet certain certification standards. Therefore, the subsequent sections are restricted to the use of measurement data on two different frequencies.

The following representation of dual-frequency linear carrier phase combinations is mainly after Wübbena [53]. The linear carrier phase combination

$$\Phi_{\alpha,\beta} = \alpha \cdot \Phi_{f_1} + \beta \cdot \Phi_{f_2} \tag{3.14}$$

with the coefficients α and β has a resulting frequency of

$$f_{\alpha,\beta} = \alpha \cdot f_1 + \beta \cdot f_2 \quad . \tag{3.15}$$

Consequently, the wavelength of the combined signal follows from:

$$\lambda_{\alpha,\beta} = \frac{c_0}{\alpha \cdot f_1 + \beta \cdot f_2} = \frac{\lambda_1 \cdot \lambda_2}{\alpha \cdot \lambda_2 + \beta \cdot \lambda_1} \tag{3.16}$$

The new ambiguity term is as well a linear combination of the integer ambiguities of the original carrier phase measurements:

$$N_{\alpha,\beta} = \alpha \cdot N_1 + \beta \cdot N_2 \tag{3.17}$$

In the following it is assumed that the original carrier phase measurements are uncorrelated, that they have all the same standard deviation σ_Φ [cycles], and that the measurement noise is normally distributed with N(0, σ_Φ). The standard deviation σ_Φ of the carrier phase measurement in units of cycles is:

$$\sigma_{\Phi} = \frac{k_n}{2\pi} \tag{3.18}$$

If only PLL thermal noise jitter, whose computation is indicated in [23], is taken into account as exclusive noise source of the carrier phase measurement, the factor k_n can be expressed as

$$k_n = \sqrt{\frac{B_n}{C/N_0} \cdot \left(1 + \frac{1}{2 \cdot T \cdot C/N_0}\right)} \quad , \tag{3.19}$$

where B_n is the receiver carrier loop noise bandwidth, T is the pre-detection integration time and C/N_0 is the carrier-to-noise ratio. Typical values of k_n are in the region of 0.06, which corresponds to a standard deviation of the carrier phase noise at L1 of less than 2 mm in the range domain. According to the law of error propagation and the assumptions made before, the standard deviation of the dual-frequency linear combination of carrier phases in units of meters is given by:

$$\sigma_{\phi,\alpha\beta} = \sigma_{\Phi} \cdot \sqrt{\alpha^2 + \beta^2} \cdot \lambda_{\alpha\beta} \tag{3.20}$$

Since the classical widelane (WL) combination serves as measurement input to the navigation filter, its characteristics are listed as an example hereafter. The widelane phase measurement is formed by setting the coefficient α to 1 and β to -1:

$$\Phi_{WL} = \Phi_{E1|L1} - \Phi_{E5a|L5} \tag{3.21}$$

By choosing the coefficients α and β as integer values, it is ensured that the widelane ambiguity N_{WL} is also an integer value. The wavelength of the widelane that is formed from the E1 (or L1) and E5a (or L5) carrier phase measurement is 0.75 cm and follows from Eq. (3.16). A disadvantage of the widelane measurement is that its standard deviation is increased compared to the original phase measurements, see Eq. (3.20). The standard deviation $\sigma_{\phi,WL}$ of the widelane is increased by a factor of 5.58 compared to the standard deviation $\sigma_{\phi,E1|L1}$ of the phase measurement on E1 (or L1). It is frequently assumed that the widelane ambiguities can be resolved more easily than the original carrier phase ambiguities since the wavelength becomes larger. Teunissen [40] has investigated the decorrelating property of the L1-L2 widelane on a theoretical level. It is shown there that the LAMBDA method (see Sect. 5.4.2) does either result in the ambiguity decorrelation of the widelane technique or that it even improves the results achieved with the widelane technique, depending on the actual ambiguity covariance matrix.

3.4.2 Dual-frequency mixed Code-Carrier Combination

Uncompensated residual ionospheric errors are the main problem associated with successful ambiguity resolution. The availability of measurements on two different frequencies offers the possibility of forming linear combinations of measurements in which ionospheric error terms of up to 1st order are canceled. However, this benefit is bought at the price of an increased noise level of the "new" measurements that result from the linear combinations. The general expression of a mixed code-carrier combination is:

$$\lambda_{lc} \cdot \Phi_{lc} = \sum_{i=1}^{N} (\alpha_i \cdot \lambda_i \cdot \Phi_i + a_i \cdot \rho_i) \quad , \tag{3.22}$$

where:

λ_{lc}: Wavelength of the linear combination

Φ_{lc}: Carrier phase of the linear combination

α_i: Weighting coefficient of the carrier phase measurement

a_i: Weighting coefficient of the pseudorange measurement

Hereafter only the combination of either GALILEO's E5a and E1 signals or the combination of GPS's L5 and L1 signals are considered for the same reasons as mentioned before. Nevertheless, it should be noted that GALILEO and modernized GPS will provide far more options in order to form useful linear combinations, for example see [16].

The constraints in order to form an ionosphere-free, geometry-preserving mixed code-carrier combination are given in Henkel et al. [17], and will be repeated here with the restriction to dual-frequency data. The geometry is preserved by the linear combination if the following constraint is fulfilled:

$$\sum_{i=1}^{2}(\alpha_i + a_i) = 1 \tag{3.23}$$

In order to form an "ionosphere-free" combination, it is exploited that the carrier phase is advanced and the code phase is delayed by ionospheric refractivity:

$$\sum_{i=1}^{2}\frac{f_1^2}{f_i^2}\cdot(\alpha_i - a_i) = 0 \tag{3.24}$$

It is assumed in Eq. (3.24), which imposes the "ionosphere-free" constraint, that higher order terms of the ionospheric refraction are negligible. Since merely dual-frequency combinations are considered in this work, only ionospheric effects up to the 1st order can be eliminated anyway. The last constraint is given by the requirement to preserve the integer nature of the ambiguities. This allows computing an integer ambiguity-fixed position solution which is more precise than an ambiguity-float solution. The integer constraint is given as

$$\alpha_i = \frac{k_i \cdot \lambda_{lc}}{\lambda_i} \quad ,i = 1,2 \quad , \tag{3.25}$$

where $k_i \in Z$ and λ_{lc} is the resulting wavelength of the linear combination.

In this work a mixed code-carrier combination is formed that is only almost "ionosphere-free", while all other constraints are fulfilled. This is considered to be justified since double-differenced observations are processed by the filter and thus only the residual ionospheric error after double-differencing has to be suppressed sufficiently. The code-carrier combination found in this work makes use of the phase measurements on E1 (or L1) and E5a (or L5) as well as the code measurement on E5a (or L5). It is characterized by:

$$\lambda_{lc}\cdot\Phi_{lc} = \alpha_1\cdot\lambda_{E1|L1}\cdot\Phi_{E1|L1} + \alpha_2\cdot\lambda_{E5a|L5}\cdot\Phi_{E5a|L5} + a_2\cdot\rho_{E5a|L5} \tag{3.26}$$

The code measurements on E1 (or L1) are not included in the code-carrier combination since they are far noisier than the E5a (or L5) code measurements. Another approach that is not considered here would be to give them low weight in the code-carrier combination. No inter-system combinations will be considered here, e.g. either a mixed L1, L5 code-carrier combination or a mixed E1, E5a code-carrier combination is formed. The numerical values of the weighting coefficients of Eq. (3.26) are listed in Table 3.1. The coefficients are found by a trade-off between high suppression of the ionospheric range errors and a large ratio of the wavelength λ_{lc} to the standard deviation σ_{lc} of the mixed code-carrier combination. Note that the standard deviation of the mixed code-carrier combination is always higher than that of the pure carrier phase and code measurements, respectively.

Table 3.1: Characteristics of the mixed code-carrier combination

GALILEO									
	σ_ϕ	σ_ρ	k_i	α_i	a_i	σ_{lc}	λ_{lc}	λ_{lc}/σ_{lc}	A_{iono}
E1	3mm	25cm	1	15.5974	0	16.19cm	2.968m	18.3	5.8e-4
E5a	4mm	5cm	-1	-11.6474	-2.9500				
Modernized GPS									
	σ_ϕ	σ_ρ	k_i	α_i	a_i	σ_{lc}	λ_{lc}	λ_{lc}/σ_{lc}	A_{iono}
L1	3mm	30cm	1	15.5974	0	24.53cm	2.968m	12.1	5.8e-4
L5	4mm	8cm	-1	-11.6474	-2.9500				

Table 3.1 exhibits the strong sensitivity of the standard deviation of the mixed-code carrier combination, σ_{lc}, on the pseudorange measurement noise σ_ρ on E5a or L5. The investigation of the decrease of the positioning accuracy in severe multipath environments is therefore of special interest when using this linear combination. The standard deviation of the linear combination under the assumption of uncorrelated and Gaussian distributed noise of carrier and code measurements is computed from:

$$\sigma_{lc} = \sqrt{\sigma_\Phi^2 \cdot \left(\alpha_1^2 \cdot \lambda_{E1/L1}^2 + \alpha_2^2 \cdot \lambda_{E5a/L5}^2\right) + \sigma_{\rho_{E5a/L5}}^2 \cdot a_2^2} \tag{3.27}$$

For the values indicated in Table 3.1 the standard deviation of the phase measurement in units of cycles has been set to $\sigma_\Phi = 0.1/(2 \cdot \pi)$. The computation of the wavelength of the linear combination is given as [16]:

$$\lambda_{lc} = \frac{\sum_{i=1}^{2} \alpha_i}{\sum_{i=1}^{2} \frac{k_i}{\lambda_i}} \tag{3.28}$$

Finally, the ionospheric amplifier A_{iono} indicated in the last column of Table 3.1 is defined as:

$$A_{iono} = \sum_{i=1}^{N} \left(\alpha_i \cdot \frac{f_1^2}{f_i^2} - a_i \cdot \frac{f_1^2}{f_i^2}\right) \tag{3.29}$$

Similarly to the mixed code-carrier combination, a geometry-preserving, ionosphere-free code-only combination can be generated. Once more the considerations are restricted in this work to the use of either GALILEO's E5a and E1 signals or GPS's L5 and L1 signals. The coefficient $a_{1,code-only}$ and $a_{2,code-only}$ of the geometry-preserving, ionosphere-free code-only combination follow from Eq. (3.23) and (3.24):

$$a_{2,code-only} = \frac{1}{1 - \frac{f_1^2}{f_2^2}} \tag{3.30}$$

$$a_{1,code-only} = -\frac{f_1^2}{f_2^2} \cdot a_{2,code-only}$$

Numerically, the coefficient $a_{1,code-only}$ is equal to 2.2606 and the coefficient $a_{2,code-only}$ is equal to -1.2606 for both GALILEO and GPS. This corresponds to a standard deviation of the code-only combination of $\sigma_{\rho,lc}$=56.87cm in case of GALILEO and of $\sigma_{\rho,lc}$=68.56cm in case of GPS. The mixed code-carrier combination and the code-only combination presented in this section can also be used as measurement input to the navigation filter. The benefit of the ionosphere-free combinations is that ionospheric delay terms need no longer to be estimated, however at the cost of an increased noise level.

3.5 Differencing between Observations

3.5.1 Single- and Double-Differences

Filter algorithms for relative positioning are derived in this work. In contrast to single-point positioning, relative positioning makes use of differencing methods in order to eliminate nuisance parameters. Single- and double-differencing are frequently applied in navigation software. Also triple-differencing is of some importance. It is, for example, applied in some cycle slip detection algorithms. However, triple-differencing will not be discussed here. More information on triple-differencing can be found in textbooks, e.g. [19] or [23]. Both differencing between code and carrier phase observations is possible. Since the procedure is the same for both types of observations, only the equations for differencing between phase measurements are indicated in the following.

Single-Differencing:

A single-differenced observable is generated by subtracting the observation from receiver B to satellite S_j from the observation from receiver A to satellite S_j. The single-differenced carrier phase observable reads

$$\Delta\phi_{c,AB}^{Sj} = \phi_{c,A}^{Sj} - \phi_{c,B}^{Sj} \quad , \tag{3.31}$$

where Δ is the single-difference operator and c is the index of the respective carrier frequency. Cancellation of nuisance parameters is only guaranteed if receiver A and receiver B take their measurements simultaneously. Single-differencing between receivers largely eliminates satellite-related hardware delays, satellite clock biases, orbital errors and, depending on the baseline length between receiver A and B, range errors due to atmospheric refraction. The residual ionospheric and tropospheric errors are correlated with the baseline length. Obviously, the propagation medium related range errors become zero for a zero-baseline where receiver A and B share the same receive antenna. In this special case, the signal propagation paths through the atmosphere are identical for both receivers. The single-differenced ionospheric error is also negligible for short baselines under normal conditions, e.g. in absence of ionospheric storms. Pseudorange and carrier phase errors induced by receiver noise and multipath are uncorrelated between receivers.

The single-differencing scheme presented in Eq. (3.31) involves differencing of the observations from different receivers. Similarly, single-differencing of the observations from one receiver, but to different satellites, is also possible. The nuisance parameters that are canceled out by differencing between satellites are different from those that are canceled out by differencing between receivers. Both satellite- and receiver-related nuisance parameters are canceled out when forming double-differences.

Double-Differencing:

Double-differencing is applied in order to additionally cancel out the receiver clock errors and biases from the receiver hardware under the assumption that the biases are identical for different receiver channels. As mentioned before, receiver-related nuisance parameters are cancelled out by taking the difference of observations from different satellites. In case of double-differencing this is achieved by taking the difference between two single-differenced observables of the same observation epoch, but of two different satellites S_j and S_k:

$$\nabla\Delta\phi_{c,AB}^{SjSk} = \Delta\phi_{c,AB}^{Sj} - \Delta\phi_{c,AB}^{Sk} = \phi_{c,A}^{Sj} - \phi_{c,B}^{Sj} - \phi_{c,A}^{Sk} + \phi_{c,B}^{Sk} \quad , \tag{3.32}$$

where $\nabla\Delta$ is the double-difference operator. The double-differenced phase observable indicated in Eq. (3.32) is rewritten in order to show all remaining error sources after double-differencing:

$$\begin{aligned}\nabla\Delta\phi_{c,AB}^{SjSk} &= \nabla\Delta r_{AB}^{SjSk} + \lambda_c \cdot \nabla\Delta N_{c,AB}^{SjSk} - \nabla\Delta d_{ion,AB}^{SjSk} \cdot \frac{f_{ion}^2}{f_c^2} + \nabla\Delta d_{orb,AB}^{SjSk} \\ &\quad + \nabla\Delta d_{trop,AB}^{SjSk} + \nabla\Delta d_{m_{\phi,c},AB}^{SjSk} + \nabla\Delta v_{\phi_c,AB}^{SjSk}\end{aligned} \tag{3.33}$$

The subscript c indicates that the respective parameter is dependent on the carrier frequency. The parameterization of the double-differenced code observable is similar to that of Eq. (3.33) except from the ambiguity term and the sign of the residual ionospheric error:

$$\begin{aligned}\nabla\Delta\rho_{c,AB}^{SjSk} &= \nabla\Delta r_{AB}^{SjSk} + \nabla\Delta d_{ion,AB}^{SjSk} \cdot \frac{f_{ion}^2}{f_c^2} + \nabla\Delta d_{orb,AB}^{SjSk} + \nabla\Delta d_{trop,AB}^{SjSk} \\ &\quad + \nabla\Delta d_{m_{\rho,c},AB}^{SjSk} + \nabla\Delta v_{\rho_c,AB}^{SjSk}\end{aligned} \tag{3.34}$$

It is justified to neglect the residual orbital error $\nabla\Delta d_{orb,AB}^{SjSk}$ in Eq. (3.33) and in Eq. (3.34) since its magnitude is very small compared to the other error sources. Furthermore, there are various models available in order to estimate the delay of the radio-navigation signals caused by the troposphere. This allows computing observables that have been largely compensated for the tropospheric delay. However, it should be mentioned that accurate estimation of tropospheric delays might fail under abnormal conditions even if the most sophisticated models were applied. Especially for signals from satellites seen under low elevation angles accurate modeling of the tropospheric delay term becomes very difficult. It is rather common to leave multipath unmodeled although there exist complex multipath models. The items mentioned so far allow for further simplification of Eq. (3.33) and Eq. (3.34). The simplified model of double-differenced carrier phase observable becomes:

$$\nabla\Delta\phi_{c,AB}^{S1S2} = \nabla\Delta r_{AB}^{S1S2} + \lambda_c \cdot \nabla\Delta N_{c,AB}^{S1S2} - \nabla\Delta d_{ion,AB}^{S1S2} \cdot \frac{f_{ion}^2}{f_c^2} + \nabla\Delta v_{\phi_c,AB}^{S1S2} \tag{3.35}$$

The same bias terms are left out in the simplified model of the double-differenced pseudorange observable:

$$\nabla\Delta\rho_{c,AB}^{SjSk} = \nabla\Delta r_{AB}^{SjSk} + \nabla\Delta d_{ion,AB}^{SjSk} \cdot \frac{f_{ion}^2}{f_c^2} + \nabla\Delta v_{\rho_c,AB}^{SjSk} \tag{3.36}$$

3.5.2 Variance-Covariance Error Propagation

The double-differenced carrier phase and pseudorange observables are obtained by linear combination of the original measurements from the reference receiver A and the user receiver B. In the following the representation of the variance-covariance error propagation due to differencing is restricted to the carrier phase observables since an analog representation can immediately be indicated for the pseudorange observables. It is assumed that the measurement noise of the original observations is white Gaussian distributed. The measurements on the carrier frequency c are summarized in an n-dimensional vector $\underline{\Phi}_{c,A}$ for the reference receiver and in an n-dimensional vector $\underline{\Phi}_{c,B}$ for the user receiver, where n is the number of satellites. First, single-differencing between receivers is considered. The n-dimensional single-differenced phase measurement vector is generated by:

$$\Delta\underline{\Phi}_{c,AB} = S \cdot \begin{bmatrix} \underline{\Phi}_{c,A} \\ \underline{\Phi}_{c,B} \end{bmatrix} \quad , \tag{3.37}$$

with the generator matrix S that reflects the linear dependency of the phase measurements:

$$S = \begin{bmatrix} I_{(n)x(n)} & -I_{(n)x(n)} \end{bmatrix} \quad , \tag{3.38}$$

where $I_{(n)x(n)}$ is the identity matrix of size (n)x(n). The covariance matrix of the single-differenced measurements results from the law of error propagation:

$$D\{\Delta\underline{\Phi}_{c,AB}\} = S \cdot \begin{bmatrix} Cov(\underline{\Phi}_{c,A}) & 0 \\ 0 & Cov(\underline{\Phi}_{c,B}) \end{bmatrix} \cdot S^T \quad , \tag{3.39}$$

where $Cov(\underline{\Phi}_c)$ is the covariance matrix of the original phase measurements. Under the assumption that all phase measurements are uncorrelated and have the same variance σ_Φ^2, then the variances of the single-differenced phase measurements are twice the variances of the original phase measurements: $\sigma_{\Delta\Phi}^2 = 2 \cdot \sigma_\Phi^2$. The single-differenced measurements are still uncorrelated if the original measurements were uncorrelated.

The covariance matrix of double-differenced observables can be derived from the original covariance matrices in a similar way. The computation of the double-differenced (n-1)-dimensional phase measurement vector is given by:

$$\nabla\Delta\underline{\Phi}_{c,AB} = D \cdot \begin{bmatrix} \underline{\Phi}_{c,A} \\ \underline{\Phi}_{c,B} \end{bmatrix} \quad , \tag{3.40}$$

with the generator matrix D

$$D = \begin{bmatrix} \underline{1}_{(n-1)} & -I_{(n-1)x(n-1)} & -\underline{1}_{(n-1)} & I_{(n-1)x(n-1)} \end{bmatrix} \tag{3.41}$$

reflecting the linear dependency of the original measurements. The single measurements in the n-dimensional vector $\underline{\Phi}_c$ are arranged such that the measurement to the reference satellite comes first. The unit vector $\underline{1}_{(n-1)}$ is an (n-1)-dimensional vector whose entries are all set to 1. By applying the law of variance-covariance error propagation, the covariance matrix of the double-differenced observables results from:

$$D\{\nabla\Delta\underline{\Phi}_{c,AB}\} = D \cdot \begin{bmatrix} Cov(\underline{\Phi}_{c,A}) & 0 \\ 0 & Cov(\underline{\Phi}_{c,B}) \end{bmatrix} \cdot D^T \tag{3.42}$$

Assuming again that the original phase measurements are uncorrelated and have all the same variance σ_Φ^2, it becomes obvious from the structure of the generator matrix D that the double-differenced measurements are no longer uncorrelated. Furthermore, the variances of the double-differenced measurements are four times larger than the variances of the original measurements: $\sigma_{\nabla\Delta\Phi}^2 = 4 \cdot \sigma_{\Phi}^2$.

4 Kalman Filtering

4.1 Filter Equations

When initially introduced by R.E. Kalman in 1960 [22], the Kalman filter solved the Wiener filtering problem of linear dynamic systems using the state space model for dynamic and random processes. The optimal filter problem is based on minimizing the sum of the mean-square errors in the state estimates. In the meantime, Extended Kalman filter (EKF) approaches have been introduced that address to the solution of nonlinear problems. Concerning GNSS navigation systems, there is a nonlinear dependency between the observations and the states of interest. However, in this section the basics of linear Kalman filtering problems are introduced first before considering the extension to nonlinear problems.

The discrete-time Kalman filter equations are developed, for example, in Brown et al. [4] and Grewal et al. [12], and a good summary of Kalman filtering can be found in [23]. The most important equations are repeated here, since they are essential for the development of the navigation filter. Kalman filtering benefits from knowledge of the system dynamics and the statistical nature of the system errors. This knowledge is used to set up a discrete-time state space model of the random process. The state space model of the linear system is

$$\underline{x}_k = \Phi_{k-1} \cdot \underline{x}_{k-1} + \underline{\omega}_{k-1} \qquad \underline{\omega}_k \sim N(\underline{0}, Q_k) \quad , \tag{4.1}$$

where $\underline{x}_k$ is the system state vector, Φ_k is the state transition matrix, $\underline{\omega}_k$ is the process noise vector and Q_k is the covariance matrix of process noise. The subscript k indicates the respective epoch. Innovation is brought into the filter by new measurements. The linear measurement model is given by

$$\underline{z}_k = H_k \cdot \underline{x}_k + \underline{v}_k \qquad \underline{v}_k \sim N(\underline{0}, R_k) \quad , \tag{4.2}$$

where $\underline{z}_k$ is the measurement vector, H_k is the measurement sensitivity matrix, $\underline{v}_k$ is the measurement noise and R_k is the covariance matrix of measurement noise. Two fundamental assumptions are made in Eq. (4.1) and in Eq. (4.2): unmodeled process noise and unmodeled measurement noise are zero-mean Gaussian processes. This should be accounted for when evaluating the Kalman filter performance. Any non-white sequences can produce non-optimal state estimates.

With the help of the state space model the new system state can be predicted from the last valid information. The a priori state estimate $\hat{\underline{x}}_k(-)$ at epoch k is obtained from extrapolation, using

$$\hat{\underline{x}}_k(-) = \Phi_{k-1} \cdot \underline{x}_{k-1}(+) \quad , \tag{4.3}$$

where $\hat{\underline{x}}_{k-1}(+)$ is the posteriori state estimate of the previous epoch. The covariance matrix of state estimation uncertainty, $P_k(-)$, is extrapolated as well, using

$$P_k(-) = \Phi_{k-1} \cdot P_{k-1}(+) \cdot \Phi_{k-1}^T + Q_{k-1} \quad . \tag{4.4}$$

The symbol '$(-)$' is used to indicate an a priori estimate, and the symbol '$(+)$' indicates estimates after the update, e.g. posteriori estimates.

So far the prediction of the system state with the help of the state model has been considered. Now the update of the predicted system state based on new measurement data is presented. The criterion for deriving optimal gain factors is the minimization of the trace of covariance matrix of state estimation $P_k(+)$. This corresponds to minimizing the sum of the mean-square errors in the state estimates. The derivation of the gain factors is given in [4] and [12]. The optimal Kalman gain matrix K_k, which assesses the weight of the measurement data from the current epoch, is computed from

$$K_k = P_k(-) \cdot H_k^T \cdot \left[H_k \cdot P_k(-) \cdot H_k^T + R_k\right]^{-1} \quad . \tag{4.5}$$

The update of the covariance matrix of state estimate uncertainty is given by

$$P_k(+) = [I - K_k \cdot H_k] \cdot P_k(-) \quad . \tag{4.6}$$

Finally, the update of the state estimate vector based on the measurements from the current epoch k is calculated from

$$\underline{\hat{x}}_k(+) = \underline{\hat{x}}_k(-) + K_k \cdot \left(\underline{z}_k - H_k \cdot \underline{\hat{x}}_k(-)\right) \quad . \tag{4.7}$$

In Eq. (4.7) the predicted state vector $\underline{\hat{x}}_k(-)$ is combined with the observations of the current epoch $\underline{z}_k$ in a minimum mean-squares sense. The posteriori state vector $\underline{\hat{x}}_k(+)$ is thus the filtered state estimate based on all prior observations and the current observations at epoch k. Under the assumptions made about the process noise and the measurement noise, e.g. $\underline{\omega}_k \sim N(\underline{0}, Q_k)$ and $\underline{v}_k \sim N(\underline{0}, R_k)$, the posteriori state estimate $\underline{\hat{x}}_k(+)$ is unbiased. It is important to note the difference between the Kalman filter estimate, whose optimization criterion is minimum sum of mean-square errors, and the least-squares estimate, whose optimization criterion is minimum sum of square errors in a deterministic sense. Brown et al. [5] have shown that under certain circumstances both estimators will lead to identical solutions. However, the advantage of Kalman filtering is that prior knowledge of the process being estimated can be incorporated constructively. If there is no or only very poor prior knowledge, the Kalman filter advantage is lost.

The Kalman Filter loop is illustrated in Figure 4.1. In this representation of the filter loop the update is computed first instead of starting with the prediction. In epoch k the prediction of the system state in epoch k+1 is determined and buffered. The prediction equations of the Kalman filter follow from Eq. (4.3) and Eq. (4.4). However, comparing the epoch indices used in the equations with those indicated in the illustration, it has to be noted that the epoch indices of the prediction are offset by one epoch. The update equations of the Kalman filter follow from Eq. (4.5), (4.6) and (4.7). When starting the filter, an initial "guess" of $\underline{\hat{x}}_0(-) = E\{\underline{x}_0\}$ and $P_0(-) = E\{\underline{\tilde{x}}_0 \cdot \underline{\tilde{x}}_0^T\}$ is required in order to initialize the buffers with the predicted system state. The problems associated with filter initialization will be addressed later in this work.

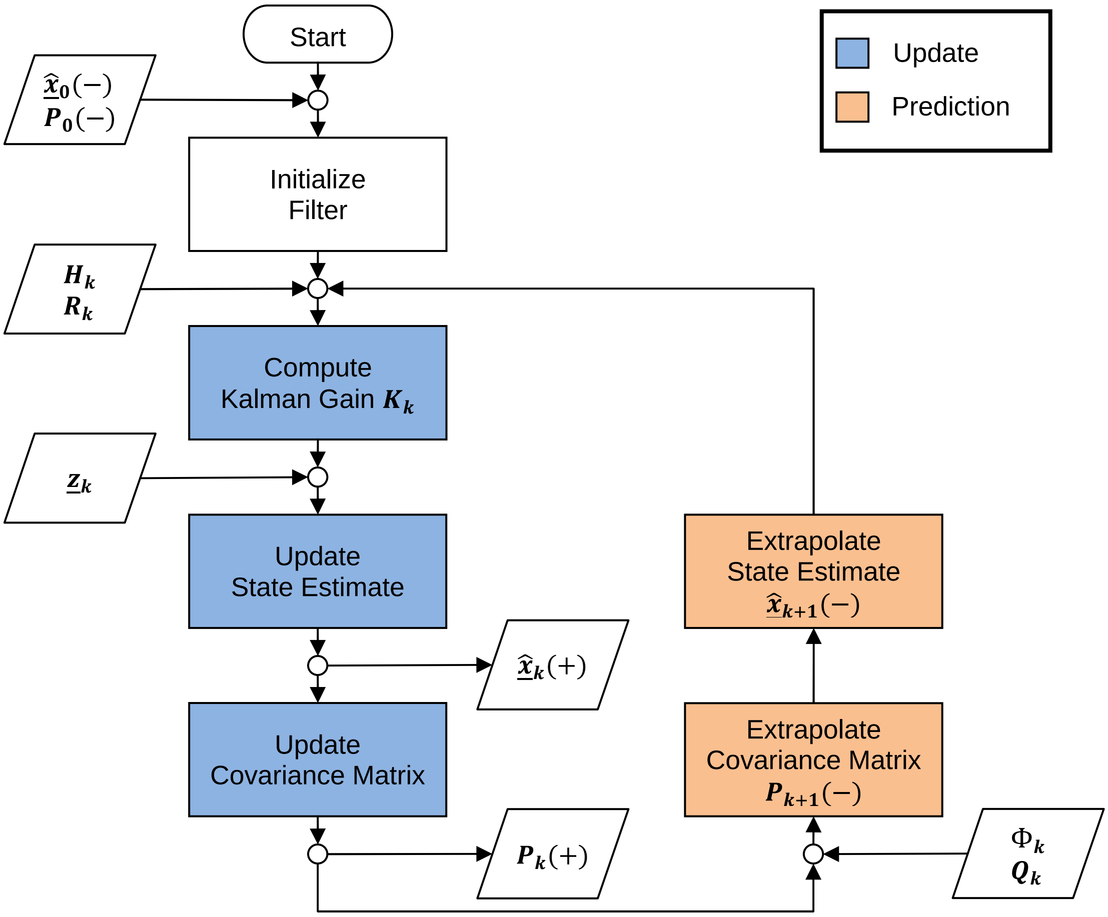

Figure 4.1: Flow-Chart of the Kalman Filter Loop

According to [19], there is a strong relationship between Kalman filtering and sequential least-squares adjustment. Sequential least-squares adjustment used for stationary processes may be considered as a sub-class of Kalman filtering. Kalman filtering addresses to the more general case where also non-stationary processes are covered. The main difference between Kalman filtering and sequential least-squares adjustment is founded in the prediction step. The proof that Kalman filtering reduces to sequential least-squares adjustment in case of a stationary process is given in [54].

4.2 Filter Convergence

It has to be considered that even a Kalman filter that has been designed for solving a linear problem may exhibit divergence problems. These problems arise from practical limits rather than from filter theory. When implementing the Kalman filter one has to deal with finite word-length effects. Round-off errors can cause instable behavior of the filter. The problem of computer round-off and methods to ease this kind of stability problem of Kalman filtering are addressed in detail in Sect. 4.3. The next kind of divergence problem is caused by bad observability of one or more system states. However, since the system observability can be determined formally, the problem of possibly unobservable states can already be detected during the filter design phase. According to Grewal et al. [12], the observability matrix O of a linear dynamic system model follows from:

$$O(H_k, \Phi_k, 1 \le k \le K) = \sum_{k=1}^{K} \left\{ \left[\prod_{i=0}^{k-1} \Phi_{k-i} \right]^T \cdot H_k^T \cdot H_k \cdot \left[\prod_{i=0}^{k-1} \Phi_{k-i} \right] \right\} \tag{4.8}$$

The system observability does not depend on the measurement inputs, but only on the measurement sensitivity matrix H_k and the state transition matrix Φ_k over the discrete time interval from $t_0 \le t \le t_K$. Equation (4.8) refers to linear systems. Nevertheless, this observability test is also applied to the linearized GNSS navigation problem in this work in order to get a rough idea if the filter states are observable.

Two further problems of Kalman filtering are listed in [54]. First, if the state transition matrix does not reflect the true physical process properly due to imprecise knowledge of the actual system behavior, or if the statistic properties of the physical process are mismodeled, the estimated states might not converge to the true values. The issue of divergence due to modeling errors should also be covered during the filter design phase. Non-convergence of a filter may also be caused by leaving one or more state variables of the dynamic system unmodeled. In the performance tests of the navigation filter, which is developed in this work, it will be investigated whether a simple linear model of the precision approach is sufficient or not. Accelerations are not modeled as additional filter states. However, the simulated physical process does comprise accelerations of the airplane. The second item listed in [54] is that the Kalman filter performance depends on accurate filter initialization. Accurate initialization with $P_0(-)$ and $\underline{\hat{x}}_0(-)$ is particularly important with respect to convergence of nonlinear filters. In this work, an ordinary least-squares solution is computed before starting the filter in order to obtain good initial estimates of the current system state.

In theory, the Kalman filter performance is characterized by the covariance matrix $P_k(+)$ of state estimation uncertainty. If the characteristic values of $P_k(+)$ are growing without bound, the theoretical filter performance diverges. The covariance matrix $P_k(+)$ solves a nonlinear discrete-time Riccati equation for the estimation uncertainty with the given initial conditions. The a priori value of the covariance matrix, $P_k(-)$, is of interest when computing the Kalman gain matrix. It is assumed that the a priori covariance matrix $P_k(-)$ can be fractionally decomposed into a numerator matrix A_k and a nonsingular denominator matrix B_k:

$$P_k(-) = A_k \cdot B_k^{-1} \tag{4.9}$$

The reason for fraction decomposition of $P_k(-)$ is to transform the nonlinear Riccati equation into a system of two simultaneous linear equations. In [12] the proof is given that $P_{k+1}(-) = A_{k+1} \cdot B_{k+1}^{-1}$ solves the discrete-time Riccati equation at t_{k+1}, where

$$\begin{bmatrix} A_{k+1} \\ B_{k+1} \end{bmatrix} = \begin{bmatrix} Q_k & I \\ I & 0 \end{bmatrix} \cdot \begin{bmatrix} \Phi_k^{-T} & 0 \\ 0 & \Phi_k \end{bmatrix} \cdot \begin{bmatrix} H_k^T \cdot R_k^{-1} \cdot H_k & I \\ I & 0 \end{bmatrix} \cdot \begin{bmatrix} A_k \\ B_k \end{bmatrix} \quad . \tag{4.10}$$

From Eq. (4.10) follows that the state transition matrices Φ_k have to be non-singular.

It is always useful to survey the diagonal terms of the posteriori covariance matrix $P_k(+)$ of state estimation uncertainty, e.g. the expected variances of the estimated states. The advantage of this approach is that the theoretical Kalman filter performance can easily be surveyed during the operational phase after the filter design phase has already been closed. An example of the coherence between the predicted performance, which is derived from the main diagonal of $P_k(+)$, and the actual performance of the filter state estimation is shown in Figure 4.2 and Figure 4.3. The example refers to the estimation of ionospheric delay terms. One time the

Vertical Ionospheric Gradient (VIG) is estimated by a sub-optimal navigation filter and the other time the double-differenced ionospheric range error is estimated by an optimal navigation filter.

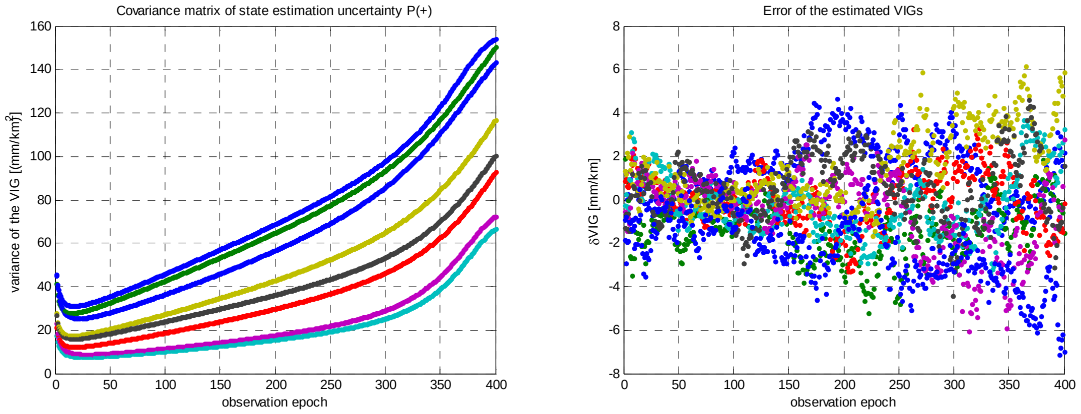

Figure 4.2: Divergence of the Vertical Ionospheric Gradient estimates (left: predicted variances, right: true estimation errors)

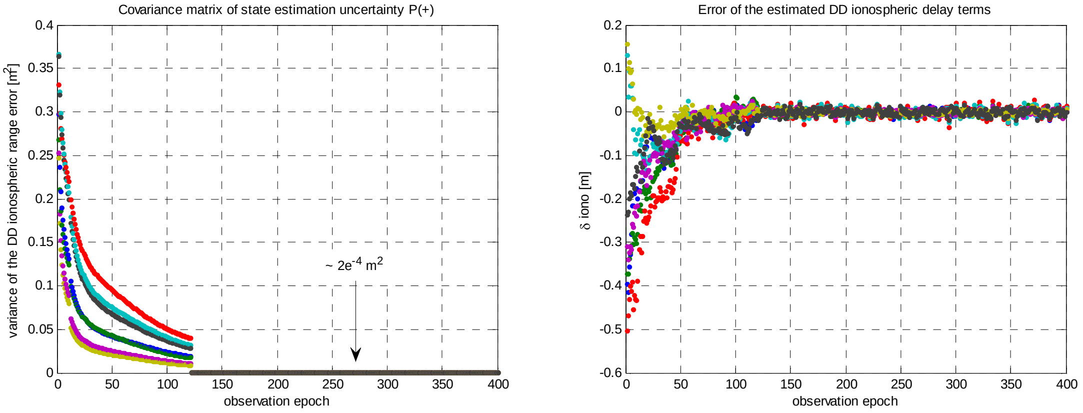

Figure 4.3: Convergence of the DD ionospheric range error estimates (left: predicted variances, right: true estimation errors)

First, the case is considered where the estimation errors of the VIGs diverge (Figure 4.2). This is properly reflected by the theoretical variances of the VIGs. During operation, it becomes obvious that the results may not be trusted since the variances of the estimated VIGs increase continuously while the filter is running. During design phase, the results of this example suggest that the design phase of that sub-optimal filter should not yet be closed. Second, the case is considered where the estimated VIGs converge (Figure 4.3). Again, there is coherence between the predicted variances and the actual estimation errors.

On the other hand, the information provided by $P_k(+)$ should not be overestimated. Even if the expected values of the estimation errors do not indicate divergence of the estimated states from the true system states, the states estimated by the filter might still diverge due to unpredictable behavior. A common approach during filter design phase is to analyze by extensive Monte Carlo simulations if the ensemble mean estimation error is indeed unbiased. An example is given below that demonstrates the mismatch between the predicted state estimation errors and the actual state estimation errors.

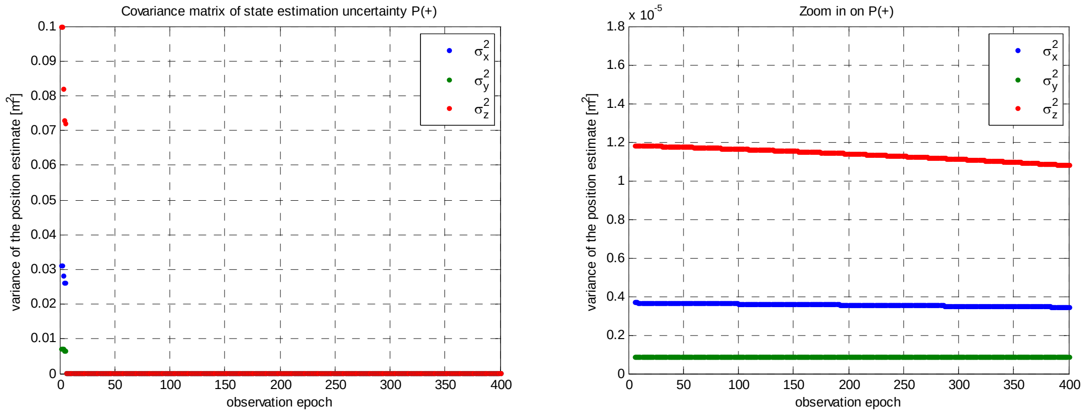

Figure 4.4: Theoretical values of the position estimation error variances

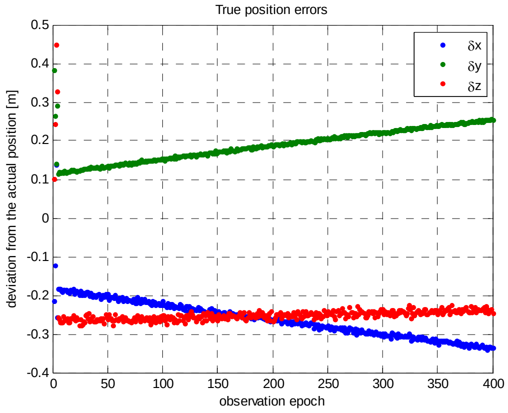

Figure 4.5: Actual errors of the position solution derived from simulation

From Figure 4.4 and Figure 4.5 it becomes obvious that the theoretical filter performance may differ significantly from the true filter performance. While the predicted variances of the position estimate errors suggest that the position estimates perfectly converge, the magnitude of the true position errors is up to 0.5 m. However, in order to demonstrate that the theoretical filter performance should not be overestimated, some errors during filter design phase have intentionally been introduced: First, a severe modeling error has been committed, e.g. state variables of the dynamic system have not been modeled - namely ionospheric delay terms. Second, the measurement variances which were fed into the filter have significantly been reduced compared to the actual variances of the measurements. Due to the introduction of modeling errors the widelane and carrier phase ambiguities were fixed to the wrong integer values after the first four observation epochs. After fixing the ambiguities with the required level of integrity, the variances of process noise of the ambiguity states have been set to zero. Consequently, the ambiguity estimates remain unaffected by new measurement information. However, the theoretical position estimate errors derived from $P_k(+)$ are not completely wrong. The bias due to wrong integer ambiguity fixing is not reflected in the theoretical values. However, the true position estimate errors - although biased - are indeed of low noise. But the trend of δx, δy and δz are not properly reflected since the actual position errors are slowly growing while the theoretical variances become smaller.

It should be mentioned here that although if the biases in the state estimates are not reflected by $P_k(+)$, there are other means in Kalman filtering in order to detect these biases. More details on fault detection are given in Sect. 6.

4.3 Numerical Stability

4.3.1 Bierman-Thornton UD Filter

There are more robust filter implementations in presence of computer round-off errors than the standard Kalman filter equations presented in Sect. 4.1. The original formulation of the Kalman filter showed only marginal stability of the numerical solution of the associated Riccati equation. Therefore, square-root filtering and UD filtering (UD: Upper diagonal matrix − Diagonal matrix factorization) have been introduced, which rely on the theoretical background of the Kalman filter, but provide better numerical stability in presence of round-off errors. If high-integrity navigation solutions were to be provided by the filter, degradation of the filter performance due to round-off errors is not tolerable. Without actually investigating the numerical stability of the filter at hand, no statement can be made about the need for more robust implementations. In this chapter, an alternative implementation to the standard Kalman filter equations is presented, and in the next chapter it will be discussed whether the numerical stability of the standard equations is sufficient for the filtering problem at hand or not.

In this work the Bierman-Thornton UD filter implementation is considered as alternative implementation since it has been shown, e.g. by Grewal et al. [13], that this implementation works well even in presence of an ill-conditioned problem. Ill-conditioning also includes large matrix dimensions. Since measurements on two different frequencies are processed by the filter, the matrix dimensions grow respectively compared to processing of only single-frequency measurement data. By reformulating the Riccati equations, the Bierman-Thornton UD filter has a modified Cholesky factor as dependent variable instead of the covariance matrix of state estimation uncertainty P_k. First, the UD factorization is defined: The covariance matrix C is factorized in an upper diagonal matrix U and a pure diagonal matrix D

$$C = U \cdot D \cdot U^T \tag{4.11}$$

by applying modified Cholesky factorization. In contrast to standard Cholesky factorization, the modified Cholesky factorization does not require the computation of square-roots.

If the GNSS measurement model is based on the use of double-differenced observations or linear combinations of observations on multiple frequencies, then different components of the measurement vector are correlated. Accordingly, the covariance matrix of measurement noise $R = E\left(\underline{v} \cdot \underline{v}^T\right)$ is not a pure diagonal matrix. In order to compute the Bierman-Corrector, a decorrelation of the measurement model is required. The procedure adopted here in order to decorrelate the measurements follows the one presented in [13]. First, modified Cholesky factorization, see Eq. (4.11), is applied to the covariance matrix of measurement noise R. As a result of the factorization, one obtains the upper triangular matrix $\mathrm{U_R}$ and the pure diagonal matrix $\mathrm{D_R}$. Second, the decorrelation of the measurement model follows from:

$$R_d = D_R \quad , \tag{4.12}$$

$$\underline{z} = U_R \cdot \underline{z}_d \quad , \tag{4.13}$$

$$H = U_R \cdot H_d \quad , \tag{4.14}$$

where the subscript d indicates the decorrelated form of the respective measurement matrix or measurement vector. Thus, the decorrelated measurement model reads:

$$\underline{z}_d = H_d \cdot \underline{x} + \underline{v}_d \quad , E\{\underline{v}_d \cdot \underline{v}_d^T\} = R_d \tag{4.15}$$

Since R_d is a pure diagonal matrix, the measurement errors are now uncorrelated. The decorrelation of the measurement model is required in order to allow for sequential processing of scalar observations when performing the observational update of the filter estimates.

The Bierman-Thornton UD filter comprises two processes. The first process is the observational update according to Bierman [1] and the second process is prediction according to Thornton [45]. The Bierman observational update processes the decorrelated measurements sequentially, e.g. a loop with n iterations is required if n is the length of the measurement vector at the current epoch. The basic problem to be solved is how to derive an efficient method for the UD factorization of the following expression:

$$\begin{aligned} D_{P(-)} - D_{P(-)} \cdot \underline{a} \cdot \left[\underline{a}^T \cdot D_{P(-)} \cdot \underline{a} + R_{d,(j,j)} \cdot I\right]^{-1} \cdot \underline{a}^T \cdot D_{P(-)} \\ = U_B \cdot D_{P(+)} \cdot U_B^T \quad , \end{aligned} \tag{4.16}$$

with the UD factorized a priori covariance matrix of state estimation uncertainty

$$P(-) = U_{P(-)} \cdot D_{P(-)} \cdot U_{P(-)}^T \quad , \tag{4.17}$$

and the n-dimensional vector

$$\underline{a} = U_{P(-)}^T \cdot H_{d,(j,1\ldots u)}^T \quad . \tag{4.18}$$

$H_{d,(j,1\ldots u)}$ is the j^th^ row of the decorrelated measurement sensitivity matrix and u is the number of unknown states. The variance that corresponds to the j^th^ measurement is given by $R_{d,(j,j)}$. As a result, the modified Cholesky decomposition of the posteriori covariance matrix of state estimation uncertainty is obtained:

$$P(+) = U_{P(+)} \cdot D_{P(+)} \cdot U_{P(+)}^T \quad , \tag{4.19}$$

where $\mathrm{U}_{\mathrm{P}(+)}$ is computed from

$$U_{P(+)} = U_{P(-)} \cdot U_B \quad . \tag{4.20}$$

One possible implementation of Bierman's observational update is shown in Table 4.1. Further details on implementation aspects of the rank 1 modification algorithm for modified Cholesky factors are given in [12].

Table 4.1: Structure Diagram of Bierman's Observational Update Algorithm

```
$\underline{x}(+) = \underline{x}(-)$
$U_{P(+)} = U_{P(-)}$
$D_{P(+)} = D_{P(-)}$
For i = 1, i ≤ number of measurements, i++
    $\underline{a} = U_{P(+)}^T \cdot H_{d,(i,1\ldots u)}^T$
    $\underline{b} = D_{P(+)} \cdot \underline{a}$
    $r = \underline{z}_{d,(i)} - H_{d,(i,1\ldots u)} \cdot \underline{x}(+)$
    $\alpha = R_{d,(i,i)}$
    $\gamma = \frac{1}{\alpha}$
    For j = 1, j ≤ number of states, j++
        $\beta = \alpha$
        $\alpha = \alpha + \underline{a}_{(j)} \cdot \underline{b}_{(j)}$
        $\lambda = -\underline{a}_{(j)} \cdot \gamma$
        $\gamma = \frac{1}{\alpha}$
        $D_{P(+),(j,j)} = \beta \cdot \gamma \cdot D_{P(+),(j,j)}$
        For k = 1, k ≤ j-1, k++
            $\beta = U_{P(+),(k,j)}$
            $U_{P(+),(k,j)} = \beta + \underline{b}_k \cdot \lambda$
            $\underline{b}_k = \underline{b}_k + \underline{b}_j \cdot \beta$
    $\underline{x}(+) = \underline{x}(+) + \gamma \cdot r \cdot \underline{b}$
```

The second process besides the Bierman observational update is the extrapolation of the system state to the next epoch. The prediction process according to Thornton uses UD-factorization of the temporal update. Thereby the robustness of the prediction in presence of computer round-off errors is improved. In order to speed up computations, the covariance matrix of process noise is UD-factorized:

$$Q = U_Q \cdot D_Q \cdot U_Q^T \tag{4.21}$$

The modified Cholesky factor U_Q is used in order to determine the modified process noise coupling matrix G_m:

$$G_m = G \cdot U_Q \tag{4.22}$$

So far, it has been assumed that the process noise coupling matrix G were the identity matrix, e.g. $G = I_{(u)x(u)}$, which corresponds to uncoupled process noise terms. This assumption will be sustained during this work. As a consequence, G_m is simply given by U_Q. For completeness, the more general form of the discrete-time system equation, which contains the process noise coupling matrix, is also indicated:

$$\underline{x}_k = \Phi_{k-1} \cdot \underline{x}_{k-1} + G \cdot \underline{\omega}_{k-1} \qquad \underline{\omega}_k \sim N(0, Q_k) \tag{4.23}$$

The reformulation of the Kalman filter prediction step according to Thornton is given in Table 4.2. For background information on the derivation of Thornton's temporal update it is referred to Thornton [45] or Grewal et al. [12].

Table 4.2: Structure Diagram of Thornton's Prediction Algorithm

```
$\underline{x}_{k+1}(-) = \Phi_k \cdot \underline{x}_k(+)$
$G = G_m$
$\vartheta = \Phi_k \cdot U_{P_k(+)}$
$U_{P_{k+1}(-)} = I$
For i = number of states, i ≥ 1, i--
    $\sigma = 0$
    For j = 1, j ≤ number of states, j++
        $\sigma = \sigma + \vartheta_{(i,j)}^2 \cdot D_{P_k(+),(j,j)}$
        j ≤ dimension of process noise
            true
                $\sigma = \sigma + G_{(i,j)}^2 \cdot D_{Q_k,(j,j)}$
    $D_{P_{k+1}(-),(i,i)} = \sigma$
    For j = 1, j ≤ i-1, j++
        $\sigma = 0$
        For k = 1, k ≤ number of states, k++
            $\sigma = \sigma + \vartheta_{(i,k)} \cdot D_{P_k(+),(k,k)} \cdot \vartheta_{(j,k)}$
        For k = 1, k ≤ dimension of process noise, k++
            $\sigma = \sigma + G_{(i,k)} \cdot D_{Q_k,(k,k)} \cdot G_{(j,k)}$
        $U_{P_{k+1}(-),(j,i)} = \frac{\sigma}{D_{P_{k+1}(-),(i,i)}}$
        For k = 1, k ≤ number of states, k++
            $\vartheta_{(j,k)} = \vartheta_{(j,k)} - U_{P_{k+1}(-),(j,i)} \cdot \vartheta_{(i,k)}$
        For k = 1, k ≤ dimension of process noise, k++
            $G_{(j,k)} = G_{(j,k)} - U_{P_{k+1}(-),(j,i)} \cdot G_{(i,k)}$
```

4.3.2 Evaluation of the Numerical Filter Stability

The Bierman-Thornton UD filter implementation presented in the previous chapter ensures that the covariance matrix of state estimation uncertainty P_k remains symmetric and positive-definite. However, it is also possible to enforce symmetry of P_k manually in order to prevent numeric instability if the implementation of the standard Kalman filter equations has been chosen:

$$P_k = \frac{1}{2} \cdot \left(P_k + P_k^T\right) \tag{4.24}$$

However, this does not yet ensure positive definiteness of the covariance matrix.

The implementation of the covariance matrix update according to Eq. (4.6) is especially susceptible to computer round-off errors. Therefore, in this work the Joseph form of the update of the covariance matrix of state estimation uncertainty is implemented:

$$P_k(+) = [I - K_k \cdot H_k] \cdot P_k(-) \cdot [I - K_k \cdot H_k]^T + K_k \cdot R_k \cdot K_k^T \tag{4.25}$$

According to Brown et al. [4] and Wendel [52], the Joseph form provides better numeric stability. Improved numeric stability by using the Joseph form has also been verified during various simulation runs with the navigation filter developed in this work, where the covariance matrix $P_k(+)$ still remained symmetric, while the formulation of the covariance matrix update according to Eq. (4.6) lead to slight asymmetry of $P_k(+)$. For example, numerical problems of the formulation given in Eq. (4.6) arise if there is large uncertainty in the initial estimate of the covariance matrix $P_0(-)$, corresponding to large values along the major diagonal. Given that in the first epoch there are on the other hand very precise measurements available, then the covariance matrix must transit from very large values to values close to zeros within a single computation step. These problems are overcome in many situations with the update equation presented in Eq. (4.25). A negative aspect of Joseph's form of the covariance matrix update is an increased computational effort compared to the simpler update form indicated in Eq. (4.6).

The Kalman filter equations introduced in Sect. 4.1 address linear problems. The navigation filter derived in this work is, however, founded on Extended Kalman filter equations. Nevertheless, the considerations on numerical stability made so far remain still valid. First, the standard EKF equations (see Appendix A) have been implemented. In analogy to Eq. (4.6), the covariance matrix update of the EKF according to Eq. (A.8) shows numeric instability. Therefore, the covariance matrix update indicated in Eq. (A.8) is replaced by the Joseph form according to Eq. (4.25). The only difference to Eq. (4.25) is that the measurement sensitivity matrix $\mathrm{H_k}$ has to be replaced by the sensitivity matrix H_k^*, which is derived from linearized observation equations. This simple modification of the covariance matrix update of the standard EKF equations ensured that $P_k(+)$ remained symmetric and positive-definite in the simulations that were performed. Although the simulation results do not suggest that additional means of symmetrizing $P_k(+)$ are required, symmetry is enforced by applying Eq. (4.24) to $P_k(+)$ as derived from the Joseph form of the covariance matrix update. Second, the Bierman-Thornton UD filter equations have been implemented. The following observations concerning numerical robustness have been made with the navigation filter developed here:

1) The covariance matrix $P_k(+)$ shows slight asymmetries due to round-off errors during the first few epochs if the standard EKF equations are implemented without any additional means to improve numerical stability.

2) If the symmetry of $P_k(+)$ is enforced by applying Eq. (4.24), no significant degradation of the filter performance due to round-off errors is observable.

3) If the Joseph form of the covariance matrix update according to Eq. (4.25) is implemented, $P_k(+)$ stays symmetric even without enforcing symmetry by Eq. (4.24).
4) The Bierman-Thornton UD filter implementation ensures positive-definiteness and symmetry of $P_k(+)$ anyway. No noticeable difference in filter performance has been observed between the Bierman-Thornton UD filter implementation and a numerically stabilized version of the standard EKF equations (Joseph form and symmetry enforcement).

In this work the filter algorithms are running on a computer platform with 52 bits in the mantissa of the standard data word so that computer round-off errors do not severely degrade the filter performance of the navigation problem at hand. The filter algorithms are implemented in MATLAB®, which is optimized for matrix operations rather than for program loops with regard to computing time. If the simulations run in a MATLAB® environment, the Bierman-Thornton UD filter implementation tends to increase the computing time significantly. The reason for the increase in computing time is founded in the sequential rank 1 modifications. Thus, single measurement data is sequentially processed in for-loops instead of using matrix notation, while matrix notation is in general to be favored when using MATLAB®. No performance degradation is observed when using the modified standard EKF equations, which are made numerically stable by applying Eq. (4.24) and Eq. (4.25). Therefore, in the following of this work the Bierman-Thornton implementation will no longer be considered. However, if the filter algorithms were to be implemented in a FPGA, it is expected that the difference in computing time would be less distinctive. Under the assumption of almost identical computing times, the Bierman-Thornton UD filter implementation seems favorable, since it is ensured that P_k stays symmetric and positive definite without additional effort.

5 Real-time Kinematic Positioning Concept

5.1 Software Overview

A navigation filter for real-time kinematic relative positioning is developed in this work. The software architecture is depicted in Figure 5.1. Double-differenced measurement data is processed by a nonlinear filter, which is described in detail in Sect. 5.2. The nonlinear filter is based on a dynamic state space model for the dynamics of the airplane. Discrete-time extended Kalman Filter equations, see Appendix A, have been implemented. In addition, the numerically robust Bierman-Thornton UD filter implementation has also been considered as alternative to the standard EKF equations. The filter loop of the EKF is very similar to that of the standard Kalman filter illustrated in Figure 4.1.

Pseudorange measurements on at least one frequency are required as filter input. The EKF supports also the processing of pseudorange measurements on multiple frequencies simultaneously. The same holds true for the instantaneous Doppler shift measurements. However, in this work most of the time dual-frequency data is used as measurement input to the filter. With respect to the carrier phase measurements, it is required that at least measurements on two different carrier frequencies are available. According to Figure 5.1, a cascading ambiguity resolution scheme is applied. It is a two-step procedure from the Widelane (WL) ambiguity-fixed solution to the Carrier Phase (CP) ambiguity-fixed solution. The software architecture can be easily extended to a three carrier ambiguity resolution scheme. With respect to the certification in civil aviation and the complexity of the receiver hardware, it is desirable to restrict the filter input data to dual-frequency measurements. In general, an ambiguity-fixed solution is derived in three steps:

1) Computation of the float solution.
2) Mapping of the float ambiguity vector $\underline{\hat{N}}$ of length m to an integer ambiguity vector $\underline{\check{N}}$ of length m, using the mapping function $S\colon \mathbb{R}^m \rightarrow \mathbb{Z}^m$. E.g. multiple float ambiguity vectors are mapped to the same integer ambiguity vector.
3) Adjustment of the float solution if the fixed integer ambiguities are accepted.

Here, item 1) is achieved by the EKF, item 2) is achieved by either the LAMBDA method or Integer Bootstrapping and item 3) is achieved by sequential application of the theory of conditional least squares adjustment. There are different quality categories of the navigation filter position solution: the filter can provide either a float solution, or widelane-fixed solution, or a carrier phase-fixed solution. An ambiguity fixed solution is only available if there is enough confidence in the integer vector derived from ambiguity resolution. Ambiguity resolution and ambiguity validation is presented in detail in Sect. 5.4. Besides the position vector, the navigation filter estimates also the velocity vector of the airplane. The user velocity is however rather a by-product of the underlying dynamic model. The quality of the velocity solution is mainly determined by the precision of the double-differenced instantaneous Doppler shift measurements. It is not considered here to augment the velocity solution by using time-derivatives of the phase measurements.

The integrity of the navigation solution is surveyed by Autonomous Filter-based fault Detection, Identification and model Adaptation (AFDIA) as described in Sect. 6. If a failure is detected, the source of the model invalidation is searched. The model can be adapted afterwards if there is enough confidence in the identification of the model invalidation. The computation of protection levels for the user position and velocity solution has to be adapted to the filter-based approach. If there is an ambiguity-fixed position solution available, the protection levels for the user position will be tighter than the protection levels for a float solution. This is especially important during the final phase of the flight and in order to make progress in the domain of auto-landing. AFDIA serves also for the detection of cycle slips after the ambiguities have already been fixed. If necessary, the ambiguity-fixed solution is abandoned and the filter steps back to a float solution. However, if there is only a single cycle slip in the carrier phase measurement data, the accuracy of the position solution does not get significantly worse and the ambiguities can be re-fixed quickly. The actual performance of the navigation filter is evaluated by tests, whose results are presented in Sect. 7 and 8.

Instead of forwarding pseudorange $\nabla\Delta\underline{\rho}_k$, widelane $\nabla\Delta\underline{\phi}_{WL,k}$ and carrier phase measurements $\nabla\Delta\underline{\phi}_{CP,k}$ to the filter, it is also supported to process ionosphere-free code-only $\nabla\Delta\underline{\rho}_{IF,k}$ and code-carrier $\nabla\Delta\underline{\phi}_{IF,k}$ combinations. If the ionosphere-free combinations are used as measurement input, the cascading ambiguity resolution scheme reduces to the resolution of the ambiguities of the code-carrier combination. The main interest of this work is, however, to obtain a carrier phase ambiguity-fixed solution. Only then the highest position accuracies can be achieved.

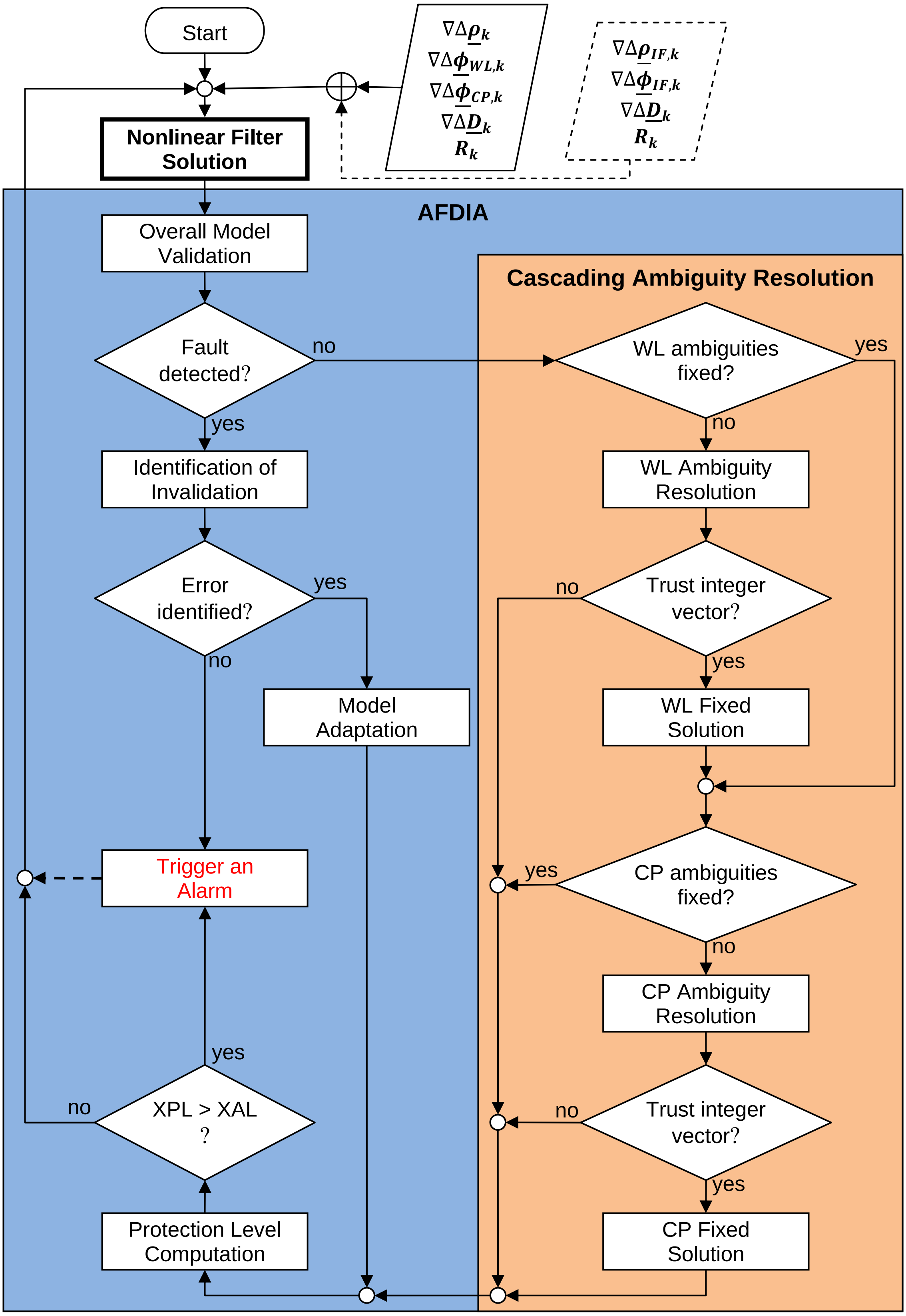

Figure 5.1: Navigation software architecture

5.2 Nonlinear Navigation Filter

5.2.1 Extended Kalman Filter

In GNSS-based positioning, the unknown user coordinates appear in nonlinear form in the pseudorange and carrier phase measurements. Due to this nonlinear measurement relationship, the standard Kalman filter equations introduced in Sect. 4.1 cannot be used immediately. Brown et al. [5] suggest two options to proceed with nonlinear relationships. One option is to implement a linearized Kalman filter. The linearization takes place about a nominal trajectory in state space. Actual measurement data has no impact on the linearization. However, in this work it is assumed that no nominal trajectory is known in advance. Therefore, the linearized Kalman filter does not fit for the problem at hand. The second option is to determine the trajectory dynamically by continuously updating the trajectory with the states estimated by the filter. Consequently, actual measurement data has an impact on the linearization. The filter is called an Extended Kalman Filter (EKF) if this method is applied. Due to the feedback of the measurement sequence into the process model, the performance of the EKF depends on the actual sample measurement sequence. For this reason, Monte-Carlo simulations are generally preferred in order to evaluate the performance of an EKF rather than following an analytical approach. The main concern associated with extended Kalman filtering is that it might diverge if the reference about which the linearization takes place is poor. In [5] it is mentioned that in practice the initial estimates of $\underline{\hat{x}}_0(-)$ and $P_0(-)$ are frequently poor. Since the a priori state estimation vector $\underline{\hat{x}}_0(-)$ forms the starting point of the linearization, it should not be too poor in order prevent that the dynamically updated trajectory drifts away from the true trajectory. In Wendel [52] the performance of a Sigma-Point Kalman filter is compared with the performance of an EKF. No significant improvement of the navigation performance could be demonstrated in simulations where realistic scenarios (limited measurement errors) were considered by using a Sigma-Point Kalman filter. However, in case of large initial state estimate errors, the Sigma-Point Kalman filter tended to converge faster than the EKF. As mentioned before, a good initial estimate of the unknown user coordinates can be derived from ordinary least-squares estimation for single-point positioning with the Newton-Raphson method. Furthermore, the linearization problem associated with GNSS measurements is rather convenient.

It is depicted in Figure 5.2 that it is important to have a good initial estimate of the user position available when starting the nonlinear filter. On the right side of Figure 5.2, the initial estimate of the user receiver coordinates has been set to the origin of the ECEF coordinate system, e.g. [0m 0m 0m]. This corresponds to an initial RMS position estimate error of approximately 6368 km. Obviously the estimated user positions during precision approach are useless for navigation. Nevertheless, the position estimates do not diverge, but they converge far too slowly since the filter does not iterate multiple times over the same solution. On the left side of Figure 5.2, the initial estimate of the user receiver coordinates has been derived from ordinary least-squares estimation for single-point positioning without applying any correction terms. Consequently, the filter is initialized with a coarse estimate of the user position that shows still an RMS position error of 65 m. However, this is already sufficient in order to get the filter started properly. Directly after starting the filter the error of the filtered position estimate is already below 0.5 m.

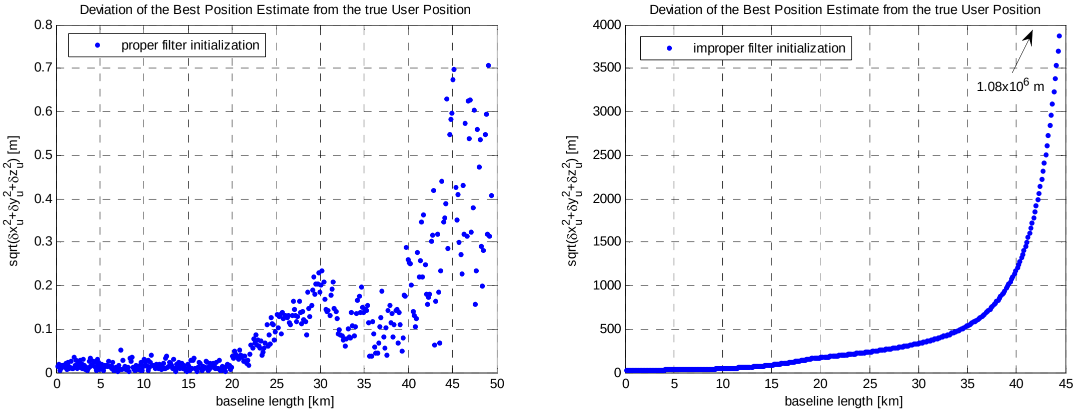

Figure 5.2: Importance of proper filter initialization

While the Kalman filter equations indicated in Sect. 4.1 refer to linear problems, the EKF equations listed in Appendix A can be used for nonlinear applications with respect to the measurement model and/or the state space model. In the special case of linear dynamic systems, Kalman filtering results in a best linear unbiased estimator (BLUE) for the state vector [19]. However, the following assumptions have to be valid: the system noise follows a Gaussian distribution with zero mean, e.g. $\underline{\omega}_k \sim N\left(\underline{0}, Q_k\right)$, and the measurement noise follows a Gaussian distribution with zero mean, e.g. $\underline{\upsilon}_k \sim N\left(\underline{0}, R_k\right)$. These same assumptions have to hold for the EKF in order to ensure good filter performance. Without any further restrictions, it does not hold in general that the EKF state estimates will converge. As mentioned in the beginning of this chapter, the filter estimates depend on the actual measurement sequence, which has an impact on the dynamically generated reference trajectory for the linearization. Furthermore, as demonstrated in the example on proper filter initialization, the estimates of the nonlinear filter do also strongly depend on a priori knowledge of the system state. Analytical proof of the exponential boundedness of the squared mean of the state estimation errors for the continuous EKF can be found in Günther [15]. However, this proof is based on some constraints. If these constraints are violated, for example if the initial state estimation errors are too large or if the measurements are very noisy, the state estimation errors might diverge. Considering the application of EKFs in practice, there are reliable methods in order to monitor if the EKF state estimates diverge. For example, by keeping track of the innovation vector, anomalies can be detected. Health monitoring of the EKF is discussed in detail in Sect. 6.

5.2.2 Linearized Observation Model

In this section the linearized observation model for relative positioning using double-differenced code and carrier phase measurements is derived. The nonlinear relationship between the observations and the user receiver coordinates is the reason for using an EKF instead of a linear Kalman filter. While there are nonlinear relationships with respect to the measurement model, a linear dynamic state space model is used in order to model the system dynamics. Therefore, only the respective observation equations have to be linearized. The general form of the linearized GNSS model is:

$$\underline{y} = H^* \cdot \underline{x} + \underline{\upsilon} \quad , \tag{5.1}$$

where H^* is the design matrix derived from linearized observation equations, $\underline{x}$ is the vector of unknowns in terms of incremental values, $\underline{y}$ is the vector of measured minus computed observations and $\underline{v}$ is the noise vector.

The mathematical model that is considered in this work is a geometry-based model, since the parameters of interest are the coordinates of the user receiver antenna. Taylor series expansion is used in order to linearize the geometric range with respect to approximate values for the user receiver coordinates $\hat{x}_U$, $\hat{y}_U$ and $\hat{z}_U$. An estimate $\hat{r}_U^S$ of the geometric range between the satellite S and the user U is obtained from:

$$\hat{r}_U^S = \sqrt{(x^S - \hat{x}_U)^2 + (y^S - \hat{y}_U)^2 + (z^S - \hat{z}_U)^2} \tag{5.2}$$

Note that all quantities of Eq. (5.2) vary with time, where the time index is not explicitly indicated. The actual user receiver coordinates $[x_U \; y_U \; z_U]$ can be expressed by an initial guess $[\hat{x}_U \; \hat{y}_U \; \hat{z}_U]$ and the respective offset $[\Delta x_U \; \Delta y_U \; \Delta z_U]$:

$$x_U = \hat{x}_U + \Delta x_U, \qquad y_U = \hat{y}_U + \Delta y_U, \qquad z_U = \hat{z}_U + \Delta z_U \tag{5.3}$$

The Taylor series expansion of a continuously differentiable function in $[x_U \; y_U \; z_U]$ is given by [3]:

$$\begin{aligned} f(\hat{x}_U + \Delta x_U, \hat{y}_U + \Delta y_U, \hat{z}_U + \Delta z_U) \\ &= f(\hat{x}_U, \hat{y}_U, \hat{z}_U) \\ &+ \frac{1}{1!}\left(\frac{\partial}{\partial \hat{x}_U}\Delta x_U + \frac{\partial}{\partial \hat{y}_U}\Delta y_U + \frac{\partial}{\partial \hat{z}_U}\Delta z_U\right) f(\hat{x}_U, \hat{y}_U, \hat{z}_U) \\ &+ \frac{1}{2!}\left(\frac{\partial}{\partial \hat{x}_U}\Delta x_U + \frac{\partial}{\partial \hat{y}_U}\Delta y_U + \frac{\partial}{\partial \hat{z}_U}\Delta z_U\right)^2 f(\hat{x}_U, \hat{y}_U, \hat{z}_U) + \cdots \end{aligned} \tag{5.4}$$

In order to linearize the function indicated in Eq. (5.4), the Taylor series expansion has to be truncated after the linear term. Making use of the Taylor series expansion and neglecting terms of higher orders, the true geometric range r_U^S can be expressed by:

$$r_U^S = \hat{r}_U^S + \left(\frac{\hat{x}_U - x^S}{\hat{r}_U^S}\Delta x_U + \frac{\hat{y}_U - y^S}{\hat{r}_U^S}\Delta y_U + \frac{\hat{z}_U - z^S}{\hat{r}_U^S}\Delta z_U\right) \tag{5.5}$$

Next, the geometry term of double-differenced observations is considered:

$$\nabla\Delta r_{AB}^{S1S2} = \left(r_A^{S1} - r_B^{S1}\right) - \left(r_A^{S2} - r_B^{S2}\right) \tag{5.6}$$

The subscript A is used for the reference receiver, whose coordinates are known precisely, and the subscript B is used for the mobile user receiver, whose coordinates are to be determined. Eq. (5.6) can be rewritten by introducing the unknown rover receiver coordinate increments Δx_B, Δy_B and Δz_B that represent the offset between an initial estimate of the user receiver location and the actual location of the user receiver. The result of the linearized geometric range with respect to the user receiver coordinates indicated in Eq. (5.5) is reused in order to reformulate the double-differenced geometry term as follows:

$$\begin{aligned} \nabla\Delta r_{AB}^{S1S2} &= \left[r_A^{S1} - \left(\hat{r}_B^{S1} + \frac{\hat{x}_B - x^{S1}}{\hat{r}_B^{S1}}\Delta x_B + \frac{\hat{y}_B - y^{S1}}{\hat{r}_B^{S1}}\Delta y_B + \frac{\hat{z}_B - z^{S1}}{\hat{r}_B^{S1}}\Delta z_B\right)\right] \\ &- \left[r_A^{S2} - \left(\hat{r}_B^{S2} + \frac{\hat{x}_B - x^{S2}}{\hat{r}_B^{S2}}\Delta x_B + \frac{\hat{y}_B - y^{S2}}{\hat{r}_B^{S2}}\Delta y_B + \frac{\hat{z}_B - z^{S2}}{\hat{r}_B^{S2}}\Delta z_B\right)\right] \end{aligned} \tag{5.7}$$

Thus, the design matrix for the geometry states $\underline{x}_{geo} = [\Delta x_B \quad \Delta y_B \quad \Delta z_B]^T$ of the linearized GNSS model for relative positioning reads:

$$H_{geo}^* = \begin{bmatrix} \frac{\hat{x}_B - x^{S2}}{\hat{r}_B^{S2}} - \frac{\hat{x}_B - x^{S1}}{\hat{r}_B^{S1}} & \frac{\hat{y}_B - y^{S2}}{\hat{r}_B^{S2}} - \frac{\hat{y}_B - y^{S1}}{\hat{r}_B^{S1}} & \frac{\hat{z}_B - z^{S2}}{\hat{r}_B^{S2}} - \frac{\hat{z}_B - z^{S1}}{\hat{r}_B^{S1}} \\ \vdots & \vdots & \vdots \\ \frac{\hat{x}_B - x^{Sj}}{\hat{r}_B^{Sj}} - \frac{\hat{x}_B - x^{S1}}{\hat{r}_B^{S1}} & \frac{\hat{y}_B - y^{Sj}}{\hat{r}_B^{Sj}} - \frac{\hat{y}_B - y^{S1}}{\hat{r}_B^{S1}} & \frac{\hat{z}_B - z^{Sj}}{\hat{r}_B^{Sj}} - \frac{\hat{z}_B - z^{S1}}{\hat{r}_B^{S1}} \end{bmatrix} \tag{5.8}$$

By introducing the line-of-sight vector $\underline{1}_B^S$ pointing from the user receiver B to the satellite S, the expression given in Eq. (5.8) can be rewritten as:

$$H_{geo}^* = \begin{bmatrix} \left(\underline{1}_B^{S1} - \underline{1}_B^{S2}\right)^T \\ \vdots \\ \left(\underline{1}_B^{S1} - \underline{1}_B^{Sj}\right)^T \end{bmatrix} \tag{5.9}$$

Note that the change of sign between Eq. (5.8) and Eq. (5.9) results from the definition of the orientation of the line of sight vector. The double-differenced geometry term is present in both the double-differenced pseudorange equations and the double-differenced carrier phase equations. Furthermore, it can be found in the double-differenced Doppler shift equations, which becomes obvious from Eq. (3.12). However, the sign of the entries of H_{geo}^* has to be inverted in order to obtain the design matrix for the velocity states $\underline{x}_{vel} = [\Delta \dot{x}_B \quad \Delta \dot{y}_B \quad \Delta \dot{z}_B]^T$. The sign inversion results from the definition of the Doppler shift scaled to range rate D_R^S as defined in Eq. (3.13). The double-differenced Doppler shift measurements are given by:

$$\nabla\Delta D_{AB}^{S1S2} = \left(D_A^{S1} - D_B^{S1}\right) - \left(D_A^{S2} - D_B^{S2}\right) \tag{5.10}$$

From Eq. (3.12) follows that the double-differenced Doppler shift measurements can be parameterized in terms of the unknown user velocity vector $\underline{\dot{X}}_B$:

$$\nabla\Delta D_{AB}^{S1S2} + \underline{\dot{X}}^{S1} \circ \left(\underline{1}_A^{S1} - \underline{1}_B^{S1}\right) - \underline{\dot{X}}^{S2} \circ \left(\underline{1}_A^{S2} - \underline{1}_B^{S2}\right) = \underline{\dot{X}}_B \circ \left(\underline{1}_B^{S2} - \underline{1}_B^{S1}\right) \tag{5.11}$$

The terms of known parameters are on the left side of the Eq. (5.11), leaving the terms of unknown parameters on the right side of the equation. In Eq. (5.11) it has already been used that the reference receiver A is static, e.g. $\underline{\dot{X}}_A = \underline{0}$. Just as before, the user velocity vector $\underline{\dot{X}}_B$ can be split into an initial estimate $\underline{\hat{\dot{X}}}_B$ and an incremental offset $\Delta\underline{\dot{X}}_B$. Finally, the design matrix for the velocity parameters can be set up as follows:

$$H_{vel} = \begin{bmatrix} \left(\underline{1}_B^{S2} - \underline{1}_B^{S1}\right)^T \\ \vdots \\ \left(\underline{1}_B^{Sj} - \underline{1}_B^{S1}\right)^T \end{bmatrix} \tag{5.12}$$

By comparing Eq. (5.12) with Eq. (5.9) it follows that $H_{vel} = -H_{geo}^*$.

In real-time kinematic positioning it is required that the exact reference receiver coordinates $\underline{X}_A$ are available at the user receiver site. Furthermore, the satellite positions and velocities are required by the user positioning software. The procedure in order to determine the satellite positions and velocities from broadcast ephemeris data is shown in Appendix B. In the next section the measurement model of the nonlinear filter is presented and the information on the measurement sensitivity matrices derived in this section can be reused.

5.2.3 Measurement Model

In this work it is assumed that both the reference station and the airplane are equipped with a dual-frequency receiver. This allows for inter-frequency combinations of the measurements. However, in the following only the linear combination of phase measurements on two different frequencies is considered in order to form a widelane observation. The selection of the GNSS frequencies is such that it is assured that they reside in an ARNS band in order to be compatible with the requirements of civil aviation. The widelane linear phase combination is used in this work as measurement input to the filter instead of simply forwarding the carrier phase measurements on two different frequencies separately to the filter. The reasoning in favor of the widelane is founded in the concrete application at hand. The characteristics of a widelane ambiguity-fixed position solution are better than those of a sole float position solution. For many applications the accuracy of a widelane ambiguity-fixed position solution is already sufficient. Therefore, it is advantageous to have a widelane ambiguity-fixed solution available, which is easier to obtain than a carrier phase ambiguity-fixed solution, as long as carrier phase ambiguity resolution may not be trusted. Many dual-frequency receivers on the market provide in addition to the pseudorange and carrier phase measurements also the instantaneous Doppler shift measurements. In the following only the Doppler shifts measured on the highest carrier frequency are included in the measurement model. However, the processing of Doppler shift measurements on multiple carrier frequencies is supported by the navigation software and has also been tested successfully.

In this section it holds that $f_2 > f_1$ and that the ionosphere reference frequency $f_{ion} = f_2$, e.g. ionospheric delay terms which are estimated by the filter are referenced to f_2. Higher order terms of the ionospheric gradient are neglected in this representation. Furthermore, signal delay due to refractivity of the troposphere is assumed to be absent in this work. Though, in general the double-differenced residual tropospheric range errors are not negligible. Multipath remains an unmodeled, non-white nuisance parameter. The following observation equations are considered in the measurement model, which have already been introduced in Sect. 3 and are repeated here for convenience:

a) Double-differenced pseudorange measurements

$$\nabla\Delta\rho_{c,AB}^{S1Sj} = \nabla\Delta r_{AB}^{S1Sj} + \nabla\Delta d_{ion,AB}^{S1Sj} \cdot \frac{f_{ion}^2}{f_c^2} + \nabla\Delta v_{\rho_c,AB}^{S1Sj} \tag{5.13}$$

b) Double-differenced phase-only widelane measurements

$$\begin{aligned}\nabla\Delta\phi_{WL,AB}^{S1Sj} = \nabla\Delta r_{AB}^{S1Sj} + \lambda_{WL} \cdot \nabla\Delta N_{WL,AB}^{S1Sj} - \lambda_{WL} \cdot \nabla\Delta d_{ion,AB}^{S1Sj} \\ \cdot \left(\frac{f_{ion}^2}{f_2^2 \cdot \lambda_2} - \frac{f_{ion}^2}{f_1^2 \cdot \lambda_1}\right) + \nabla\Delta v_{\phi_{WL},AB}^{S1Sj}\end{aligned} \tag{5.14}$$

c) Double-differenced carrier phase measurements

$$\nabla\Delta\phi_{c,AB}^{S1Sj} = \nabla\Delta r_{AB}^{S1Sj} + \lambda_c \cdot \nabla\Delta N_{c,AB}^{S1Sj} - \nabla\Delta d_{ion,AB}^{S1Sj} \cdot \frac{f_{ion}^2}{f_c^2} + \nabla\Delta v_{\phi_c,AB}^{S1Sj} \tag{5.15}$$

d) Double-differenced Doppler shift measurements

$$\nabla\Delta D_{c,AB}^{S1Sj} = -\nabla\Delta\dot{r}_{AB}^{S1Sj} + \nabla\Delta v_{D_c,AB}^{S1Sj} \tag{5.16}$$

All measurements indicated so far are summarized in the measurement vector $\underline{z}_k$. The actual measurements at epoch k are compared with the predicted measurements. From Eq. (A.10) follows that the predicted measurements are computed differently if an EKF is used, e.g. the predicted measurements follow from $\underline{\hat{z}}_k = \underline{h}_k\left(\underline{\hat{x}}_k(-)\right)$ instead of using $\underline{\hat{z}}_k = H_k \cdot \underline{\hat{x}}_k(-)$. Consequently, the prediction of the measurements at epoch k follows directly from inserting the predicted state vector $\underline{\hat{x}}_k(-)$ into the nonlinear measurement functions $\underline{h}_k$. The EKF is updated at epoch k using the information from the innovations, which is the difference between the actual measurements $\underline{z}_k$ and the predicted measurements $\underline{\hat{z}}_k$:

$$
\begin{aligned}
&\left(\underline{z}_k - \underline{\hat{z}}_k\right) \\
&= \begin{pmatrix}
\nabla\Delta\rho_{1,AB}^{S1S2} \\
\vdots \\
\nabla\Delta\rho_{1,AB}^{S1Sn} \\
\nabla\Delta\rho_{2,AB}^{S1S2} \\
\vdots \\
\nabla\Delta\rho_{2,AB}^{S1Sn} \\
\nabla\Delta\phi_{WL,AB}^{S1S2} \\
\vdots \\
\nabla\Delta\phi_{WL,AB}^{S1Sn} \\
\nabla\Delta\phi_{2,AB}^{S1S2} \\
\vdots \\
\nabla\Delta\phi_{2,AB}^{S1Sn} \\
\nabla\Delta D_{2,AB}^{S1S2} \\
\vdots \\
\nabla\Delta D_{2,AB}^{S1Sn}
\end{pmatrix}_k \\
&- \begin{pmatrix}
\nabla\Delta\hat{r}_{AB}^{S1S2} + \nabla\Delta\hat{d}_{ion,AB}^{S1S2} \cdot \frac{f_2^2}{f_1^2} \\
\vdots \\
\nabla\Delta\hat{r}_{AB}^{S1Sn} + \nabla\Delta\hat{d}_{ion,AB}^{S1Sn} \cdot \frac{f_2^2}{f_1^2} \\
\nabla\Delta\hat{r}_{AB}^{S1S2} + \nabla\Delta\hat{d}_{ion,AB}^{S1S2} \\
\vdots \\
\nabla\Delta\hat{r}_{AB}^{S1Sn} + \nabla\Delta\hat{d}_{ion,AB}^{S1Sn} \\
\nabla\Delta\hat{r}_{AB}^{S1S2} + \lambda_{WL} \cdot \nabla\Delta\widehat{N}_{WL,AB}^{S1S2} - \nabla\Delta\hat{d}_{ion,AB}^{S1S2} \cdot \lambda_{WL} \cdot \left(\frac{1}{\lambda_2} - \frac{f_2^2}{f_1^2 \cdot \lambda_1}\right) \\
\vdots \\
\nabla\Delta\hat{r}_{AB}^{S1Sn} + \lambda_{WL} \cdot \nabla\Delta\widehat{N}_{WL,AB}^{S1Sn} - \nabla\Delta\hat{d}_{ion,AB}^{S1Sn} \cdot \lambda_{WL} \cdot \left(\frac{1}{\lambda_2} - \frac{f_2^2}{f_1^2 \cdot \lambda_1}\right) \\
\nabla\Delta\hat{r}_{AB}^{S1S2} + \lambda_2 \cdot \nabla\Delta\widehat{N}_{2,AB}^{S1S2} - \nabla\Delta\hat{d}_{ion,AB}^{S1S2} \\
\vdots \\
\nabla\Delta\hat{r}_{AB}^{S1Sn} + \lambda_2 \cdot \nabla\Delta\widehat{N}_{2,AB}^{S1Sn} - \nabla\Delta\hat{d}_{ion,AB}^{S1Sn} \\
-\nabla\Delta\hat{\dot{r}}_{AB}^{S1S2} \\
\vdots \\
-\nabla\Delta\hat{\dot{r}}_{AB}^{S1Sn}
\end{pmatrix}_{k,(-)}
\end{aligned}
\tag{5.17}
$$

The index k after the brackets in Eq. (5.17) indicates the current observation epoch. The '$(-)$' symbol in the subscript of the second bracket, which contains the predicted observations, indicates that the predicted measurements are based on a priori state estimates that are derived from extrapolation as indicated in Eq. (A.7). So far, the ambiguity terms $\nabla\Delta\widehat{N}_{AB}^{S1Sj}$ are treated as floating numbers.

The actual states of interest are the position and velocity vector of the user receiver. The widelane and carrier phase ambiguities as well as the ionospheric delay terms have also to be included in the state vector in order to model the physical process properly. According to Kalman filter theory, an optimal filter leaves only white Gaussian noise terms as unmodeled error sources. In this work tropospheric delay terms are neglected and therefore also excluded from the simulated physical process. Thus, the state vector comprises the following parameters:

$$\underline{x}_k = \begin{pmatrix} x_{B,k} \\ y_{B,k} \\ z_{B,k} \\ \dot{x}_{B,k} \\ \dot{y}_{B,k} \\ \dot{z}_{B,k} \\ \nabla\Delta N_{WL,AB}^{S1S2} \\ \vdots \\ \nabla\Delta N_{WL,AB}^{S1Sn} \\ \nabla\Delta N_{2,AB}^{S1S2} \\ \vdots \\ \nabla\Delta N_{2,AB}^{S1Sn} \\ Ion_{2,k}^{1} \\ \vdots \\ Ion_{2,k}^{i} \end{pmatrix} \tag{5.18}$$

The EKF can be operated with total estimates of the system states instead of incremental quantities. The derivation can be found in [5]. Keeping track of the total estimates in the EKF rather than incremental ones is adopted here. In Eq. (5.18) the terms $Ion_{2,k}^{i}$ have been introduced, which serve as placeholders for the actual ionosphere-related quantities that are to be estimated with respect to the reference frequency f_2. Three different ionosphere models are implemented in this work. They are presented in detail in Sect. 5.3.

Using the results of the linearization of the GNSS observation model as derived in Sect. 5.2.2, the measurement sensitivity matrix H_k^* can be expressed by:

$$H_k^* = \begin{pmatrix} H_{geo,k}^* & 0 & 0 & 0 & H_{ion,1,k} \\ H_{geo,k}^* & 0 & 0 & 0 & H_{ion,2,k} \\ H_{geo,k}^* & 0 & \lambda_{WL} \cdot I_{(n-1)x(n-1)} & 0 & H_{ion,WL,k} \\ H_{geo,k}^* & 0 & 0 & \lambda_2 \cdot I_{(n-1)x(n-1)} & -H_{ion,2,k} \\ 0 & H_{vel,k} & 0 & 0 & 0 \end{pmatrix} \tag{5.19}$$

Note that apart from the inverse sign of the single matrix entries, $H_{geo,k}^*$ corresponds to $H_{vel,k}$, e.g. $H_{vel,k} = -H_{geo,k}^*$. The negative sign is due to the definition of range rate measurement D_c^{Sj} made in Eq. (3.13). $H_{geo,k}^*$ and $H_{vel,k}$ are (n-1)x(3) matrices, where n is the number of satellites used in the navigation solution. The identity matrices multiplied by the respective wavelength in the third and fourth column of H_k^* account for the ambiguity terms of the phase measurements. In the last column of H_k^*, the design matrices $H_{ion,c,k}$ are introduced which serve as placeholders for the ionospheric measurement sensitivity matrices. They are also dependent on the concrete ionosphere model in use and will therefore be discussed in Sect. 5.3. The inverse sign of $H_{ion,2,k}$ in the second and fourth column of Eq. (5.19) results from the fact that the phase velocity is advanced compared to the propagation in vacuum, while the group velocity is delayed when passing through the ionosphere.

Finally, the covariance matrix of measurement noise R is derived. If the measurement model reflects the physical process properly, it should hold that the measurement noise is white Gaussian, e.g. $\underline{v}_k \sim N(0, R_k)$ as indicated in Eq. (A.2). The stochastic model should account for cross-correlations and time-correlations of the GNSS measurements. The issue of time-correlations becomes more severe if high sampling rates are considered. Here it is assumed in the derivation of the covariance matrix of measurement noise that time-correlations are negligible. In the simulations a low sampling rate of 1 Hz is considered. The focus of the stochastic measurement model presented here is directed to the cross-correlations of measurements due to double-differencing and inter-frequency combinations. The variance-covariance error propagation due to double-differencing has already been introduced in detail in Sect. 3.5.2, so that the results can be reused here. The covariance matrix R for the concrete measurement model at hand reads:

$$R_k = \begin{bmatrix} D\left\{\nabla\Delta\underline{\rho}_{1,AB}\right\} & 0 & 0 & 0 \\ 0 & D\left\{\nabla\Delta\underline{\rho}_{2,AB}\right\} & 0 & 0 \\ 0 & 0 & D\left\{\nabla\Delta\underline{\phi}_{AB}\right\} & 0 \\ 0 & 0 & 0 & D\left\{\nabla\Delta\underline{D}_{2,AB}\right\} \end{bmatrix}_k \tag{5.20}$$

, with $\nabla\Delta\underline{\phi}_{AB}^T = \left[\nabla\Delta\underline{\phi}_{WL,AB}^T \quad \nabla\Delta\underline{\phi}_{2,AB}^T\right]$. The dispersions of the double-differenced pseudorange measurements and range rate measurements follow immediately from Eq. (3.42). The general form of the error propagation due to double-differencing reads:

$$D\left\{\nabla\Delta\underline{m}_{AB}\right\} = D \cdot \begin{bmatrix} Cov(\underline{m}_A) & 0 \\ 0 & Cov(\underline{m}_B) \end{bmatrix} \cdot D^T \tag{5.21}$$

, where D is the double-difference generator matrix according to Eq. (3.41) and m is a placeholder for the respective measurement type. When computing the dispersion of the widelane and carrier phase measurements $D\left\{\nabla\Delta\underline{\phi}_{AB}\right\}$, it has to be considered that the widelane and carrier phase measurements are correlated due to the inter-frequency linear combination. The stochastic measurement model for a geometry-based cascading ambiguity resolution scheme using phase measurements on three different frequencies is depicted in Zhang et al. [57]. This stochastic model for inter-frequency combinations of phase measurements can be broken down to dual-frequency application. The dispersion of the widelane and carrier phase measurements in the range domain becomes:

$$D\left\{\nabla\Delta\underline{\phi}_{AB}\right\} = L \cdot \begin{bmatrix} D\left\{\nabla\Delta\underline{\Phi}_{1,AB}\right\} & 0 \\ 0 & D\left\{\nabla\Delta\underline{\Phi}_{2,AB}\right\} \end{bmatrix} \cdot L^T \tag{5.22}$$

, where L is a frequency-dependent scaling matrix that accounts for the linear combination of the carrier phase measurements on f_1 and f_2 in order to form the widelane:

$$L = \begin{bmatrix} -\lambda_{WL} \cdot I_{(n-1)x(n-1)} & \lambda_{WL} \cdot I_{(n-1)x(n-1)} \\ 0 & \lambda_2 \cdot I_{(n-1)x(n-1)} \end{bmatrix} \tag{5.23}$$

Note that scaling with the matrix L has also the effect of transiting from the space of cycles to the space of ranges, since $D\left\{\nabla\Delta\underline{\Phi}_{AB}\right\}$ is the dispersion of the phase measurements in units of cycles[2]. The derivation of the covariance matrix R of measurement noise completes the description of the measurement model.

5.2.4 State Space Model

So far the GNSS measurement model used in the EKF has been presented. In this chapter the state space model is described, which is chosen to be a pure linear model in contrast to the measurement model. The landing approach of the airplane is modeled as straight flight condition with constant velocity. Positive and negative accelerations are treated as white Gaussian noise in this model. The differential state equations of the airplane's dynamics during the final approach in matrix representation read:

$$\frac{d}{dt}\begin{pmatrix}x_B\\ y_B\\ z_B\\ \dot{x}_B\\ \dot{y}_B\\ \dot{z}_B\end{pmatrix}=\begin{bmatrix}0&0&0&1&0&0\\0&0&0&0&1&0\\0&0&0&0&0&1\\0&0&0&0&0&0\\0&0&0&0&0&0\\0&0&0&0&0&0\end{bmatrix}\cdot\begin{pmatrix}x_B\\ y_B\\ z_B\\ \dot{x}_B\\ \dot{y}_B\\ \dot{z}_B\end{pmatrix}+\begin{pmatrix}0\\0\\0\\ \omega_{\ddot{x}_B}\\ \omega_{\ddot{y}_B}\\ \omega_{\ddot{z}_B}\end{pmatrix}\quad, \tag{5.24}$$

where $\omega_{\ddot{x}_B}$, $\omega_{\ddot{y}_B}$ and $\omega_{\ddot{z}_B}$ are assumed to be white noise processes that reflect random accelerations of the airplane. In discrete time, the user position vector $\underline{X}_B$ and the velocity vector $\dot{\underline{X}}_B$ at epoch k can be expressed by a linear combination of $\underline{X}_B$ and $\dot{\underline{X}}_B$ from the previous epoch k-1:

$$\begin{pmatrix}\underline{X}_{B,k}\\ \dot{\underline{X}}_{B,k}\end{pmatrix}=\begin{pmatrix}\underline{X}_{B,k-1}\\ \dot{\underline{X}}_{B,k-1}\end{pmatrix}+\begin{pmatrix}\Delta t\cdot\dot{\underline{X}}_{B,k-1}\\ \underline{0}\end{pmatrix}+\underline{\omega}_{k-1}\quad,\quad\underline{\omega}_{k-1}\sim N\left(\underline{0},Q_{PV,k-1}\right)\quad, \tag{5.25}$$

where Δt denotes the time-span between the observation epochs k-1 and k. The covariance matrix of the position and velocity process noise is denoted as Q_{PV}. The assumption that accelerations of the airplane are normally distributed with zero-mean does only hold for short phases of the landing approach (see Figure 5.3).

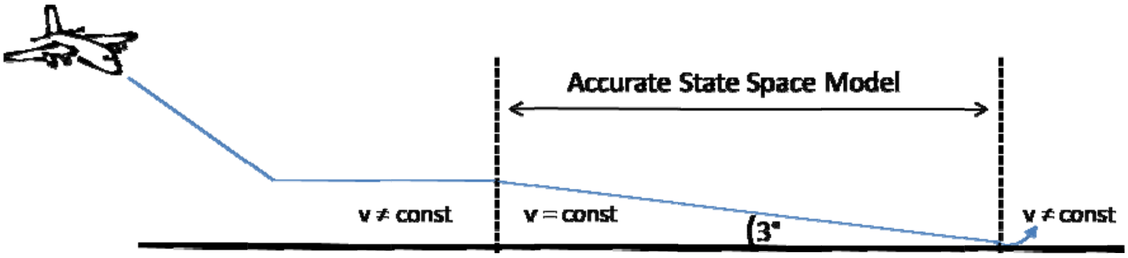

Figure 5.3: State space model of the landing approach

It is investigated in simulations whether this simple state space model of the airplane's dynamics is sufficient in order to achieve the required position accuracies. A more accurate state space model of the final phase of the flight can be obtained by extending the model by states for the airplane's accelerations. In absence of cycle slips, the initially unknown widelane and carrier phase ambiguities stay constant during different observation epochs. The assumptions about the system dynamics are summarized in the state transition matrix:

$$\Phi_{k-1}=\begin{bmatrix}1&0&0&\Delta t&0&0&\cdots&0\\0&1&0&0&\Delta t&0&&\\0&0&1&0&0&\Delta t&&\\0&0&0&1&0&0&\cdots&0\\0&0&0&0&1&0&&\\0&0&0&0&0&1&&\\\vdots&&&\vdots&&&I_{(2n-2)x(2n-2)}&\\0&&&0&&&&\Phi_{ion}\end{bmatrix} \tag{5.26}$$

The first (6)x(6) entries of the state transition matrix follow from the linear dynamic model for the user position and velocity states given in Eq. (5.25). The identity matrix of size (2n-2)x(2n-2) reflects that the (n-1) widelane ambiguities and the (n-1) carrier phase ambiguities stay constant between different observation epochs. Again, the matrix Φ_{ion} will be specified when presenting the different ionosphere models. The covariance matrix of process noise associated with the state space equations is given by:

$$Q_{k-1}=\begin{bmatrix}Q_{PV}&0&0&0\\0&Q_{N_{WL}}&0&0\\0&0&Q_{N_2}&0\\0&0&0&Q_{ion}\end{bmatrix}_{k-1} , \tag{5.27}$$

where the covariance matrix of position- and velocity-related process noise Q_{PV} follows from

$$Q_{PV}=\begin{bmatrix}S_p\cdot\frac{\Delta t^3}{3}&0&0&S_p\cdot\frac{\Delta t^2}{2}&0&0\\0&S_p\cdot\frac{\Delta t^3}{3}&0&0&S_p\cdot\frac{\Delta t^2}{2}&0\\0&0&S_p\cdot\frac{\Delta t^3}{3}&0&0&S_p\cdot\frac{\Delta t^2}{2}\\S_p\cdot\frac{\Delta t^2}{2}&0&0&S_p\cdot\Delta t&0&0\\0&S_p\cdot\frac{\Delta t^2}{2}&0&0&S_p\cdot\Delta t&0\\0&0&S_p\cdot\frac{\Delta t^2}{2}&0&0&S_p\cdot\Delta t\end{bmatrix} . \tag{5.28}$$

The parameter S_p denotes the spectral amplitude of the random walk process. The derivation of Eq. (5.28) is indicated in Brown et al. [5], where the variances and covariances of the random walk process are computed from:

$$E\{x_i(\Delta t)x_i(\Delta t)\}=\int_0^{\Delta t}\int_0^{\Delta t}u\cdot v\cdot S_p\cdot\delta(u-v)dudv=S_p\cdot\frac{\Delta t^3}{3} , \tag{5.29}$$

$$E\{x_{i+3}(\Delta t)x_{i+3}(\Delta t)\}=\int_0^{\Delta t}\int_0^{\Delta t}1\cdot 1\cdot S_p\cdot\delta(u-v)dudv=S_p\cdot\Delta t , \tag{5.30}$$

$$E\{x_i(\Delta t)x_{i+3}(\Delta t)\}=\int_0^{\Delta t}\int_0^{\Delta t}1\cdot v\cdot S_p\cdot\delta(u-v)dudv=S_p\cdot\frac{\Delta t^2}{2} , \tag{5.31}$$

where δ is the Dirac delta function. The subscript i ranges from 1…3 and corresponds to either the x-, y- or the z-component of the position and velocity vector, e.g. $x_1 = x_B$, $x_4 = \dot{x}_B$,… . Besides the stochastic model for the random walk process, a stochastic model for the ambiguities is required. In principle, estimating the initially unknown integer ambiguities with an EKF corresponds to estimating constant values if it is supposed that there are no cycle slips. As a consequence, the covariance matrices of process noise that correspond to the ambiguity terms, $Q_{N_{WL}}$ and Q_{N_2}, are zero matrices in theory. In practice, the variances of the double-differenced ambiguities are set to values greater than zero. Here it is chosen to perform a continuous downscaling of the ambiguity variances:

$$Q_{N_{WL},k} = \sigma^2_{N_{WL},k} \cdot I_{(n-1)x(n-1)} \quad , \tag{5.32}$$

$$Q_{N_2,k} = \sigma^2_{N_2,k} \cdot I_{(n-1)x(n-1)} \quad . \tag{5.33}$$

As long as the filter still works with float ambiguities, the variances $\sigma^2_{N_{WL},k}$ and $\sigma^2_{N_2,k}$ are decreased with time. It is ensured that the variances will never go below a lower limit as long as the ambiguities are not fixed. After accepting the integer ambiguities, the covariance matrices $Q_{N_{WL},k}$ and $Q_{N_2,k}$ are set to zero-matrices. Successful integer ambiguity fixing is also reflected by the covariance matrix of state estimation uncertainty P_k. The entries which correspond to uncertainties in the ambiguity estimates are set to zero after accepting the integer ambiguities.

This leaves the sub-matrix Q_{ion} in Eq. (5.27) as only unspecified entry. The process noise covariance matrix Q_{ion}, which corresponds to a concrete stochastic ionosphere model, is derived in the following chapter for three different ionosphere models.

5.3 Stochastic Modeling of the Ionosphere

5.3.1 LAAS Model of the Differential Ionospheric Ranging Error

The indication of precise and globally valid models for the electron content in the atmosphere is hardly possible. The electron content varies amongst others with the day time, the season, the sun cycle and the geomagnetic activity. Although a great part of the ranging errors caused by ionospheric delay cancel out when double-differencing between observations, the residual ionospheric error is not necessarily negligible. Especially when the baseline length between the reference receiver and the user receiver increases or in presence of ionosphere storms, uncompensated residual ionospheric range errors may severely degrade the navigation solution. Therefore, the differential ionospheric errors are estimated as separate states in the EKF.

The first model which is considered is the Local Area Augmentation System (LAAS) model of the differential ionospheric ranging error after [28]. It aims at estimating the single-differenced ionospheric range error as a function of the vertical ionospheric gradient (VIG):

$$\Delta d^{Sj}_{ion,AB} = VIG^{Sj}_{AB} \cdot \frac{\left\| \underline{X}_A - \underline{\hat{X}}_B \right\|_2}{\sqrt{1 - \left(\frac{R_e \cdot cos(E^{Sj})}{R_e + h_I} \right)^2}} \quad , \tag{5.34}$$

where:

$\Delta d_{ion,AB}^{Sj}$: Single-differenced ionospheric ranging error due to spatial decorrelation of the delays caused by the ionosphere at the receiver sites *A* and *B*

VIG_{AB}^{Sj}: Vertical ionospheric gradient with respect to the reference frequency f_{ion} and the constellation of satellite S_j and receiver *A* and *B*

R_e: Mean radius of the earth (6368 km)

E^{Sj}: Satellite elevation angle of S_j (in this work the satellite elevation angle at the reference receiver site is chosen)

h_I: Mean ionospheric shell height

Note that Eq. (5.34) results from the LAAS ionospheric model by setting the smoothing time constant to zero. In this work h_I is assumed to be 350 km, which is according to [13] also used as the mean ionospheric shell height in Klobuchar's ionospheric delay model. The procedure of modeling the VIG for each observed satellite as additional state in a covariance analysis has already been proposed by Pervan et al. [33]. Thus, if there are n satellites in view, also n VIGs have to be included as separate states in the filter:

$$\begin{pmatrix} Ion_{2,k}^{1} \\ \vdots \\ Ion_{2,k}^{i} \end{pmatrix} = \begin{pmatrix} VIG_{2,k}^{S1} \\ \vdots \\ VIG_{2,k}^{Sn} \end{pmatrix} \tag{5.35}$$

According to [28], it is reasonably conservative to set the standard deviations of the VIGs to $\sigma_{VIG} = 2mm/km$ in most locations and at most times, but it may also be as high as $\sigma_{VIG} = 8mm/km$ in equatorial regions. The expected variance σ_{VIG}^2 of the vertical ionospheric gradient is used in order to set up the sub-matrix Q_{ion} of the covariance matrix of process noise:

$$Q_{ion} = \sigma_{VIG}^2 \cdot I_{(n)x(n)} \tag{5.36}$$

The sensitivity of the ionospheric state estimation on the parameter σ_{VIG}^2 has to be investigated, since this parameter is generally not known precisely in advance. It is assumed that the VIGs are just driven by a white-noise process. Therefore, the sub-matrix for the ionospheric terms of the state transition matrix simply becomes the identity matrix:

$$\Phi_{ion} = I_{(n)x(n)} \tag{5.37}$$

The LAAS model of the differential ionospheric ranging error refers to the single-differenced ionospheric range error. However, the measurement model presented in Sect. 5.2.3 is based on double-differenced measurements. An estimate of the residual double-differenced ionospheric range error $\nabla\Delta\hat{d}_{ion,AB}^{S1Sj}$ is obtained by differencing the single-differenced ionospheric range errors, see Eq. (5.34), between different satellites:

$$\nabla\Delta\hat{d}_{ion,AB}^{S1Sj} = \Delta\hat{d}_{ion,AB}^{S1} - \Delta\hat{d}_{ion,AB}^{Sj} = \left\|\underline{X}_A - \hat{\underline{X}}_B\right\|_2 \cdot \left(\frac{\widehat{VIG}_{AB}^{S1}}{\sqrt{1 + \left(\frac{R_e \cdot cos(E^{S1})}{R_e + h_I}\right)^2}} - \frac{\widehat{VIG}_{AB}^{Sj}}{\sqrt{1 + \left(\frac{R_e \cdot cos(E^{Sj})}{R_e + h_I}\right)^2}} \right) \tag{5.38}$$

As stated before, the frequency-dependent VIGs are referenced to the carrier frequency f_2. Neglecting terms of higher orders, the additional delay of L-band signals caused by ionospheric refraction is proportional to 1/f². Therefore, simple scaling can be applied in order to derive the different matrices $H_{ion,c,k}$:

$$H_{ion,c,k} = \frac{f_2^2}{f_c^2} \cdot \begin{pmatrix} m_{ion,k}^{S1} & -m_{ion,k}^{S2} & 0 & \cdots & 0 \\ m_{ion,k}^{S1} & 0 & -m_{ion,k}^{S3} & \cdots & 0 \\ \vdots & \vdots & \vdots & \ddots & \vdots \\ m_{ion,k}^{S1} & 0 & 0 & \cdots & -m_{ion,k}^{Sn} \end{pmatrix} , \tag{5.39}$$

with:

$$m_{ion,k}^{Sj} = \frac{\left\|\underline{X}_A - \underline{\hat{X}}_B\right\|_2}{\sqrt{1 + \left(\frac{R_e \cdot cos(E^{Sj})}{R_e + h_I}\right)^2}} \tag{5.40}$$

The frequency-dependent scaling factor for the residual ionospheric terms of the widelane measurements follows from Eq. (5.14). Thus, the measurement sensitivity matrix of the double-differenced widelane ionospheric range errors becomes:

$$\begin{aligned} H_{ion,WL,k} = -\lambda_{WL} \cdot \left(\frac{1}{\lambda_2} - \frac{f_2^2}{f_1^2 \cdot \lambda_1}\right) \\ \cdot \begin{pmatrix} m_{ion,k}^{S1} & -m_{ion,k}^{S2} & 0 & \cdots & 0 \\ m_{ion,k}^{S1} & 0 & -m_{ion,k}^{S3} & \cdots & 0 \\ \vdots & \vdots & \vdots & \ddots & \vdots \\ m_{ion,k}^{S1} & 0 & 0 & \cdots & -m_{ion,k}^{Sn} \end{pmatrix} \end{aligned} \tag{5.41}$$

There is one main drawback associated with the application of the LAAS differential ionosphere model in this work. It has been designed for the processing of single-differenced measurements. However, if double-differenced measurements are processed, there arises the problem of bad observability: there are n-1 double-differenced observations, but n VIGs have to be estimated. As indicated before, it is possible to set up an appropriate measurement sensitivity matrix even when using double-differenced observations. But the observability test according to Eq. (4.8) reveals that the observability matrix O has a rank deficiency of 1 if a discrete time interval of only one single epoch is considered. By extending the discrete time interval to two epochs, the observability matrix O is already of full rank, but still bad conditioned. From Kalman filter theory it is known that bad observability of system states is reflected by the covariance matrix of state estimation uncertainty $P_k(+)$. On the left side of Figure 5.4 it is shown that the main diagonal terms of $P_k(+)$, which correspond to the predicted variances of the VIGs, indicate that the VIG estimation errors diverge due to bad observability.

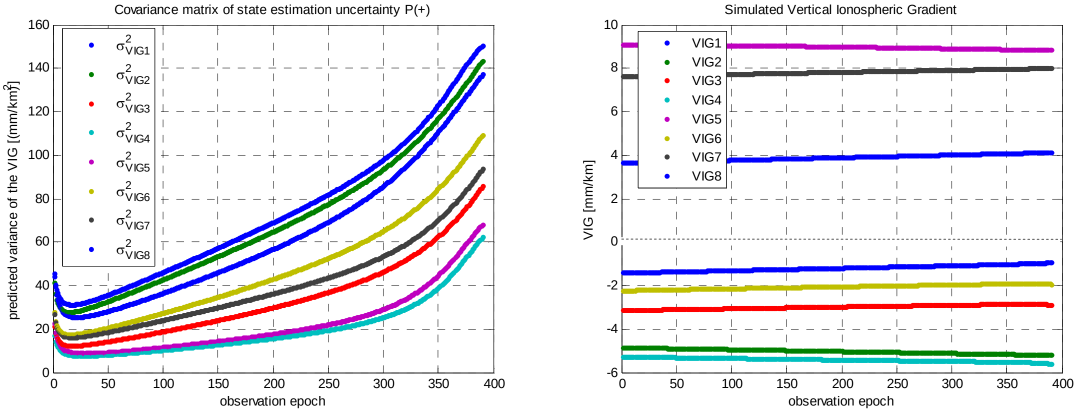

Figure 5.4: Bad observability of the Vertical Ionospheric Gradients

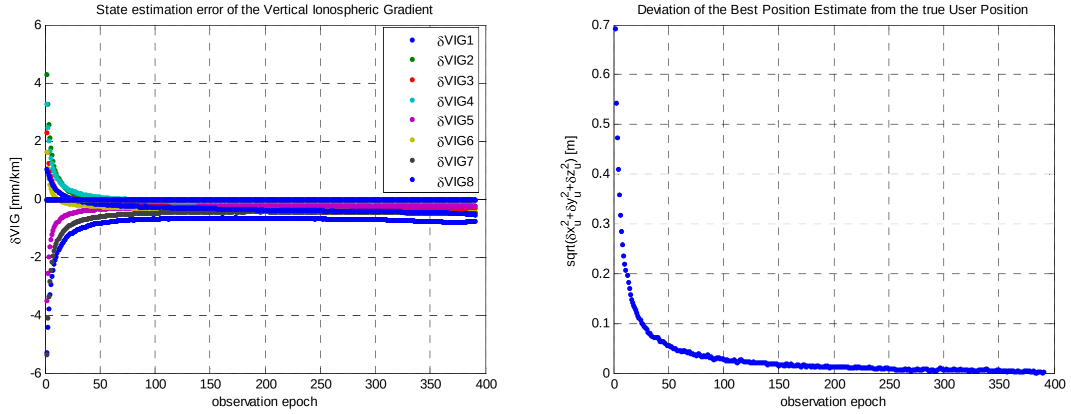

Figure 5.5: Good performance of the ionospheric state estimation despite of bad observability

On the other hand, by comparing the simulated VIGs illustrated on the right side of Figure 5.4 with the remaining estimation errors of the VIGs illustrated on the left side Figure 5.5, one can see that the estimation of the VIGs with the LAAS model works quite well despite of using double-differenced observations. On the other hand, the results refer to a noise-free simulation scenario, e.g. only propagation delay due to ionospheric refractivity has been simulated. In Sect. 7.2.4 test results are presented when using this ionosphere model in a multipath environment.

5.3.2 Double-difference Ionosphere Model

A second approach that addresses to the modeling of the stochastic behavior of the double-differenced ionospheric range error instead of the single-differenced ionospheric range error is presented in Goad et al. [11]. The placeholders for the ionosphere terms introduced in Eq. (5.18) can therefore be filled with:

$$\begin{pmatrix} Ion_{2,k}^{1} \\ \vdots \\ Ion_{2,k}^{i} \end{pmatrix} = \begin{pmatrix} \nabla\Delta d_{ion,2,k}^{S1S2} \\ \vdots \\ \nabla\Delta d_{ion,2,k}^{S1Sn} \end{pmatrix} \tag{5.42}$$

In this approach "virtual" measurements of the double-differenced ionospheric range errors are introduced. The original measurement vector $\underline{z}_k$ is extended by the virtual measurements to the new measurement vector $\underline{z}_{ext,k}$:

$$\underline{z}_{ext,k} = \begin{pmatrix} \underline{z}_k \\ \underline{0}_{(n-1)} \end{pmatrix} \tag{5.43}$$

From Eq. (5.43) follows that the n-1 pseudo-measurements of the double-differenced ionospheric range errors are all set to zero. This corresponds to ideal spatial correlation of the ionospheric range errors. The variance $\sigma^2_{\nabla\Delta d_{ion,AB}}$ of the pseudo-measurements is calculated from:

$$\sigma^2_{\nabla\Delta d_{ion,AB}} = \sigma^2_\infty \cdot \left(1 - e^{-2\cdot\frac{|\delta|}{D}}\right) \quad , \tag{5.44}$$

where $\sigma^2_\infty = 2\mathrm{m}^2$ is the empirically found upper limit of the double-differenced ionospheric variance at a distance of 1500 km. The change of the baseline length between two successive epochs is represented by δ, and D represents the first order correlation distance of the double-differenced ionosphere. The extended covariance matrix of measurement noise becomes:

$$R_{ext,k} = \begin{bmatrix} R_k & 0 \\ 0 & \sigma^2_{\nabla\Delta d_{ion,AB}} \cdot I_{(n-1)x(n-1)} \end{bmatrix} \tag{5.45}$$

Since the double-differenced residual ionospheric range errors are estimated directly, the resulting measurement sensitivity matrix of the ionospheric terms simplifies to

$$H_{ion,c,k} = \frac{f_2^2}{f_c^2} \cdot I_{(n-1)x(n-1)} \tag{5.46}$$

and for the widelane measurements the matrix of ionospheric terms is given by

$$H_{ion,WL,k} = -\lambda_{WL} \cdot \left(\frac{1}{\lambda_2} - \frac{f_2^2}{f_1^2 \cdot \lambda_1}\right) \cdot I_{(n-1)x(n-1)} \quad . \tag{5.47}$$

The pseudo-measurements which have been introduced here have also to be reflected by the measurement sensitivity matrix. The extended measurement sensitivity matrix reads:

$$H_{ext,k} = \begin{bmatrix} & H_k & \\ 0_{(n-1)x(2n+4)} & & I_{(n-1)x(n-1)} \end{bmatrix} \tag{5.48}$$

This completes the extensions of the measurement model. Next, the placeholders of state space model are filled. The variance of the prediction error of the double-differenced ionosphere is approximated by:

$$\sigma^2_{pion,AB} = \sigma^2_\infty \cdot \left(1 - e^{-2\cdot\left(\frac{|\tau|}{T} + \frac{|\delta|}{D}\right)}\right) \quad , \tag{5.49}$$

where τ is the sampling time interval and T is the first order correlation time of the double-differenced ionosphere. Adopting the values indicated in [11], T is set to 64 minutes and D is set to 1500 km. When comparing Eq. (5.44) with Eq. (5.49), it becomes obvious that the variance of the ionospheric prediction error $\sigma^2_{pion,AB}$ will always be larger than the variance of the pseudo-measurements of the double-differenced ionospheric range errors. It has to be discussed whether this is useful or not with respect to precise positioning. After the variance of the ionospheric prediction error has been defined, the sub-matrix Q_{ion} can be indicated as:

$$Q_{ion} = \sigma^2_{pion,AB} \cdot I_{(n-1)x(n-1)} \tag{5.50}$$

The state equations of the double-differenced ionosphere read:

$$\nabla\Delta d^{S1Sj}_{ion,2,k+1} = \nabla\Delta d^{S1Sj}_{ion,2,k} \cdot e^{-\left(\frac{|\tau|}{T}+\frac{|\delta|}{D}\right)} + v_{ion,k} \tag{5.51}$$

Consequently, the ionospheric prediction operator is an exponential function with respect to the sampling time τ and the baseline length change δ. It is assumed that $v_{ion,k}$ is white Gaussian noise. The exponential prediction function of the double-differenced ionosphere can also be found in the sub-matrix Φ_{ion} of the state transition matrix:

$$\Phi_{ion} = e^{-\left(\frac{|\tau|}{T}+\frac{|\delta|}{D}\right)} \cdot I_{(n-1)x(n-1)} \tag{5.52}$$

When evaluating the exponential function indicated in Eq. (5.52) with realistic values for the sampling rate and the velocities of the airplane, it becomes obvious that Φ_{ion} virtually reduces to the identity matrix.

5.3.3 Single-difference Ionosphere Model

The double-difference ionosphere model presented in the previous section has the drawback that it does not reflect the elevation-dependency of the residual ionospheric range errors. This drawback is overcome with the third model presented in this section, which was originally developed for estimating the single-differenced ionospheric range errors. However, it can be adopted in order to estimate the double-differenced range errors. In contrast to the adaptation of the LAAS differential ionosphere model, here the adaptation from single-differences to double-differences does not cause bad observability of the ionospheric states. This is ensured by including the double-differenced ionospheric range errors instead of the single-differenced ionospheric range errors in the system state vector:

$$\begin{pmatrix} Ion^1_{2,k} \\ \vdots \\ Ion^i_{2,k} \end{pmatrix} = \begin{pmatrix} \nabla\Delta d^{S1S2}_{ion,2,k} \\ \vdots \\ \nabla\Delta d^{S1Sn}_{ion,2,k} \end{pmatrix} \tag{5.53}$$

Since the states to be estimated are identical with those presented in Eq. (5.42), it follows that $H_{ion,c,k}$ corresponds to that of Eq. (5.46) and $H_{ion,WL,k}$ corresponds to that of Eq. (5.47). However, here no pseudo-measurements of the double-differenced ionospheric range errors are introduced into the measurement model.

Wübbena [53] suggests a stochastic model for the single-differenced ionospheric range error, which is exponentially correlated with the baseline length $\left\|\underline{X}_A - \hat{\underline{X}}_B\right\|_2$ between the user receiver and reference receiver:

$$\sigma^2_{\Delta d_{ion,AB}} = \sigma^2(E^{Sj}) \cdot e^{\frac{\|\underline{X}_A - \hat{\underline{X}}_B\|_2}{d}} \quad , \tag{5.54}$$

where d is the correlation distance. Unlike D in Goad's ionosphere model [11], the correlation distance d is assumed to be between 200…400 km. The variance of the single-differenced ionospheric range error in zenith is set to $\sigma^2(90°) = (3cm)^2$. In [53] it is suggested to model the dependency on the satellite elevation angle as:

$$\sigma^2(E^{Sj}) = SF^2 \cdot \sigma^2(90°) \tag{5.55}$$

The parameter SF in Eq. (5.55) is the Slant Factor, which is defined as:

$$SF = sec\left\{arcsin\left[\frac{R_e \cdot cos\left(E^{Sj}\right)}{R_e + h_I}\right]\right\} \tag{5.56}$$

By applying the trigonometric properties $arcsin(x) = arccos\sqrt{1-x^2}$ for $0 \leq x \leq 1$ and $sec(x) = 1/cos\ (x)$ to Eq. (5.56), it follows that the same definition of the slant factor is also used by the LAAS differential ionosphere model in Eq. (5.34).

The variance of the double-differenced ionospheric range error is derived from Eq. (5.54) by applying the law of error propagation:

$$\sigma^2_{\nabla\Delta d^{S1Sj}_{ion,AB}} = \left(SF^2_{S1} + SF^2_{Sj}\right) \cdot \sigma^2(90^\circ) \cdot e^{\frac{\left\|\underline{X}_A - \underline{\hat{X}}_B\right\|_2}{d}} \tag{5.57}$$

The elevation-dependent covariance matrix of process noise Q_{ion} becomes:

$$Q_{ion} = S_{ion} \cdot \begin{bmatrix} \sigma^2_{\Delta d^{S1}_{ion,AB}} & \cdots & 0 \\ \vdots & \ddots & \vdots \\ 0 & \cdots & \sigma^2_{\Delta d^{Sn}_{ion,AB}} \end{bmatrix} \cdot S^T_{ion} \quad , \tag{5.58}$$

with the single-difference ionospheric generator matrix S_{ion}

$$S_{ion} = \left[\underline{1}_{(n-1)} \quad -I_{(n-1)x(n-1)}\right] \quad . \tag{5.59}$$

Finally, the state transition sub-matrix Φ_{ion} has to be derived. In this work it is assumed that the discrete-time state equation of the double-differenced ionospheric range error can be indicated as follows:

$$\nabla\Delta d^{S1Sj}_{ion,2,k+1} = \nabla\Delta d^{S1Sj}_{ion,2,k} \cdot \left(1 + e^{\frac{\left\|\underline{X}_A - \underline{\hat{X}}_B\right\|_2}{d}} \cdot \frac{\frac{d}{dt}\left(\left\|\underline{X}_A - \underline{\hat{X}}_B\right\|_2\right)}{d} \cdot \Delta t\right) + \upsilon_{ion,k} \tag{5.60}$$

From Eq. (5.60) follows that Φ_{ion} can be expressed by:

$$\Phi_{ion} = \left(1 + e^{\frac{\left\|\underline{X}_A - \underline{\hat{X}}_B\right\|_2}{d}} \cdot \frac{\frac{d}{dt}\left(\left\|\underline{X}_A - \underline{\hat{X}}_B\right\|_2\right)}{d} \cdot \Delta t\right) \cdot I_{(n-1)x(n-1)} \tag{5.61}$$

The measurement model and the state space model used in the EKF are now completely defined for all three stochastic ionosphere models. It is also provided by the software to omit modeling of the double-differenced residual ionospheric errors, e.g. the residuals are treated as white Gaussian noise.

5.4 Integer Ambiguity-fixed Navigation Solution

5.4.1 Integer-nature preserving GNSS Model

The general form of the linearized GNSS model has already been introduced in Sect. 5.2.2. In this section the integer-nature preserving GNSS model is presented, since carrier phase measurements are used in addition to pseudorange measurements in order to derive a navigation solution. A general approach is to start with the GNSS model presented in Eq. (5.1), which neglects the integer-nature of the carrier phase ambiguities. The resulting position solution is referred to as float solution. Afterwards, a GNSS model is introduced that distinguishes between real-valued and integer parameters. The mathematical model of double-differenced linearized observation equations which explicitly accounts for the integer nature of the ambiguities is

$$\underline{y} = A \cdot \underline{N} + B \cdot \underline{b} + \underline{\upsilon}_* \quad , \tag{5.62}$$

where:

A, B: Design matrices

$\underline{\mathrm{y}} \in \mathbb{R}^{\mathrm{n}}$: Vector of residuals between measured and computed double-differenced observations

$\underline{N} \in \mathbb{Z}^{\mathrm{m}}$: Vector of double-differenced integer ambiguities

$\underline{b} \in \mathbb{R}^{\mathrm{p}}$: Vector of remaining real-valued states excluding the integer ambiguities

$\underline{\upsilon}_* \in \mathbb{R}^{\mathrm{n}}$: Noise vector

Note that in this and the following sub-sections the double-difference operator $\nabla\Delta$ is skipped in order to simplify notations. Furthermore, a second change of notation is carried out. The measurement vector $\underline{z}$ of Eq. (5.1) is now denoted as $\underline{y} \in \mathbb{R}^n$, while the m-dimensional vector $\underline{z} \in \mathbb{Z}^m$ will represent a vector of integer-values. In order to distinguish between float and integer estimates, in the following a hat above the parameter $\hat{\square}$ indicates that the parameter is a float estimate, while an inverse hat above a parameter $\check{\square}$ indicates that the parameter is an integer estimate.

Teunissen et al. [42] state that the performance of ambiguity resolution is expected to be better for geometry-based models than for geometry-free models. In this work it is intuitive to use a geometry-based model since the baseline solution is of interest rather than the integer ambiguities themselves. Additional redundancy is introduced by linking all ranges to the same baseline solution and changes of the relative receiver-satellite geometry over time can be exploited beneficially. So far, the integer-nature of the double-differenced ambiguities has been neglected. As a result, the float solution of the system states was obtained. In the float solution of state estimates both the real-valued parameters $\underline{b}$, like the user position and the user velocity, and the actually integer-valued ambiguities $\underline{N}$ are given as real numbers:

$$\begin{pmatrix} \underline{\hat{N}} \\ \underline{\hat{b}} \end{pmatrix} , \begin{bmatrix} Q_{\underline{\hat{N}}} & Q_{\underline{\hat{N}},\underline{\hat{b}}} \\ Q_{\underline{\hat{b}},\underline{\hat{N}}} & Q_{\underline{\hat{b}}} \end{bmatrix} \tag{5.63}$$

The float solution vector indicated in Eq. (5.63) corresponds to the vector of state estimates $\underline{\hat{x}}(+)$, and its covariance matrix to the covariance matrix of state estimation uncertainty $P(+)$. In the next sub-sections two different procedures of integer ambiguity resolution will be presented, which are implemented in the navigation software. After having found the integer ambiguity vector $\underline{\check{N}}$, in [21] the following approach is presented in order to compute the fixed solution $\underline{\check{\mathrm{b}}}$ of the actual parameters of interest:

$$\underline{\check{b}} = \underline{\hat{b}} - Q_{\underline{\hat{b}},\underline{\hat{N}}} \cdot Q_{\underline{\hat{N}}}^{-1} \cdot \left(\underline{\hat{N}} - \underline{\check{N}}\right) \tag{5.64}$$

The covariance matrix $Q_{\underline{\check{b}}}$ of the fixed solution follows from applying the law of error propagation:

$$Q_{\underline{\check{b}}} = Q_{\underline{\hat{b}}} - Q_{\underline{\hat{b}},\underline{\hat{N}}} \cdot Q_{\underline{\hat{N}}}^{-1} \cdot Q_{\underline{\hat{N}},\underline{\hat{b}}} \tag{5.65}$$

Eq. (5.64) and Eq. (5.65) result from the sequential application of the theory of conditional least squares adjustment. Thus a re-computation of the solution with fixed ambiguities is not required, which is an important implementation aspect. The accuracy of the fixed solution is at the centimeter-level provided that $\underline{\breve{N}}$ corresponds to the true integer ambiguity vector $\underline{N}$. In RTK applications like landing approaches, integer ambiguity resolution is more difficult than in static applications. The assessment of the reliability of the estimated integer ambiguity vector $\underline{\breve{N}}$ plays a major role in high-integrity carrier phase-based positioning for precision landing. Therefore, the integer ambiguity estimators presented hereafter have to be judged by the capability of quantifying the probability of wrong integer ambiguity fixing rather than by the integer ambiguity resolution success rates.

5.4.2 LAMBDA Method and Integer Ambiguity Validation

The LAMBDA method, which has been proposed by Teunissen [39] in 1993, is applied in this work in order to compute integer least squares ambiguity estimates $\underline{\breve{N}}$ from a vector of float ambiguities $\underline{\hat{N}}$ and their associated covariance matrix $Q_{\underline{\hat{N}}}$. The determination of the float solution is accomplished by disregarding the integer constrains on the ambiguities as described in Sect. 5.2. However, by taking into account the integer nature of the ambiguities, an even more precise position solution can be derived provided that the integer ambiguities are fixed correctly. LAMBDA is an acronym for "Least-squares AMBiguity Decorrelation and Adjustment", which points to the two basic steps involved in the computation of $\underline{\breve{N}}$: In the first step, the float ambiguities and their covariance matrix are decorrelated. In the second step, a discrete search strategy based on sequential conditional least squares adjustment is applied in order to determine the integer ambiguities. Applying a decorrelating ambiguity transformation prior to the sequential conditional least-squares adjustment has the advantage that the discrete search can be performed more efficiently. The float ambiguities $\underline{\hat{N}}$ are decorrelated by applying the transformation:

$$\underline{\hat{z}} = Z^T \cdot \underline{\hat{N}} \tag{5.66}$$

The transformation matrix Z is chosen such that the covariance matrix $Q_{\underline{\hat{z}}}$ of the decorrelated float ambiguities $\underline{\hat{z}}$ resembles more a diagonal matrix than the original covariance matrix $Q_{\underline{\hat{N}}}$. The covariance matrix of the decorrelated ambiguities is calculated from:

$$Q_{\underline{\hat{z}}} = Z^T \cdot Q_{\underline{\hat{N}}} \cdot Z \tag{5.67}$$

The transformation depicted in Eq. (5.66) is referred to as Z-transformation in the context of ambiguity resolution with the LAMBDA method. The Z-matrix has the following properties: its entries are integer values and its entries are chosen such that the volume of the search space is preserved by the Z-transformation, e.g. the number of candidate grid points is transformation-invariant. The performance of the integer ambiguity search is improved by designing the Z-matrix such that it reduces the correlation between the float ambiguities as far as possible. More details on the construction of the Z-matrix can be found in Teunissen [44]. The re-parameterized ambiguity integer least-squares problem reads

$$\min_{\underline{z}} \left[\left(\underline{\hat{z}} - \underline{z}\right)^T \cdot Q_{\underline{\hat{z}}}^{-1} \cdot \left(\underline{\hat{z}} - \underline{z}\right) \right] \quad , \quad \underline{z} \in \mathbb{Z}^m \tag{5.68}$$

and the search space of the integer least-squares problem is defined by

$$\sum_{i=1}^{m} \frac{\left(\hat{z}_{i|I} - z_i\right)^2}{\sigma_{\hat{z}_{i|I}}^2} \leq \chi^2 \quad , \tag{5.69}$$

where:

$\hat{z}_{i|I}$: ith least-squares ambiguity estimate, conditioned on a fixing of the previous (i-1) ambiguities, which is denoted by ‘|I’

z_i: ith ambiguity, which corresponds to the true (decorrelated) ambiguity

$\sigma^2_{\hat{z}_{i|I}}$: variance of the ith conditional least-squares ambiguity estimate

A detailed description of the LAMBDA method is given in [19], while here it is sufficient to outline the general idea behind the LAMBDA method. After having found the decorrelated integer vector $\underline{\check{z}}$ from integer least-squares adjustment, the integer ambiguity vector $\underline{\check{N}}$ is obtained from the following retransformation:

$$\underline{\check{N}} = Z^{-T} \cdot \underline{\check{z}} \tag{5.70}$$

Finally, the fixed solution is obtained from Eq. (5.64) and (5.65). However, some quality checks should be performed before accepting the fixed solution. Wrong integer ambiguity fixing may cause severe biases on the baseline solution that are not acceptable for precision landing. The integer ambiguities are validated with the help of the ratio test, which is frequently applied for integer ambiguity validation in navigation software:

$$\frac{\left\|\underline{\hat{N}} - \underline{\check{N}}_{2nd}\right\|^2_{G^{-1}_{\underline{\hat{N}}}}}{\left\|\underline{\hat{N}} - \underline{\check{N}}\right\|^2_{G^{-1}_{\underline{\hat{N}}}}} = \frac{\left(\underline{\hat{N}} - \underline{\check{N}}_{2nd}\right)^T \cdot G^{-1}_{\underline{\hat{N}}} \cdot \left(\underline{\hat{N}} - \underline{\check{N}}_{2nd}\right)}{\left(\underline{\hat{N}} - \underline{\check{N}}\right)^T \cdot G^{-1}_{\underline{\hat{N}}} \cdot \left(\underline{\hat{N}} - \underline{\check{N}}\right)} > k_c \quad , \tag{5.71}$$

where k_c is the critical value of acceptance, $\underline{\check{N}}$ is the best integer least-squares ambiguity estimate and $\underline{\check{N}}_{2nd}$ is the second-best integer least-squares ambiguity estimate. The cofactor matrix $G_{\underline{\hat{N}}}$ of the float ambiguities follows from $Q_{\underline{\hat{N}}} = \sigma^2 \cdot G_{\underline{\hat{N}}}$. The integer ambiguity vector $\underline{\check{N}}$ is only accepted if the ratio of the weighted ambiguity distance norms is greater than the critical value k_c. However, the determination of the critical value for a maximum allowable probability of wrong integer ambiguity fixing is non-trivial. Frequently the critical value is found empirically. Comparing different critical values indicated in literature, the empirically found critical value of 3 gives an upper limit for most applications. In order to be even more conservative, k_c is set to 4 in this work. Since the choice of the critical value for the ratio test is rather intuitively, this method of integer ambiguity fixing and validation will only serve for the purpose of comparison. Analytical determination of the critical value for a fixed fail rate is not possible since the stochastic variances of the second-best and the best integer least-squares estimate are dependent. Another approach is to find the critical value by extensive simulations. This approach might be appealing in post-processing software, but otherwise the computational effort can generally not be afforded. Further information on variations of the ratio test and the problems of the ratio test associated with classical hypothesis testing can be found in Verhagen [47]. There it is also mentioned that if the confidence in the float solution was not sufficient, an integer test that takes into account the randomness of the fixed ambiguities should be applied in addition to the ratio test. The integer test is based on testing the following two hypotheses against another:

$$\begin{aligned} H_1&: \quad \underline{y} = A \cdot \underline{N} + B \cdot \underline{b} + \underline{v}_* \quad , \underline{N} \epsilon \mathbb{R}^m \quad , \underline{b} \epsilon \mathbb{R}^p \quad , \underline{v}_* \epsilon \mathbb{R}^n \\ H_2&: \quad \underline{y} = A \cdot \underline{N} + B \cdot \underline{b} + \underline{v}_* \quad , \underline{N} \epsilon \mathbb{Z}^m \quad , \underline{b} \epsilon \mathbb{R}^p \quad , \underline{v}_* \epsilon \mathbb{R}^n \end{aligned} \tag{5.72}$$

The difference between H_1 and H_2 is that one time it is assumed that the ambiguity vector $\underline{N}$ is a real-valued vector, and the other time it is assumed that the ambiguity vector $\underline{N}$ is an integer vector. The integer test which is used in practice is defined by:

$$\frac{\left\|\underline{\hat{N}} - \underline{\check{N}}\right\|^2_{G^{-1}_{\underline{\hat{N}}}}}{m \cdot \hat{\sigma}^2} < F_{1-\alpha}(m, n-m-p) \quad , \tag{5.73}$$

where m is the number of integer ambiguities to be estimated, n is the dimension of the measurement vector and p is the number of the float parameters to be estimated. The quantile $F_{1-\alpha}(m, n-m-p)$ is the unique solution of the critical value x in the F cumulative distribution function, see Eq. (2.15), for a given level of significance α. The estimated variance factor $\hat{\sigma}^2$ is computed from:

$$\hat{\sigma}^2 = \frac{\underline{\hat{e}}^T \cdot G_{\underline{y}}^{-1} \cdot \underline{\hat{e}}}{n-m-p} \quad , \tag{5.74}$$

with the measurement residual vector $\underline{\hat{e}}$ of the float solution and the cofactor matrix $G_{\underline{y}}$ of measurement noise. Only if the integer test is passed, the outcome of the ratio test will be considered at all. Otherwise, the float solution should be kept as best solution which is currently available. In [48] it is stated that if the float solution was affected by biased observations, e.g. due to multipath on the pseudorange measurements, incorrect integer ambiguity fixing might occasionally occur although the formal precision and the success rate based on the stochastic model, which does not account for multipath, are very high.

Precision landing has stringent integrity requirements and the probability of wrong integer ambiguity fixing has to be known precisely. The fail rate of integer ambiguity fixing cannot be indicated analytically for the integer estimator introduced in this section. Therefore, in the next section an integer ambiguity estimator is presented which allows for real-time computation of the exact probability of wrong ambiguity fixing.

5.4.3 Integer Bootstrapping

There exists a great variety of integer estimators and a good summary of the most important methods can be found in [47]. Integer estimation with the LAMBDA method, which is very popular in practice, has already been introduced in the previous section. Here a second integer estimator is presented, which is frequently used when a certain integrity risk requirement has to be kept since the probability of wrong integer ambiguity fixing can be computed analytically. There are several decision criterions on which the selection of a concrete integer estimator can be based on:

1) Opportunity to compute the exact probability of wrong integer ambiguity fixing
2) Low additional computational effort of the integer estimation method
3) High success rate of the integer estimator (few epochs to fix the float ambiguities correctly)

As mentioned before, the first item is important in order to determine the integrity risk associated with the carrier phase ambiguity-fixed position solution. The second and third item is of great practical relevance for RTK applications. The availability of the navigation system is influenced by the success rate of the integer estimator if the HAL and VAL specifications were very restrictive. With respect to high success rates, the LAMBDA method outperforms Integer Bootstrapping (IB), e.g. see [47]. Nevertheless, in this work integer bootstrapping is considered to be the better choice for reliable ambiguity estimation due to the item listed in 1). Integer bootstrapping, which is also referred to as conditional rounding, is a sequential rounding scheme that takes into account the correlations between the entries of the float ambiguity vector $\underline{\hat{N}}$, see e.g. Blewitt [2]. The first entry of the m-dimensional float ambiguity vector is simply rounded to its nearest integer. Afterwards, the m-1 remaining float ambiguities are corrected by taking into account their correlation with the first, now fixed ambiguity. Then, the second entry of the float ambiguity vector is rounded to its nearest integer and a correction to the remaining m-2 float ambiguities is applied. This procedure is repeated until all m ambiguities of the vector $\underline{\hat{N}}$ are fixed to integers. After having applied the conditional rounding to all float ambiguity entries, the resulting integer estimate ambiguity vector $\underline{\breve{N}}$ is given by:

$$\underline{\breve{N}} = \begin{pmatrix} [\hat{N}_1] \\ [\hat{N}_{2|1}] \\ [\hat{N}_{3|1\ldots2}] \\ \vdots \\ [\hat{N}_{m|M}] \end{pmatrix} = \begin{pmatrix} [\hat{N}_1] \\ \left[\hat{N}_2 - \frac{\sigma_{\hat{N}_2,\hat{N}_1}}{\sigma^2_{\hat{N}_1}} \cdot \left(\hat{N}_1 - \breve{N}_1\right)\right] \\ \left[\hat{N}_3 - \frac{\sigma_{\hat{N}_3,\hat{N}_1}}{\sigma^2_{\hat{N}_1}} \cdot \left(\hat{N}_1 - \breve{N}_1\right) - \frac{\sigma_{\hat{N}_3,\hat{N}_{2|1}}}{\sigma^2_{\hat{N}_{2|1}}} \cdot \left(\hat{N}_{2|1} - \breve{N}_2\right)\right] \\ \vdots \\ \left[\hat{N}_m - \sum_{i=1}^{m-1} \frac{\sigma_{\hat{N}_m,\hat{N}_{i|I}}}{\sigma^2_{\hat{N}_{i|I}}} \cdot \left(\hat{N}_{i|I} - \breve{N}_i\right)\right] \end{pmatrix} , \tag{5.75}$$

where $|I$ indicates that the ith ambiguity is conditioned on the previous i-1 sequentially rounded ambiguities. Rounding to the nearest integer is represented by squared brackets [.]. In order to ease the computations of the variances and covariances indicated in Eq. (5.75), modified Cholesky factorization is applied to the symmetric positive definite ambiguity covariance matrix $Q_{\nabla\Delta\underline{\hat{N}}}$. Note that modified Cholesky factorization has already been introduced in Sect. 4.3.1 in the context of deriving a numerically robust implementation of the Kalman filter equations. Instead of UD factorization, here the term LD factorization (LD: Lower diagonal matrix, Diagonal matrix) is preferred in literature. The covariance matrix $Q_{\nabla\Delta\underline{\hat{N}}}$ is factorized in a lower diagonal matrix L and a pure diagonal matrix D:

$$Q_{\nabla\Delta\underline{\hat{N}}} = L \cdot D \cdot L^T \tag{5.76}$$

The factorization algorithm behind Eq. (4.11) and Eq. (5.76) is essentially the same. The upper triangle of the matrix L is all-zeros and the matrix's main diagonal is all-ones. The lower triangle of the matrix L contains the entries of interest for computing the bootstrapped ambiguities:

$$L = \begin{bmatrix} 1 & 0 & 0 & \cdots & 0 \\ \frac{\sigma_{\hat{N}_2,\hat{N}_1}}{\sigma^2_{\hat{N}_1}} & 1 & 0 & \cdots & 0 \\ \frac{\sigma_{\hat{N}_3,\hat{N}_1}}{\sigma^2_{\hat{N}_1}} & \frac{\sigma_{\hat{N}_3,\hat{N}_{2|1}}}{\sigma^2_{\hat{N}_2}} & 1 & \cdots & 0 \\ \vdots & \vdots & \vdots & \ddots & \vdots \\ \frac{\sigma_{\hat{N}_m,\hat{N}_1}}{\sigma^2_{\hat{N}_1}} & \frac{\sigma_{\hat{N}_m,\hat{N}_{2|1}}}{\sigma^2_{\hat{N}_{2|1}}} & \frac{\sigma_{\hat{N}_m,\hat{N}_{3|1\ldots2}}}{\sigma^2_{\hat{N}_{3|1\ldots2}}} & \cdots & 1 \end{bmatrix} , \tag{5.77}$$

and the diagonal matrix D contains the variances along its main diagonal

$$diag(D) = \left(\sigma^2_{\hat{N}_1},\ \sigma^2_{\hat{N}_{2|1}},\ \sigma^2_{\hat{N}_{3|1\ldots2}},\ \cdots\ \sigma^2_{\hat{N}_{m|M}}\right) \ . \tag{5.78}$$

The square-root of the conditional ambiguity variances will be used for computing the success rate of the integer bootstrapping estimator. From Eq. (5.75) to (5.78) it becomes clear that the ordering of the float ambiguity vector has impact on the outcome of the integer estimation. The sensitivity of the outcome on the ordering of the float ambiguities can significantly be reduced by applying an ambiguity transformation with decorrelating properties. Near-optimal performance of IB is achieved if the ambiguities are almost uncorrelated after the transformation. Teunissen [43] recommends applying the decorrelating Z-transformation of the LAMBDA method, see Eq. (5.66), before rounding the float ambiguities sequentially.

An important selection criterion in favor of the IB estimator is the opportunity to determine the fail rate of integer ambiguity fixing exactly and at a low computational expense. The exact success probability P_S of IB for biased measurements is given by [41]:

$$P_S = P(\underline{\breve{N}} = \underline{N}) = \prod_{i=1}^{m} \left[\Phi\left(\frac{1 - 2 \cdot b_{\hat{N}_{i|I}}}{2 \cdot \sigma_{\hat{N}_{i|I}}} \right) + \Phi\left(\frac{1 + 2 \cdot b_{\hat{N}_{i|I}}}{2 \cdot \sigma_{\hat{N}_{i|I}}} \right) - 1 \right] \quad , \tag{5.79}$$

where $\Phi(x)$ is the standardized normal distribution as indicated in Eq. (2.4) and $b_{\hat{N}_{i|I}}$ are the conditional ambiguity biases. The conditional standard deviations $\sigma_{\hat{N}_{i|I}}$ of the ambiguities follow from Eq. (5.78). According to Figure 5.1 the cascading ambiguity resolution is only called by the program loop under the fault-free hypothesis. In absence of measurement biases Eq. (5.79) reduces to:

$$P_S = P(\underline{\breve{N}} = \underline{N}) = \prod_{i=1}^{m} \left[2 \cdot \Phi\left(\frac{1}{2 \cdot \sigma_{\hat{N}_{i|I}}} \right) - 1 \right] \tag{5.80}$$

Since there are only two possible outcomes of the IB estimator, e.g. $\underline{\breve{N}} = \underline{N} \in \mathbb{Z}^m$ or $\underline{\breve{N}} = \underline{z} \in \mathbb{Z}^m \backslash \{\underline{N}\}$, the exact probability of false integer ambiguity fixing P_F simply follows from:

$$P_F = P(\underline{\breve{N}} \neq \underline{N}) = 1 - P_S = 1 - \prod_{i=1}^{m} \left[2 \cdot \Phi\left(\frac{1}{2 \cdot \sigma_{\hat{N}_{i|I}}} \right) - 1 \right] \tag{5.81}$$

A maximum allowable fail rate of integer ambiguity estimation can be derived from the integrity risk. By comparing the maximum allowable fail rate with the result of Eq. (5.81), it can be decided whether or not to accept the ambiguity-fixed solution. More details on partitioning the overall integrity risk are given in Sect. 6.2.

The arguments in favor of using IB in this work can be summarized as follows: First, the success rate of integer ambiguity estimation shows close-to-optimal performance if LAMBDA's cycle ambiguity decorrelation is used prior to the sequential rounding. Second, integer bootstrapping is computationally simple compared to many other methods. Third, the exact fail rate of ambiguity fixing can be indicated without the need of complex calculations. However, the fail-rate of IB is fixed for a specific underlying model. In the meantime, Integer Aperture Bootstrapping (IAB) has been introduced by Teunissen [43], which provides a controllable fail-rate of ambiguity fixing. There are two items that influence the success rate of integer ambiguity estimation. The first item is the probability density function of the float vector. Its probability density function is dependent on the strength of the mathematical model from which the float solution is derived. The second item is the integer estimator that has been chosen. If both the mathematical model and the integer estimator are fixed, than the fail-rate of integer ambiguity resolution is also fixed. In order to provide a flexible fail-rate, an integer aperture estimator can be chosen instead of an integer estimator. In contrast to the class of integer estimators, both integer and float values may result from the class of integer aperture estimators, since the pull-in regions have gaps. The size of the aperture parameter follows from the desired fail-rate. Nevertheless the IAB estimator is not applied in this work since the computational load increases compared to IB and it is assumed that the benefits of IAB are only marginal.

6 Filter-based Integrity Monitoring

6.1 Basic Principle of AFDIA

An approach for Autonomous Filter-based fault Detection, Identification and model Adaptation (AFDIA) is depicted in this and the following sections for the previously derived navigation filter. The GNSS model for relative positioning is based on the use of two receivers simultaneously, and the quality control presented here is performed on a baseline level. Note that there is the possibility of single receiver quality control, which is very useful for the reference receiver since its exact position is known in advance. The a-priori knowledge of the reference receiver position can be exploited in data-snooping algorithms at the reference receiver site. However, the following investigations focus on integrity monitoring at the user receiver site. The navigation filter processes both pseudorange and carrier phase measurements simultaneously. Positive aspects of using carrier phase data with respect to integrity monitoring are lower levels of multipath errors and measurement noise, resulting in smaller protection levels and improved separation between different error channels. One negative aspect is that the initial cycle count is unknown and has to be resolved successfully before carrier phase-based positioning becomes possible. A further negative aspect is that the effects of undetected cycle slips on the position estimate contribute to the overall integrity risk. According to Yun et al. [55] filter-based integrity monitoring provides better performance than snapshot RAIM algorithms due to a reduction of the measurement noise by filtering. This is particularly important as long as the navigation solution is mainly based on noisy pseudorange measurements. Furthermore, the detection of ramp errors, which are more difficult to detect than large step failures, is favored by a filter-based integrity monitoring approach. Diesel et al. [7] showed that this can be achieved by estimating the mean of the innovation vector over a long period of time and using the averaged innovation vector in order to detect anomalies. The present version of AFDIA is developed for identifying data anomalies from the current observation epoch, but it is recognized that there is further potential in detecting old model invalidations by introducing a moving window for past observation epochs.

AFDIA comprises the detection of unspecified model errors on the basis of an overall model test and, if an inconsistency has been detected, the identification of the model error as well as, if possible, the adaptation of the model. Horizontal and vertical protection levels are derived for the user position and velocity estimates. The relative positioning concept described in Sect. 5 makes use of double-differenced observables. In consequence, if the reference satellite fails all double-differenced observables will be affected simultaneously. If a failure of the reference satellite is detected, the navigation system is declared unavailable and no attempt is made to adapt the model. An improvement would be to implement a second simultaneously running filter which works with a different reference satellite or to develop a double-differencing scheme that does not rely on one single reference satellite.

Both past and present information have an impact on the position and velocity solution due to filtering. Snapshot RAIM algorithms can therefore not be adopted without any modifications. AFDIA can be applied even if only one satellite is in view since the filter-based minimum mean-squares solution relies on both present and past observations. This is a great advantage of filter-based approaches compared to snapshot RAIM. High availability of AFDIA is achieved even in presence of signal shading, for example when the airplane flies a turn.

6.2 Breakdown of the Integrity Risk

The position solution of the navigation filter is based on pseudorange measurements and carrier phase measurements. Since the carrier phase measurements are ambiguous the reliability of ambiguity resolution does also impact the overall integrity risk. Previous work on high-integrity carrier phase-based position, see e.g. Pervan et al. [33], does also resort to Integer Bootstrapping in combination with LAMBDA cycle ambiguity decorrelation in order to derive an ambiguity fixed position solution. Other approaches, see e.g. Feng et al. [10], use the LAMBDA method together with the ratio test for integer ambiguity validation. However, the approach presented in [10] does not account for the contribution of wrong integer ambiguity fixing to the integrity risk in the position domain. Therefore, in the following the IB estimator is considered which eases the partitioning of the integrity risk associated with the ambiguity-fixed solution.

There are two viewpoints when partitioning the integrity risk. The first viewpoint is conservative, since it considers the excess of the computed protection level under H_0, e.g. no bias present,

$$I_{0,spec} = P\left(\left|\hat{x}_{v,B} - x_{v,B}\right| > VPL_0\right) \tag{6.1}$$

rather than the excess of the alert limit by the resulting position estimation error due to wrong ambiguity fixing. As usual, the parameter $\hat{x}_{v,B}$ is the vertical component of the estimated user position vector and $x_{v,B}$ is the true vertical component of the user position vector. The considerations are restricted to the vertical component since there the requirements are harder to fulfill. $I_{0,spec}$ is the specified integrity risk and VPL_0 is the vertical protection level under the hypothesis H_0, which corresponds to the fault-free case. Furthermore, it is assumed that Wrong integer ambiguity Fixing (WF) will always cause an error in the position domain that is larger than the computed protection level under H_0:

$$P\left(\left|\hat{x}_{v,B} - x_{v,B}\right| > VPL_0 | WF\right) = 1 \tag{6.2}$$

The second viewpoint is to admit wrong integer ambiguity fixing as long as the resulting position error does not exceed the specified alert limit VAL:

$$I_0 = P\left(\left|\hat{x}_{v,B} - x_{v,B}\right| > VAL\right) \tag{6.3}$$

In order to derive a tighter bound on the integrity risk, an efficient approach to computing the following expression is required:

$$\begin{aligned} P\left(\left|\hat{x}_{v,B} - x_{v,B}\right| > VAL | WF\right) \cdot P_F &= \sum_{i=1}^{\infty} \left\{ P\left(\left|\hat{x}_{v,B} - x_{v,B}\right| > VAL | WF_i\right) \cdot P_{F,i} \right\} \\ &\neq 1 \cdot P_F \quad , \end{aligned} \tag{6.4}$$

where P_F is the overall probability of false integer ambiguity fixing, $P_{F,i}$ is the probability of incorrectly fixing the i^{th} integer ambiguity vector candidate, which does not correspond to the true ambiguity vector, and WF_i is the event of incorrectly fixing the i^{th} integer ambiguity vector candidate. This approach has recently been proposed by Khanafseh et al. [24]. At first glance, this suggests being the better approach since it is not unnecessarily conservative and yet theoretically sound. At second glance, the concrete structure of the navigation software has to be considered in order to judge the impact of wrong ambiguity fixing on the overall integrity risk in the position domain. In this work the more conservative approach is favored because the user position is estimated by an EKF. Although momentarily the acceptance of wrong integer ambiguities may result in a position error that is below the specified alert limit, the position error will increase over time if false ambiguity fixing is not detected at a later time. However, it has to be questioned if wrong integer ambiguity fixing can still be detected by the EKF at a later point of time when the biased reference trajectory, which is used for linearization, is offset from the true user trajectory for many epochs. The implemented fault detection algorithm would have to go through large sequences of old data in order to detect when the model invalidation actually took place. When adapting the model after an error has been identified that occurred some time ago, some recursive form of correction is required. In this work error detection is restricted to the current observation epoch, assuming that no error has occurred in the previous observation epochs. On the one hand, this reduces the computational burden significantly. On the other hand, it has to be assumed that wrong ambiguity fixing will lead to intolerable high position errors with some time delay between the occurrence of the error and the undetected excess of the alert limit, since reliable detection of old model invalidations is no longer controllable. From a practical viewpoint, it is desirable to fly a missed approach rather sooner than later if it is assumed that the position error due to wrong ambiguity fixing increases with time.

The conservative approach of the derivation of the maximum allowable probability of false integer ambiguity fixing P_F from the specified integrity risk $I_{0,spec}$ follows from [32]:

$$\begin{aligned} I_{0,spec} &= P\left(\left|\hat{x}_{v,B} - x_{v,B}\right| > VPL_0\right) \\ &= P\left(\left|\hat{x}_{v,B} - x_{v,B}\right| > VPL_0 | CF\right) \cdot P_S \\ &+ P\left(\left|\hat{x}_{v,B} - x_{v,B}\right| > VPL_0 | WF\right) \cdot P_F \quad , \end{aligned} \tag{6.5}$$

where CF denotes the event of correct integer ambiguity fixing. If the IB estimator is used for integer ambiguity estimation, than it holds that the success rate P_S of integer ambiguity fixing is given by:

$$P_S = 1 - P_F \tag{6.6}$$

Note that if an integer aperture estimator was used, Eq. (6.6) would not be valid in general. By substituting Eq. (6.2) and Eq. (6.6) in Eq. (6.5) and solving for P_F, the maximum admissible probability of false integer ambiguity fixing becomes a function of the specified integrity risk $I_{0,spec}$ and the probability of missed detection conditioned on correct integer ambiguity fixing:

$$P_F = \frac{I_{0,spec} - P\left(\left|\hat{x}_{v,B} - x_{v,B}\right| > VPL_0 | CF\right)}{1 - P\left(\left|\hat{x}_{v,B} - x_{v,B}\right| > VPL_0 | CF\right)} \tag{6.7}$$

When inserting $I_{0,spec} = 2 \cdot 10^{-9}$ and $P\left(\left|\hat{x}_{v,B} - x_{v,B}\right| > VPL_0 | CF\right) = 1 \cdot 10^{-9}$ into Eq. (6.7), it follows that $P_F \approx 1 \cdot 10^{-9}$.

Now the navigation filter architecture which is depicted in Figure 5.1 is considered. First, the fault-free integrity risk is investigated. Several assumptions are made in the derivation of the fault-free integrity risk: One issue is that it is assumed that position errors that exceed VPL_0 are not detectable by the fault detection algorithm. This seems reasonable since under H_0 there are no concrete measurement outliers, but the occurrence of $\left|\hat{x}_{v,B} - x_{v,B}\right| > VPL_0$ is rather due to wide spectrum of normal operation of the nonlinear filter. The second issue is that it is assumed that position errors due to wrong model adaptation are negligible under H_0. For example, if the probability of false alarm P_{FA} of the fault detection algorithm is set to $1 \cdot 10^{-7}$ and the probability of wrong error identification is $P_{WID} = 2 \cdot 10^{-9}$, then the product of both probabilities is indeed negligible. In this work a Cascading Ambiguity Resolution (CAR) scheme is applied. In consequence, both the widelane and the carrier phase ambiguities can be fixed wrongly, which corresponds to the events WF_{WL} and WF_{CP}. The complementary events are CF_{WL} and CF_{CP}. In consequence Eq. (6.5) has to be adapted in order to account for the cascading resolution scheme:

$$
\begin{aligned}
I_{0,CAR,spec} &= P\left(\left|\hat{x}_{v,B}-x_{v,B}\right|>VPL_0\right)\\
&= P\left[\left|\hat{x}_{v,B}-x_{v,B}\right|>VPL_0|(CF_{WL},CF_{CP})\right]\cdot P_{S,WL}\cdot P_{S,CP}\\
&+ P\left[\left|\hat{x}_{v,B}-x_{v,B}\right|>VPL_0|(WF_{WL},CF_{CP})\right]\cdot P_{F,WL}\cdot P_{S,CP}\\
&+ P\left[\left|\hat{x}_{v,B}-x_{v,B}\right|>VPL_0|(CF_{WL},WF_{CP})\right]\cdot P_{S,WL}\cdot P_{F,CP}\\
&+ P\left[\left|\hat{x}_{v,B}-x_{v,B}\right|>VPL_0|(WF_{WL},WF_{CP})\right]\cdot P_{F,WL}\cdot P_{F,CP}
\end{aligned} \tag{6.8}
$$

The most pessimistic approach is to assume that any wrong ambiguity fixing causes a position error that violates the protection level under H_0. Under this assumption Eq. (6.8) simplifies to:

$$
\begin{aligned}
I_{0,CAR,spec} &= P\left(\left|\hat{x}_{v,B}-x_{v,B}\right|>VPL_0\right)\\
&= P\left[\left|\hat{x}_{v,B}-x_{v,B}\right|>VPL_0|(CF_{WL},CF_{CP})\right]\cdot P_{S,WL}\cdot P_{S,CP}\\
&+ P_{F,WL}\cdot P_{S,CP}+P_{S,WL}\cdot P_{F,CP}+P_{F,WL}\cdot P_{F,CP}
\end{aligned} \tag{6.9}
$$

The resulting integrity risk becomes approximately $I_{0,CAR,spec}\approx 3\cdot 10^{-9}$ if $P\left[\left|\hat{x}_{v,B}-x_{v,B}\right|>VPL_0|(CF_{WL},CF_{CP})\right]=1\cdot 10^{-9}$, $P_{F,WL}=\left(1-P_{S,WL}\right)=1\cdot 10^{-9}$ and $P_{F,CP}=\left(1-P_{S,CP}\right)=1\cdot 10^{-9}$ are inserted into Eq. (6.9). In Figure 6.1 the consequences of wrong integer ambiguity fixing in the position domain are shown. The resulting horizontal position error $\delta\hat{x}_{h,B}$ exceeds the horizontal protection level HPL_0 already after having fixed the widelane ambiguities wrongly by altogether 5 cycles, while the resulting vertical position error $\delta\hat{x}_{v,B}$ exceeds the vertical protection level VPL_0 after having fixed the carrier phase ambiguities wrongly by altogether 112 cycles. It seems that the resulting position errors do not drift away after having fixed the integer ambiguities wrongly. The reason, however, is found in the short observation time which is considered in Figure 6.1. During the short period of time there is not much change in the relative receiver-satellite geometry. In this concrete example, severe multipath has been simulated, error identification and model adaptation have been disabled and the probabilities of false integer ambiguity fixing have been set to $P_{F,WL}=0.5$ and $P_{F,CP}=0.5$.

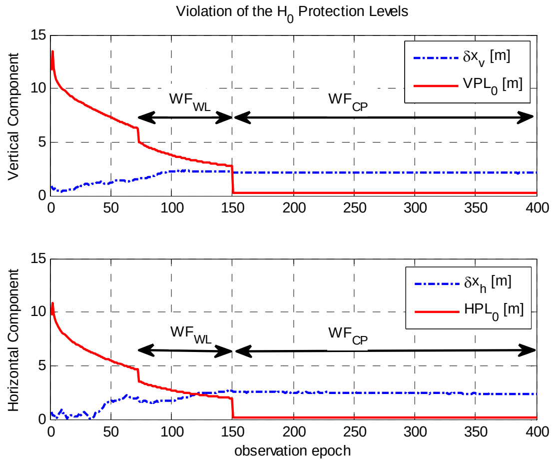

Figure 6.1: Violation of the H$_0$ protection levels due to wrong integer ambiguity fixing

Next, the integrity risk under H_1 is considered, e.g. it is assumed that there is a bias in the measurement data:

$$
I_{1,spec}=P\left(\left|\hat{x}_{v,B}-x_{v,B}\right|>VPL_1\right)\quad, \tag{6.10}
$$

where VPL_1 is the protection level if one bias is present in the measurement data. The probability of missed detection $P_{MD,1}$ under H_1 is defined as:

$$P_{MD,1} = P\left(\left|\hat{x}_{v,B} - x_{v,B}\right| > VPL_1 | \bar{d}\right) \quad , \tag{6.11}$$

where $|\bar{d}$ stands for "under the condition that the violation is not detected". If it occurs that the position error exceeds VPL_1 and this event is not detected by the fault detection algorithm, the cascading ambiguity resolution scheme is called next in the program loop. It is assumed here that if $\left|\hat{x}_{v,B} - x_{v,B}\right| > VPL_1$ before calling the CAR scheme, it will also hold that $\left|\hat{x}_{v,CAR,B} - x_{v,B}\right| > VPL_1$ after finishing CAR; e.g. it is assumed that ambiguity fixing will not reduce the position error by chance. It can also happen that the fault detection algorithm detects the violation of the protection level VPL_1, but the succeeding fault identification algorithm identifies the wrong model error. It is assumed conservatively that model adaptation based on a wrongly identified model error will always lead to position errors larger than VPL_1. Under the assumptions made so far, the integrity risk under H_1 can be indicated as:

$$I_{1,spec} = P\left(\left|\hat{x}_{v,B} - x_{v,B}\right| > VPL_1\right) = P_{MD,1} + P_{WID} \cdot \left(1 - P_{MD,1}\right) \tag{6.12}$$

By setting the probability of missed detection to $P_{MD,1} = 1 \cdot 10^{-9}$ and the probability of wrong model error identification to $P_{WID} = 2 \cdot 10^{-9}$, it follows that $I_{1,spec} \approx 3 \cdot 10^{-9}$.

There remain some concluding remarks on the determination of the integrity risk of the nonlinear navigation filter. First, since the hypotheses H_0 and H_1 are mutually exclusive, the approximated overall integrity risk is not given by the sum of $I_{0,spec}$ and $I_{1,spec}$, but by the maximum of $I_{0,spec}$ and $I_{1,spec}$. Second, the event space covered by H_0 and H_1 is not equal to the overall event space. The occurrence of multiple measurement biases simultaneously is not covered in this approach. It is acknowledged here that it is rather optimistic to assume that there is only one bias at a time, especially since multipath and cycle slips belong to the group of biases under consideration. Therefore, $max\left(I_{0,spec}, I_{1,spec}\right)$ is no overbound of the actual integrity risk. Furthermore, the actual performance of the EKF is data-driven due to the internal feedback of the measurement data into the system model. The performance is also dependent on the precision of the filter initialization. To conclude, the actual integrity risk of the navigation filter solution has to be derived from extensive simulations, since any analytical approach would require introducing assumptions on the measurement input data and the precision of the filter initialization.

6.3 Fault Detection

Anomalous measurement data has to be detected and rejected. This can for example be achieved by AFDIA, where bad measurement data is identified and the model is adapted afterwards provided that there is enough confidence in the error identification. If no fault detection algorithms were implemented at all, the filter estimates might seriously be corrupted by bad measurement data. Grewal et al. [13] state that degradation of the state estimates due to temporary component failures or signal corruption can persist for some time, since the Kalman filter has infinite impulse response. The same holds true for the EKF, whereas the consequences of undetected faults may even be worse due to continuous adaptation of the trajectory which serves as reference for linearization.

In filter-based approaches, the innovation vector is usually used for health monitoring. Some information provided by the innovation vector is already useful during the filter design phase in order to detect discrepancy between the model and the real system, other information is also useful for online surveying of the filter performance. The innovation vector is defined as the difference between the actual measurements $\underline{z}_k$ and the projected measurements $\hat{\underline{z}}_k$:

$$\underline{r}_k = \underline{z}_k - \hat{\underline{z}}_k = \underline{z}_k - \underline{h}_k\big(\hat{\underline{x}}_k(-)\big) \tag{6.13}$$

Since an EKF is used, $\hat{\underline{z}}_k$ follows from inserting the a-priori state estimates $\hat{\underline{x}}_k(-)$ into the nonlinear observation equations. In contrast, snapshot RAIM algorithms use the measurement residual vector $\underline{r}_{lsq}$ in order to compute the test statistic:

$$\underline{r}_{lsq} = \underline{y} - H \cdot \hat{\underline{x}}_{lsq} \tag{6.14}$$

, where $\underline{y}$ is the vector of observations, H is the measurement sensitivity matrix and $\hat{\underline{x}}_{lsq}$ is the least-squares solution of the states. It is assumed that the innovation vector $\underline{r}_k$ of the EKF has the following properties in absence of biases, see e.g. [7]:

$$E\{\underline{r}_k\} = \underline{0} \tag{6.15}$$

and

$$E\{\underline{r}_k \cdot \underline{r}_k^T\} = Q_{\underline{r}_k} = R_k + H_k^* \cdot P_k(-) \cdot H_k^{*T} \tag{6.16}$$

From Eq. (6.16) follows that the covariance matrix $Q_{\underline{r}_k}$ of the innovation vector depends both on the actual measurement noise at epoch k and the predicted state estimation uncertainty. The expectation of $\underline{r}_k$ is only zero in absence of biases. By computing the means of the innovations important information on the filter health is obtained. If the means are non-zero, sensor biases or mismodeled output biases may deteriorate the results. The detection of anomalous measurement data can be based on the likelihood function of the innovations, see e.g. [13]:

$$\mathcal{L}(\underline{r}_k) = e^{-\frac{1}{2}\cdot \underline{r}_k^T \cdot Q_{\underline{r}_k}^{-1} \cdot \underline{r}_k} \tag{6.17}$$

The associated log-likelihood is:

$$\log\big[\mathcal{L}(\underline{\mathrm{r}}_{\mathrm{k}})\big] = -\frac{1}{2} \cdot \underline{r}_k^T \cdot Q_{\underline{r}_k}^{-1} \cdot \underline{r}_k \tag{6.18}$$

The next property of the innovation vector is used in global model validation, where error detection is extended to several observation epochs in order to support the detection of unmodeled trends (ramp errors):

$$E\{\underline{r}_j \cdot \underline{r}_k^T\} = 0 \quad , \quad j \neq k \quad , \tag{6.19}$$

e.g. the innovation vectors are independent for different observation epochs. Eq. (6.19), which is also called innovations property, is fulfilled if all noise sources are Gaussian white noise and if the physical system is modeled correctly. By keeping track of the relative frequency of data anomalies trends can be detected. Global model error detection by using a moving window of designated length is covered in [7] and [44]. Here all further considerations are restricted to the innovation vector from the current epoch and innovation vectors from former epochs are not buffered.

Model validation in the context of least-squares estimation has already been introduced in Sect. 2.2.2. Some modification of the hypothesis test is required here, since Kalman filtering is a generalized form of recursive least-squares estimation. According to Teunissen [44], recursive least-squares estimation produces optimal estimators of the state, which are unbiased and have minimum variance within the class of linear unbiased estimators. However, it has to be kept in mind that a nonlinear filter approach is used since the geometry-based measurement model contains the user position states in nonlinear form. In general it holds that misspecifications in the functional model have to be detected in order to prevent severe degradation of the filter performance. The detection of misspecifications is accomplished by hypothesis testing. Similar to Eq. (2.23) and Eq. (2.25), the null hypothesis H_0 and the alternative hypothesis H_1 for the filter-based approach read:

$$H_0: \quad \tilde{\underline{\mathrm{z}}}_{\mathrm{k}} = \underline{h}_k\left(\tilde{\underline{\mathrm{x}}}_{\mathrm{k}}\right) + \tilde{\underline{\upsilon}}_k \tag{6.20}$$

$$H_1: \quad \tilde{\underline{\mathrm{z}}}_{\mathrm{k}} = \underline{h}_k\left(\tilde{\underline{\mathrm{x}}}_{\mathrm{k}}\right) + E_k \cdot \underline{\varepsilon} + \tilde{\underline{\upsilon}}_k \tag{6.21}$$

Just as in Sect. 2.2.2, E_k represents a known design matrix of model errors and $\underline{\varepsilon}$ an unknown vector of biases. If n_k is the number of measurements at epoch k and q is the number of different model errors under consideration, then $\tilde{\underline{\mathrm{z}}}_{\mathrm{k}}$ is of size $\mathrm{n_k x1}$, E_k is of size $\mathrm{n_k xq}$ and $\underline{\varepsilon}$ is of size qx1. The randomness of variables is here explicitly indicated by a tilde $\tilde{\square}$. The recursive nature of the estimation procedure has to be accounted for in contrast to the model validation scheme presented in Sect. 2.2.2. This implies that fault detection has to be performed recursively as well. As time-series of measurements are considered in the filtering process, in principle also the time of occurrence of model invalidation has to be determined. However, the application at hand requires that the integrity monitoring is performed in real-time. In [44] a local detection procedure is proposed which can be executed in real-time. The local test, which is performed at epoch k, depends only on the predicted state vector $\tilde{\hat{\underline{\mathrm{x}}}}_{\mathrm{k}}$ at epoch k and on the observations $\tilde{\underline{\mathrm{z}}}_{\mathrm{k}}$ at epoch k. It is assumed that either no model errors have occurred so far or that model errors have been identified successfully and that an appropriate model adaptation has been applied afterwards. Model validation uses the information provided by the innovation vector of the navigation filter, see Eq. (6.13). The properties of the innovation vector in absence of biases have already been indicated in (6.15), (6.16) and (6.19).The hypotheses of a local test are less complex to test against each other than the hypotheses of a global test which considers possible misspecifications from the first epoch to the current epoch. In case of a local test the hypotheses simplify to:

$$H_0^k: \quad \mathrm{E}\{\tilde{\underline{r}}_k\} = \underline{0} \tag{6.22}$$

$$H_1^k: \quad \mathrm{E}\{\tilde{\underline{r}}_k\} = E_{\underline{r}_k} \cdot \underline{\varepsilon} \tag{6.23}$$

In order to detect model invalidation at epoch k, no restrictions are imposed on the moment of 1st order given in Eq. (6.23), e.g.:

$$H_1^k: \quad \mathrm{E}\{\tilde{\underline{r}}_k\} \in \mathbb{R}^{\mathrm{n_k}} \tag{6.24}$$

Consequently, the matrix $E_{\underline{r}_k}$ is square and regular of size $\mathrm{n_k x n_k}$, and the number of degrees of freedom becomes $q = \mathrm{n_k}$. According to [44], the test statistic $\tilde{T}_k$, which corresponds to the local test, is given by:

$$\tilde{T}_k = \frac{\tilde{\underline{r}}_k^T \cdot Q_{\underline{r}_k}^{-1} \cdot \tilde{\underline{r}}_k}{n_k} \tag{6.25}$$

Thus, the test statistic is the weighted sum of squared innovations divided by the degrees of freedom. Due to the filter-based approach the degrees of freedom is equal to the number of measurements at epoch k. In contrast, the degrees of freedom of the least squares approach presented in Sect. 2.2.2 follows from the number of measurements reduced by the number of unknown states. The covariance matrix $Q_{\underline{r}_k}$ of the innovation vector has already been indicated in Eq. (6.16). By comparing Eq. (6.25) with Eq. (2.18) and under the assumption that all white-noise sources are Gaussian, it becomes obvious that the test statistic has an F-distribution with $\mathrm{n_k}$ and ∞ degrees of freedom:

$$\tilde{T}_k \sim F(n_k, \infty, \lambda) \tag{6.26}$$

The noncentrality parameter λ is zero in absence of biases. Finally, the decision threshold $D_{\alpha,\mathrm{k}}$ at epoch k for a given level of significance α can be computed from the cumulative F-distribution function indicated in Eq. (2.15) by solving

$$F_{F,\mathrm{n_k},\infty}\left(D_{\alpha,\mathrm{k}}\right) = 1 - \alpha \tag{6.27}$$

for the quantile $D_{\alpha,\mathrm{k}}$. It is assumed that the functional model is valid if $\tilde{T}_k < D_{\alpha,k}$. From Sect. 2.1.3 it is known that $n_k \cdot \tilde{T}_k = \tilde{T}_k^*$ has a χ^2-PDF with $\mathrm{n_k}$ degrees of freedom:

$$\tilde{T}_k^* = n_k \cdot \tilde{T}_k \sim \chi^2(n_k, \lambda) \tag{6.28}$$

In the navigation filter algorithms implemented in this work, the square root of $\tilde{T}_k^*$ is actually used as test statistic of the local test:

$$\tilde{T}_{k,localTst} = \sqrt{\underline{\tilde{r}}_k^T \cdot Q_{\underline{\tilde{r}}_k}^{-1} \cdot \underline{\tilde{r}}_k} \tag{6.29}$$

The associated decision threshold $D_{\mathrm{k,localTst}}$ depends on the maximum allowable probability of missed detection $P_{MD,1}$:

$$F_{\chi^2,\mathrm{n_k}}\left(D_{\mathrm{k,localTst}}^2\right) = 1 - P_{MD,1} \tag{6.30}$$

If $\tilde{T}_{k,localTst} \geq D_{k,localTst}$ the underlying model is considered to be invalid and some action has to be undertaken. Either the model error is identified with the required level of confidence and the model can be adapted or an alert flag has to be raised.

6.4 Identification of Model Errors and Adaptation

In case that an unspecified model error has been detected by the local test described in the previous section, it is desirable to identify the model error and adapt the model afterwards. Successful identification of biases and model adaptation enhance the system availability. In civil aviation the availability of a reliable navigation solution is one of the hardest requirements to meet. Instead of model adaptation, it is also possible to exclude for example a satellite from the navigation solution. According to Wendel [52], the rejection of measurements may lead to state estimate errors that grow with time. Thus, the innovation also starts to grow. If the growth of state estimate errors is not precisely reflected by the covariance matrix of state estimation uncertainty P_k, further measurements may be rejected that were not biased. This has to be prevented at any rate. In this work the concept of fault detection, identification and model adaptation is adopted instead of the concept of fault detection and exclusion.

On the one hand, it is sufficient to indicate only one alternative hypothesis for the detection of unspecified model errors, e.g. see Eq. (6.24). On the other hand, it is necessary to formulate several alternative hypotheses in order to identify the model error. The number of alternative hypotheses can grow very large if the identification of multiple biases simultaneously shall also be covered. So far the proposed AFDIA scheme applies to single-channel biases, also in theory an extension to multiple biases is possible. Since AFDIA does not only aim at the detection and exclusion of faulty satellites, but also at the identification of cycle slips and multipath, it is acknowledged that multiple-channel biases are far more likely to occur.

In the following the vector of model errors $\underline{\varepsilon}$ is reduced to a scalar ε. For one-dimensional model errors the matrix E_k reduces to a vector $\underline{e}_k$. Per measurement type (ρ_c, ϕ_c, D_c), altogether as many alternative hypotheses are specified as there are satellites in view. The number of different measurement types is given by $\mathrm{t_m}$, the number of satellites in view is given by $\mathrm{s_k}$ and the number of double-differenced measurements at epoch k is given by $\mathrm{n_k}$ ($\mathrm{n_k}$ comprises all different measurement types). The alternative hypotheses $H_{1,i}^k$ are formulated such that $\underline{e}_{k,i}$ becomes a vector of length $\mathrm{n_k}$:

$$H_{1,i}^k\!: \quad \mathrm{E}\{\underline{\tilde{r}}_k\} = \underline{e}_{k,i} \cdot \varepsilon \quad , i = 1 \dots t_m \cdot s_k \tag{6.31}$$

The $\mathrm{i^{th}}$ vector $\underline{e}_{k,i}$ is set up such that there is either one biased double-differenced measurement or that all $\mathrm{s_k} - 1$ double-differenced measurements are biased of some measurement type. The case with $\mathrm{s_k} - 1$ biased double-differenced measurements corresponds to anomalous data from the reference satellite, since all double-differenced observables from one measurement type are affected simultaneously if the reference satellite signal is corrupted. In order to test the alternative hypotheses against the null hypothesis $H_0^k\!: \quad \mathrm{E}\{\underline{\tilde{r}}_k\} = \underline{0}$, the following test statistics are computed:

$$\tilde{T}_i^k = \frac{\underline{e}_{k,i}^T \cdot Q_{\underline{r}_k}^{-1} \cdot \underline{\tilde{r}}_k}{\sqrt{\underline{e}_{k,i}^T \cdot Q_{\underline{r}_k}^{-1} \cdot \underline{e}_{k,i}}} \quad , i = 1 \dots t_m \cdot s_k \tag{6.32}$$

Teunissen [44] indicates that the test statistics have a standardized normal distribution $\tilde{T}_i^k \sim N(0,1)$ under H_0^k. The most likely model error results from a search for the largest value among all test statistics:

$$\tilde{T}_{max}^k = \max_i\left(\left|\tilde{T}_i^k\right|\right) \tag{6.33}$$

The identification of the model error is only trusted if it holds that:

$$\tilde{T}_{max}^k \geq D_{\alpha/2} \tag{6.34}$$

, with the decision threshold $D_{\alpha/2}$. Here the level of significance α corresponds to the probability of wrong identification P_{WID} according to Sect. 6.2. The decision threshold D_{WID} is derived from the standardized normal distribution given in Eq. (2.4) such that it holds that $\Phi(D_{\mathrm{WID}}) = 1 - P_{WID}/2$. If the model error is identified with the required level of confidence, the model is adapted. Therefore, the least-squares estimator of the model error and its variance has to be computed:

$$\tilde{\hat{\varepsilon}}_k = \frac{\tilde{T}_j^k}{\sqrt{\underline{e}_{k,j}^T \cdot Q_{\underline{r}_k}^{-1} \cdot \underline{e}_{k,j}}} \tag{6.35}$$

$$\sigma_{\hat{\varepsilon},k}^2 = \frac{1}{\underline{e}_{k,j}^T \cdot Q_{\underline{r}_k}^{-1} \cdot \underline{e}_{k,j}} \tag{6.36}$$

The subscript j refers to the $\mathrm{j^{th}}$ test statistic with the largest absolute value. The vector of state estimates $\tilde{\hat{\underline{x}}}_k(+)$ and its covariance matrix $P_k(+)$ are updated by:

$$\tilde{\hat{\underline{x}}}_{k,a}(+) = \tilde{\hat{\underline{x}}}_k(+) - K_k \cdot \underline{e}_{k,j} \cdot \tilde{\hat{\varepsilon}}_k \tag{6.37}$$

$$P_{k,a}(+) = P_k(+) + K_k \cdot \underline{e}_{k,j} \cdot \sigma_{\hat{\varepsilon},k}^2 \cdot \underline{e}_{k,j}^T \cdot K_k^T \tag{6.38}$$

The adapted vector of state estimates $\tilde{\hat{\underline{x}}}_{k,a}(+)$ and its covariance matrix $P_{k,a}(+)$ are used to re-compute the prediction of the state estimate vector $\tilde{\hat{\underline{x}}}_{k+1,a}(-)$ and its covariance matrix $P_{k+1,a}(-)$ for the next epoch.

The proposed scheme of AFDIA is capable of detecting cycle slips after the initial ambiguities have already been fixed. There are several possibilities to proceed after a cycle slip has been detected. One option is to clear the integer ambiguity buffer and to restart with a float solution. With respect to the availability of tight protection levels during the final phase of the flight this option is not considered here. A further option is to re-fix the integer ambiguity on the basis of the adapted user position solution and the resulting theoretical range. This kind of ambiguity fixing is however not considered to be safe enough. One could also simply exclude the satellite where the cycle slip has occurred from the navigation solution. This might however deteriorate the PDOP (Position Dilution Of Precision) and if several cycle slips occur the system availability is endangered. Now the procedure is described which is indeed applied in this navigation filter. After successful ambiguity fixing, the integer ambiguities are not removed from the vector of state estimates. The fact that the ambiguities have already been fixed is reflected by the covariance matrix of process noise, or more precisely by the zero-matrix $Q_{N_{WL}}$ (and the zero-matrix Q_{N_2}). Furthermore, the uncertainty in the ambiguity estimates is removed, e.g. the covariance matrix of state estimation uncertainty P_k is adapted with respect to the ambiguity variance-covariance entries. If a cycle slip is detected, the variance of process noise that corresponds to the respective ambiguity is set to a value significantly different from zero. All other ambiguity variances of process noise are set to a value very close to zero. Because there is only noticeable uncertainty of just one single ambiguity term, the ambiguities can be re-fixed very quickly by the standard procedure, e.g. most of the time within five epochs. This procedure exploits the stochastic model of the EKF beneficiary. High availability of the ambiguity-fixed solution is ensured even in presence of cycle slips and without introducing additional integrity risk due to ad-hoc strategies for ambiguity re-fixing.

6.5 Protection Levels

If GNSS equipment is used as primary means of navigation for safety-critical applications, it is necessary to indicate an upper bound for the maximum position error which cannot be detected by health monitoring algorithms. Of course the upper bound has to be determined by probabilistic means. Thus, there remains an integrity risk that the maximum position error is above the computed upper bound without being detected. In aviation both the vertical and the horizontal component of the user position vector have to be protected against excessive errors. This is reflected by the specified VAL and HAL. In this work protection levels are computed in parallel to the navigation solution. If the horizontal or vertical protection level is above the respective alert limit, then the navigation filter solution is declared unavailable and an alert flag is raised. The usage of a filter-based approach instead of some snapshot algorithm in order to derive the navigation solution has to be reflected by the computation of the protection levels. Similarly to the breakdown of the integrity risk described in Sect. 6.2, the fault-free normal operation of the filter is investigated as well as the filter operation in presence of a bias. While in snapshot RAIM algorithms the fault-free operation is sometimes neglected since the protection levels are effectively determined by the biased case, in a filter-based approach the fault-free normal operation should be evaluated as well. Before the determination of the protection levels is further investigated, a coordinate transformation from global to local coordinates is performed, since the HAL, VAL, HPL and VPL are user-referenced. The user position and velocity vector coordinates are computed in the ECEF frame. The indication of the horizontal and vertical protection and alert limits however refers to a local ENU frame. The origin of the local coordinate system is in general located at the GNSS antenna phase center at the airplane (see e.g. [36]). Therefore, the matrices involved in the computation of the protection levels have to be transformed. The coordinate transformation from ECEF to ENU has already been indicated in Eq. (3.2) and the computation of the rotation matrix is repeated here for convenience:

$$R^{ENU} = \begin{bmatrix} -\sin\lambda_B & \cos\lambda_B & 0 \\ -\sin\varphi_B\cos\lambda_B & -\sin\varphi_B\sin\lambda_B & \cos\varphi_B \\ \cos\varphi_B\cos\lambda_B & \cos\varphi_B\sin\lambda_B & \sin\varphi_B \end{bmatrix} , \tag{6.39}$$

where φ_B and λ_B are the latitude and longitude in WGS-84 of the user receiver antenna phase center. The vector of system states comprises the carrier phase ambiguities and ionosphere terms in addition to the user position and velocity vector. Therefore, the overall rotation matrix Rot has to transform position- and velocity-related terms, while ambiguity- and ionosphere-related terms remain unaffected:

$$Rot = \begin{bmatrix} R^{ENU} & 0 & 0 \\ 0 & R^{ENU} & 0 \\ 0 & 0 & I_{(no_{states}-6)x(no_{states}-6)} \end{bmatrix} \tag{6.40}$$

The rotation is applied to the P-, H- and K-matrix, which are used for the computation of the protection levels. The transformation of the covariance matrix of state estimation uncertainty P is derived from:

$$E\{\underline{\tilde{x}} \cdot \underline{\tilde{x}}^T\} = P \tag{6.41}$$

$$E\left\{Rot \cdot \underline{\tilde{x}} \cdot \left(Rot \cdot \underline{\tilde{x}}\right)^T\right\} = Rot \cdot P \cdot Rot^T = P^{ENU} \tag{6.42}$$

Similarly, the measurement sensitivity matrix H can be found in the ENU-system:

$$\underline{\tilde{z}} = H \cdot \underline{\tilde{x}} \tag{6.43}$$

$$\underline{\tilde{z}} = H^{ENU} \cdot Rot \cdot \underline{\tilde{x}} \tag{6.44}$$

By comparing Eq. (6.43) with Eq. (6.44), it follows that:

$$H^{ENU} = H \cdot \mathrm{Rot}^{-1} \tag{6.45}$$

The modified Kalman gain matrix K^{ENU} is derived by inserting H^{ENU} and P^{ENU} into Eq. (A.5):

$$\begin{aligned} K^{ENU} = {} & Rot \cdot P \cdot Rot^T \cdot (H \cdot \mathrm{Rot}^{-1})^T \\ & \cdot [H \cdot \mathrm{Rot}^{-1} \cdot Rot \cdot P \cdot Rot^T \cdot (H \cdot \mathrm{Rot}^{-1})^T + R_k]^{-1} = Rot \cdot K \end{aligned} \tag{6.46}$$

Now the protection levels referenced to the local ENU coordinate system can be computed from the transformed matrices.

The processing of carrier phase measurements in addition to pseudorange measurements does not require much change of classical pseudorange-based RAIM algorithms. However, the protection levels will become tighter thanks to the low-noise carrier phase measurements. The main reason why classical snapshot RAIM algorithms cannot be applied here is founded in the usage of an EKF for navigation. An approach to define protection levels for a Kalman filter-based navigation solution has already been proposed by Feng et al. [10]. The procedure of calculating the fault-free protection levels during normal filter operation is adopted in this work. In order to determine the filter performance, the information provided by the EKF can be used immediately. The first three main diagonal elements of the covariance matrix $P_k^{ENU}(+)$ contain the theoretical variances of the position estimate uncertainty in x_{east}, x_{north} and x_{up}. The theoretical standard deviations of the horizontal and vertical position estimate uncertainty are given by:

$$\sigma_{H,k} = \sqrt{P^{ENU}_{k,(1,1)}(+) + P^{ENU}_{k,(2,2)}(+)} \quad , \quad \sigma_{V,k} = \sqrt{P^{ENU}_{k,(3,3)}(+)} \tag{6.47}$$

The posteriori covariance matrix of state estimation uncertainty, $P^{ENU}_k(+)$, is only meaningful in terms of state estimation errors if the state transition matrix Φ^* and the measurement sensitivity matrix H^* in the implemented filter reflect the physical model accurately. More insight on sub-optimal filter analysis can be found in [5]. Note that some aspects with respect to the predicted variance and the actual variance of the state estimation errors have already been discussed in Sect. 4.2. In contrast to the approach presented in [10], here sigma-overbounding is introduced on the theoretical standard deviations of position estimation uncertainty. An inflation factor f_{Pos} is defined for this purpose. Now the horizontal and vertical error bounds $HPL_{0,k}$ and $VPL_{0,k}$, which refer to the fault-free condition, can be indicated. They are computed from the standard deviations of the position estimate uncertainties, the inflation factors and the probabilities of missed detection $P_{0,MD\_V} = P\left[\left|\hat{x}_{v,B} - x_{v,B}\right| > VPL_0 | (CF_{WL}, CF_{CP})\right]$ and $P_{0,MD\_H} = P\left[\left|\hat{x}_{h,B} - x_{h,B}\right| > HPL_0 | (CF_{WL}, CF_{CP})\right]$ as derived from the specified integrity risk:

$$HPL_{0,k} = k_{0,MD\_H} \cdot \sigma_{H,k} \cdot f_{Pos,H} \quad , \quad VPL_{0,k} = k_{0,MD\_V} \cdot \sigma_{V,k} \cdot f_{Pos,V} \tag{6.48}$$

It is assumed that the user's position error is characterized by a normal distribution. This allows for computing the scalar factors k_{0,MD_*}, which reflect the probabilities of missed detection, from a standardized normal distribution [36]:

$$\Phi\left(k_{0,MD\_*}\right) = 1 - \frac{1}{2} \cdot P_{0,MD\_*} \tag{6.49}$$

The definition of $\Phi(x)$ is according to Eq. (2.4). The $k_{0,MD}$ factor, which bounds the user's position with 6.109 sigma (two-sided Gaussian), is shown in Figure 6.2. It corresponds to a probability of missed detection $P_{0,MD} = 1 \cdot 10^{-9}$ per sample.

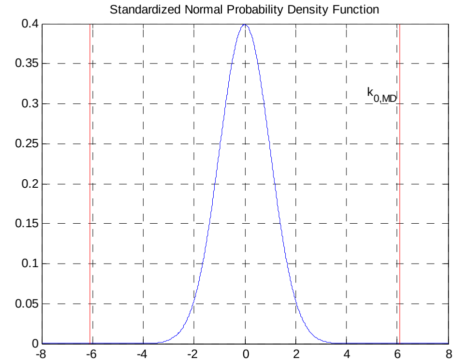

Figure 6.2: Bounding of the user's position during normal operation

Since it comes without additional effort, the protection levels for the user's velocity $vel\_HPL_{0,k}$ and $vel\_VPL_{0,k}$ under the fault-free condition can be indicated as well:

$$\begin{aligned} vel\_HPL_{0,k} &= k_{0,MD\_H} \cdot \sigma_{vel,H,k} \cdot f_{Vel,H} \quad , \\ vel\_VPL_{0,k} &= k_{0,MD\_V} \cdot \sigma_{vel,V,k} \cdot f_{Vel,V} \quad , \end{aligned} \tag{6.50}$$

with the theoretical standard deviations of the horizontal and vertical component of the velocity estimation uncertainty:

$$\sigma_{vel,H,k} = \sqrt{P^{ENU}_{k,(4,4)}(+) + P^{ENU}_{k,(5,5)}(+)} \quad , \quad \sigma_{vel,V,k} = \sqrt{P^{ENU}_{k,(6,6)}(+)} \tag{6.51}$$

The second error bound that is considered refers to the presence of a bias and follows from a projection of the test statistic to the position domain. This approach requires determining the maximum SLOPE, e.g. the maximum ratio of the position error to the test statistic. When computing the SLOPE factors it is assumed that there is a single bias in the measurement error vector. The detection of multiple biases simultaneously is not covered in this thesis. The projection of the test statistic to the position domain with the help of the largest SLOPE is illustrated in Figure 6.3. The illustration corresponds to snapshot RAIM. But the general idea of assessing the protection level in presence of a single bias resembles that of the filter-based RAIM approach.

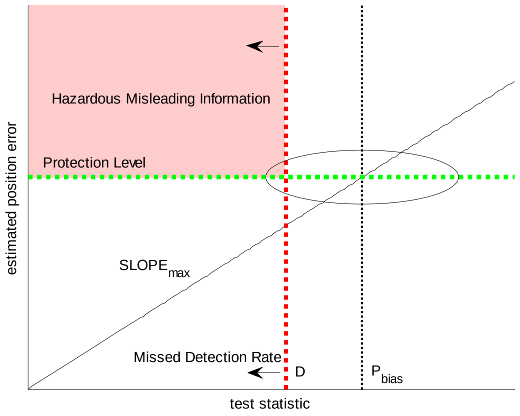

Figure 6.3: Derivation of the protection level in presence of a bias

The red-dotted line displayed in Figure 6.3 indicates the detection threshold D that depends on the probability of false alarm P_{FA} as derived from the continuity risk and the degrees of freedom of the test statistic. The computation of D follows from Eq. (2.33), where it has to be remembered to take the square-root of D if $\sqrt{WSSE}$ serves as test statistic. The black-dotted line in Figure 6.3 indicates the minimum detectable bias P_{bias}. It is shifted to the right of the detection threshold D in order to keep the missed detection rate as low as specified by the probability of missed detection $P_{MD,1}$. The protection level for the position estimate in presence of a bias results from the intersection of P_{bias} with the maximum SLOPE factor. A bias on the satellite signal measurement with the largest SLOPE results in the smallest test statistic, e.g. this bias will be the most difficult to detect. The navigation system will provide the user with Hazardous Misleading Information (HMI) if the resulting position error is above the protection level, but no alert flag can be raised because the test statistic is below the decision threshold D. The corresponding area is red-shaded in Figure 6.3.

The determination of the SLOPE in case of a Kalman filter-based approach is derived hereafter and compared with the SLOPE calculation of snapshot RAIM. In snapshot RAIM the position error vector $\delta\underline{x}_P$ is defined as:

$$\delta \underline{x}_P = \hat{\underline{x}}_{lsq} - \underline{x} \tag{6.52}$$

For simplicity a non-weighted least-squares approach is considered. By substituting the least squares estimate $\hat{\underline{x}}_{lsq}$ by

$$\hat{\underline{x}}_{lsq} = (H^T \cdot H)^{-1} \cdot H^T \cdot \underline{y} \quad , \tag{6.53}$$

it is shown in [23] that a single range bias on the i^th^ satellite signal measurement corresponds to a position error vector

$$\delta \underline{x}_{P,i} = (H^T \cdot H)^{-1} \cdot H^T \cdot \underline{b_i} \quad . \tag{6.54}$$

The range bias error vector $\underline{b_i}$ has a range bias b in row i, and zero elements elsewhere. The horizontal and vertical component of the position errors of the least-squares approach, δH_i and δV_i, follow immediately from Eq. (6.54):

$$\delta H_i = \sqrt{\delta \underline{x}_{P,i,(1)}^2 + \delta \underline{x}_{P,i,(2)}^2} \tag{6.55}$$

$$\delta V_i = \sqrt{\delta \underline{x}_{P,i,(3)}^2} \tag{6.56}$$

Now the filter-based approach is considered. The derivation of protection levels for Kalman filter solutions has first been proposed by Diesel et al. [7]. For clearness, the most important filter equations are repeated hereafter. The posteriori state estimation vector is given by

$$\hat{\underline{x}}_k(+) = \hat{\underline{x}}_k(-) + K_k \cdot \left(\underline{z}_k - \hat{\underline{z}}_k\right) \quad , \tag{6.57}$$

where the difference $\underline{z}_k - \hat{\underline{z}}_k$ corresponds to the innovation vector $\underline{r}_k$. From Eq. (6.57) follows that a range bias b_i is mapped to the domain of posteriori states by:

$$\delta \underline{x}_{k,i}(+) = K_k \cdot \underline{b_i} \tag{6.58}$$

If one is interested in the horizontal position error, only the first two elements of $\delta \underline{x}_{k,i}(+)$ have to be considered. The horizontal position error $\delta H_{k,i}(+)$ is:

$$\delta H_{k,i}(+) = \sqrt{\delta \underline{x}_{k,i,(1)}^2(+) + \delta \underline{x}_{k,i,(2)}^2(+)} \tag{6.59}$$

Analogously, the vertical position error $\delta V_{k,i}(+)$ results from the third element of $\delta \underline{x}_{k,i}(+)$:

$$\delta V_{k,i}(+) = \sqrt{\delta \underline{x}_{k,i,(3)}^2(+)} \tag{6.60}$$

In the next step, the test statistics of both snapshot RAIM and filter-based RAIM are compared. Snapshot RAIM uses the residual vector from the least-squares solution $\underline{r}_{lsq}$ in order to compute the test statistic. The least-squares measurement residual vector results from:

$$\underline{r}_{lsq} = \underline{y} - \hat{\underline{y}}_{lsq} = \underline{y} - H \cdot \hat{\underline{x}}_{lsq} = [I - H \cdot (H^T \cdot H)^{-1} \cdot H^T] \cdot \underline{y} \tag{6.61}$$

The mapping function S_{lsq} is introduced in order to facilitate further considerations:

$$S_{lsq} = I - H \cdot (H^T \cdot H)^{-1} \cdot H^T \tag{6.62}$$

Similarly a mapping function S_k can be derived for the filter-based approach. In contrast to snapshot RAIM, the innovation vector is used in order to compute the test statistic. It has to be determined how a single measurement bias propagates to the innovation vector $\underline{r}_k$. Since the innovation vector is defined by $\underline{r}_k = \underline{z}_k - \underline{\hat{z}}_k$, it follows that

$$\delta \underline{r}_{k,i} = I \cdot \underline{b}_i \quad , \tag{6.63}$$

and thus the mapping function S_k for the filter-based approach reduces to

$$S_k = I \tag{6.64}$$

The SLOPE is defined as the no-noise ratio of the position error to the test statistic for both snapshot RAIM and filter-based RAIM. The computation of the SLOPE factors for snapshot RAIM follows from Eq. (6.55), (6.56) and (6.62):

$$HSLOPE_{lsq,i} = \frac{\delta H_i}{\sqrt{S_{lsq,(i,i)}} \cdot |b|} \tag{6.65}$$

$$VSLOPE_{lsq,i} = \frac{\delta V_i}{\sqrt{S_{lsq,(i,i)}} \cdot |b|} \tag{6.66}$$

, where $|b|$ is the magnitude of the bias in row i. Note that the magnitude of the bias has no impact on the SLOPE factors. The bias $|b|$ cancels out when forming the ratio of the position error to the test statistic, e.g. $|b|$ is also contained in δH_i and δV_i, respectively.

The SLOPE factors for the filter-based RAIM approach follow from Eq. (6.59), (6.60) and (6.64):

$$HSLOPE_{k,i} = \frac{\delta H_{k,i}(+)}{1 \cdot |b|} = \sqrt{K_{k,(1,i)}^2 + K_{k,(2,i)}^2} \tag{6.67}$$

$$VSLOPE_{k,i} = \frac{\delta V_{k,i}(+)}{1 \cdot |b|} = \sqrt{K_{k,(3,i)}^2} \tag{6.68}$$

Obviously the SLOPE factors depend only on the Kalman gain if the test statistic is based on the innovation vector. Although it is not explicitly indicated in Eq. (6.67) and (6.68), it should be noted that K^{ENU} as derived in Eq. (6.46) is used for the computation of the SLOPE.

In absence of noise the test statistic and the position error are related by a linear model. In order to compute the protection levels, the measurement noise has to be considered as well. Since the measurement noise has great impact on the magnitude of the minimum detectable bias P_{bias}, the advantage of using carrier phase measurements becomes clear. First, the computation of P_{bias} in case of snapshot RAIM is considered. According to [23], the parameter $P_{bias,lsq}$ is dependent on the noncentrality parameter λ of a chi-square distribution and the standard deviation σ_ρ of the pseudorange measurements:

$$P_{bias,lsq} = \sqrt{\lambda} \cdot \sigma_\rho \tag{6.69}$$

This simple expression for $P_{bias,lsq}$ results from the fact that a non-weighted least squares approach is considered. However, no single standard deviation for all measurements can be used in the filter-based approach. First, different types of measurements are used as input to the filter. The standard deviations of the carrier phase measurements are obviously different from the standard deviations of the pseudorange measurements. Second, elevation-dependent standard deviations are considered. Third, the measurements forwarded to the filter are highly correlated due to double-differencing and inter-frequency combinations. Fourth, due to the filter-based approach the a priori covariance matrix of state estimation uncertainty has also influence on the minimum detectable bias. All these aspects have to be taken into account when computing

$P_{bias,k}$ for the filter-based approach. According to [44], the minimum detectable bias can be computed from

$$P_{bias,k,i} = \sqrt{\lambda} \cdot \frac{1}{\sqrt{\underline{b}_i^T \cdot Q_{\underline{r}_k}^{-1} \cdot \underline{b}_i}} \tag{6.70}$$

under the assumption that no invalidation of the model has taken place prior to the present epoch k of testing. The noncentrality parameter λ is chosen such that the probability of missed detection $P_{MD,1}$ is not exceeded for the given detection threshold D (see Figure 6.3):

$$\int_0^D f_{\chi^2,\upsilon,\lambda}(x)\,dx = P_{MD,1} \tag{6.71}$$

The definition of the non-central chi-square PDF $f_{\chi^2,\upsilon,\lambda}(x)$ is given in Eq. (2.11). The number of degrees of freedom υ follows from the number of double-differenced measurements at epoch k. The probability of false alarm P_{FA} is reflected by the decision threshold D.

Sigma overbounding is frequently applied in order to cover the non-Gaussian tails of the actual distribution of measurement errors. This technique is adopted here for the PDF of the innovation vector. An inflation factor f_r, which is multiplied by the standard deviation of a Gaussian distribution, is introduced in order to account for the following effects:

- Unexpected sigma violations
- Process mixing of Gaussian distributions (time-varying errors, normalization by a theoretical sigma)
- No perfect synchronization of the reference and user receiver data

More insight on the determination of inflation factors can be found in Lee [25], where different inflation factors are combined in order to provide an overall inflation factor during LAAS operation.

By multiplying the maximum SLOPE with the minimum detectable bias and the inflation factor, the protection level under the assumption that there exists a bias on the ith satellite measurement is obtained from:

$$HPL_{1,k} = \max_i\left(HSLOPE_{k,i} \cdot P_{bias,k,i}\right) \cdot f_r \tag{6.72}$$

$$VPL_{1,k} = \max_i\left(VSLOPE_{k,i} \cdot P_{bias,k,i}\right) \cdot f_r \tag{6.73}$$

For completeness, the protection levels for the user velocity estimates in presence of a bias are also indicated. The derivation is analog to that of the protection levels for the position estimates. The velocity SLOPE factors are computed from:

$$vel\_HSLOPE_{k,i} = \sqrt{K_{k,(4,i)}^2 + K_{k,(5,i)}^2} \tag{6.74}$$

$$vel\_VSLOPE_{k,i} = \sqrt{K_{k,(6,i)}^2} \tag{6.75}$$

Finally, the user velocity protection levels in presence of a bias are completely specified by:

$$vel\_HPL_{1,k} = \max_i\left(vel\_HSLOPE_{k,i} \cdot P_{bias,k,i}\right) \cdot f_r \tag{6.76}$$

$$vel\_VPL_{1,k} = \max_i\left(vel\_VSLOPE_{k,i} \cdot P_{bias,k,i}\right) \cdot f_r \tag{6.77}$$

The protection levels of rare normal operation $HPL_{0,k}$ and $VPL_{0,k}$ have been derived under the assumption of absence of biases. The protection levels that correspond to the biased case are $HPL_{1,k}$ and $VPL_{1,k}$. Since both hypotheses exclude each other, the overall protection levels are given by the larger values of the protection levels for the fault-free and the biased case:

$$HPL_k = \max\left(HPL_{0,k}, HPL_{1,k}\right) \tag{6.78}$$

$$VPL_k = \max\left(VPL_{0,k}, VPL_{1,k}\right) \tag{6.79}$$

And for the overall protection levels for the user velocity estimates it holds that:

$$vel\_HPL_k = \max\left(vel\_HPL_{0,k}, vel\_HPL_{1,k}\right) \tag{6.80}$$

$$vel\_VPL_k = \max\left(vel\_VPL_{0,k}, vel\_VPL_{1,k}\right) \tag{6.81}$$

In the WAAS MOPS [36] it is stated that HPL_0 and VPL_0 are usually not emphasized by snapshot RAIM algorithms. The protection levels that are determined for the single-failure case, e.g. HPL_1 and VPL_1, clearly exceed the protection levels of the fault-free case. This holds not true in general for filter-based approaches. As mentioned in the beginning of this chapter, the protection levels $HPL_{0,k}$ and $VPL_{0,k}$, which refer to the rare normal filter operation, definitely contribute to the integrity risk. This has also been verified during various simulation runs.

As long as $HPL_k < HAL$ and $VPL_k < VAL$, it is assumed that the filter-based navigation solution is reliable. However, there is no analytic proof that the integrity risk and the continuity risk are not exceeded with the proposed AFDIA scheme. Due to the usage of an EKF, whose performance is data-driven, it is recommended to assess the actual integrity and continuity risk by test. Of course this will cause serious trouble if it has to be proofed that the integrity risk is as small as 10^{-9}.

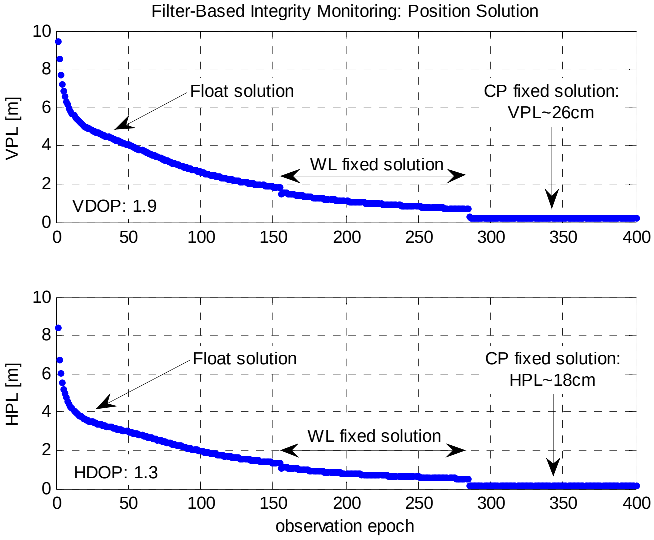

Figure 6.4: Typical protection levels of the filter-based approach (position solution)

In Figure 6.4 the protection levels for the user position solution are displayed for a typical landing approach. Altogether 8 satellites are in view at both the reference station and the airplane during the whole landing approach. The satellite geometry is good as indicated by the DOP-values which are displayed in the sub-plots. The widelane ambiguities are fixed in epoch 154 and the carrier phase ambiguities are fixed in epoch 284. After ambiguity fixing the protection levels become smaller. The accuracy of the position solution is then mainly determined by the noise of the carrier phase measurements and uncompensated residual ionospheric range errors. After ambiguity fixing the pseudorange measurements are low-weighted by the Kalman gain. The VAL of CAT IIIc precision approach is 5.3 m. The vertical protection level is already below 5.3 m before the widelane ambiguities can be resolved after the navigation filter has been running for a while (less than 50 epochs). Since the computation of the protection levels for the user velocity solution is also supported, the respective protection levels are displayed in Figure 6.5. The protection levels are in general below 1 m/s and hardly affected by ambiguity resolution. The reason for this is that the velocity solution is solely based on the instantaneous Doppler shift measurements. Furthermore, the protection levels are rather high since double-differenced Doppler measurements are processed and thus the measurement noise is amplified due to double-differencing. The user velocity solution is only considered as a useful by-product and it is not in the focus of this work.

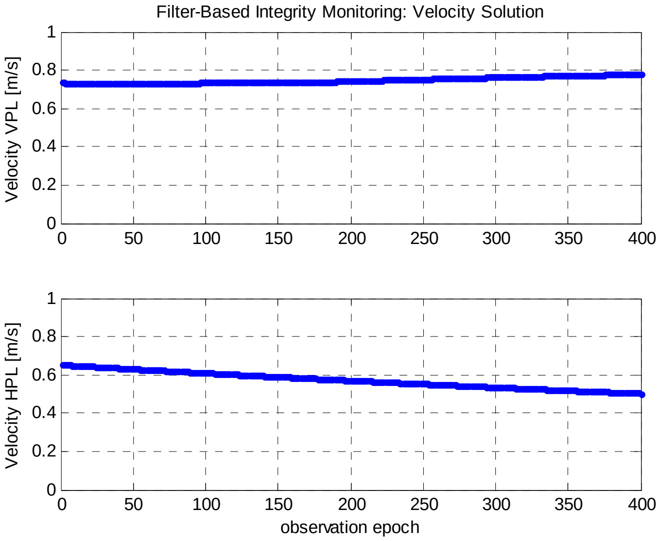

Figure 6.5: Typical protection levels of the filter-based approach for the velocity solution

7 Monte-Carlo Simulations

7.1 Simulation Environment

7.1.1 Measurement Input Data

The Satellite Navigation (SatNav) Toolbox 3.0 provided by GPSoft® forms the basis of the simulation environment used in this work. Nevertheless, some modifications with respect to the generation of pseudorange and carrier phase measurements are required in order to reflect the progress made in GNSS receiver technology. Furthermore, the modeling of instantaneous Doppler shift measurements has to be added, which is not integrated in the SatNav toolbox. In this section the generation of the navigation signals, which are processed by the navigation filter, is described. Both the simulation of GALILEO and GPS signals is supported. The GNSS signals of interest for civil aviation have to reside in an ARNS band. Here GALILEO's E1 and E5a signal and GPS's L1 and L5 signal are considered. In Table 7.1 the characteristics of these navigation signals are summarized. The indicated values are after [29] and date back to 2006.

Table 7.1: Extract of GALILEO and modernized GPS signal characteristics

	Channel	**Frequency [MHz]**	**Carrier Wavelength [m]**
GALILEO E1	E1-B	1575.42	0.1903
GALILEO E5a	E5a-I	1176.45	0.2548
GPS L1 (present)	-	1575.42	0.1903
GPS L5	I5	1176.45	0.2548
	Modulation	**Chip rate [Mc/s]**	**Data / Symbol Rate**
GALILEO E1	BOC(1,1)	1.023	250 sps
GALILEO E5a	BPSK10	10.23	50 sps
GPS L1 (present)	BPSK	1.023	50 bps
GPS L5	QPSK	10.23	100 sps

Simulation of thermal receiver noise:

Pseudorange measurement noise is simulated with the help of a random number generator. The standard deviation that corresponds to the respective navigation signal type is multiplied by a normally distributed random number $x \sim N(0,1)$. The noise level of the pseudorange measurements is varied during different simulation runs. In order to get an impression of the expected magnitude of pseudorange measurement noise, the standard deviations $\sigma_{\rho E5a}$, $\sigma_{\rho E1}$ and $\sigma_{\rho L1}$, which have been derived from real-signal measurements, are indicated in Table 8.1. However, in the software simulations more pessimistic values for the standard deviations are used when evaluating the filter performance.

The carrier phase noise in units of cycles is also assumed to be normally distributed with zero-mean and a standard deviation of 0.012 cycles. This corresponds to approximately 2.3 mm on E1 (or L1). The received power is elevation-dependent and the measurement noise level increases for low signal strengths. Therefore, an elevation-dependent scaling factor for the standard deviations is introduced:

$$k_\sigma = 1 + \frac{1}{2} \cdot e^{-\frac{E^{Sj}}{15°}} \tag{7.1}$$

The satellite elevation angle E^{Sj} of Eq. (7.1) has to be inserted in units of degrees. In Figure 7.1 the run of the scaling factor over the satellite elevation angle is displayed. Both pseudorange and carrier phase measurement standard deviations are scaled by this elevation-dependent factor.

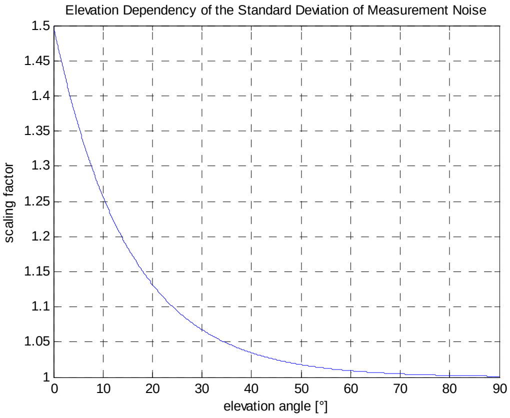

Figure 7.1: Scaling factor for the standard deviations of thermal receiver noise

Simulation of propagation delay/advance caused by ionospheric refraction:

Ionospheric refraction causes a path length difference, d_{ion}, between the measured range and the true geometric range. The modeling of signal delays/advances due to the ionosphere follows from [23]. The magnitude of d_{ion} depends on the electron density along the propagation path, which is represented by the Total Electron Content (TEC) in units of electrons/m^2. If the TEC is referenced to the vertical direction through the ionosphere, it is denoted as VTEC. The TEC can be approximated by multiplying the VTEC with the obliquity factor. The obliquity factor F reflects the dependency of the ionospheric delay on the satellite elevation angle:

$$F = \frac{1}{\sqrt{1 - \left(\frac{R_e \cdot cos(E^{Sj})}{R_e + h_I}\right)^2}} \quad , \tag{7.2}$$

where:

R_e: Mean radius of the earth

E^{Sj}: Elevation angle of satellite S_j

h_I: Mean ionospheric shell height

The special committee 159 of RTCA [36] also proposes to use the definition of the obliquity factor according to Eq. (7.2) for WAAS airborne equipment. In literature this model is referred to as "single-layer model", since it is assumed that all electrons are concentrated within a very thin layer at medium ionospheric shell height. According to Wanninger [51], the validity of the single-layer model is restricted to satellite elevation angles above 30°. There exist further models for the obliquity factor, resulting in a similar run of the elevation-dependent scaling factor. Generally, it can be stated that the lower the elevation angle, the higher is the delay due to an increased propagation path through the ionosphere. The definitions made so far allow for indicating the ionospheric path delay as:

$$d_{ion} = F \cdot \frac{40.3 \cdot VTEC}{f^2} \tag{7.3}$$

The pseudorange measurement is increased by d_{ion}, while the carrier phase measurement is reduced by d_{ion}. This corresponds to a delay of the group velocity v_g and an advance of the phase velocity v_p due to ionospheric refraction:

$$\begin{aligned} v_g &\approx \frac{c_0}{1 + \frac{40.3 \cdot n_e}{f^2}} \quad , \\ v_p &\approx \frac{c_0}{1 - \frac{40.3 \cdot n_e}{f^2}} \quad , \end{aligned} \tag{7.4}$$

where n_e is the electron density. Higher order terms of the refractive index have been neglected in Eq. (7.4). Typical values which are used in the simulations for the VTEC are between $1 \cdot 10^{18} \frac{el}{m^2}$ and $3 \cdot 10^{18} \frac{el}{m^2}$. These values are already beyond the average VTECs.

Measurement errors due to atmospheric refraction comprise also the delay of the signals when passing through the troposphere. Tropospheric range errors are neither estimated by the navigation filter nor simulated as nuisance parameters hereafter. It has to be considered that the overall filter performance will degrade if the assumption that the residual double-differenced tropospheric range errors are negligible is no longer valid.

Simulation of multipath:

The magnitude of pseudorange and carrier phase measurement errors due to multipath is assumed to depend on the satellite elevation angle. Zappavigna [56] proposes to use an inverse tangent run of the multipath scaling factor M over the satellite elevation angle E^{Sj}:

$$M = 1 - \frac{tan^{-1}\left(E^{Sj}\right)}{tan^{-1}\left(\frac{\pi}{2}\right)} \tag{7.5}$$

The satellite elevation angle E^{Sj} has to be inserted into Eq. (7.5) in units of radian. The factor M is used in the simulations in order to scale the zero-angle equivalent pseudorange multipath error which is provided by the SatNav toolbox. There are two different multipath error models available: in the first model a time constant of approximately 2 minutes and a standard deviation of approximately 1.6 m are considered, while the time constant of the second model is approximately 15 s and the standard deviation is reduced to approximately 0.4 m. The error of the carrier phase measurement due to multipath in units of meters is computed from the pseudorange multipath error by multiplying it with the factor $0.02 \cdot \lambda$. Examples of pseudorange and carrier phase multipath errors for both models are given in Figure 7.2 and Figure 7.3. Satellite 8 is always seen under an elevation angle above 60°, while satellite 19 is always seen under an elevation angle below 8°. The first multipath error model is applied for the reference receiver site. The second multipath error model, which is characterized by a lower standard deviation and a lower time constant of the multipath error, is applied for the receiver located at the airplane. Thereby it is reflected that multipath characteristics due to reflections from the surface of the airplane are different from those of ground-based multipath.

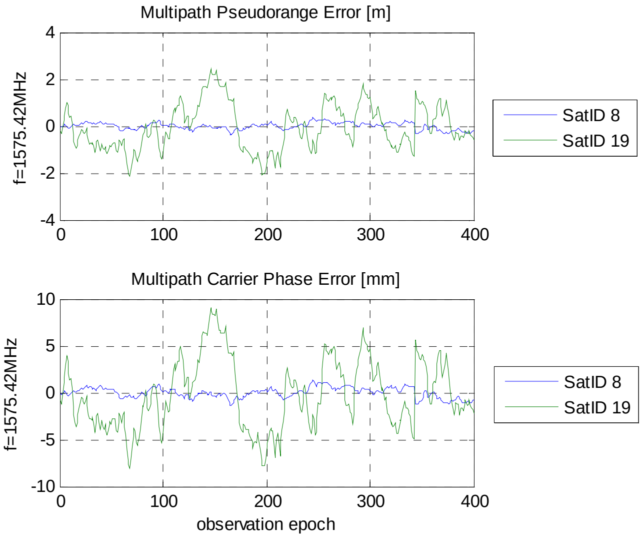

Figure 7.2: Multipath Error Model 1 (used for the reference station)

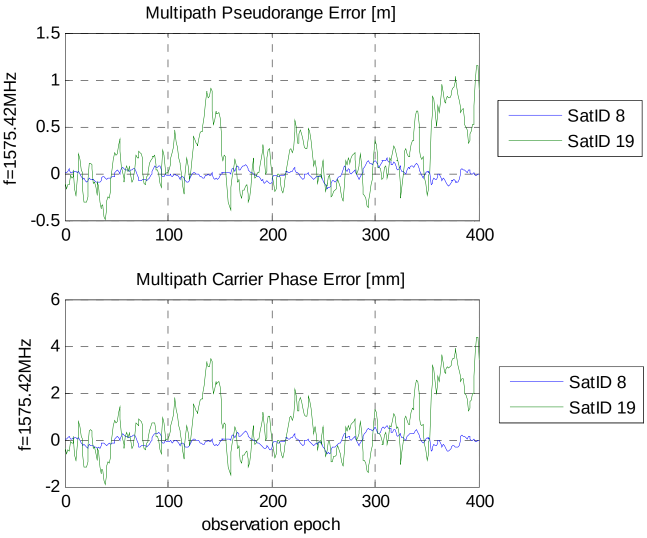

Figure 7.3: Multipath Error Model 2 (used for the airplane)

According to [44], the maximum multipath error on L1 carrier phase measurements is about 5 cm. In the simulations a constant scaling factor is used in addition to the elevation-dependent scaling factor M in order to upscale or downscale the magnitude of multipath errors.

Further GNSS error sources are not considered here. Especially those biases that cancel out when double-differencing between observations, e.g. clock errors, are not simulated. The most critical simplification of the simulated measurement data compared to real measurement data is founded in the neglecting of troposphere-induced range errors.

7.1.2 Simulation of the Precision Approach

A simple physical model of the airplane's dynamics during precision approach is chosen for the simulations. However, it is tried to use realistic values with respect to the decline rate during the final approach. Accelerations are also simulated in order to verify if it is justified to use a state space model in the EKF which neglects systematic accelerations. The airplane's absolute velocity ranges from 270 knots (= 500 km/h) at the beginning of the simulation to 196.5 knots (= 364 km/h) at the end of the simulation. Jittering of the airplane's trajectory due to cross-wind is not considered. In Figure 7.4 and in Figure 7.5 the simulated descent of the airplane is displayed, one time as a function of the observation epoch and the other time as a function of the baseline length between the user receiver and the reference receiver. According to Kaplan [23], an EKF designed for solving a navigation problem stabilizes in a few hundred iterations. Here are altogether only 408 observation epochs considered, since the maneuver time span of precision landing is limited as well as the broadcast radius in order to transmit the reference receiver data to the airplane. In Pervan et al. [33] the relationship between system availability and data broadcast radius has been examined for carrier phase DGPS navigation. The maximum data broadcast radius considered there was 50 nmi (= 92.6 km). In the simulation results presented here the broadcast radius is restricted to 50 km. It is desirable to keep the broadcast radius small with regard to the required infrastructure and possible interference between different airport service volumes. In the real-signal tests, whose results are presented in Sect. 8, the data broadcast radius is extended to approximately 75 km. Although no extensive system availability analysis has been made in this work, the data broadcast radius is not considered to be a very critical parameter with regard to the performance of this navigation filter.

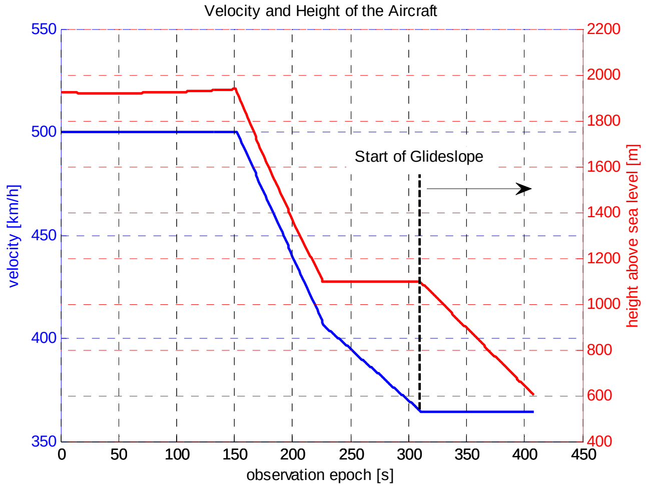

Figure 7.4: Dynamics of the airplane during precision approach

When starting the simulation, the distance between the user receiver, which is installed at the airplane, and the reference receiver, which is located in the vicinity of the landing strip, is about 50 km. After touchdown, which corresponds to the last simulated observation epoch, the airplane is about 160 m away from the reference station. A low receiver sampling rate of 1 Hz is considered and the simulation time is limited to the last 6.8 minutes of the final flight phase before touchdown.

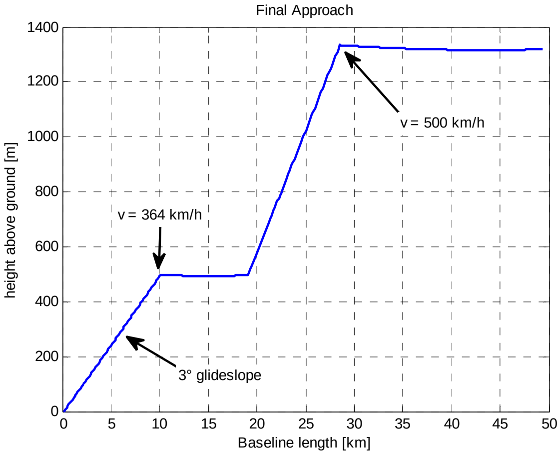

Figure 7.5: Final approach of the airplane

The reference receiver is located in the vicinity of the airstrip in Oberpfaffenhofen at $\varphi_A = 48°4'13.32''$, $\lambda_A = 11°16'6.94''$ and $h_A = 600m$. The flight path has been chosen arbitrarily: the height above ground is decreased as shown in Figure 7.5 and the latitude of the airplane changes, while the longitude is left constant.

7.1.3 Integrity Monitoring Parameters

The expected alert limits of a CAT IIIc approach are $HAL = 15.5m$ and $VAL = 5.3m$. As soon as the widelane ambiguities are fixed, the computed horizontal and vertical protection levels for the filter-based position solution are smaller than 5.3 m. Therefore, the achievable magnitude of the protection levels is investigated rather than the violation of a specific alert limit. Further applications like automated cargo-traffic, which are also of interest, might require far smaller alert limits than CAT III precision approaches. The integrity monitoring parameters (see Table 7.2) are not chosen such that the expected CAT IIIc requirements are fulfilled exactly, but the order of magnitude will be very similar. Note that here the same tight error bounds are used for both the horizontal and the vertical position component while in civil aviation the requirements for the horizontal component are more relaxed during precision approach.

Table 7.2: Error probabilities, critical values and sigma-overbounding

Normal Operation ($I_{0,CAR,spec}$)		
Integer Bootstrapping	Probability of false widelane integer ambiguity fixing	
	$P_{F,WL} = 1 \cdot 10^{-9}$	
	Probability of false carrier phase integer ambiguity fixing	
	$P_{F,CP} = 1 \cdot 10^{-9}$	
User Position Bounding	$P\left[\lvert \hat{x}_{h,B} - x_{h,B} \rvert > HPL_0 \mid (CF_{WL}, CF_{CP})\right]$	$P\left[\lvert \hat{x}_{v,B} - x_{v,B} \rvert > VPL_0 \mid (CF_{WL}, CF_{CP})\right]$
	$P_{0,MD\_H} = 1 \cdot 10^{-9}$ $\rightarrow k_{0,MD\_H} = 6.12$	$P_{0,MD\_V} = 1 \cdot 10^{-9}$ $\rightarrow k_{0,MD\_V} = 6.12$
	Horizontal position inflation factor	Vertical position inflation factor
	$f_{Pos,H} = 1.2$	$f_{Pos,V} = 1.2$

Fault Mode ($I_{1,spec}$)	
Fault Detection	Probability of false alarm
	$P_{FA} = 1 \cdot 10^{-7}$
	Probability of missed detection
	$P_{MD,1} = 1 \cdot 10^{-9}$
Fault Identification	Probability of wrong error identification
	$P_{WID} = 2 \cdot 10^{-9}$
Sigma Overbounding	Innovation inflation factor
	$f_r = 2.8$

The associated integrity risk is expected to be at the order of $3 \cdot 10^{-9}$. As mentioned before, there is no analytic proof that the integrity risk is indeed bounded by $3 \cdot 10^{-9}$ for this EKF-based approach. Unfortunately, the required number of simulated precision approaches is too high in order to assess the actual integrity risk by simulations. For this reason other filter performance parameters than the integrity risk are evaluated in the following. The simulation results presented hereafter are based on the small error probabilities indicated in Table 7.2. Only the IB estimator is listed in Table 7.2, since it offers the chance to compute the probability of false integer ambiguity fixing exactly. If the LAMBDA method is used for ambiguity resolution, the validation of the integer ambiguities is based on the ratio test together with an integer test. The levels of significance of the integer test are set to $\alpha_{WL} = 2 \cdot 10^{-5}$ and $\alpha_{CP} = 2 \cdot 10^{-5}$ and the critical values of the ratio test are set to $k_{c,WL} = 4$ and $k_{c,CP} = 4$. If not indicated otherwise, the IB estimator is used for ambiguity resolution.

7.2 Evaluation of the Filter Performance

7.2.1 Dependency on the Satellite Geometry

Two different satellite constellations are considered in the simulations. The first constellation is derived from an arbitrary GPS RINEX file and the second constellation is derived from a GALILEO simulation scenario generated by the Spirent HW simulator.

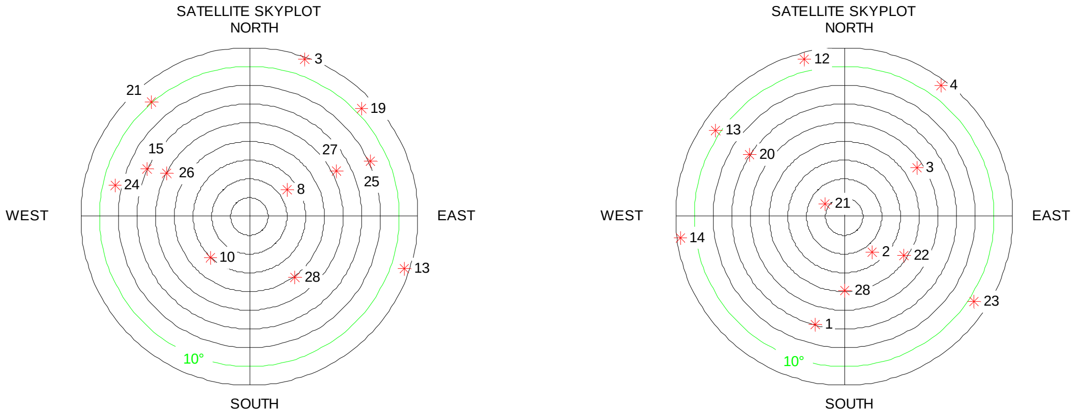

Figure 7.6: Sky-plot of the satellites during precision approach (left: GPS constellation; right: GALILEO constellation)

Since the received signal power, the propagation path length through the ionosphere and multipath are elevation-dependent, an elevation mask is used to exclude satellites seen under low elevation angles. Receiver elevation mask angles between 5° and 30° are considered here. The number of satellites used in the navigation solution varies with different settings for the receiver elevation mask angle. In Table 7.3 the corresponding DOP values are indicated for the GPS and GALILEO satellite constellation of Figure 7.6. The DOP values do not change significantly during the maneuver time.

Table 7.3: DOP values in dependency of the receiver elevation mask

Constellation	Elevation Mask	# Satellites	HDOP	VDOP	PDOP
GPS	20°	6	1.52	3.51	3.83
	10°	8	1.34	1.94	2.36
	5°	10	1.29	1.70	2.13
GALILEO	30°	6	1.99	3.01	3.61
	10°	7	1.28	2.44	2.76
	5°	9	1.02	1.15	1.54

Dual-frequency pseudorange, carrier phase and Doppler shift measurements on $f_1 = 1176.45MHz$ and $f_2 = 1575.42MHz$ are simulated and forwarded to the navigation filter as measurement input. The following standard deviations are used for the simulation of measurement noise: $\sigma_{\rho L1/E1}(90^\circ) = 30cm$, $\sigma_{\rho L5/E5a}(90^\circ) = 10cm$, $\sigma_{\Phi}(90^\circ) = 0.012$ cycles and $\sigma_{\mathrm{D}}(90^\circ) = 0.1Hz$. Vertical total electron contents between $VTEC_{min} = 1 \cdot 10^{18}\,\frac{el}{m^2}$ and $VTEC_{max} = 2 \cdot 10^{18}\,\frac{el}{m^2}$ are considered. The Ionosphere Model 3, see Sect. 5.3.3, is used in the navigation filter in order to estimate the double-differenced ionospheric range errors. The parameters of this ionosphere model are set to $\sigma^2(90^\circ) = (3cm)^2$ and $d = 300km$. Furthermore, the spectral amplitude of the random walk process in the covariance matrix of process noise is considered to be $S_p = 3\,\frac{m^2}{s^2}\frac{rad}{s}$. The estimated standard deviations, which are used to compute the covariance matrix of measurement noise R, are set to $\hat{\sigma}_{\rho L1/E1} = 40cm$, $\hat{\sigma}_{\rho L5/E5a} = 20cm$, $\hat{\sigma}_{\Phi} = 0.0159$ cycles and $\hat{\sigma}_{\mathrm{rr},f_2} = 0.02\,\frac{\mathrm{m}}{\mathrm{s}}$. Note that the measurement noise due to thermal receiver noise has been chosen rather pessimistically. On the other hand, no multipath errors have been simulated in this concrete simulation scenario.

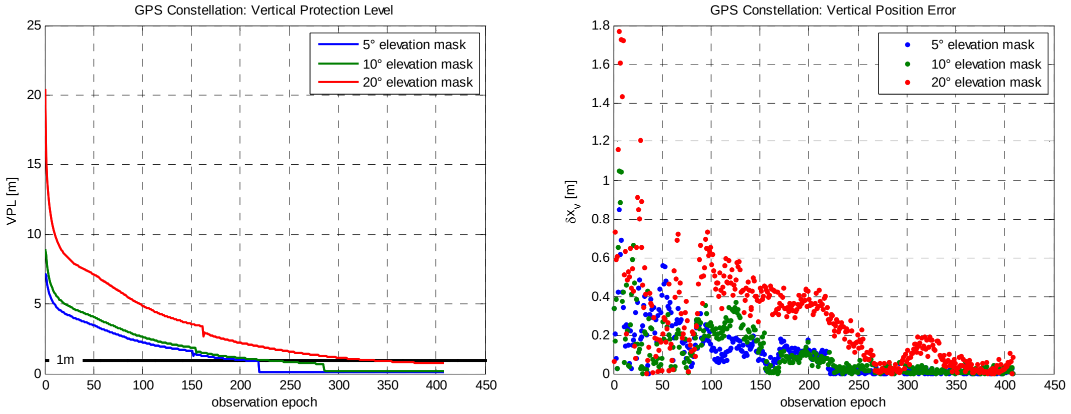

Figure 7.7: Vertical protection levels and position errors for the GPS constellation

The simulation results for the vertical protection levels in dependence of the receiver elevation mask angle are shown in Figure 7.7 for the GPS satellite constellation. Besides the VPLs, also the vertical component of the user position error, δx_v, is plotted, which is always clearly below the computed protection level. As expected from the DOP values, the results for the horizontal position component are even better, and therefore not displayed. A widelane ambiguity-fixed solution is obtained in observation epoch 152 (5° elevation mask), 155 (10° elevation mask) and 162 (20° elevation mask). A carrier phase ambiguity-fixed solution is obtained in observation epoch 219 (5° elevation mask) and in observation epoch 286 (10° elevation mask). No carrier phase ambiguity resolution with $P_{F,CP} = 1 \cdot 10^{-9}$ is possible if the elevation mask angle is set to 20°. Here the VPLs of the carrier phase ambiguity-fixed position solutions are between 15 cm (5° elevation mask) and 20 cm (10° elevation mask).

Next, the GALILEO constellation is considered. The measurement standard deviations are not modified with respect to GPS. This ensures that the test outcomes are only influenced by the variation of satellite geometry.

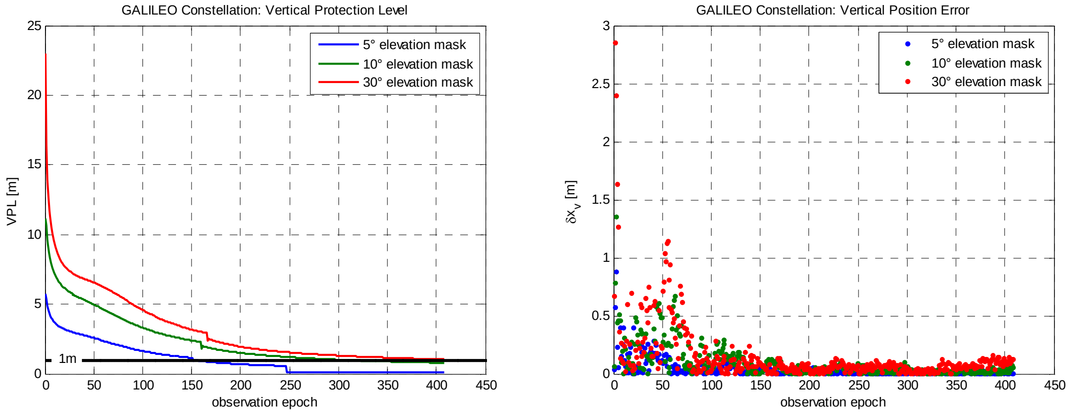

Figure 7.8: Vertical protection levels and position errors for the GALILEO constellation

Independent from the setting of the elevation mask angle, the widelane ambiguities could always be fixed successfully in either epoch 152 (5° elevation mask), or in epoch 160 (10° elevation mask), or in epoch 166 (30° elevation mask). A carrier phase ambiguity-fixed solution could only be determined for an elevation mask angle of 5° in epoch 247. Even if applying sigma-overbounding, the VPL for the vertical position component of the carrier phase ambiguity-fixed solution becomes as low as 10 cm at the end of the simulation run. However, this seems reasonable when having a look at the maximum deviation of the vertical position component from the true position, which is below 2 cm. For the GALILEO constellation with only 6 or 7 visible satellites no carrier phase ambiguity-fixed solution was obtained. Nevertheless, the protected position accuracy of the widelane ambiguity-fixed position solution is still sufficient for CAT IIIc precision approach. In all six simulation runs the VPL of the float solution is below 5 m after the navigation filter has been running for 100 epochs. The baseline length between the reference receiver and the user receiver at observation epoch 100 is approximately 35.6 km.

The actual satellite constellation is decisive for resolving the ambiguities successfully since a geometry-based mathematical model is used for ambiguity resolution. On the one hand, the satellite geometries considered here do not correspond to the worst case constellation. On the other hand, the measurement noise has been chosen rather pessimistically. In the near future both GALILEO and GPS signals can be tracked simultaneously. Therefore, it is assumed that poor satellite geometries will no longer be the limiting factor if combined GALILEO and GPS measurements were processed simultaneously by the filter. The test results suggest that the number of satellites in view is very important for the confidence in carrier phase integer ambiguity vector. The widelane ambiguities could be fixed for all constellations listed in Table 7.3. However, the computed probability of false carrier phase ambiguity fixing, $P_{F,CP}$, was only smaller than $1 \cdot 10^{-9}$ if at least 8 satellites were visible simultaneously. If a combined GALILEO and GPS constellation is considered, a minimum number of 8 visible satellites will easily be achievable. The results presented in this section were obtained in absence of multipath. The influence of multipath on the filter performance will be investigated separately.

7.2.2 Changes in the Satellite Constellation

During the flight phase new satellites may appear and other satellites may set while the nonlinear filter is already running. Only those satellites which are seen above the specified elevation mask at both the reference receiver site and the user receiver site are included into the navigation solution. So far it is assumed that the reference satellite will not change. Since the time span of precision approach is limited, it is reasonable to assume that one can keep the same reference satellite during the whole approach. However, if the reference satellite fails, it would be advantageous to have for example a second filter running in parallel which uses a different reference satellite. Then one could switch between the two filters if a reference satellite failure was detected. The reference satellite is excluded from the further considerations. A setting satellite can easily be removed from the filter by deleting the respective rows and columns which correspond to this satellite from the matrices and vectors. In Figure 7.9 the variation of the horizontal and vertical protection level is shown for the case that one of the tracked satellites sets. In this example the carrier phase ambiguities have already been fixed before the satellite is excluded from the navigation solution. Therefore, the carrier phase measurements are given the most weight within the filter and dominate the position accuracy as well as the magnitude of the protection levels.

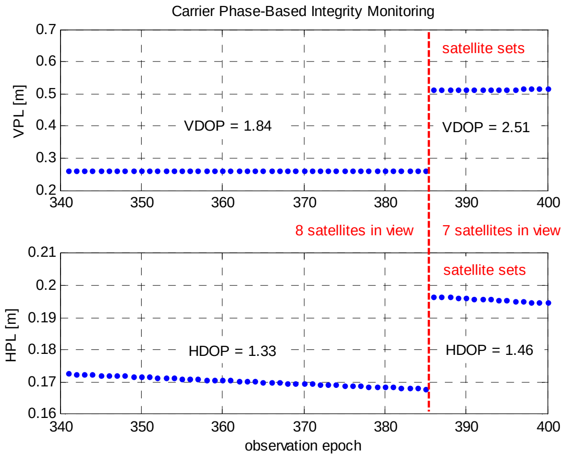

Figure 7.9: Variation of the protection levels due to a setting satellite

The indicated protection levels for the carrier phase ambiguity-fixed position solution refer to moderate DOP values. However, the influence of a setting satellite on the VPL can be clearly seen from Figure 7.9. When one of the eight satellites' elevation angles falls below the elevation mask of 15°, the VDOP changes by 36% and the VPL almost doubles. The impact of the satellite exclusion on the HPL is less severe, since the change of the HDOP is also less significant. It should be mentioned that in this example the measurement variances in R_k have not been scaled by an elevation-dependent function. The variation of the protection levels due to a setting satellite is assumed to be less distinctive if elevation-dependent measurement variances were used.

Besides the event that a satellite may set it is also possible that a new satellite rises while the navigation filter is still running. There are several possibilities how to treat the newly appeared satellite. The simplest approach would be to simply ignore the new satellite. This might be acceptable for short time periods such as the maneuver time of a final landing approach. But the navigation filter should be started some time before actually landing in order to let the filter solution stabilize and to provide enough time for reliable ambiguity resolution. There is a second aspect against this simple approach as long as the carrier phase ambiguities have not yet been fixed. It has been observed in simulations that the availability of a further satellite may significantly reduce the computed probability of wrong integer ambiguity fixing of the IB estimator. Thus, it can happen that the carrier phase integer ambiguity vector is accepted after including the new satellite into the solution, while otherwise no carrier phase ambiguity-fixed position solution could have been derived. It seems that the reliability of the integer ambiguity vector increases with the number of satellites in view in absence of biases. Therefore, a strategy is applied in this work that includes rising satellites at once. The inclusion of new satellites is unproblematic as long as the initial integer ambiguities of all other satellites have not yet been resolved. If the double-differenced ambiguities of the other satellites were already fixed, the following procedure is applied in order to include the measurements from the new satellite: In the epoch the new satellite appears, the measurements from this new satellite are still excluded at first and the navigation solution is computed as before. Afterwards, an initial guess of the new unknown double-differenced ambiguities is derived from the fixed solution:

$$\breve{N}_{*,init} = \left[\nabla\Delta\Phi_{*,AB}^{S_{ref}S_x} - \frac{\nabla\Delta\hat{r}_{AB}^{S_{ref}S_x}}{\lambda_*} \right] \quad , \tag{7.6}$$

where the squared brackets denote rounding to the nearest integer, S_x is the satellite that has just appeared and the symbol ‘*’ can be replaced by the corresponding frequency index (e.g. either ‘WL’ or ‘CP’). The double-differenced range estimate is computed from the ambiguity-fixed position solution:

$$\nabla\Delta\hat{r}_{AB}^{S_{ref}S_x} = \left\|\underline{X}_A - \underline{X}^{S_{ref}}\right\|_2 - \left\|\underline{X}_A - \underline{X}^{S_x}\right\|_2 - \left\|\hat{\underline{X}}_B - \underline{X}^{S_{ref}}\right\|_2 + \left\|\hat{\underline{X}}_B - \underline{X}^{S_x}\right\|_2 \tag{7.7}$$

Although the accuracy of the estimated user position vector $\hat{\underline{X}}_B$ is rather good in case of a fixed solution, it is not completely safe to use Eq. (7.6) in order to fix the missing integer ambiguities of the new satellite. Therefore, in the software a flag is set which indicates that the ambiguities are not fixed. Since all ambiguities except from the one of the newly appeared satellite have already been fixed, their variances are set to be almost zero in the stochastic model. Only the variance of the new double-differenced ambiguity is set to a higher value. Due to the good initial estimate of the new ambiguity and the low variances of all other ambiguities the integer ambiguities can be (re-)fixed almost immediately. On the one hand this allows keeping a very precise position estimate and low protection levels even directly after including the measurements from the new satellite. On the other hand ambiguity resolution of the new ambiguities is still safe by stepping back to an interim float solution. This approach, which benefits from the stochastic model in the EKF, is also used for re-fixing the ambiguities if a cycle slip on one of the phase measurements has been detected.

The effects of including a new satellite into the position solution is shown in Figure 7.10 for the case that the widelane ambiguities have already been fixed. In observation epoch 178 the number of satellites in view, which are above the specified elevation mask angle of 10°, increases from 8 to 9 satellites. The fixed solution is lost during the next 12 observation epochs because of including the new satellite. All widelane ambiguities are re-fixed safely in observation epoch 190. Now, with 9 satellites in view instead of 8 satellites, reliable carrier phase ambiguity resolution is speeded up. In observation epoch 255 the carrier phase ambiguities are fixed.

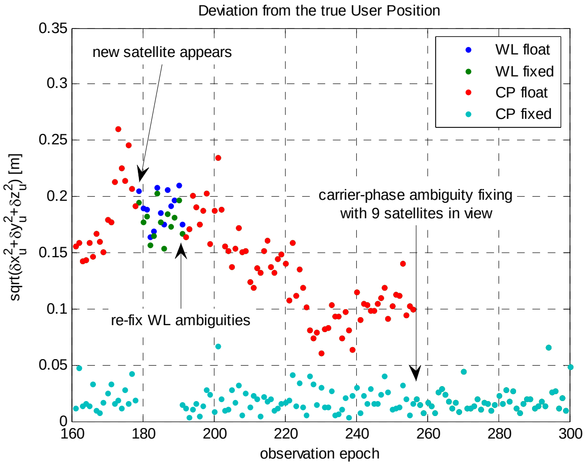

Figure 7.10: Inclusion of a rising satellite into the filter solution

Hardly any change of the protection levels is observable when the number of satellites is increased from 8 to 9 satellites. The HDOP improves only marginally from 1.34 to 1.30 and the VDOP slightly improves from 1.90 to 1.81 in this example by including the rising satellite in the navigation solution. If the stochastic model is set up conveniently, stepping back from a widelane ambiguity-fixed solution to a widelane ambiguity-float solution due to the inclusion of a new satellite has hardly any impact on the current precision of the position solution and on the protection levels. However, if the ninth satellite was not included at all, a carrier phase ambiguity-fixed solution would not be obtained before observation epoch 284. Since in this example the enclosure of the ninth satellite did only slightly improve the DOP values, there are for sure examples where it is even more important to support the filter adaptation to changes in the satellite constellation.

7.2.3 Influence of the Dynamic System Model

The discrete-time state equations used in the EKF in order to model the airplane's dynamics during the landing approach have been described in Sect. 5.2.4. It is assumed that the final approach can be modeled as straight flight condition with constant velocity. In this section it is investigated whether the final phase of the flight can indeed be represented by such a simple state space model. From Sect. 7.1.2 follows that systematic decelerations are present in the physical model of the airplane's dynamics in this simulation environment. There are also some phases of the flight where the straight flight condition with constant velocity is fulfilled. The most interesting parameter with respect to the influence of the dynamic system model on the filter performance is the spectral amplitude of the random walk S_p. The same simulation setup as described in Sect. 7.2.1 is used. Here the GPS constellation and an elevation mask angle of 10° are applied.

First, the confidence in the state space model is overrated, e.g. the process noise variances of the position and velocity states are set to very low values. For this purpose the spectral amplitude of the random walk is set to $S_p = 0.01 \frac{m^2}{s^2} \frac{rad}{s}$, which is definitely very optimistic. The effect of using lower variances for the position and velocity states in the process model than the actual variances of the physical system is shown in Figure 7.11:

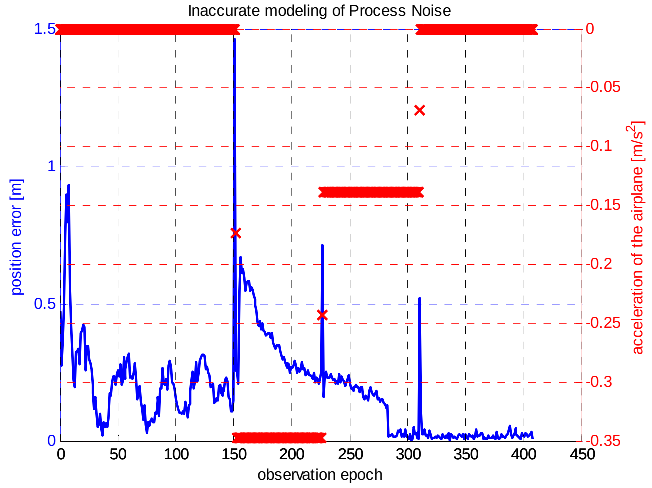

Figure 7.11: Error spikes in the position solution due to incorrect process noise settings

The presence of constant minor decelerations does not have much impact on the position estimate accuracy. In observation epoch 283 the carrier phase ambiguities are fixed correctly although the airplane's velocity is not constant during this phase of the flight. However, every time the acceleration changes slightly between successive observation epochs a position error spike can be detected. It has also to be considered that no significant accelerations are present in the simulated physical model. It is expected that the results would be even worse if real flight tests were considered given that the process noise variances are chosen to be that low.

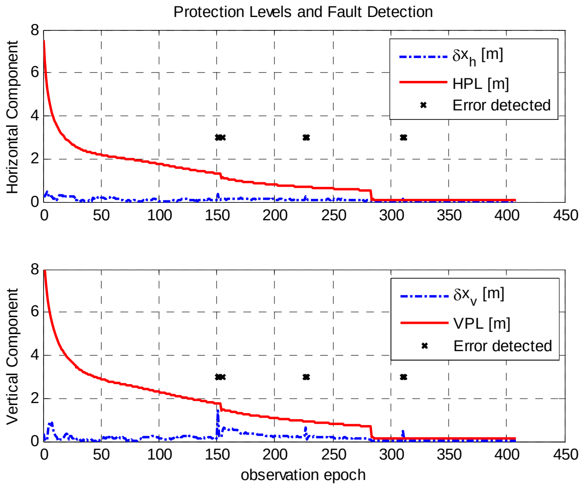

Figure 7.12: Excess of the protection level due to incorrect process noise settings

In Figure 7.12 it is shown that the vertical component of the position estimation error exceeds the VPL one time. However, this does not mean that the integrity risk requirement is violated. It is ensured by the implemented fault detection algorithms that any excess of the protection levels is detected properly (within the specified probability of missed detection). The epochs where (unspecified) overall model invalidations are detected are marked by black crosses. In this example more faults are detected than there are violations of the VPL and HPL. The protection levels have been enlarged by applying sigma-overbounding. The presence of smaller errors can still be detected, but their detection is less probable than required by the integrity risk. Furthermore, also the excess of the velocity protection levels is detected by the unspecific fault detection algorithms as shown in Figure 7.15. Thus, the black crosses displayed in the figures refer to the first step of AFDIA, e.g. to the detection of overall model invalidations and not to the identification of the error source. Although the integrity of the position solution is not violated by reducing S_p, the continuity is endangered by misspecifying the variances of the dynamic model. Errors due to incorrect setting of process noise variances cannot be compensated by the proposed AFDIA scheme, because so far it is assumed that model invalidations are due to anomalous measurement data.

Next, it is investigated what happens if there is no confidence in the dynamic model. High process noise variances are assigned to the position and velocity states if S_p is set to a very large value. Hereafter, a pessimistic assumption is made with respect to the spectral amplitude of the random walk, e.g. $S_p = 50\frac{m^2}{s^2}\frac{rad}{s}$.

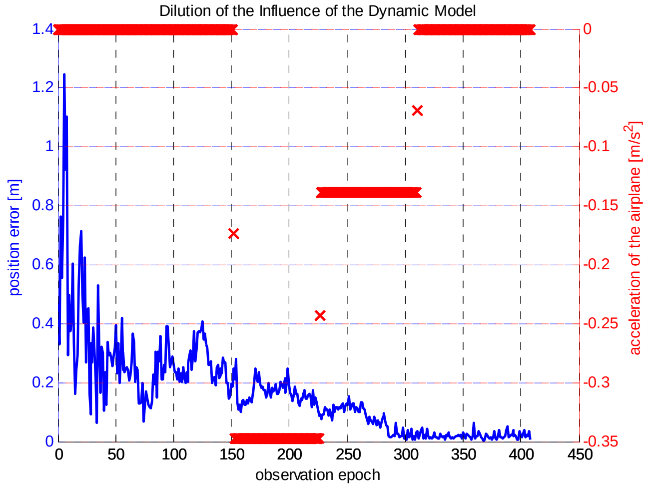

Figure 7.13: High process noise variances alleviate the effects of unmodeled accelerations

When comparing Figure 7.11 with Figure 7.13, it becomes obvious that the navigation filter performs better if high variances for the position and velocity process noise were chosen instead of too low variances. Only during the first few epochs after starting the filter the resulting position estimation errors are slightly smaller if S_p was set to $0.01\frac{m^2}{s^2}\frac{rad}{s}$ instead of $50\frac{m^2}{s^2}\frac{rad}{s}$.

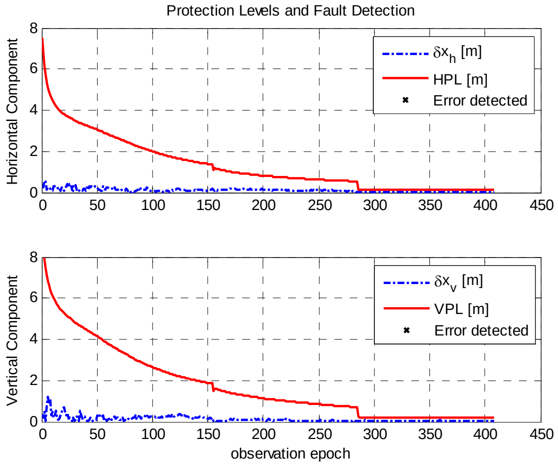

Figure 7.14: Good filter performance despite of a weak dynamic model

The protection levels are hardly influenced by the concrete value of S_p. Therefore, it is suggested to choose the variances of process noise rather pessimistic than too optimistic. It is also illustrated in Figure 7.15 with respect to the velocity estimates that there is no benefit of setting the variances of process noise too tight. During the phases of flight with constant velocity the velocity estimate errors are almost identical for different spectral amplitudes S_p. Whenever the acceleration of the airplane changes between two successive epochs, the velocity protection levels are exceeded if S_p was set to $0.01 \frac{m^2}{s^2} \frac{rad}{s}$ and the fault detection algorithm raises an alarm. An alarm is still raised if S_p was set to $1 \frac{m^2}{s^2} \frac{rad}{s}$, although the position and velocity estimation errors are only slightly increased and do not yet exceed the protection levels when the acceleration changes. These investigations refer to the availability of good satellite geometry. It will be discussed later in this work how the impact of S_p on the protection levels changes if the satellite geometry was poor.

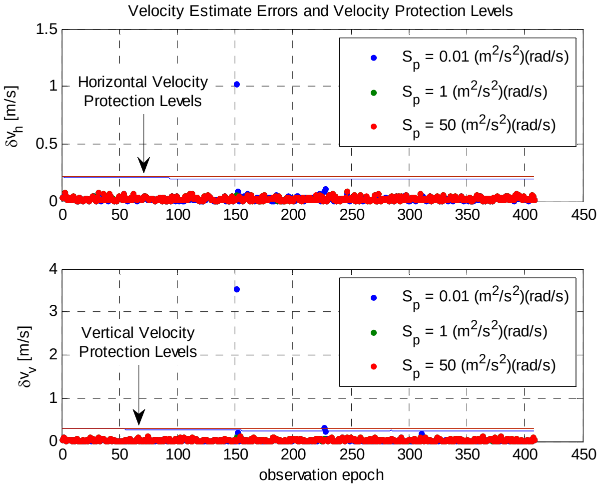

Figure 7.15: Dependency of the user velocity accuracy on the variances of process noise

According to [29], the 95th percentiles of the horizontal velocity error are $0.08\frac{m}{s}$ for constant velocity scenarios if the velocity estimates were based on pseudorange rates. The user velocity estimates derived from this navigation filter are vaguely less accurate, since double-differenced Doppler shift measurements are used to determine the velocity. Measurement noise amplification due to double-differencing contributes to enhanced noise of the velocity estimates.

Next, it is discussed why in this example almost the same results are obtained for $S_p = 1\frac{m^2}{s^2}\frac{rad}{s}$ and $S_p = 50\frac{m^2}{s^2}\frac{rad}{s}$. Therefore, the a priori and the posteriori covariance matrix of state estimation uncertainties $P_k(-)$ and $P_k(+)$ are examined with respect to the user position and velocity states. It holds that the predicted state estimates for the next observation epoch are less (or at best equally) precise than the filtered state estimates of the current observation epoch:

$$P_{k+1}(-) \geq P_k(+) \tag{7.8}$$

Furthermore, the Kalman gain is optimized such that the posteriori state estimates are more (or at worst equally) precise than the a priori state estimates:

$$P_k(-) \geq P_k(+) \tag{7.9}$$

As shown in Figure 7.16 and in Figure 7.17, the deviation of the variances of the predicted state estimates from the variances of the posteriori filtered state estimates depends on the magnitude of process noise. The actual parameters of interest when evaluating the filter performance are the variances of the posteriori filtered state estimates. They are represented by green bars in Figure 7.16 and Figure 7.17. One can see that a low value of the spectral amplitude of the random walk process S_p does hardly reduce the posteriori state estimation uncertainty. The variances of the position estimation uncertainty, which are depicted in the following figure, are computed from the first three main diagonal terms of the covariance matrices of state estimation uncertainty:

$$\sigma_{pos}^2 = P_{(1,1)} + P_{(2,2)} + P_{(3,3)} \tag{7.10}$$

In analogy, the variances of the velocity estimation uncertainty follow from:

$$\sigma_{vel}^2 = P_{(4,4)} + P_{(5,5)} + P_{(6,6)} \tag{7.11}$$

Consequently, the variances are not subdivided into a horizontal and vertical component in the following plots.

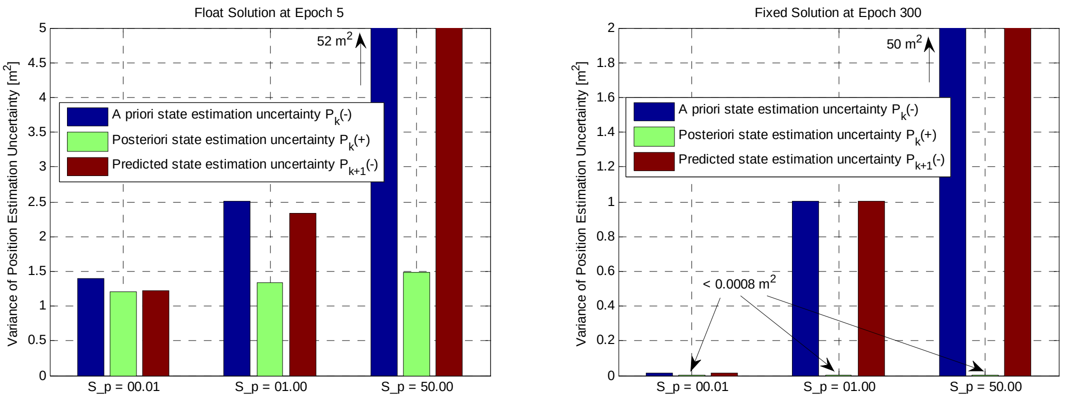

Figure 7.16: Theoretical variances of the position estimation uncertainties in dependence of the spectral amplitude of the random walk process

As soon as the carrier phase ambiguities are fixed, the dynamic state space model does hardly have any impact on the position estimates. Only if the measurement standard deviations in R were very high or the satellite geometry was very poor, the state space model would effectively contribute to the accuracy of the state estimates. As long as the uncertainty of the a priori state estimates is far above the uncertainty of the posteriori state estimates, it can be concluded that the filtered state estimates mainly depend on the measurement input data from the current observation epoch. It is essential for the filter performance that the variances of process noise are not set to lower values than the actual physical variances, whereas in this concrete simulation scenario it is rather uncritical if the variances of process noise were set to significantly larger values. To conclude, the accuracy of the position estimates is here determined by the quality of the GNSS measurements rather than the accuracy of the dynamic state space model.

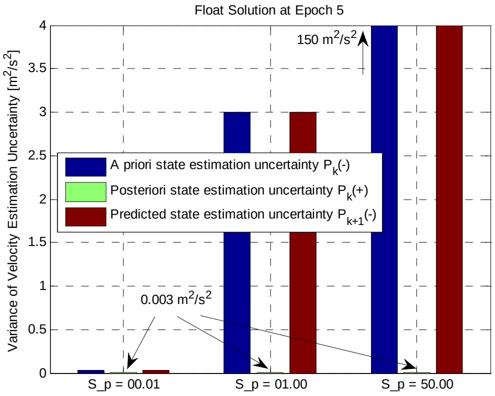

Figure 7.17: Theoretical variances of the velocity estimation uncertainties in dependence of the spectral amplitude of the random walk process

The theoretical variances of the velocity estimation uncertainties are hardly influenced by ambiguity fixing, since the velocity estimates depend mainly on the double-differenced Doppler shift measurements. Therefore, the theoretical variances of the velocity estimation uncertainties are more or less the same for observation epoch 5 and observation epoch 300. Since the filter performance results are quite good if the variances of process noise are set to high values, it is assumed here that there is no need to introduce a dynamic model that accounts for systematic accelerations. However, if the variances of process noise are set to low values, the model invalidations can be indeed observed as shown in Figure 7.11 and Figure 7.12.

7.2.4 Ionosphere Models and Multipath

So far only the Ionosphere Model 3 according to Sect. 5.3.3 has been considered. Now the three different stochastic models for the ionosphere are compared with one another on the basis of simulation results. The parameters of the different ionosphere models, which can be varied in a sensitivity analysis, are shortly summarized:

- **Model 1** (according to Sect. 5.3.1): Variance of the Vertical Ionospheric Gradient σ^2_{VIG}

- **Model 2** (according to Sect. 5.3.2): Upper limit of the double-differenced ionospheric variance σ_∞^2, first order correlation distance of the double-differenced ionosphere D and first order correlation time of the double-differenced ionosphere T
- **Model 3** (according to Sect. 5.3.3): Single-differenced ionospheric variance $\sigma^2(90°)$ and correlation distance of the differential ionosphere d

One common reference simulation scenario is used hereafter, which is described in Table 7.4.

Table 7.4: Simulation scenario for the evaluation of different ionosphere models

Satellite constellation: GPS, elevation mask angle 5° Signal characteristics: GALILEO E5a and E1					
$\sigma_{\rho E1}(90°)$	$\sigma_{E5a}(90°)$	$\sigma_\Phi(90°)$	$\sigma_D(90°)$	$VTEC_{max}$	$VTEC_{min}$
$18cm$	$5cm$	$0.012cycles$	$0.09Hz$	$3\cdot 10^{18}\frac{el}{m^2}$	$1\cdot 10^{18}\frac{el}{m^2}$

First, multipath is not simulated and the residual double-differenced tropospheric range error will not be considered. Since GALILEO signals are used, the pseudorange measurements are low-noisy in absence of multipath. The simulated measurement data after double-differencing is displayed in Figure 7.18 as a function of the baseline length between the reference receiver and the user receiver.

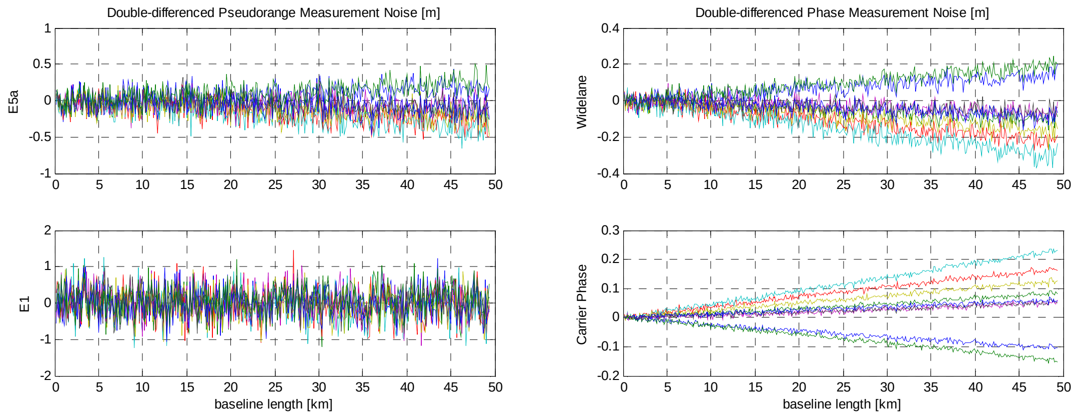

Figure 7.18: Measurement noise after double-differencing (excluding multipath)

The absence of multipath is also reflected by the covariance matrix of measurement noise R. On the other hand, the VTEC values which are used to simulate the ionospheric range errors correspond to high ionospheric activity. In this normal operation performance test the ionosphere model parameters are set as follows:

Model 1: $\sigma_{VIG}^2 = \left(2\frac{mm}{km}\right)^2$

Model 2: $\sigma_\infty^2 = 2m^2$, $D = 1500km$ (or $D = 500km$), $T = 64min$

Model 3: $\sigma^2(90°) = (3cm)^2$, $d = 300km$

The Ionosphere Model 1 is examined first. From Figure 7.19 follows that the protection levels decrease with the decrease of the baseline length. A widelane ambiguity-fixed solution is already available when the airplane is still 34 km away from the reference station, and after further 10 km also the carrier phase ambiguities are fixed. The protection levels for the carrier phase ambiguity-fixed solution are at the order of 10 cm, which seems justified when comparing the protection levels with the small position estimation errors. However, the position accuracy is only that good because tropospheric errors and multipath errors are neglected. After starting the navigation filter, it takes some epochs until the estimation of the VIGs stabilizes.

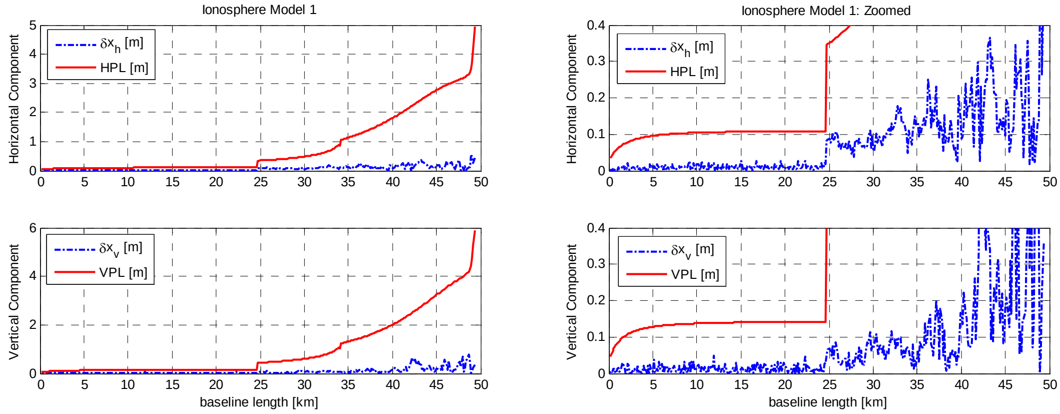

Figure 7.19: Ionosphere Model 1 - position estimation errors and protection levels

Unlike the previous example, the protection levels which are obtained when using the Ionosphere Model 2 do not vary significantly with the change of the baseline length. As described in Sect. 5.3.2, pseudo-measurements for the double-differenced residual ionospheric range error are introduced when using this ionosphere model. The pseudo-measurements equal zero. The filter does not succeed in estimating the double-differenced ionospheric range errors due to the introduction of pseudo-measurements. However, it is still better to use the 2nd ionosphere model than neglecting the residual ionospheric range errors completely. At least it is reflected to some degree that the residual ionospheric range errors are not negligible and cannot be characterized by white Gaussian noise.

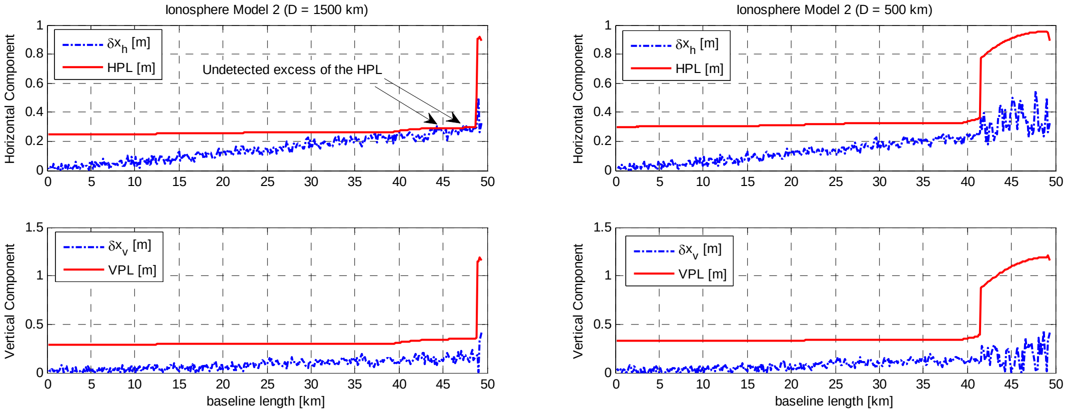

Figure 7.20: Performance of Ionosphere Model 2 in dependency of the correlation distance *D*

If the first order correlation distance is set to $D = 1500km$, the HPL is exceeded two times without being detected by the overall model validation. The widelane ambiguities are fixed correctly short after starting the filter. The resulting protection levels for the widelane ambiguity-fixed solution are too low because the standard deviations of the ionospheric pseudo-measurements are lower than the standard deviations of process noise which refer to the double-differenced ionospheric range errors. Consequently, the computed protection levels reflect that the stochastic model suggests the absence of large ionosphere errors. If there is high ionospheric activity, the protection levels will be exceeded due to the presence of large residual ionospheric range errors which are not estimated properly. The excess cannot be detected by AFDIA, because the filter is provided with pseudo-measurements and pseudo-measurement variances of the ionosphere which do not reflect the actual environmental parameters. The filter estimates of the double-differenced ionospheric range errors on E1 are confronted with the actual ionospheric range errors in Figure 7.21.

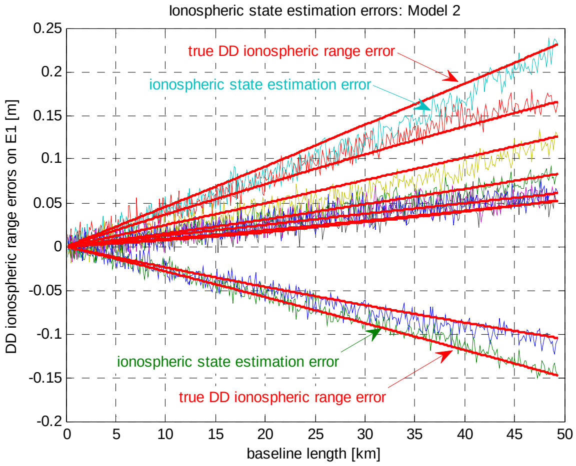

Figure 7.21: Bad performance of the double-differenced ionospheric range error estimation with Ionosphere Model 2

The setting of the stochastic double-differenced ionosphere parameters according to [11] seems to be too optimistic given that there is high ionospheric activity. In a second simulation run the first order correlation distance is reduced to $D = 500km$. The effect of reducing the correlation distance is that it takes longer to fix the widelane ambiguities. The position estimation errors do no longer exceed the protection levels. Though, the problem that the ionospheric states are not estimated adequately due to the pseudo-measurements is not yet solved. While the widelane ambiguity-fixed solution is soon available, no carrier phase ambiguity-fixed solution can be derived with this Ionosphere Model for the given simulation scenario. Next it is shown that the filter performance with the Ionosphere Model 2 is still better than assuming that the residual ionospheric range errors were negligible from the very beginning. In Figure 7.22 the results of a simulation run are displayed where only thermal receiver noise has been considered in the stochastic models.

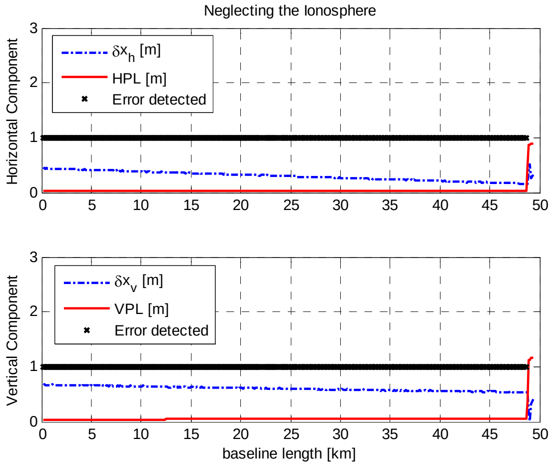

Figure 7.22: Excess of the protection levels when neglecting the residual ionospheric range errors

It is detected that the position estimation errors exceed the protection levels when neglecting the double-differenced ionospheric range errors. The reason why an alarm can be raised here while the excess of the protection levels has not been detected when using the Ionosphere Model 2 is that here the carrier phase ambiguities are fixed wrongly short after starting the filter. This means that not the cause of the model invalidation is detected, e.g. the illegal neglecting of the residual ionospheric range errors, but the effect of the model invalidation, e.g. wrong carrier phase ambiguity fixing. It becomes obvious from the example with the Ionosphere Model 2 and the example where the ionospheric refraction is neglected that any too optimistic view-point on the residual double-differenced ionospheric errors will lead to protection levels that do not effectively bound the position estimation errors.

Finally, the Ionosphere Model 3 is investigated. Just as the Ionosphere Model 1, it does not make use of pseudo-measurements for the unknown ionospheric terms. Therefore, better performance in estimating the unknown double-differenced ionospheric range errors may be expected compared to the usage of Ionosphere Model 2:

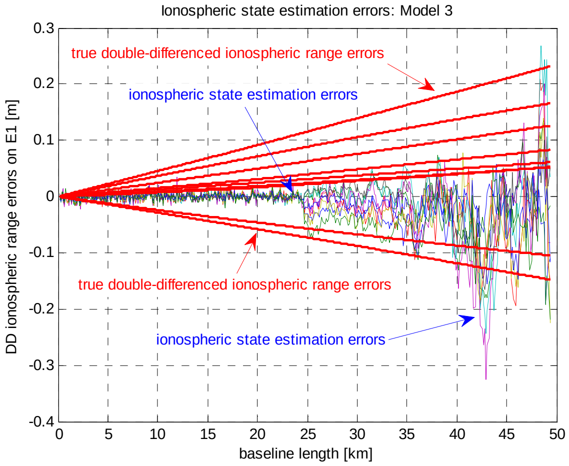

Figure 7.23: Good performance of the double-differenced ionospheric range error estimation with Ionosphere Model 3

It takes some time until the filter estimates of the double-differenced ionospheric range errors stabilize. After initializing the filter, the measurements which are given the most weight in the filter solution are the pseudorange measurements. It is rather difficult to estimate the double-differenced range errors on E1, which are smaller than 30 cm, from noisy double-differenced pseudorange measurements. As a function of time and baseline length, the phase measurements become more and more important for the filter solution and the estimation of the ionosphere errors also improves. As soon as the carrier phase ambiguities are fixed, the residual ionospheric range errors are almost perfectly estimated by the filter. The run of the protection levels as a function of the baseline length when implementing the Ionosphere Model 3 is similar to that of the Ionosphere Model 1. The widelane ambiguities are fixed at a distance of 34 km to the reference station and the carrier phase ambiguities are fixed at a baseline length of 24.5 km.

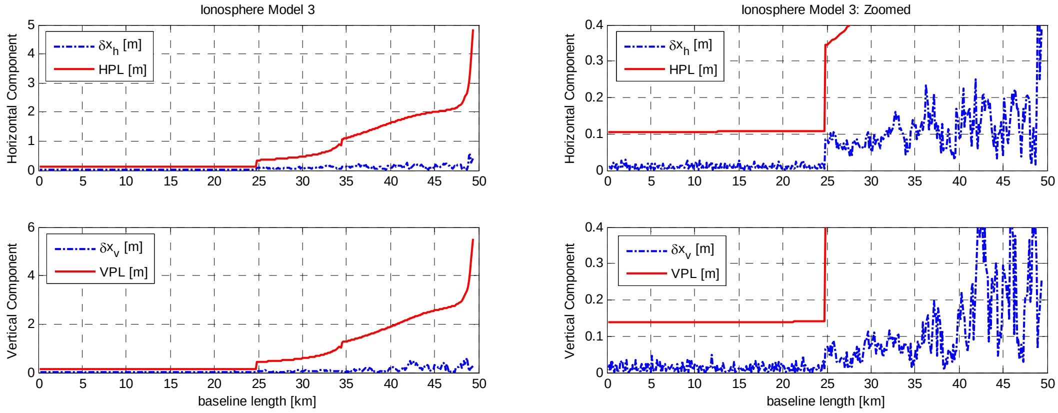

Figure 7.24: Ionosphere Model 3 - position estimation errors and protection levels

In absence of multipath and tropospheric range errors, the VPL of the carrier phase ambiguity-fixed solution is as low as 14 cm. The protection levels do hardly vary after all ambiguities have been fixed. In contrast, if the Ionosphere Model 1 was used, the protection levels of the carrier phase ambiguity-fixed solution continued to decrease for baseline lengths below 5 km. The run of the protection levels for the different ionosphere models is summarized in Figure 7.25. The first order correlation distance D of the Ionosphere Model 2 has been set to 500 km hereafter.

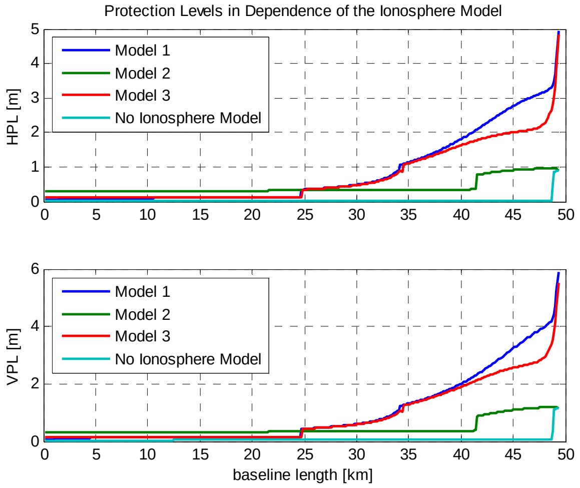

Figure 7.25: Protection levels as a function of the baseline length in dependence of the Ionosphere Model

Apart from the first 10 km after starting the filter, the resulting protection levels for the Ionosphere Model 1 and the Ionosphere Model 3 are almost identical. The results that are obtained when using these two ionosphere models seem reasonable when comparing the position estimation errors with the protection levels. It is assumed that the Ionosphere Model 3 performs slightly better during the first few epochs since the double-differenced ionospheric range error states are better observable than the VIG states when using double-differenced measurement data. If ionospheric refraction is neglected, the carrier phase ambiguities are almost immediately fixed. However, they are fixed to the wrong integer values and the navigation solution has to be declared unavailable since the fault detection algorithm raises an alarm. When using the Ionosphere Model 2, pseudo-measurements of the double-differenced ionospheric range errors are introduced in the measurement model. The widelane ambiguities can be fixed correctly sooner than with one of the other ionosphere models. Though, the introduction of zero-valued pseudo-measurements and low associated measurement variances is risky. For example, if there is a solar storm the excess of the protection levels will not be detected. To conclude, in absence of multipath the usage of either Ionosphere Model 1 or Ionosphere Model 3 is recommended.

It is of special interest to examine the effects of unmodeled non-white error sources on the overall filter performance. Measurement errors due to multipath are not modeled in this filter and the previously presented results were obtained in absence of multipath. Now multipath errors are included in the simulated measurement data, but no separate states for multipath errors are introduced in the filter model. If the presence of severe multipath on all channels is not reflected by increased measurement noise in the covariance matrix R, it is likely that the widelane ambiguities are fixed to the wrong integers. The fault detection algorithm will frequently raise an alarm, but the succeeding fault identification does not provide reliable results because it has to cope with multiple-channel biases instead of single-channel biases. In order to prevent false ambiguity fixing, the pseudorange and carrier phase measurement standard deviations, which are used in order to set up R, have to be increased. Thus, measurement errors due to multipath are treated as white Gaussian noise sources with high variance. The simulated multipath errors are depicted in Figure 7.26, where all receiver channels are affected by multipath to some degree. In the following simulations the standard deviations of measurement noise are increased to $\hat{\sigma}_{\rho E1} = 1m$, $\hat{\sigma}_{\rho E5a} = 70cm$ and $\hat{\sigma}_{\Phi} = 0.0318$ cycles.

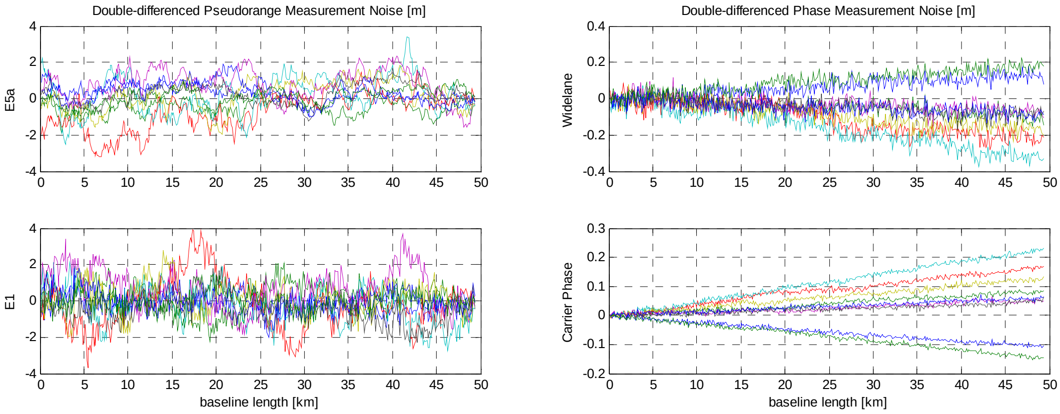

Figure 7.26: Measurement noise after double-differencing in a severe multipath environment

In a multipath environment it turns out that the introduction of pseudo-measurements of the double-differenced ionospheric range errors is quite helpful. In this environment the Ionosphere Model 2 outperforms the Ionosphere Models 1 and 3. Introducing ionospheric pseudo-measurements of low measurement uncertainty in the measurement model has the advantage that unmodeled multipath errors of high amplitudes do not intrude into the process of ionosphere state estimation. Hence the ionosphere estimates do not drift off because of multipath.

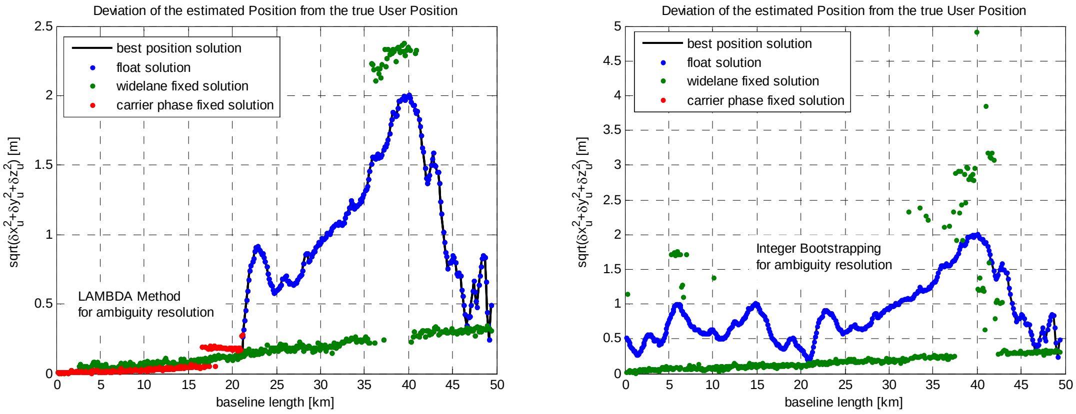

Figure 7.27: Filter performance in a severe multipath environment (Ionosphere Model 2)

On the left side of Figure 7.27 the position estimation errors are shown for the case that the ambiguities are resolved with the LAMBDA method. The integer test and the ratio test are passed and therefore at a distance of 21 km to the reference station a widelane ambiguity-fixed solution is available and the last 2.5 km of the flight even a carrier phase ambiguity-fixed solution is available. The VPL of the float solution starts with 10 m and reduces to 2.2 m after a while. The VPL of the carrier phase ambiguity-fixed solution is only 18 cm. Both the HPL and the VPL are never exceeded although severe multipath is present. However, the exact probability of false integer ambiguity fixing is unknown. On the right side of Figure 7.27 the results are shown when the IB estimator is used for ambiguity resolution. Since the measurement variances are set to very high values, successful ambiguity resolution with $P_F = 1 \cdot 10^{-9}$ is not possible. From the run of the green dots, which represent the widlane ambiguity-fixed solution, one can also see that the integer least-squares estimator of the LAMBDA method performs better than the IB estimator. Although the ambiguities cannot be resolved with the required reliability, the resulting protection levels for the float solution are still below the expected alert limits of a CAT IIIc precision approach.

As stated before, if no pseudo-measurements of the ionosphere terms are used in the measurement model, there is the threat that non-white error sources cause the ionospheric state estimates to drift off. This effect is shown in Figure 7.28, where the presence of severe multipath on multiple channels prevents the convergence of the double-differenced ionospheric range error estimates. In consequence, there is no chance to fix the widelane ambiguities correctly. While ionospheric range errors have the same magnitude for both the code and the carrier phase measurements, multipath errors on the carrier phases are less severe. For this reason it is a great disadvantage if unmodeled multipath errors intrude into the ionosphere state estimation. Then also the carrier phase measurements are severely deteriorated.

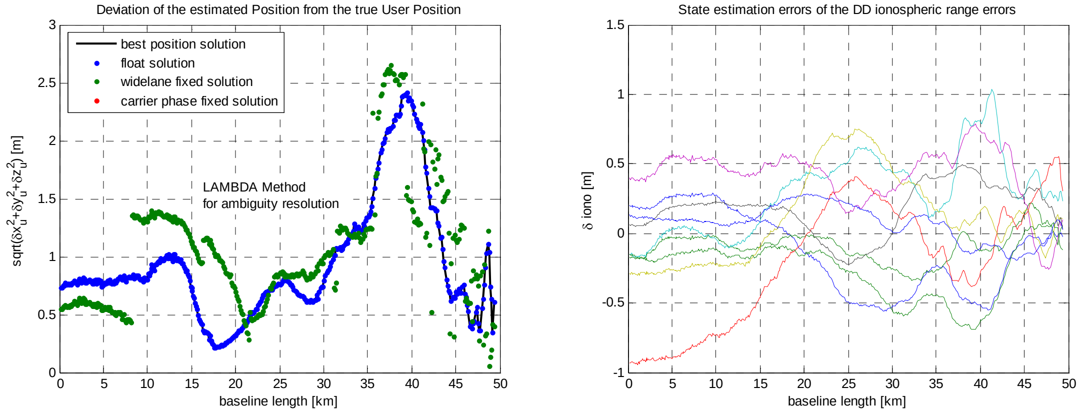

Figure 7.28: Bad performance of the Ionosphere Model 3 in presence of severe multipath

There are several methods in order to reduce the probability that severe multipath deteriorates the measurement quality, for example special care in the design of receive antenna patterns. Since the coordinates of the reference receiver antenna are known in advance, it can be monitored if the reference receiver measurements were biased by severe multipath. Therefore, in the following a more moderate multipath scenario is considered. First, the multipath errors are scaled down. Second, it is no longer assumed that there is multipath on all receiver channels simultaneously. Multipath errors are modeled only for those satellites which are seen below an elevation angle of 30°. In this test this means that measurements from 4 out of 10 satellites are biased, which corresponds to 4 biased double-differenced measurements and 5 unbiased double-differenced measurements. The resulting simulation scenario is expected to be more realistic with respect to multipath errors occurring during a landing approach. Hereafter the standard deviations of measurement noise, which reflect the presence of multipath, are set to $\hat{\sigma}_{\rho E1} = 40cm$, $\hat{\sigma}_{\rho E5a} = 18cm$ and $\hat{\sigma}_{\Phi} = 0.0318$ cycles. The filter performance in dependence of the implemented ionosphere model is investigated once more, but now in presence of biased measurements. In Figure 7.29 the VPLs are displayed as a function of the baseline length for the three different ionosphere models. In addition, the vertical components of the position estimation errors are plotted in order to verify if the position errors are indeed below the protection levels. The IB estimator is used for ambiguity resolution.

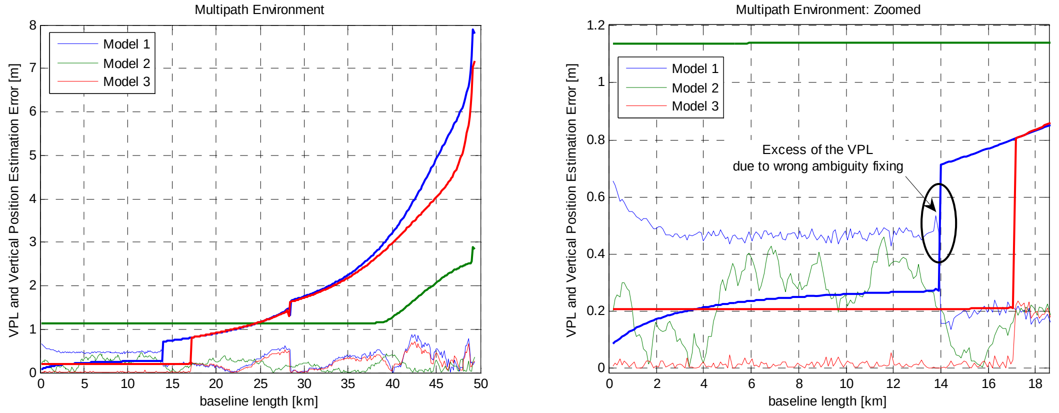

Figure 7.29: Vertical Protection Levels and position estimation errors for different ionosphere models in presence of multipath

No ambiguity-fixed solution is derived when using the Ionosphere Model 2. However, if the LAMBDA method were used for ambiguity resolution instead of IB, both the widelane ambiguities at a baseline length of 48.5 km and the carrier phase ambiguities at a baseline length of 3.4 km could be fixed correctly (see Figure 7.30). Nevertheless, the vertical position component of the float solution estimate error stays below 50 cm all the time even in presence of multipath on 4 receiver channels. The VPL of the float solution is below 1.20 m during the final approach. Filtering and the usage of carrier phase measurements in addition to pseudorange measurements make it possible to achieve such low protection levels for a float solution in a multipath environment.

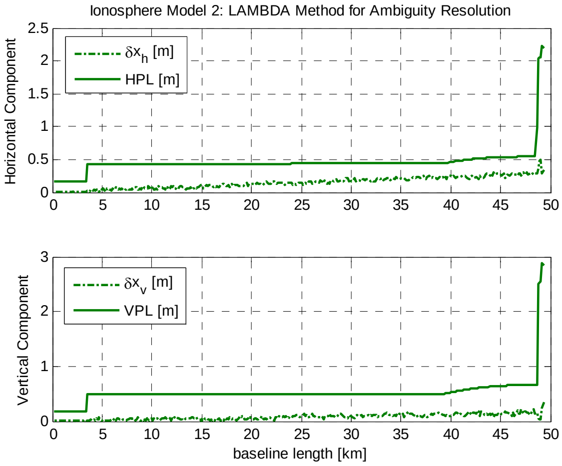

Figure 7.30: Ambiguity resolution with the LAMBDA method in a multipath environment (Ionosphere Model 2)

The best filter performance is observed when the Ionosphere Model 3 is implemented. The widelane ambiguities are fixed 28 km before touchdown and the carrier phase ambiguities are fixed 17 km before touchdown. In presence of biased measurements the VPL of the carrier phase ambiguity-fixed solution is as low as 21 cm.

In a multipath environment it shows clearly that the Ionosphere Model 1 should not be used. The VIGs are not observable within a single epoch and the VIG estimates diverge in presence of measurement biases. As a result also the user position estimates start to diverge short before landing (see Figure 7.31). Furthermore, the integer ambiguities are fixed wrongly since the covariance matrix of state estimation uncertainty is corrupted by the non-white measurement biases. The divergence of the state estimates during the last few epochs before landing is detected by the fault detection algorithm. However, the excess of the VPL due to wrong ambiguity fixing is not detected immediately. Single-differenced measurements between receivers should be used if the VIGs were to be estimated by the filter, since the problem of bad observability of the VIGs can be overcome when using single-difference measurements. Note that the actual probability of false ambiguity fixing does not correspond to the theoretical probability of false ambiguity fixing $P_F = 1 \cdot 10^{-9}$. In presence of unmodeled biases the actual probability of false ambiguity fixing is higher than $1 \cdot 10^{-9}$. Not only multipath errors are unmodeled biases, but also measurement offsets due to strong interfering signals at nearby carrier frequencies.

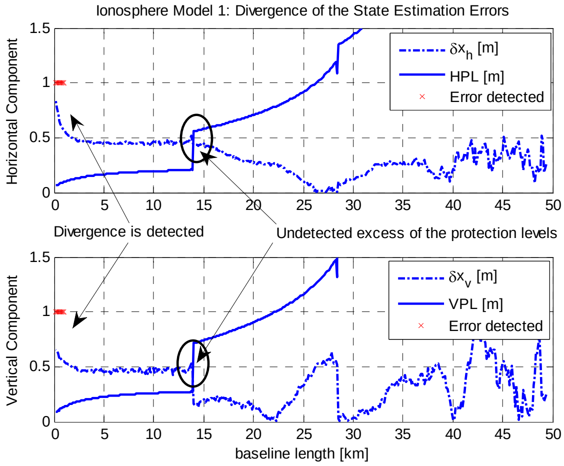

Figure 7.31: Divergence of the position estimates in presence of biases due to bad observability of the VIGs

Finally, the information provided by the innovation vector is investigated. The results presented hereafter refer to the usage of the Ionosphere Model 3. Range errors due to multipath can be observed in the low-noise innovations computed from the pseudorange measurements on E5a as shown in Figure 7.32. After the widelane ambiguities have been fixed the position solution depends mainly on the phase measurements, which are less affected by multipath range errors. Therefore the presence of multipath can be detected in the E5a innovations after ambiguity fixing. Besides the measurement biases also abrupt changes of the airplane's dynamics can be observed in the pseudorange innovations. The innovations of the first epoch directly after starting the filter are not completely displayed in the figures since their magnitude is far larger than the innovations during all following epochs.

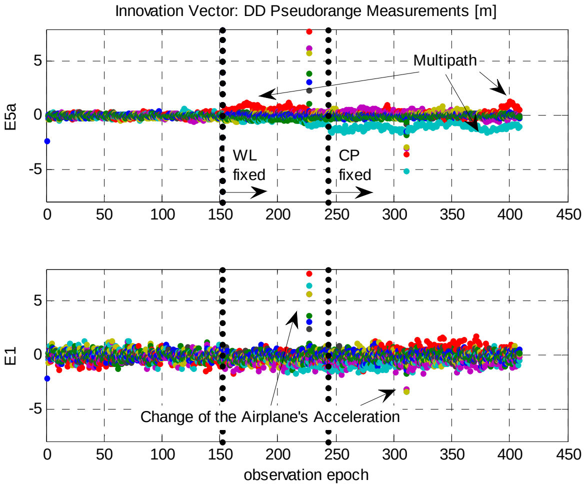

Figure 7.32: Pseudorange measurement innovations (Ionosphere Model 3)

The innovations of the widelane and carrier phase measurements are illustrated in Figure 7.33. Besides the change of the airplane's acceleration between two succeeding epochs also the phases of flight with non-constant velocity are observable in the phase measurement innovations. The widelane and the carrier phase innovations are far less influenced by multipath than the pseudorange innovations.

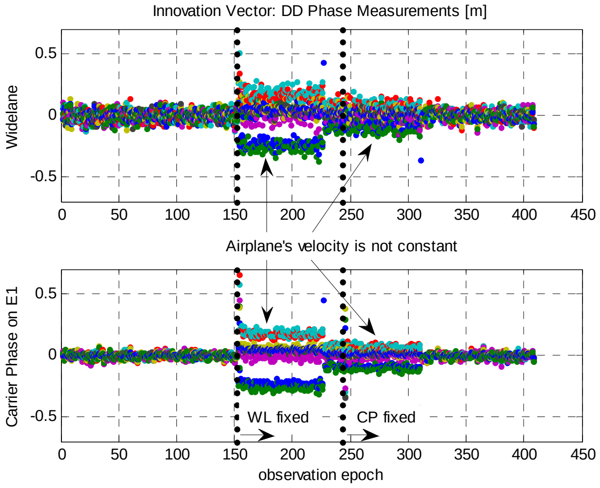

Figure 7.33: Phase measurement innovations (Ionosphere Model 3)

7.2.5 Performance of the Ionosphere-free Code-Carrier Combination

The simulation runs of the previous chapter are repeated, but this time with the ionosphere-free, geometry-preserving measurement combinations as derived in Sect. 3.4.2. In consequence, no ionosphere model has to be implemented and the ionosphere states are removed from the EKF state estimation vector. According to [16] the reliability of ambiguity resolution is improved by maximizing the ratio between the wavelength and the standard deviation of the mixed code-carrier linear combination. The double-differenced pseudorange measurements on E1 and E5a are replaced by the double-differenced ionosphere-free code-only combination $\nabla\Delta\underline{\rho}_{IF,code-only}$, where the coefficients of the linear combination follow from Eq. (3.30). Furthermore, the double-differenced widelane and carrier phase measurements are replaced by a double-differenced ionosphere-free code-carrier combination $\nabla\Delta\underline{\phi}_{IF,code-carrier}$, which is computed from Eq. (3.26). The coefficients of the linear combination with a wavelength of 2.968 m are indicated in Table 3.1. Consequently, the new measurement vector, which is forwarded to the navigation filter, reads:

$$\underline{z}_k = \begin{bmatrix} \nabla\Delta\underline{\rho}_{IF,code-only} & \nabla\Delta\underline{\phi}_{IF,code-carrier} & \nabla\Delta\underline{D}_2 \end{bmatrix}_k^T \tag{7.12}$$

If the ordering of the single measurements in the measurement vector is $\nabla\Delta\underline{\rho}_{E5a}$, $\nabla\Delta\underline{\rho}_{E1}$, $\nabla\Delta\underline{\Phi}_{E5a}$ and $\nabla\Delta\underline{\Phi}_{E1}$, then the generator matrix L of the ionosphere-free combinations is given by:

$$L = \begin{bmatrix} a_{2,code-only} \cdot I & a_{1,code-only} \cdot I & 0 & 0 \\ a_2 \cdot I & 0 & \alpha_2 \cdot I & \alpha_1 \cdot I \end{bmatrix} \tag{7.13}$$

The generator matrix L is also used for variance-covariance error propagation due to the inter-frequency combinations. If there are n satellites in view, then the size of the identity matrices I and the zero-matrices 0 is $(n-1)x(n-1)$.

First, no multipath is simulated. The measurement noise is also rather low, see Table 7.4, due to the usage of the expected GALILEO signal characteristics.

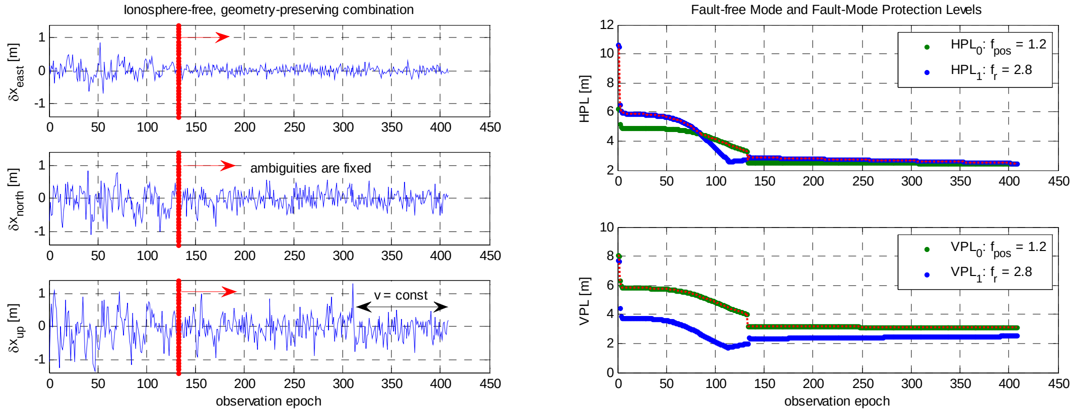

Figure 7.34: Performance of the ionosphere-free code-carrier combination in absence of multipath

On the left side of Figure 7.34 it shows clearly with respect to the up-component of the position estimation error that the accuracy of the ambiguity-fixed solution becomes only better in absence of systematic accelerations. The high noise of the ambiguity-fixed position solution is explained by the comparably high standard deviation of the double-differenced code-carrier combination, which is here $\sigma_{\nabla\Delta\phi,IF,code-carrier} = 42.5cm$. On the right side of Figure 7.34 the corresponding protection levels are shown. The overall protection levels, which are illustrated by red-dotted lines, result from the maximum of the fault-free and the fault mode protection levels. Reliable fixing of the ambiguities of the ionosphere-free code-carrier combination is possible at a baseline length of 31 km. The HPL of the ambiguity-fixed code-carrier combination starts with 3 m directly after ambiguity fixing and goes back to 2.5 m at the end of the approach. The results for the VPL are only slightly different: it starts with 3.2 m and goes back to 3.12 m. A great benefit of the ionosphere-free combinations is that there is no restriction to short baselines due to the spatial decorrelation of the ionospheric errors, which are cancelled here completely (at least the terms up to the 1st order). The run of the fault-free mode protection levels, which is illustrated by the green lines, is as expected. The VPL_0 is always larger than the HPL_0, which is explained by better values of the HDOP than the VDOP. The fault-free mode protection levels decrease as soon as the ambiguities of the code-carrier combination are fixed. For better comprehension of the run of the fault-mode protection levels, the SLOPEs are plotted in Figure 7.35.

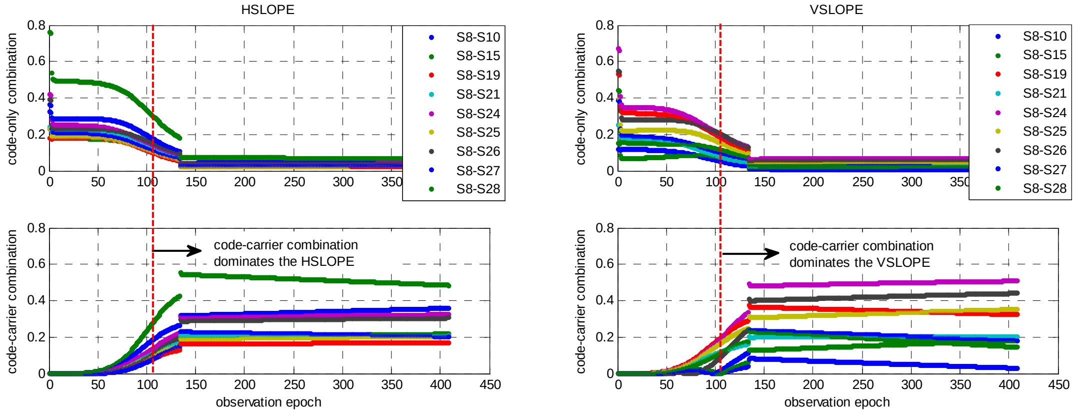

Figure 7.35: SLOPE factors for the computation of the fault-mode protection levels (left: HSLOPE, right: VSLOPE)

The SLOPE factors are computed from the Kalman gain matrix K according to Eq. (6.67) and Eq. (6.68). It shows that the maximum HSLOPE is larger than the maximum VSLOPE. From the GPS sky-plot, which is depicted in the left side of Figure 7.6, follows that the satellite with SVID 28 is decisive for the HDOP. On the other hand, there is no severely outstanding satellite with respect to the VDOP. Consequently, the fault mode protection level for the horizontal component is worse than that of the vertical component. Starting from approximately observation epoch 110 the SLOPE-factors of the code-carrier combination are already larger than the SLOPE-factors of the code-only combination, although the ambiguities of the code-carrier combination are not fixed before observation epoch 132. This is also reflected by the run of the fault-mode protection levels.

Now the performance is investigated in a multipath environment. Just as in the performance tests of the different ionosphere models in presence of multipath, only for those satellites multipath errors are simulated which are seen below an elevation angle of 30°. The standard deviations of measurement noise are adapted to the multipath environment and set to $\hat{\sigma}_{\rho E1} = 40cm$, $\hat{\sigma}_{\rho E5a} = 18cm$ and $\hat{\sigma}_{\Phi} = 0.0318$ cycles. As a result, the computed protection levels increase.

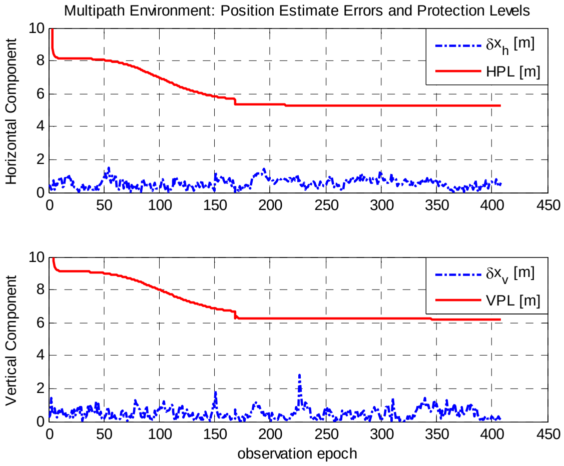

Figure 7.36: Performance of the ionosphere-free code-carrier combination in presence of multipath

The ambiguities of the code-carrier combination are fixed successfully in observation epoch 169. However, the accuracy of the position estimates in presence of multipath does not improve. Filtering reduces already the noise of the ionosphere-free code-only combination significantly. As the ambiguity-fixed solution is not only based on carrier-phase measurements but on a code-carrier combination, multipath errors still have strong impact on the accuracy of the position solution. If the vertical alert limit were 5.3 m, the navigation system would always be declared unavailable because the VPL is still 6.2 m at the end of the approach. When plotting the innovations of the code-only and the code-carrier combination (see Figure 7.37), it becomes obvious that the velocity of the airplane is no longer constant starting from observation epoch 150. In addition, the simulated multipath errors are also larger during the second half of the considered maneuver time. This also explains why the ambiguity-fixed solution is not more precise than shown in Figure 7.36. Since the measurement noise of the ionosphere-free code-carrier combination is far higher than that of a widelane or carrier phase measurement, the availability of a precise dynamic state space model of the precision approach would be advantageous. In contrast, if the solution is based on low-noise carrier phase measurements, the state space model is hardly decisive for the final position accuracy.

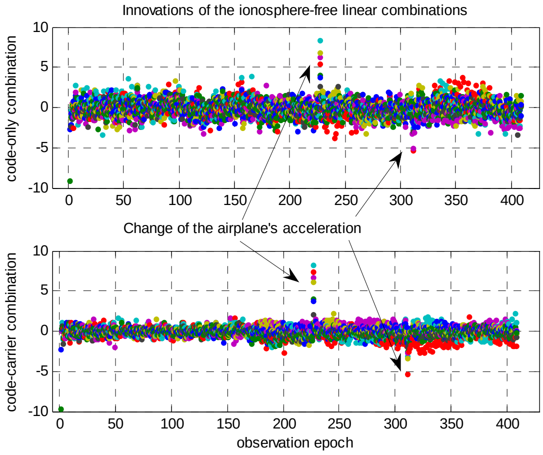

Figure 7.37: Innovations of the ionosphere-free linear combinations in presence of multipath

It is recommended that no double-differenced observations should be used when ionosphere-free linear combinations of measurements are considered. The measurement noise is already enhanced by the inter-frequency combinations of measurements, and double-differencing causes additional amplification of the measurement noise. Therefore, single-differenced or even non-differenced measurements should be used. It is expected that this navigation filter works better if the pure carrier phase measurements are forwarded to the EKF and if the ionospheric nuisance parameters are estimated explicitly. But if no double-differencing were applied, it is likely that the VPL of the ionosphere-free code-carrier combination would stay below 5.3 m even in presence of multipath. There are two further options to reduce the noise of the position solution derived from the ionosphere-free code-carrier combination. The first option is to model accelerations in the state space model systematically by adding three additional states for the user acceleration. Then the process noise can be reduced and the dynamic system model will efficiently contribute to a reduced noise position solution. The second option is to introduce an ionosphere-free carrier-only combination for the purpose of smoothing. The following ionosphere-free carrier-only combination is suggested [37]:

$$\Phi_{IF,carrier-only} = 154 \cdot \Phi_{E1|L1} - 115 \cdot \Phi_{E5a|L5} \tag{7.14}$$

The wavelength of this combination is only $\lambda_{IF,carrier-only} = 2.8mm$ and therefore the integer ambiguities of this combination should not be resolved, but $\Phi_{IF,carrier-only}$ can be used as additional filter input for smoothing. The noise of this carrier-only combination in the range domain is only $\sigma_{\Phi,IF,carrier-only} = 0.012 \cdot \sqrt{154^2 + 115^2} \cdot 0.0028m = 6.5mm$ with $\sigma_{\Phi}(90°) = 0.012$cycles. Furthermore, the carrier-only combination is less affected by multipath than the code-carrier combination. This concept of smoothing is considered as a promising extension of the current ionosphere-free approach.

7.2.6 Cycle Slip and Outlier Detection and Correction

In the previous chapter only the detection of failures has been considered, but not the identification of the error sources. The proposed AFDIA scheme cannot cope with multiple biases simultaneously. Therefore multiple channels which are biased by multipath simultaneously cannot be identified. In the following the occurrence of measurement biases is restricted to one bias at a time. First, it is investigated if the AFDIA scheme can identify an outlier in the pseudorange measurements properly. For this purpose severe multipath on a single channel is simulated on E5a. The measurement standard deviations, which are used in order to set up the covariance matrix R, do not reflect the presence of a bias. Thus the weight factor for the biased measurement is the same as the weight factors for the unbiased measurements directly after starting the filter. The benefit from enabling the filter-based fault identification and model adaptation is shown in Figure 7.38. The biased double-differenced pseudorange measurement on E5a causes position estimation errors up to 0.9 m. Since the covariance matrix R does not indicate that there is a biased measurement within the data set, the computed protection levels will be low. The presence of anomalous measurement data is detected properly by the algorithm for the overall model validation and the error source is identified correctly with the required level of confidence. By adapting the model after successful fault identification the maximum position estimation error stays below 0.5 m. The widelane ambiguities are fixed in observation epoch 84. If AFDIA is enabled, the widelane ambiguities are fixed correctly. Without AFDIA one widelane integer ambiguity is fixed wrongly by one cycle. The horizontal and vertical component of the position estimation error stay always below the computed protection levels if AFDIA is enabled, while otherwise the computed protection levels are exceed (eventually without raising an alarm).

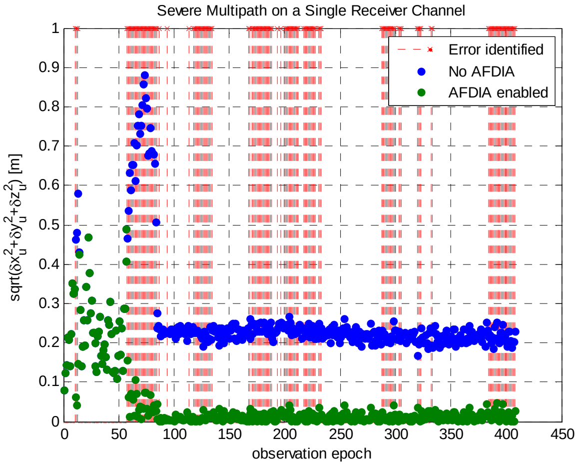

Figure 7.38: Improvement of the user position estimates by error identification and model adaptation

The measurement residual vectors after adapting the model are shown in Figure 7.39. For this example of multipath detection on a single channel the Ionosphere Model 3 has been used in the simulations. The measurement residuals on E5a which are plotted in red refer to the biased double-differenced measurements. Starting from observation epoch 60 the anomalous measurement data on E5a is detected frequently. By enabling AFDIA the magnitude of the single-channel bias is estimated properly and the navigation solution is corrected with the help of this estimated bias. In observation epoch 84 the widelane ambiguity-fixed position solution is available. Since there is multipath on one of the pseudorange measurements on E5a, there is also multipath on one of the carrier phase measurements on E5a. The multipath error on the carrier phase measurement is far less severe and is therefore not detected. From the carrier phase measurement residuals on E1 one can infer that the model adaptation performs quite well. The measurement residuals should be all white Gaussian noise since the E1 carrier phase measurements are unbiased. Only the residuals from that satellite whose E5a measurements are biased jitter slightly. It is assumed that it is more difficult to detect creeping multipath over several epochs than a pseudorange outlier that occurs only once. Here it has been demonstrated that the model adaptation works fine over several observation epochs without having to exclude the satellite from the navigation solution.

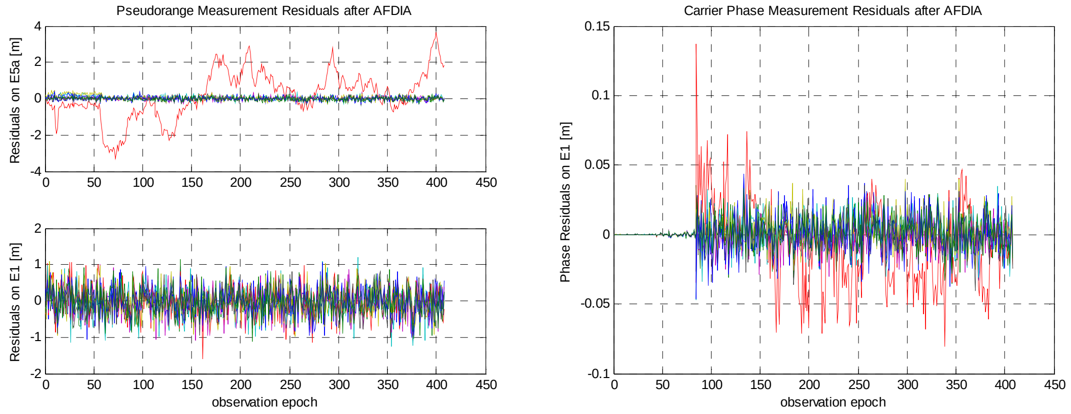

Figure 7.39: Double-differenced measurement residuals after model adaptation

A second error source which has to be considered in carrier phase-based positioning is the occurrence of cycle slips. In order to keep the high accuracy of the ambiguity-fixed position solution, cycle slips have to be detected and the integer ambiguities have to be adapted. Cycle slips can be detected with the proposed AFDIA scheme as long as only one cycle slip occurs at a time. The simulated measurement noise is increased to $\sigma_{\rho E1}(90°) = 24cm$ and $\sigma_{\rho E5a}(90°) = 8cm$ and no multipath is simulated. In the following simulation run a series of cycle slips on E1 and E5a is generated.

Table 7.5: Simulation of cycle slips

Carrier Frequency	**E5a**		**E1**	
Observation Epoch	60	280	200	350
Satellite SVID	28	24	15	24
# Cycles	10	5	3	1

A cycle slip on the E5a carrier phase measurement has only an impact on the double-differenced widelane measurement. In contrast, a cycle slip on E1 impacts both the double-differenced widelane measurement and the double-differenced E1 carrier phase measurement. The procedure which is applied here to deal with cycle slips does not require distinguishing between cycle slips on E5a or E1. The cycle slip recovery is only sensitive with respect to the satellite ID. Both the widelane and the carrier phase ambiguities which correspond to this satellite are reset to float ambiguities. In Figure 7.40 it is demonstrated that all simulated cycle slips are detected immediately in the respective observation epoch and that the SVID is identified correctly. The cycle slips on E1 are either detected in the E1 phase measurements (right side of Figure 7.40) or in the widelane measurements (left side of Figure 7.40). As mentioned before, the distinction between cycle slips on E5a and E1 is not essential for the succeeding recovery procedure. Even the cycle slip by only one cycle is detected correctly in the widelane measurements at observation epoch 350.

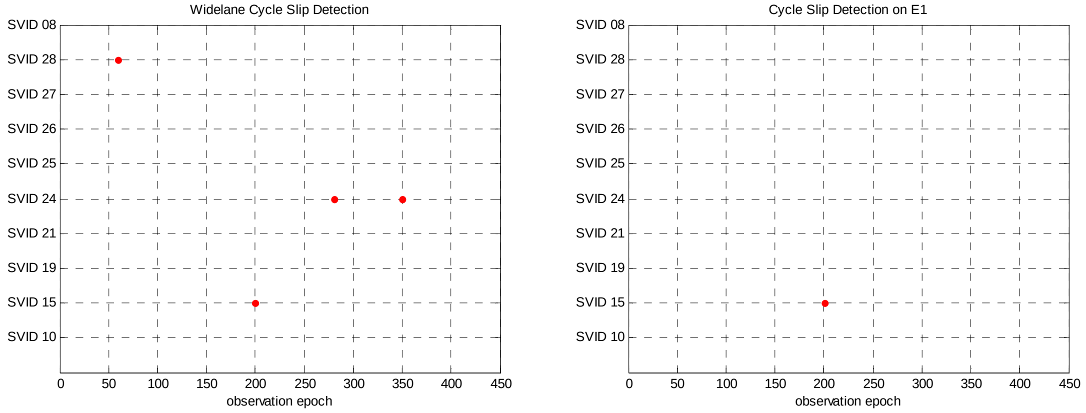

Figure 7.40: Detection and identification of cycle slips

Appropriate manipulation of the covariance matrices ensures that the float ambiguities can be re-fixed quickly without any significant loss of the position estimate accuracy while the float ambiguities are not yet re-fixed. In Figure 7.41 it is shown that the quality of the best solution which is currently available remains unaffected by cycle slips, while the ambiguity-fixed solution may jump. The track of the best solution is indicated by the black line, which does not follow the jumps of the ambiguity-fixed solution if a cycle slip occurs.

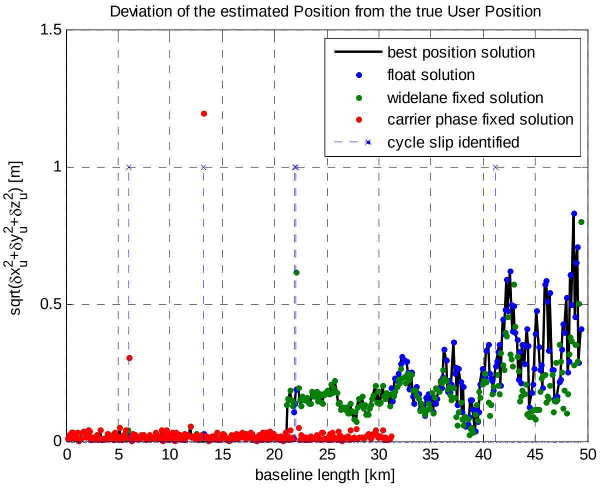

Figure 7.41: Performance of AFDIA in presence of cycle slips on E5a and E1

The widelane ambiguities are re-fixed within the next three epochs and the carrier phase ambiguities are re-fixed within the next eight epochs after a cycle slip has been detected. The accuracy of the interim float solution is not worse than the accuracy of the ambiguity-fixed solution. This seems reasonable as long as only one cycle slip occurs at a time. The HPL of the carrier phase ambiguity-fixed solution is 15 cm and the VPL is 20 cm. If a cycle slip is detected, the protection levels increase only marginally by 2 cm. Thus, the availability of the navigation system due to cycle slips is not endangered. If AFDIA was disabled, the position estimation errors would increase significantly as shown in Figure 7.42.

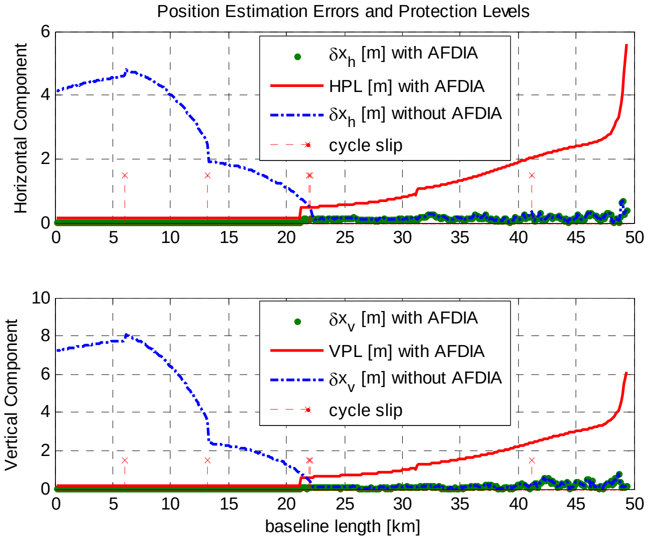

Figure 7.42: Protection levels in presence of cycle slips on E5a and E1

Cycle slips on the reference satellite measurements influence all double-differenced carrier phase measurements simultaneously. This event can be identified by AFDIA, but so far no advanced recovery scheme for reference satellite failures is foreseen. The most comfortable solution would be to switch to a second filter which is running in parallel to the first filter, but uses a different reference satellite. In this chapter good performance of AFDIA in presence of single-channel biases could be verified. If multiple channel biases shall be covered, further extensions of the fault identification and model adaption algorithms are required. Also the computation of the protection levels would have to be adapted, since presently it is assumed that there is only one bias at a time. The simulation results presented so far refer to the usage of simulated measurement data. The next step in order to validate the navigation filter performance is to use real receiver measurements. This allows crosschecking the results obtained from Monte-Carlo simulations. The results of the real signal tests are presented in Sect. 8.

8 Real-Signal Tests

8.1 Signal Generator and GALILEO Receiver

The GALILEO E1 and E5a navigation signals used in the real-signal tests are provided by a full constellation hardware simulator. The wavefront simulator is composed of two integrated GSS 7790 racks from Spirent. The GPS/GALILEO test rack, which is depicted in Figure 8.1, is integrated with digital signal processing components developed by DLR.

Figure 8.1: Multi-Output GPS/GALILEO Wavefront Simulator

The integrated GPS/GALILEO test rack allows for simultaneous generation of GALILEO and GPS signals on multiple frequencies. For the real-signal tests presented here, the GALILEO E1 and E5a signals as well as the GPS L1 signals were simulated simultaneously. The GPS L1 signal is required by the GPS+GALILEO EuroPak L1L5E5a receiver from Novatel in order to derive valid time information. However, only the GALILEO signals are forwarded to the navigation filter. The receiver data is logged to file with the help of the gpsolution-software from Novatel in order to support offline data evaluation. Later, the receiver data is forwarded to the navigation filter as quasi online-stream. No post-processing features are implemented, since real-time updates of the navigation solution are required during precision approach and landing.

Before starting with the actual simulations of the precision approach, typical noise characteristics of the signal measurements are determined. For this purpose a zero-baseline test is performed. Furthermore, it is verified with the help of this test if it is justified to record data of the same scenario sequentially in two independent simulation runs, resulting in only two different receiver clock biases, but leaving other error sources unaffected by the sequential recording. The landing approach of an airplane with a GNSS antenna mounted on its top is simulated with the GPS/GALILEO wavefront simulator. The signals are acquired by a Novatel receiver during two successive simulations runs where the same simulation scenario is replayed. When merging the data of both test runs afterwards, a zero-baseline test can be performed. In this concrete setup, it is a moving zero-baseline since the airplane approaches the airport. The frequency standard of the receiver is less stable than the frequency standard of the wavefront simulator. Therefore double-differencing is applied in order to cancel out the receiver clock biases.

In the following the noise level of the double-differenced receiver measurements is determined. The only disturbance that has been simulated intentionally is signal refraction due to the ionosphere. Ionospheric range errors cancel out for zero baselines anyhow. When comparing the noise characteristics of the GALILEO signals with those of the GPS signals it has to be considered that they refer to different receive power levels. The simulated transmit power for GALILEO and GPS signals was different. For GALILEO signals the Carrier-to-Noise density ratio C/N_0 is in the range of 44…47dB-Hz and for GPS signals the C/N_0 is only in the range of 41…43dB-Hz. Typical measurement noise of the Novatel receiver derived from the zero-baseline test is depicted in Figure 8.2 and Figure 8.3.

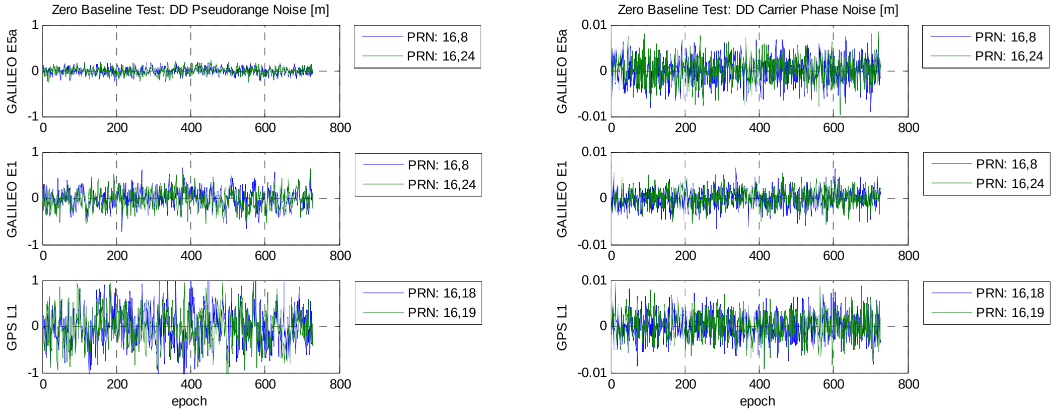

Figure 8.2: Receiver measurement noise of pseudorange (left) and carrier phase (right) measurements after double-differencing

The Novatel receiver also forwards the instantaneous carrier Doppler frequency. This observation is useful in order to determine the velocity of the airplane without the need of differentiating the pseudorange or carrier phase measurement.

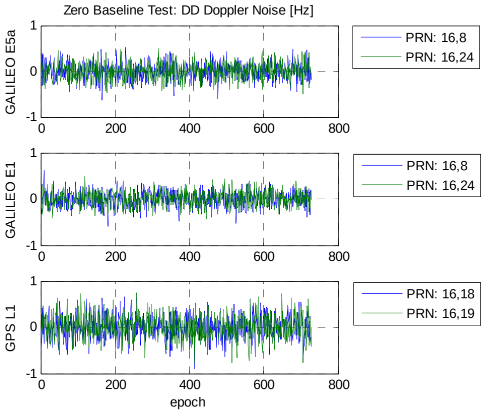

Figure 8.3: Receiver measurement noise of the instantaneous Doppler shift measurements after double-differencing

Instead of using empirical values for the measurement standard deviations which may be weighted in dependence of the satellite elevation angle, it is preferable to use the standard deviations estimated by the receiver at hand. Accurate modeling of the actual measurement noise can significantly improve the filter performance compared to an imprecise stochastic measurement model. In Table 8.1 typical values of the standard deviations $\hat{\sigma}_{\mathrm{RX}}$ provided by the receiver are confronted with the measured standard deviations σ_{meas} derived from the zero-baseline test. Note that the standard deviations listed in Table 8.1 refer to non-differenced measurements while the measurement noise which has been plotted in the previous figures refers to double-differenced measurements, e.g. there is a factor of 2 between them with regard to the standard deviations.

Table 8.1: Typical measurement standard deviations of the Novatel receiver

	$\hat{\sigma}_{\phi,\mathrm{RX}}$ [mm]	$\sigma_{\phi,\mathrm{meas}}$ [mm]	$\hat{\sigma}_{\rho,\mathrm{RX}}$ [cm]	$\sigma_{\rho,\mathrm{meas}}$ [cm]	$\hat{\sigma}_{\Delta f,\mathrm{RX}}$ [Hz]	$\sigma_{\Delta f,\mathrm{meas}}$ [Hz]
GALILEO E1	1.2…2.2	1.0	18…25	10	N/A	0.083
GALILEO E5a	1.5…2.5	1.4	2…3	3.8	N/A	0.092
GPS L1	1.7…2.5	1.4	28…36	20	N/A	0.125

The Novatel GPS+GALILEO receiver provides altogether 16 channels for signal tracking. In order to acquire GALILEO signals on two different frequencies, the present receiver firmware only provides a mode where 5 channels can be configured for the reception of GALILEO E1, further 5 channels for the reception of GALILEO E5a and the remaining 6 channels for the reception of GPS L1. Consequently, only 5 GALILEO satellites can be tracked simultaneously when measuring both E5a and E1 signals. Although a filter-based approach is used for positioning, it would still be desirable to have more than 5 satellites in view with regard to reliable ambiguity resolution and fault identification. Therefore, each simulation scenario is repeated twice with different GALILEO satellite PRNs assigned to the receiver channels. The relative positioning software requires both the raw measurement data from the user receiver and the raw measurement data from the reference receiver. Altogether two different simulation scenarios are required: one for the reference receiver located in the vicinity of the airstrip and one for the user receiver mounted on the top of the airplane. Thus, in total four simulation runs (see Table 8.2) are necessary in order to provide a complete data set for relative positioning since only one Novatel receiver is available.

Table 8.2: Simulation setup for the real signal test

Spirent Simulation Run 1: User RX (airplane approaches the airport)																
	GALILEO E1					GALILEO E5a					GPS L1					
RX channel	0	1	2	3	4	5	6	7	8	9	10	11	12	13	14	15
PRN	23	9	22	17	15	23	9	22	17	15	19	16	12	5	18	21
Spirent Simulation Run 2: User RX (airplane approaches the airport)																
	GALILEO E1					GALILEO E5a					GPS L1					
RX channel	0	1	2	3	4	5	6	7	8	9	10	11	12	13	14	15
PRN	16	1	24	25	8	16	1	24	25	8	19	16	12	5	18	21
Spirent Simulation Run 3: Reference RX (stationary near the airstrip)																
	GALILEO E1					GALILEO E5a					GPS L1					
RX channel	0	1	2	3	4	5	6	7	8	9	10	11	12	13	14	15
PRN	23	9	22	17	15	23	9	22	17	15	19	16	12	5	18	21
Spirent Simulation Run 4: Reference RX (stationary near the airstrip)																
	GALILEO E1					GALILEO E5a					GPS L1					
RX channel	0	1	2	3	4	5	6	7	8	9	10	11	12	13	14	15
PRN	16	1	24	25	8	16	1	24	25	8	19	16	12	5	18	21

Normally, the receiver clock error cancels when forming single-differences between satellites and the satellite clock errors cancel when forming single-differences between receivers. Thus no clock errors have to be estimated when using double-differenced observables. However, the simulation setup described so far comprises four simulation runs in order to gather the complete data set for relative positioning. If the Novatel receiver clock is free-running and the wavefront simulator clock also tends to drift, it is no longer guaranteed that the clock errors indeed cancel out when forming double-differences between measurement data gathered during different simulation runs. This is demonstrated in the following example, where data from all four simulation runs is processed simultaneously. Here the remaining clock error after double-differencing, $\varepsilon_{\mathrm{clk,DD}}$, is given by:

$$\begin{aligned}\varepsilon_{clk,DD} = {} & \left[\left(dt_{run3}^{Sref} - dt_{RX,run3}\right) - \left(dt_{run4}^{Sj} - dt_{RX,run4}\right)\right] \\ & - \left[\left(dt_{run1}^{Sref} - dt_{RX,run1}\right) - \left(dt_{run2}^{Sj} - dt_{RX,run2}\right)\right]\end{aligned} \tag{8.1}$$

The indices "$run(k)$" indicate the respective simulation run as derived from Table 8.2. The satellite clock errors are indicated by dt^S and the receiver clock errors by dt_{RX}. If no distinction between different runs is necessary, as it is generally the case in relative positioning, one can see from Eq. (8.1) that all satellite- and receiver-related clock errors cancel out when differencing between receivers and satellites, e.g. $\varepsilon_{clk,DD} \approx 0$. Of course it is still required that the reference receiver and the user receiver take their measurements (almost) simultaneously in order to cancel out the satellite clock errors. Satellite clock errors are the minor error source since the satellites are provided with very stable frequency standards. The same holds true for the wavefront simulator. However, the Novatel receiver clock is less stable. Therefore, if no precautions are taken the receiver clock errors will no longer cancel out since $dt_{RX,run3} \neq dt_{RX,run4}$ and $dt_{RX,run1} \neq dt_{RX,run2}$. This problem could not fully be overcome by connecting an external very stable 10 MHz frequency standard to the receiver.

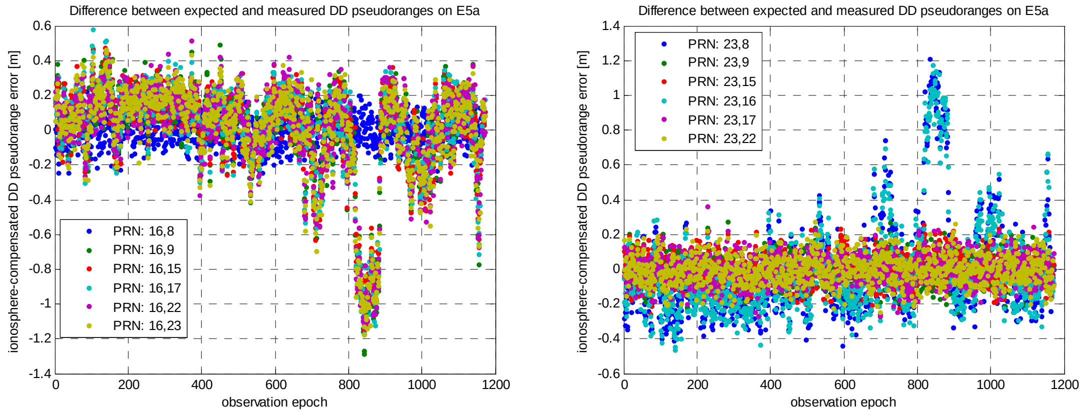

Figure 8.4: Double-differenced E5a pseudorange measurements from simulation run 1, 2, 3 and 4

The plot shown on the left side of Figure 8.4 comprises one satellite-satellite combination, e.g. the combination of PRN 16 and PRN 8 (blue-dotted), where only measurements from two different simulation runs are involved. In all other satellite-satellite combinations measurements from four different simulation runs are involved. Only the double-differenced pseudorange error of the combination PRN 16 – PRN 8 is within the expected range of pure receiver noise. The plot shown on the right side of Figure 8.4 comprises two satellite-satellite combinations, e.g. PRN 23 – PRN 8 (blue-dotted) and PRN 23 – PRN 16 (turquoise-dotted), where measurements from four different simulation runs are involved. Only the double-differenced pseudorange errors of these two combinations are beyond the expected range. All other satellite-satellite combinations involve only measurements from two different simulation runs. As it turns out, the measurement data from all four simulation runs cannot be combined without introducing additional errors due to bad synchronization. Therefore, all further considerations are restricted to the use of 5 GALILEO satellites which were tracked during the simulation runs 1 and 3. Thereby it is ensured that there are only two receiver clock errors: the reference receiver clock error and the user receiver clock error. They cancel out when double-differencing between observations.

8.2 Simulation Scenario

The signal generator provides several options in order to simulate GNSS related error sources. In the real-signal tests performed in this work only ionosphere-induced signal disturbances are considered. Klobuchar's model as described in IS-GPS-200 [20] is used by the signal generator in order to simulate ionospheric refraction. In Figure 8.5 the ionospheric range errors on E5a before and after differencing between receivers are displayed. The greatest part of the ionospheric range errors is eliminated by double-differencing and the residual errors are smaller than 25 cm.

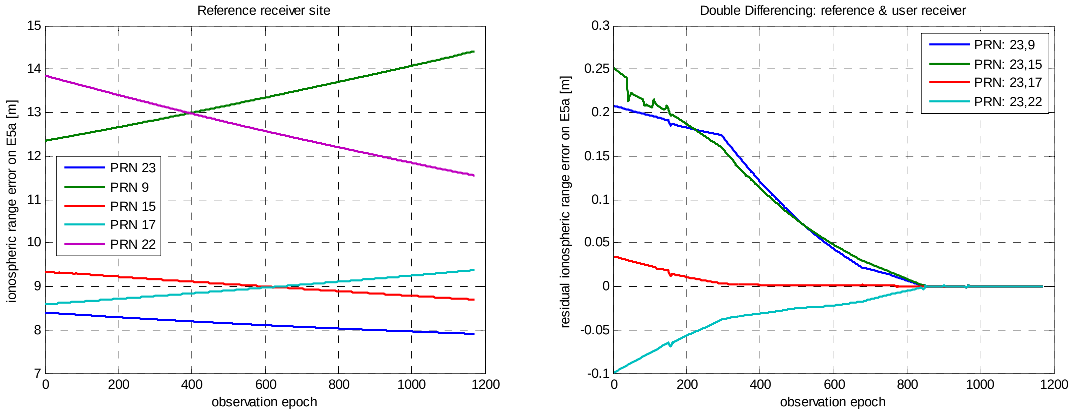

Figure 8.5: Ionospheric range errors on E5a simulated by the signal generator (left: before differencing between receivers, right: after differencing between receivers)

Two different dynamics simulation files have to be generated. The first file contains the dynamics of the airplane during the flight phase, the precision approach, the landing and the deceleration after landing. The simulated dynamics of the airplane are depicted in Figure 8.6.

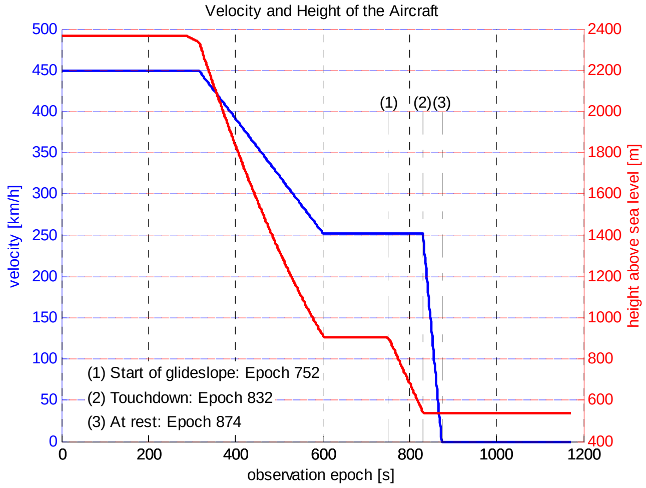

Figure 8.6: Simulated approach of the airplane

The second file contains the static position of the reference receiver antenna located in the vicinity of the airstrip. The receiver antenna coordinates are set to 49° 3.22’ N, 11° 4.30’ E and a height of 540 m above sea level. The location of the reference receiver and the ground track of the airplane are displayed in Figure 8.7.

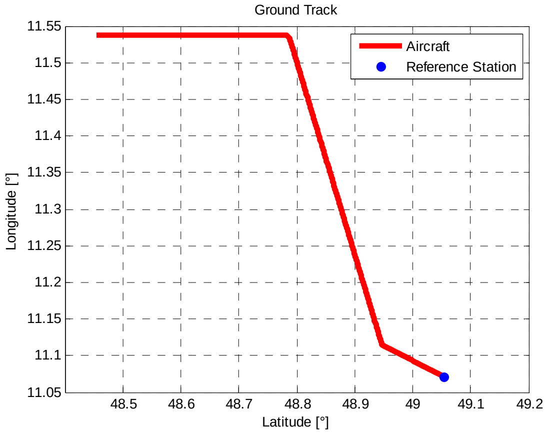

Figure 8.7: Ground track of the flight and final approach

After the airplane has landed and decelerated, it is only 33 m away from the reference station. Then the airplane is at rest and data logging is continued for approximately further 5 minutes before the data acquisition of the Novatel receiver is stopped.

In Figure 8.8 the sky plot of the remaining GALILEO satellites from simulation run 1 and run 3 is shown. All five satellites are tracked by both the reference receiver and the user receiver during the whole landing approach. Satellite 23 is chosen automatically by the navigation software as reference satellite, since it is seen under the largest elevation angle. The sky plots for the reference receiver site and for the user receiver site are almost the same. The satellite positions when starting the simulation are marked in red and the satellite positions at the end of the simulation are marked in blue.

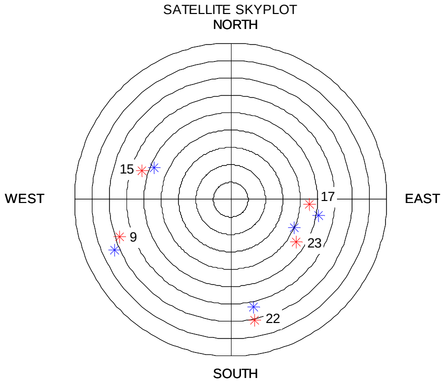

Figure 8.8: Sky plot of the satellites from the reference receiver site

The quality of the reduced satellite constellation is considered next. The entries of the measurement sensitivity matrix, which refer to the position estimate vector and the user clock error, are used for the computation of the dilution of precision (DOP). Following the notation introduced by Misra and Enge [29], the geometry-dependent, (n)x(4), user-satellite matrix is denoted as G hereafter:

$$G = \begin{bmatrix} \left(-\underline{1}_B^{S1}\right)^T & 1 \\ \vdots & \vdots \\ \left(-\underline{1}_B^{Sn}\right)^T & 1 \end{bmatrix} \tag{8.2}$$

The definition of the line of sight vector $\underline{1}_B^{Sj}$ from the user receiver to the satellite is just as before. The mapping matrix $\mathrm{D_P}$, which depends only on the current geometry, is computed in order to evaluate the quality of the user-satellite geometry:

$$D_{P,ENU} = R_{ENU} \cdot \left(G_{ECEF}^T \cdot G_{ECEF}\right)^{-1} \cdot R_{ENU}^T \tag{8.3}$$

In Eq. (8.3) it has been assumed that the geometry matrix G refers to the global ECEF coordinate frame, while the DOP values which are to be determined shall refer to the ENU coordinate frame. The rotation matrix $\mathrm{R_{ENU}}$ follows from Eq. (6.39). The squares of the DOP values of interest can be found along the main diagonal of $\mathrm{D_{P,ENU}}$:

$$D_{P,ENU} = \begin{bmatrix} EDOP^2 & * & * & * \\ * & NDOP^2 & * & * \\ * & * & VDOP^2 & * \\ * & * & * & TDOP^2 \end{bmatrix}, \tag{8.4}$$

where EDOP, NDOP, VDOP and TDOP are the east-, north-, vertical- and time- dilution of precision. Besides the DOPs listed so far, frequently also the horizontal DOP, e.g. $\mathrm{HDOP} = \sqrt{\mathrm{EDOP}^2 + \mathrm{NDOP}^2}$, and the position DOP, e.g. $\mathrm{PDOP} = \sqrt{\mathrm{EDOP}^2 + \mathrm{NDOP}^2 + \mathrm{VDOP}^2}$, are of interest. While the DOP values can be used in order to determine the expected RMS position errors in a standard least-squares approach for standalone GNSS by multiplying the DOP values with the standard deviation of the user range error, this is in general not true for a filter-based approach. Thus, the indicated DOP values may not directly be related to the position estimate uncertainty in this work. Nevertheless, poor DOP values are still good indicators for possibly increased noise of the estimated position solution. The DOP values which correspond to the user-satellite geometry shown in Figure 8.8 are listed in Table 8.3.

Table 8.3: DOP values of the real-signal test for the reference receiver site

	EDOP	NDOP	HDOP	VDOP	PDOP
Start of Simulation	1.938	3.281	3.811	9.477	10.215
End of Simulation	1.181	2.044	2.361	5.281	5.785

The DOP values for the airplane's locations during the simulation run are almost the same as those for the reference receiver site. From Table 8.3 follows that the VDOP improves significantly during the whole simulation run, and consequently also the PDOP does.

8.3 Test Results

As described in the previous sections, the double-differenced observables are only affected by amplified receiver noise (due to double-differencing) and the residual ionospheric range errors after double-differencing. Consequently, it is important to notice that the test results presented hereafter refer to a low measurement error scenario. The filter performance under moderate conditions is investigated when using real receiver measurements in order to crosscheck the assumptions made in the Monte-Carlo simulations. While the measurement noise is rather low in this test, it is sort of worst case scenario with respect to the satellite constellation:

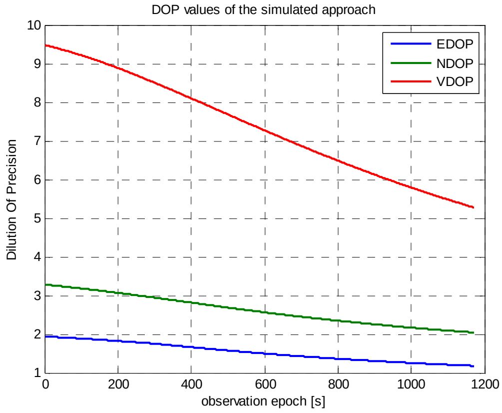

Figure 8.9: Change of the DOP values computed for the airplane's locations during the approach

The DOP values computed for the reference receiver location are almost the same as those computed for the airplane's locations (see Table 8.3). From the DOP-values shown in Figure 8.9 it is expected that the up-component of the position and velocity estimates is the worst, followed by the north-component and the best estimates are expected for the east-component. This is verified with the help of the following test setup: The standard deviations in order to generate the measurement covariance matrix R are adopted as provided by the Novatel receiver. Carrier phase and pseudorange measurements on E5a and E1 are forwarded to the filter as well as instantaneous Doppler measurements on E1. The spectral amplitude of the random walk process is assumed to be $S_p = 5\frac{m^2}{s^2}\frac{rad}{s}$. The following test results are based on the usage of the Ionosphere Model 3 in order to estimate the double-differenced ionospheric range errors. In Figure 8.10 and in Figure 8.11 it is shown that the up-component of the position and velocity estimation error vector is indeed larger than the east- and north-component. The widelane ambiguities are resolved in observation epoch 47, which corresponds to a baseline length of 69.8 km, and the carrier phase ambiguities in observation epoch 203, which corresponds to a baseline length of 53.6 km. These results are surprising, since the satellite geometry is poor and the probabilities of false integer ambiguity fixing have been set to $P_{F,WL} = 1 \cdot 10^{-9}$ and $P_{F,CP} = 1 \cdot 10^{-9}$. In many publications on ambiguity resolution it is stated that many visible satellites improve the performance of ambiguity resolution if a geometry-based model was used. For example, Teunissen et al. [42] have investigated the ambiguity resolution success rate in dependency of the number of visible satellites. The success rate with only 4 satellites in view is significantly lower than the success rate with 8 satellites in view. High ambiguity resolution success rates could already be achieved with 6 visible satellites if two epochs of data, separated by 10 minutes, were considered. Walsh et al. [49] indicate that with 7 or more satellites in view rapid convergence to an ambiguity-fixed solution can be achieved. However, here are only 5 visible satellites, which is already a difficult scenario with regard to reliable integer ambiguity resolution and high success rates of the ambiguity resolution. The filter-based approach alleviates the availability of few measurements to some degree. In this concrete test fast ambiguity resolution is favored by low measurement noise. Especially the E5a pseudorange measurement standard deviations provided by the Novatel receiver are very low, e.g. see Table 8.1. Since there are no unmodeled biases present in the measurement data, also the estimation of the residual ionospheric range errors works well. The availability of an ambiguity-fixed solution in this real-signal test is better than in the Monte-Carlo simulations due to reduced measurement standard deviations. While the accuracy of the east- and north-component of the user position and velocity vector are similar to those in the Monte-Carlo simulations, the accuracy of the up-component is worse here. This effect can be explained by the poor VDOP in this real-signal test. The VDOPs in the Monte-Carlo simulations were always significantly better.

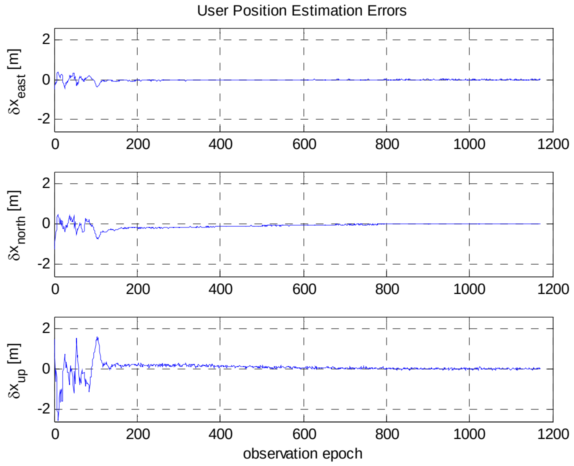

Figure 8.10: East-, north- and up-component of the user position estimation errors (Ionosphere Model 3)

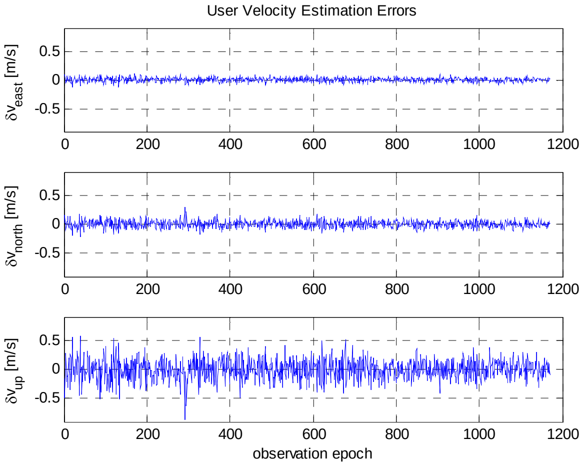

Figure 8.11: East-, north- and up-component of the user velocity estimation errors (Ionosphere Model 3)

For comparison, the simulation is repeated with the ionosphere-free code-only and code-carrier combinations. The velocity estimates remain almost unaffected. However, the position accuracy, which has been obtained with the Ionosphere Model 3 after the widelane and carrier phase ambiguities have been resolved successfully (see Figure 8.10), cannot be achieved with the ionosphere-free combinations (see Figure 8.12). Instead of position estimation errors at the centimeter-level, the position estimation errors of the ambiguity-fixed code-carrier solution are at the meter-level. The ambiguities of the code-carrier combination are fixed in observation epoch 130. Nevertheless, especially the up-component of the user position vector stays rather noisy due to poor VDOPs. The protection levels for the position solution derived from the ionosphere-free combinations will also be higher than 5.3 m in this test. Therefore, in the real-signal tests the ionosphere-free combinations will no longer be considered, since the position estimation errors are not at the desired centimeter- or decimeter-level. It is assumed that the ionosphere-free combinations are better suited for single-point positioning than for relative positioning. The results of the cascading ambiguity resolution approach from the widelane fixed to the carrier phase fixed solution are more promising with respect to this navigation filter as long as no smoothing with a carrier-only combination is implemented in the ionosphere-free approach.

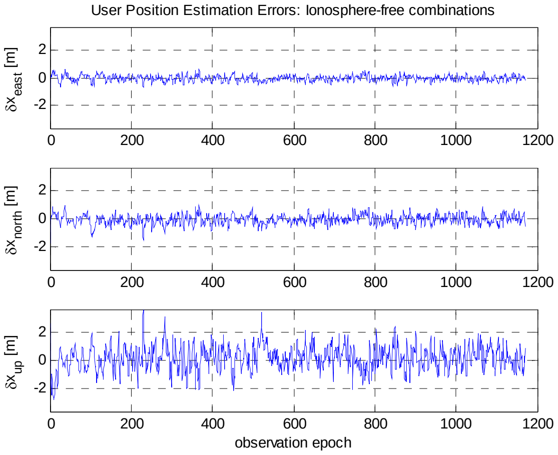

Figure 8.12: East-, north- and up-component of the user position estimation errors (usage of the ionosphere-free code-carrier combinations)

Next, the protection levels are investigated. The noncentrality parameter λ, which is used for the computation of the MDB, is larger than in the previous Monte-Carlo simulations since it depends on the number of degrees of freedom. The number of degrees of freedom is determined by the number of measurements, which is now significantly smaller. Here are only 5 satellites in view and only the instantaneous Doppler shift measurements on E1 are processed. For example, if it is assumed that $P_{FA} = 1 \cdot 10^{-7}$, $P_{MD,1} = 1 \cdot 10^{-9}$ and that the number of measurement equals 54 (10 satellites in view: 3x9x2 double-differenced carrier phase, Doppler shift and pseudorange measurements on E5a and E1), the noncentrality parameter is set to $\lambda = 3.312$. The analytically derived value for λ would be even smaller, but a value of 3.312 is chosen as lower limit for the noncentrality parameter. The MDB approaches zero for very large numbers of degrees of freedom. It is preferred here to be more conservative by setting $\lambda_{\min} = 3.312$. The same considerations are repeated with only 5 visible satellites instead of 10 visible satellites. In the real-signal test there are only 2x4x2 double-differenced carrier phase and pseudorange measurements on E5a and E1 and 1x4 double-differenced Doppler shift measurements on E1. Consequently, the number of degrees of freedom reduces to 20, and the analytically derived noncentrality parameter increases to $\lambda = 46.26$. As a result, the MDB is far larger than in the previous example. So far, the position variance inflation factor f_{pos} has been set to 1.2 and the innovation variance inflation factor f_r has been set to 2.8. It is illustrated in Figure 8.13 that the protection levels HPL_0, VPL_0, vel_HPL_0 and vel_VPL_0 of fault-free normal operation, which are represented in the plots by the green lines, are of the same magnitude as the protection levels in the Monte-Carlo simulations. In contrast to the protection levels under the assumption of fault-free normal operation, the fault mode protection levels, e.g. HPL_1, VPL_1, vel_HPL_1 and vel_VPL_1, are considerably above the protection levels which can be achieved with 6 or more visible satellites. The fault mode protection levels are displayed in Figure 8.13 for two different innovation inflation factors f_r. It has to be verified by test if the value of $f_r = 2.8$ is too conservative. In Grewal et al. [13] it is suggested to find the decision threshold for the chi-square distributed test statistic, which is computed from the innovations, from the operational values rather than the theoretical values. The same seems to hold true for the noncentrality parameter λ of the chi-square distribution. Here it is proposed to use the analytically derived noncentrality parameter λ, which is already conservative compared to the operational values, and to scale the sigma of the innovations with a flexible inflation factor f_r, which is at minimum 1 if there are only few measurements available and at maximum 2.8 if there are many measurements available. Since the overall protection level is derived from the maximum of the fault-free mode protection level and the fault mode protection level, it can be concluded from the test results that there is no benefit from having an ambiguity-fixed solution available with respect to the protection levels. As long as the mapping of the MDB to the position domain results in large position errors due to the poor satellite geometry, the fault mode protection levels will clearly dominate the normal operation protection levels. Note that the HPLs and VPLs during the first few epochs after starting the filter are not displayed in Figure 8.13, since they exceed the upper limit of 10 m. The small peaks of the position solution protection levels between observation epoch 200 and 900 are caused by transient increase of the measurement standard deviations forwarded by the receiver.

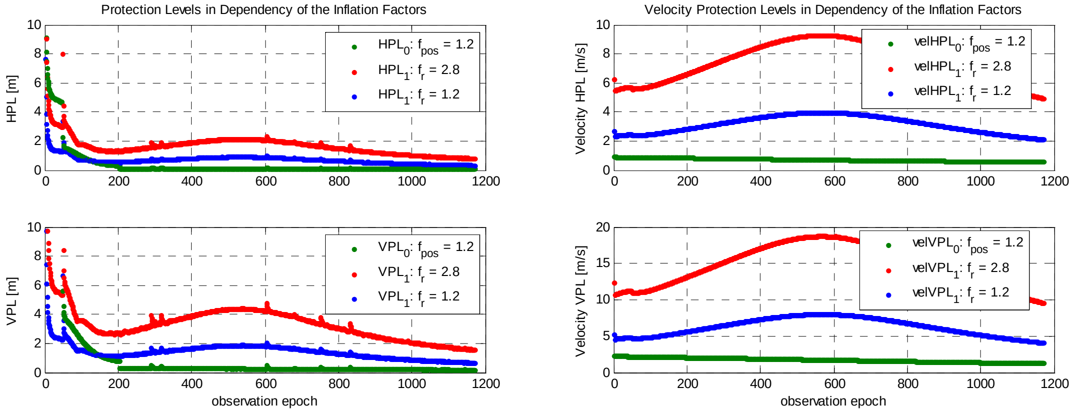

Figure 8.13: Protection levels in dependence of the inflation factors (left: position, right: velocity)

If one of the satellites fails, the filter performance is strongly dependent on an accurate state space model. Therefore, the importance of the parameter S_p increases with respect to the magnitude of the protection levels for the fault mode if there are only 5 visible satellites. Just like in the Monte-Carlo simulations, the linear state equations used in the EKF do not perfectly model the physical dynamic model of the airplane (see Figure 8.14).

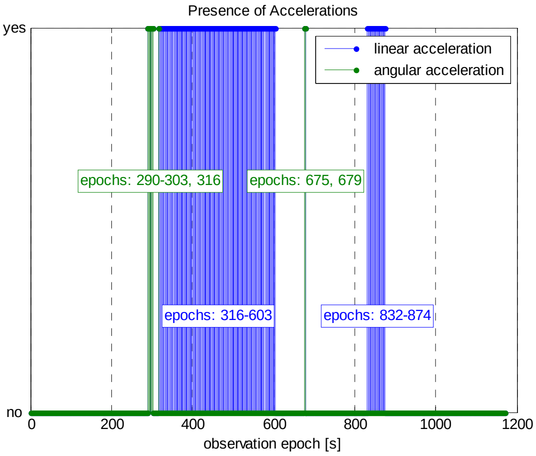

Figure 8.14: Accelerations of the airplane in dependency of the observation epoch

By choosing a very small spectral amplitude $S_p = 0.01 \frac{m^2}{s^2} \frac{rad}{s}$, the fault mode protection levels decrease considerably. In Figure 8.15 it is depicted that low velocity protection levels can be achieved by reducing the process noise of the dynamic system model significantly even if an innovation inflation factor of $f_r = 2.8$ is used. The drawback of reducing S_p is that in presence of accelerations there are error spikes in the velocity and position estimates. These spikes are detected correctly by the fault detection algorithm. It is assumed that f_r can be set to a lower value than 2.8 since also those increased velocity estimation errors are detected, which are still considerably below the computed protection levels. For example, the horizontal component of the velocity estimation error is $0.3 \frac{m}{s}$ below the horizontal velocity protection level during the time interval from epoch 832 to 874. Nevertheless, the increased velocity estimation errors due to the presence of accelerations are detected. As long as the straight flight condition is fulfilled, the vertical component of the velocity estimation error reduces considerably compared to the simulation run with $S_p = 5\frac{m^2}{s^2}\frac{rad}{s}$.

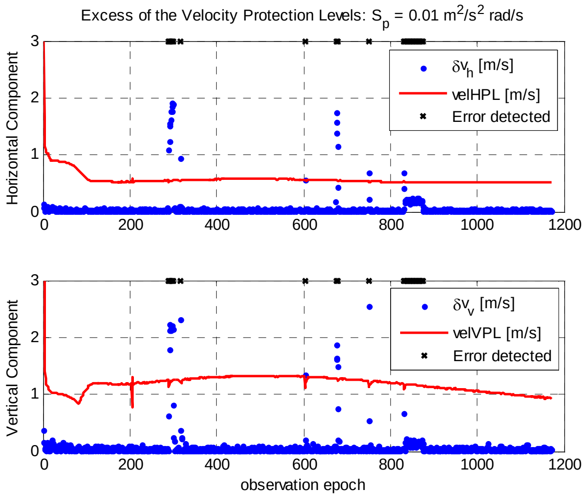

Figure 8.15: Excess of the velocity protection levels due to incorrect process noise modeling

The test run is repeated with modified parameters. The spectral amplitude of the random walk is set to $S_p = 1\frac{m^2}{s^2}\frac{rad}{s}$ and the inflation factor of the innovations is reduced to $f_r = 1.2$. Artificially generated errors are introduced into the real measurement data in order to verify if the reduction of the inflation factor is justified. One carrier phase measurement on E1 is manipulated by one cycle starting from observation epoch 260, which corresponds to a cycle slip in epoch 260. Furthermore, in observation epoch 650 a code outlier on E5a is simulated by adding 1.5 m to the actual pseudorange measurement. If both errors are identified successfully, the new parameter $f_r = 1.2$ is accepted in this simulation. In reality, the finding of appropriate inflation factors is far more complex, see e.g. [25]. As shown in Figure 8.16 both errors which have been introduced into the measurement data are detected and identified properly. By enabling model adaptation the best position solution available is not corrupted. If the airplane's acceleration changes significantly between two successive observation epochs, further model invalidations are detected. The source of the model invalidations cannot be identified, because the model errors are caused by the violation of the straight flight condition. In the velocity solution minor error spikes can be observed in the respective epochs, while the position solution remains unaffected as shown in Figure 8.16.

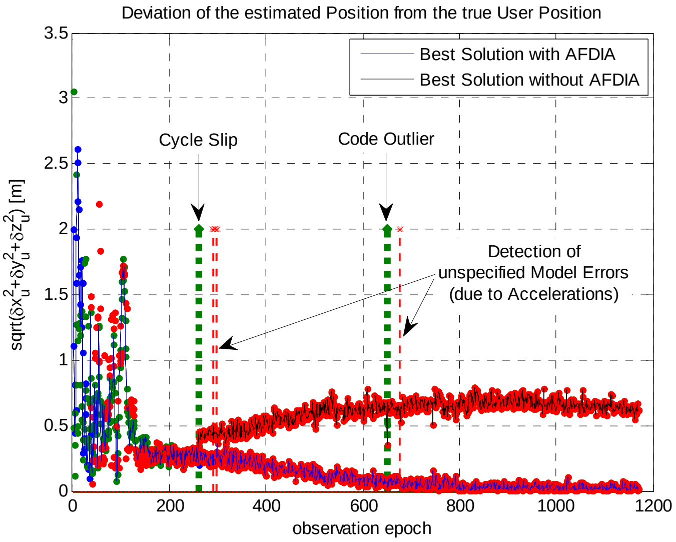

Figure 8.16: Successful detection and identification of small errors

The position and velocity variances in the covariance matrix of process noise are decreased by reducing S_p from $5\,\frac{m^2}{s^2}\frac{rad}{s}$ to $1\,\frac{m^2}{s^2}\frac{rad}{s}$. In consequence, the number of epochs required in order to resolve the widelane ambiguities reduces by 12 epochs. The resulting protection levels for $f_r = 1.2$ are displayed in Figure 8.17. There is still an order of magnitude between HPL_0 and HPL_1 and between VPL_0 and VPL_1 after the carrier phase ambiguities have been fixed correctly. As demonstrated before, biases that cause far smaller errors in the position domain than protected by the HPL and VPL are identified and corrected successfully. However, the protection levels are computed such that $P_{MD,1} = 1 \cdot 10^{-9}$, which suggests that smaller errors than protected by the HPL and VPL can still be detected, but with less certainty.

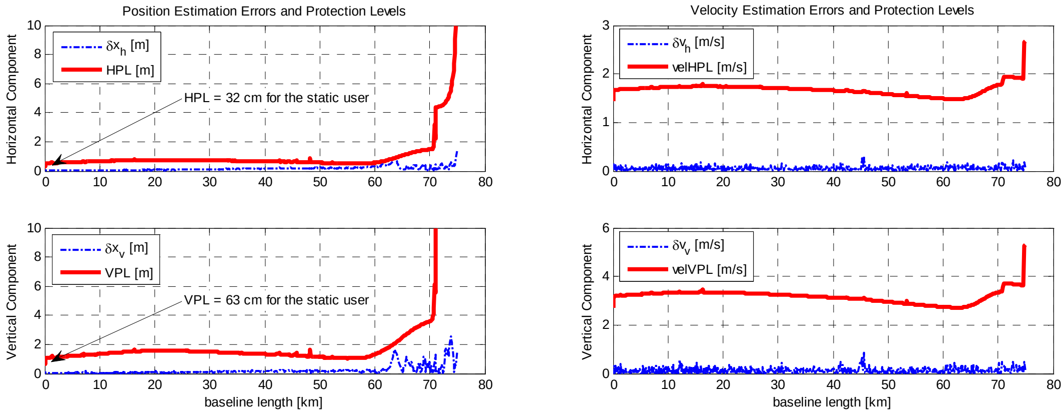

Figure 8.17: Navigation filter performance with 5 visible satellites

The scenario with only 5 visible satellites is pessimistic with respect to the satellite geometry, especially if combined GPS and GALILEO constellations are considered. On the other hand, signal shading is still an issue if the navigation filter shall be employed for applications like automated cargo traffic in the vicinity of large buildings. With respect to aviation, it is expected that more than 5 satellites will be in view. The protection levels for the carrier phase ambiguity-fixed solution are therefore expected to be below 1 m. Even in this scenario the protection levels stay below 2 m during the last 60 km of the flight because of the availability of low-noise measurement data. The VPL is below the expected CAT IIIc vertical alert limit of 5.3 m already at a large distance to the reference station. To conclude, the plausibility of the results obtained from the Monte-Carlo simulation could be verified successfully with the help of the real-signal tests.

9 Conclusions and Outlook

9.1 Recommendations

The navigation filter presented in this work does not account for range errors induced by the troposphere, e.g. it has been assumed that tropospheric refractivity can be modeled perfectly. In land-based applications the residual ionospheric range errors after double-differencing between observables are in most cases larger than the residual tropospheric range errors. If measurements on two or more frequencies are available, ionosphere-free measurement combinations can be formed. Alternatively, the ionospheric delay terms can be estimated more accurately if measurements on more than one frequency are processed because of the dispersive nature of the ionosphere. In contrast to the ionospheric delay terms the tropospheric delays are independent from the frequency in the considered GNSS frequency bands. However, the tropospheric range errors at the reference receiver site and at the user receiver site are highly correlated for short and medium baselines. For this reason the residual tropospheric range errors after differencing the observations between receivers are frequently neglected in land-based applications. In aeronautical applications large geodetic height differences between the reference receiver and the rover receiver have to be considered. The tropospheric range errors at the reference- and user-site decorrelate with growing height difference. Thus, it is no longer justified to neglect the residual tropospheric range errors in aeronautical applications. Pervan et al. [33], who have investigated carrier phase-based DGPS for landing applications, propose to add an additional state in the covariance analysis that accounts for the error in the local tropospheric refraction index. In a first step standard tropospheric corrections are applied. In a second step the LAAS tropospheric error model is applied in order to correct for the residual differential tropospheric range error:

$$\Delta d_{tropo,AB}^{Sj} = \Delta n \cdot \frac{h_0 \cdot \left[1 - e^{-\Delta h / h_0}\right]}{\sqrt{0.002 + sin^2(E^{Sj})}} \quad , \tag{9.1}$$

where:

$\Delta d_{tropo,AB}^{Sj}$:	Residual differential tropospheric range error after differencing the observations between receiver A and B
Δn:	Difference between the estimated and the actual local index of tropospheric refractivity
h_0:	Troposphere scale height
Δh:	Height difference between the reference receiver and the user receiver
E^{Sj}:	Elevation angle of the satellite S_j

The LAAS tropospheric error model presented in Eq. (9.1) can be more easily adapted to the usage of double-differenced observations than the LAAS ionospheric error model. Here only one additional parameter, Δn, has to be included into the vector of state estimates independent from the number of visible satellites instead of one additional parameter per satellite, e.g. $VIG^{S1}...VIG^{Sn}$. Therefore, it is expected that the developed navigation filter algorithms, which are based on double-differenced observations, can be easily extended in order to account for residual tropospheric range errors. It is proposed to evaluate the filter performance after these adaptations on the basis of real GPS measurements. This prevents possible mismodeling of both the simulated measurement data and the filter correction algorithmic, which might compensate if both were mismodeled in the same way.

The navigation filter performance results, which were presented in Sect. 7 and 8, showed that the availability of an ambiguity-fixed solution and the magnitude of the protection levels are dependent on the satellite geometry. In the near future integrated GPS/GALILEO system solutions are likely to gain influence wherever high integrity of the navigation solution is required. Mowlam et al. [30] indicate that combined GPS/GALILEO integer ambiguity estimation is especially well-suited for safety-critical applications. However, it is also stated that if a large set of ambiguities has to be resolved, the maximum distance between the reference receiver and the user receiver has to be restricted to short baselines in order to maintain high ambiguity resolution success rates. By limiting the service volume of relative positioning to the vicinity of the airport, for example to a maximum baseline length of 10 km, combined GPS/GALILEO integer ambiguity estimation seems to be promising with respect to high-integrity relative positioning. Further investigations are required in order to quantify the benefit from combined GPS/GALILEO system solutions concerning the filter approach which has been presented here. For medium and long baselines it is unlikely that a large set of ambiguities can be fixed with the required success probability of integer ambiguity fixing. It is suggested to use partial ambiguity resolution for large sets of ambiguities. High accuracy of the position solution can be achieved even if not all ambiguities were fixed to integer values. Besides ambiguity resolution, the second argument in favor of using both GPS and GALILEO measurements is that the DOP values of the combined constellation are certainly better than those of a single constellation. It has been demonstrated in the real-signal test with only 5 visible satellites that poor DOP values cause an increase of the fault mode protection levels. If high availability of the navigation solution is required, it is desirable that faults are not only detected, but also identified and excluded or compensated reliably.

In the past it has been proposed by several authors to install pseudolites in the vicinity of the airstrip. This improves the geometry and especially the VDOP gets better. A concept for precision landing with GPS augmented by integrity pseudolites has already been proposed by Cohen et al. [6] in 1993. One main aspect in order to judge the practicability of carrier phase based positioning for landing applications is the availability of its associated integrity measures. According to Pervan et al. [34], there are several benefits of installing pseudolites under the approach path of the airplane: First, the pseudolite-augmented constellation provides large geometry changes when the airplane flies by the pseudolites. This facilitates the integer ambiguity resolution in real-time. The pure satellite constellation does hardly change during the short maneuver time and long observation time spans as in geodetic survey are impracticable. Second, the availability of classical and carrier phase based RAIM is enhanced by additional measurements from pseudolites compared to an un-augmented GPS-only constellation. As soon as GALILEO is fully operational, the second aspect will no longer be of great importance. But large geometry changes in a very short time-span, which favor successful ambiguity resolution, can indeed only be achieved by using additional pseudolite signals. There remain two last comments on the usage of pseudolite signals for precision landing. It is favorable to know that the pseudolite signals are not disturbed by atmospheric refraction as soon as the airplane flies at low altitude. One can profit from this knowledge when developing new integrity monitoring algorithms. Contrariwise, multipath might be a problem with respect to pseudolite signals and caution is required to ensure that the pseudolites do not operate as jammers. Jamming can easily be prevented by signal pulsing at the expense of an increased noise level of the pseudolite signals. Multipath is more likely to occur along the propagation path between the pseudolite and the reference receiver than along the propagation path between the pseudolite and the receiver located at the airplane. Since the true geometric range between the reference station and the pseudolites is known exactly, the occurrence of multipath can be detected easily.

In this work the navigation solution is provided by an extended Kalman filter. So far only GNSS measurements have been processed by the filter. However, the filter-based approach is well-suited to be extended to the integration of GNSS and INS (Inertial Navigation System) measurements. The most probable state estimate is derived from Kalman filtering by combining two optimally weighted estimates of a variable. Titterton et al. [46] list the following items in favor of combining complementary INS and GNSS measurements: The first important aspect is that both measurement types show different error characteristics. While position estimates derived from GNSS pseudorange measurements are rather noisy, but not affected by long-term drifts, the position estimates derived from INS measurements are rather smooth, but frequently exhibit long-term drifts. The second aspect is that with INS and GNSS equipment different quantities are measured. GNSS receivers provide the measurement of pseudoranges, carrier phases and range-rates, while INS sensors provide the measurement of specific force accelerations. Since only GNSS is susceptible to jamming or signal shading, the availability of the navigation solution can be improved by the integrated GNSS and INS approach. These considerations on augmenting GNSS with INS mainly refer to pseudorange-based navigation. It is still an open issue if the effort of integrating GNSS and INS is justified if the accuracy of carrier phase based relative positioning serves as reference.

9.2 Summary

A nonlinear navigation filter for high-integrity carrier phase based relative positioning has been developed. Both the user position vector and the user velocity vector are estimated. The ambiguities of the phase measurements and ionospheric terms are included into the state estimation vector as nuisance parameters, which have to be estimated as well in order to derive a precise position solution. The investigations have been restricted to dual-frequency GNSS measurement data. Either GALILEO’s E5a and E1 signals or GPS’s L5 and L1 signals are processed, since these signals reside in an ARNS band. Thereby compatibility with the requirements of civil aviation is ensured. Three different measurement types, e.g. pseudoranges, carrier phases and Doppler shifts, are processed by the filter. The measurements from the reference receiver and the user receiver are double-differenced in order to cancel out satellite- and receiver-related biases. A great part of propagation medium-related range errors is cancelled as well. The ionospheric and tropospheric range errors decorrelate with growing baseline lengths between the reference receiver and the user receiver. Thus, the residual medium-related range errors are not negligible in general. The performance of three different ionosphere models has been compared on the basis of simulation results. When using the first ionosphere model, additional states for the vertical ionospheric gradients, one for each visible satellite, are introduced. It is assumed that this ionosphere model works fine if single-differenced measurements are processed. However, after the adaptation to double-differenced measurements an observability problem arises. If there are n satellites in view, also n independent VIGs have to be estimated. They are not observable from $n-1$ double-differenced measurements within a single epoch. While still good performance is achieved in absence of unmodeled biases, the state estimation errors may diverge as soon as multipath errors are present. The second ionosphere model has been developed for estimating the double-differenced ionospheric range error directly. In consequence, there are no problems due to bad observability of the system states. Additional pseudo-measurements of the double-differenced ionospheric range errors are introduced in the measurement model. These pseudo-measurements are always set to zero as if the ionospheric range errors were perfectly correlated. Since the measurement noise variances are always lower than the process noise variances of the double-differenced ionospheric range errors, the filter cannot succeed in estimating the residual ionospheric range errors precisely when using the second ionosphere model. In contrast to neglecting the ionospheric range errors at all, it is prevented with this ionosphere model that the ambiguities are fixed too quickly to the wrong integer values. In presence of unmodeled measurement biases it has been demonstrated that the usage of pseudo-measurements for the double-differenced ionospheric range errors is advantageous in order to prevent the unmodeled biases from incorporating into the ionosphere state estimates. The last ionosphere model that has been investigated does also aim at estimating the double-differenced ionospheric range errors. In contrast to the second model, no pseudo-measurements are introduced. The estimation of the residual ionospheric range errors works well in absence of biases. If there are unmodeled biases on several receiver channels, the ionosphere terms are no longer estimated properly. This is in coincidence with the theory of Kalman filtering, where all unmodeled error sources have to be white Gaussian noise. Therefore, it should be considered to model multipath and the residual tropospheric range errors systematically.

Instead of estimating the ionospheric terms it has also been considered to form ionosphere-free code-only and code-carrier combinations. However, the measurement noise is amplified by forming inter-frequency combinations according to the law of variance-covariance error propagation. The position accuracies which can be achieved when utilizing the ionosphere-free combinations are worse than those of the widelane and carrier phase ambiguity-fixed position solutions. It is recommended that the ionosphere-free measurement combinations should not be additionally double-differenced, which causes further amplification of the measurement noise. Presumably the utilization of ionosphere-free combinations is particularly suited for single-point positioning. Furthermore, it is recommended to use an ionosphere-free carrier-only combination with a short wavelength as additional measurement input to the filter, whose ambiguities are not resolved, but which serves for smoothing.

Numerical stability of the EKF equations has also been investigated. The Bierman-Thornton UD filter implementation did not show any numerical problems. However, the computation time in MATLAB® was increased considerably. Slight asymmetries of the covariance matrix $P_k(+)$ were observed when using the standard EKF equations without any means to improve numerical robustness. This problem can be overcome for the navigation filter at hand by implementing the Joseph form of the covariance matrix update of state estimation uncertainty. If the algorithms were to be implemented in hardware instead of in MATLAB®, the Bierman-Thornton UD filter implementation might be preferable.

Protection levels are computed for the user position and velocity estimates. Two different types of protection levels are derived: one protection level under the assumption of fault-free normal operation and one protection level under the assumption that there is one bias in the measurement data. The final protection level is given by the maximum of both values. It has to be considered that the presence of multiple measurement biases simultaneously is not covered in the computation of the protection levels. Provided that the satellite geometry is good and low-noise measurements of future GALILEO are available, the VPL of the float solution becomes as low as 1 m after the filter has been running for several hundreds of epochs. The float solution is smoothed by carrier phase measurements, which are still given some weight in the filter-based approach even if no ambiguity fixing is possible with the required probability of success. Under the precondition of good satellite geometry, the VPL of the carrier phase ambiguity-fixed solution is below 20 cm for a probability of false alarm of $P_{FA} = 1 \cdot 10^{-7}$ and an associated integrity risk of $\approx 3 \cdot 10^{-9}$. Sigma-overbounding is applied in the computation of the protection levels in order to account for non-Gaussian tails of the error distributions. However, the inflation factors do not include the uncertainty of tropospheric delay terms. No attempt is made to guess the effects of partially compensated tropospheric range errors on the magnitude of the protection levels. It should be acknowledged that the protection levels will increase when including the uncertainty due to tropospheric refraction in the filter approach. In the real-signal tests it has shown that the importance of a precise dynamic state space model in the EKF increases when the number of visible satellites decreases. The accuracy of the ambiguity-fixed position solution might be very well, which is properly reflected by the fault-free protection levels. However, the fault mode protection levels are far above the fault-free mode protection levels if there were view visible satellites and high process noise. The position estimation errors will exceed the protection levels without being detected if the ambiguities were fixed wrongly. Therefore, reliable ambiguity resolution is the key to high-integrity carrier phase based positioning. Furthermore, the stochastic models of the measurement noise and of the process noise have to reflect the physical conditions adequately. For example, if the presence of unmodeled multipath is not reflected by increased measurement variances, the protection levels may be exceeded without being detected. The actual integrity risk associated with the navigation filter solutions has to be found by extensive simulations. The problem associated with an analytical approach is that the results of the EKF are dependent on the actual measurement sequence and the filter initialization. Since relative positioning is considered here, the error budget of the real-time data link between the reference station and the user has to be accounted for as well when trying to specify the overall integrity risk.

Just like in pseudorange-based snapshot RAIM, a fault detection algorithm is implemented which has to detect the excess of the fault-mode protection levels. The test statistic of the filter-based approach is based on the square root of the weighted sum of squared innovations. In order to provide high continuity of the navigation solution, the fault detection algorithm has been extended to Autonomous Filter-based fault Detection, Identification and model Adaptation (AFDIA). Again, only the identification of single-channel biases is supported, although there is in theory no upper limit for the number of biases which can be identified. In the Monte-Carlo simulations good performance of AFDIA could be demonstrated. All cycle slips and even creeping multipath errors on one channel were identified correctly. Model adaptation ensures that the high accuracy and the availability of the navigation solution are not endangered. Also artificially generated cycle slips and code outliers in the receiver measurement data were identified successfully in the real-signal tests.

To conclude, good performance of the navigation filter could be verified in the Monte-Carlo simulations and in the real-signal tests as long as the model assumptions were kept. Frequently carrier phase ambiguity-fixed solutions could be derived when the airplane was still more than 20 km away from the reference receiver. However, in presence of multiple unmodeled biases, the protection levels were exceeded without being detected and the probability of false integer ambiguity resolution increased. Further investigations are required in order to find out which error sources have to be modeled systematically within the filter, for example multipath and tropospheric delay. As long as all error sources are white Gaussian noise, the navigation filter provides very accurate position solutions and protection levels.

V. Appendix

A. Extended Kalman Filter Equations

The extension of the standard discrete-time Kalman filter equations to nonlinear dynamic models and/or nonlinear measurement models leads to the formulation of the discrete-time extended Kalman filter (EKF). In the following the essential filter equations of the EKF are summarized. It is referred to [12] for the derivation of the equations. The problem is formulated in discrete state-space. The equations presented hereafter refer to the case where both the dynamic model and the measurement model are nonlinear:

$$\underline{x}_k = \underline{f}_{k-1}\left(\underline{x}_{k-1}\right) + \underline{\omega}_{k-1}, \qquad \underline{\omega}_k \sim N(0, Q_k) \tag{A.1}$$

$$\underline{z}_k = \underline{h}_k\left(\underline{x}_k\right) + \underline{\upsilon}_k, \qquad \underline{\upsilon}_k \sim N(0, R_k) \tag{A.2}$$

1) Computation of the a priori covariance matrix of state estimation uncertainty:

$$P_k(-) = \Phi^*_{k-1} \cdot P_{k-1}(+) \cdot \Phi^{*T}_{k-1} + Q_{k-1} \quad , \tag{A.3}$$

where the linear approximation of the state transition matrix is calculated from partial derivatives:

$$\mathit{\Phi}^*_{k-1} \approx \left.\frac{\partial \underline{f}_k(\underline{x})}{\partial \underline{x}}\right|_{\underline{x}=\underline{\hat{x}}_{k-1}(-)} \tag{A.4}$$

2) Computation of the Kalman gain:

$$K_k = P_k(-) \cdot H^{*T}_k \cdot \left[H^*_k \cdot P_k(-) \cdot H^{*T}_k + R_k\right]^{-1} \quad , \tag{A.5}$$

where the linear approximation of the measurement sensitivity matrix is computed from

$$H^*_k \approx \left.\frac{\partial \underline{h}_k(\underline{x})}{\partial \underline{x}}\right|_{\underline{x}=\underline{\hat{x}}_k(-)} \tag{A.6}$$

and the a priori estimate of the state vector at time k follows from

$$\underline{\hat{x}}_k(-) = \underline{f}_{k-1}\left(\underline{\hat{x}}_{k-1}(+)\right) \quad . \tag{A.7}$$

3) Computation of the posteriori covariance matrix of state estimation uncertainty:

$$P_k(+) = [I - K_k \cdot H^*_k] \cdot P_k(-) \tag{A.8}$$

4) Computation of the posteriori estimate of the state vector at time k:

$$\underline{\hat{x}}_k(+) = \underline{\hat{x}}_k(-) + K_k \cdot \left(\underline{z}_k - \underline{\hat{z}}_k\right) \quad , \tag{A.9}$$

where the predicted measurement at time k is computed from

$$\underline{\hat{z}}_k = \underline{h}_k\left(\underline{\hat{x}}_k(-)\right) \quad . \tag{A.10}$$

B. Ephemeris Data

The position and velocity vector of the satellites in the ECEF coordinate system are calculated from ephemeris data broadcast in the navigation message. The determination of the satellite ECEF position vector from ephemeris data is described in IS-GPS-200 [20]. In this representation the determination of the satellite velocity vector is indicated as well. The velocity vector is derived from the first order derivative of the position vector by applying the chain-, product- and quotient-rule of differentiation. The results have been counterchecked with the satellite velocity determination from broadcast ephemeris published in [35]. The respective first order derivatives are listed in the right column of Table 9.1 in addition to the standard formulas for the calculation of the satellite position vector taken from the IS-GPS-200, which are indicated in the left column of Table 9.1. The depiction is restricted to present GPS broadcast ephemeris.

Table 9.1: Satellite position and velocity from ephemeris data

WGS 84 value of the earth's gravitational constant	
$\mu = 3.986005 \cdot 10^{14}\ m^3/s^2$	
WGS 84 value of the earth's rotation rate	
$\dot{\Omega}_e = 7.2921151467 \cdot 10^{-5}\ rad/s$	
Semi-major axis ($\sqrt{A}$: square root of the semi-major axis from ephemeris data)	
$A = \left(\sqrt{A}\right)^2$	
Computed mean motion in rad/s	
$n_0 = \sqrt{\frac{\mu}{A^3}}$	
Actual total time difference between the GPS system time at transmission (t) and the epoch time (t_{oe}) (t_{oe}: reference time of ephemeris from ephemeris data)	
$t_k = t - t_{oe}$ If $t_k > 302400s$: $t_k = t_k - 604800s$ If $t_k < -302400s$: $t_k = t_k + 604800s$	
Corrected mean motion (Δn: mean motion difference from computed value from ephemeris data)	
$n = n_0 + \Delta n$	
Mean anomaly (M_0: Mean anomaly at reference time from ephemeris data)	
$M_k = M_0 + n \cdot t_k$	$\dot{M}_k = n$
Kepler's Equation for eccentric anomaly; eccentric anomaly E_k may be solved iteratively (e: eccentricity from ephemeris data)	

$M_k = E_k - e \cdot \sin E_k$	$\dot{E}_k = \dfrac{n}{1 - e \cdot \cos E_k}$
True anomaly	
$\upsilon_k = \tan^{-1}\left(\dfrac{\sqrt{1-e^2} \cdot \sin E_k}{\cos E_k - e}\right)$	$\dot{\upsilon}_k = \dfrac{\dot{E}_k \cdot \sin E_k \cdot (1 + e \cdot \cos \upsilon_k)}{(1 - e \cdot \cos E_k) \cdot \sin \upsilon_k}$
Argument of latitude (ω: argument of perigee from ephemeris data)	
$\Phi_k = \upsilon_k + \omega$	$\dot{\Phi}_k = \dot{\upsilon}_k$
Argument of latitude correction (second harmonic perturbation) (C_{us}: amplitude of the sine harmonic correction term to the argument of latitude from ephemeris data) (C_{uc}: amplitude of the cosine harmonic correction term to the argument of latitude from ephemeris data)	
$\delta u_k = C_{us} \cdot \sin(2\Phi_k) + C_{uc} \cdot \cos(2\Phi_k)$	$\delta \dot{u}_k = 2 \cdot \dot{\Phi}_k \cdot [C_{us} \cdot \cos(2\Phi_k) - C_{uc} \cdot \sin(2\Phi_k)]$
Radius correction (second harmonic perturbation) (C_{rs}: amplitude of the sine harmonic correction term to the orbit radius from ephemeris data) (C_{rc}: amplitude of the cosine harmonic correction term to the orbit radius from ephemeris data)	
$\delta r_k = C_{rs} \cdot \sin(2\Phi_k) + C_{rc} \cdot \cos(2\Phi_k)$	$\delta \dot{r}_k = 2 \cdot \dot{\Phi}_k \cdot [C_{rs} \cdot \cos(2\Phi_k) - C_{rc} \cdot \sin(2\Phi_k)]$
Inclination correction (second harmonic perturbation) (C_{is}: amplitude of the sine harmonic correction term to the angle of inclination from ephemeris data) (C_{ic}: amplitude of the cosine harmonic correction term to the angle of inclination from ephemeris data)	
$\delta i_k = C_{is} \cdot \sin(2\Phi_k) + C_{ic} \cdot \cos(2\Phi_k)$	$\delta \dot{\mathrm{i}}_k = 2 \cdot \dot{\Phi}_k \cdot [C_{is} \cdot \cos(2\Phi_k) - C_{ic} \cdot \sin(2\Phi_k)]$
Corrected argument of latitude	
$u_k = \Phi_k + \delta u_k$	$\dot{u}_k = \dot{\upsilon}_k \cdot \{1 + 2 \cdot [C_{us} \cdot \cos(2\Phi_k) - C_{uc} \cdot \sin(2\Phi_k)]\}$
Corrected radius	
$r_k = A \cdot (1 - e \cdot \cos E_k) + \delta r_k$	$\dot{r}_k = A \cdot e \cdot \sin E_k \cdot \dot{E}_k + 2 \cdot \dot{\upsilon}_k \cdot [C_{rs} \cdot \cos(2\Phi_k) - C_{rc} \cdot \sin(2\Phi_k)]$
Corrected inclination (i_0: inclination angle at reference time from ephemeris data) ($IDOT$: rate of inclination angle from ephemeris data)	
$i_k = i_0 + \delta i_k + IDOT \cdot t_k$	$\dot{\mathrm{i}}_k = IDOT + 2 \cdot \dot{\upsilon}_k \cdot [C_{is} \cdot \cos(2\Phi_k) - C_{ic} \cdot \sin(2\Phi_k)]$
X-coordinate in orbital plane	
$x_k^* = r_k \cdot \cos u_k$	$\dot{x}_k^* = \dot{r}_k \cdot \cos u_k - y_k^* \cdot \dot{u}_k$
Y-coordinate in orbital plane	
$y_k^* = r_k \cdot \sin u_k$	$\dot{y}_k^* = \dot{r}_k \cdot \sin u_k + x_k^* \cdot \dot{u}_k$
Corrected longitude of ascending node (Ω_0: longitude of ascending node of orbital plane at weekly epoch from ephemeris data)	

($\dot{\Omega}$: rate of right ascension from ephemeris data)	
$\Omega_k = \Omega_0 + \left(\dot{\Omega} - \dot{\Omega}_e\right) \cdot t_k - \dot{\Omega}_e \cdot t_{oe}$	$\dot{\Omega}_k = \dot{\Omega} - \dot{\Omega}_e$
ECEF x-coordinate	
$x_k = x_k^* \cdot \cos \Omega_k - y_k^* \cdot \cos i_k \cdot \sin \Omega_k$	$\dot{x}_k = \cos \Omega_k \cdot \left(\dot{x}_k^* - y_k^* \cdot \cos i_k \cdot \dot{\Omega}_k\right) -$ $\sin \Omega_k \cdot \left(x_k^* \cdot \dot{\Omega}_k + \dot{y}_k^* \cdot \cos i_k - y_k^* \cdot \sin i_k \cdot \dot{i}_k\right)$
ECEF y-coordinate	
$y_k = x_k^* \cdot \sin \Omega_k + y_k^* \cdot \cos i_k \cdot \cos \Omega_k$	$\dot{y}_k = \sin \Omega_k \cdot \left(\dot{x}_k^* - y_k^* \cdot \cos i_k \cdot \dot{\Omega}_k\right) +$ $\cos \Omega_k \cdot \left(x_k^* \cdot \dot{\Omega}_k + \dot{y}_k^* \cdot \cos i_k - y_k^* \cdot \sin i_k \cdot \dot{i}_k\right)$
ECEF z-coordinate	
$z_k = y_k^* \cdot \sin i_k$	$\dot{z}_k = \dot{y}_k^* \cdot \sin i_k + y_k^* \cdot \cos i_k \cdot \dot{i}_k$

VI. Bibliography

[1] G.L. Bierman (1977). *Factorization Methods for Discrete Sequential Estimation*. Mathematics in Science and Engineering, vol. 128, Academic, New York.

[2] G. Blewitt (1989). *Carrier-phase ambiguity resolution for the Global Positioning System applied to geodetic baselines up to 2000 km*. Journal of Geophysical Research, 94(B8), 10, pp. 10187-10203.

[3] I.N. Bronstein, K.A. Semendjajew, G. Musiol, H. Mühlig (2001). *Taschenbuch der Mathematik*. 5. Auflage, Harri Deutsch Verlag, Frankfurt am Main.

[4] R.G. Brown (1992). *A Baseline GPS RAIM Scheme and a Note on the Equivalence of Three RAIM Methods*. NAVIGATION, Journal of the Institute of Navigation, vol. 39, no. 3, fall 1992, pp. 301-316.

[5] R.G. Brown, P.Y.C. Hwang (1997). *Introduction to random signals and applied Kalman filtering*. 3rd edition, John Wiley & Sons, New York.

[6] C.E. Cohen, B. Pervan, H.S. Cobb, D. Lawrence, J.D. Powell, B.W. Parkinson (1993). *Real-Time Cycle Ambiguity Resolution using a Pseudolite for Precision Landing of Airplane with GPS*. DSNS-93, Amsterdam, The Netherlands, March-April 1993.

[7] J. Diesel, J. Luu (1995). *GPS/IRS AIME: Calculation of Thresholds and Protection Radius Using Chi-Square Methods*. Proceedings of the ION GPS-95, Palm Springs, CA, Sep. 12-15, 1995, pp. 1959-1964.

[8] FAA Panel (2002). *Navigation and Landing Transition Strategy*. Federal Aviation Administration, Washington, D.C., August, 2002.

[9] FAA Panel (2008). *GNSS Evolutionary Architecture Study. Phase I – Panel Report*. Federal Aviation Administration GNSS Program Office, February, 2008.

[10] S. Feng, W. Ochieng, T. Moore, C. Hill, C. Hide (2008). *Carrier phase-based integrity monitoring for high-accuracy positioning*. GPS Solutions, Springer-Verlag, Berlin, Heidelberg.

[11] C.C. Goad, M. Yang (1997). *A New Approach to Precision Airborne GPS Positioning for Photogrammetry*. Photogrammetric Engineering & Remote Sensing, vol. 63, no. 9, September 1997, pp. 1067-1077.

[12] M.S. Grewal, A.P. Andrews (2001). *Kalman Filtering. Theory and Practice Using MATLAB®*. 2nd edition, John Wiley & Sons, New York, Chichester, Weinheim, Brisbane, Singapore, Toronto.

[13] M.S. Grewal, L.R. Weill, A.P. Andrews (2001). *Global Positioning Systems, Inertial Navigation, and Integration*. John Wiley & Sons, New York, Chichester, Weinheim, Brisbane, Singapore, Toronto.

[14] C. Günther (2008). *Satellite Navigation – Lecture Notes*. Lecture notes 2008, Technische Universität München.

[15] S. Günther (1999). *Analyse des Schätzfehlers für das zeitkontinuierliche erweiterte Kalman-Filter*. Berichte aus der Steuerungs- und Regelungstechnik, Shaker Verlag, Aachen.

[16] P. Henkel, C. Günther (2008). *Joint L-/C-Band Code and Carrier Phase Linear Combinations for Galileo*. Research Article, Hindawi Publishing Corporation, International Journal of Navigation and Observation, vol. 2008, Article ID 651437.

[17] P. Henkel, C. Günther (2008). *Precise Point Positioning with multiple Galileo frequencies*. Proceedings of the Positioning, Location and Navigation Symposium (PLANS), Monterey, USA, May 2008, pp. 592-599.

[18] N. Henze (2008). *Stochastik für Einsteiger*. 7. Auflage, Vieweg Verlag, Wiesbaden.

[19] B. Hofmann-Wellenhof, H. Lichtenegger, J. Collins (1997). *Global Positioning System. Theory and Practice*. 4th edition, Springer-Verlag, Wien, New York.

[20] JPS Joint Program Office (2004). *Interface Specification IS-GPS-200. Navstar GPS Space Segment/Navigation User Interfaces*. Revision D, El Segundo, 7 December 2004.

[21] P. Joosten (2001). *The LAMBDA-Method: MATLAB™ Implementation*. Version 2.1, Mathematical Geodesy and Positioning, Delft University of Technology, Netherlands, March 2001.

[22] R.E. Kalman (1960). *A New Approach to Linear Filtering and Prediction Problems*. Journal of Basic Engineering (ASME), vol. 28D, March 1960, pp. 35-37.

[23] E.D. Kaplan, C.J. Hegarty (2006). *Understanding GPS: principles and applications*. 2nd edition, Artech House, Boston, London.

[24] S. Khanafseh, B. Pervan (2008). *A new approach for calculating position domain integrity risk for cycle resolution in carrier phase navigation systems*. Position, Location and Navigation Symposium 2008, IEEE/ION, pp. 583-591.

[25] J. Lee (2005). *GPS-based aircraft landing systems with enhanced performance: beyond accuracy*. Dissertation at the department of aeronautics and astronautics of Standford University, Stanford, March 2005.

[26] Y.C. Lee (1986). *Analysis of Range and Position Comparison Methods as a Means to provide GPS Integrity in the User Receiver*. Proceedings of the Annual Meeting of the Institute of Navigation, Seattle, WA, June 24-26, 1986, pp. 1-4.

[27] E.L. Lehmann, J.P. Romano (2005): *Testing Statistical Hypotheses*. 3rd edition, Springer Texts in Statistics, Springer Science & Business Media, New York.

[28] G.T. McGraw, T. Murphy, M. Brenner, S. Pullen, A.J. van Dierendonck (2000). *Development of the LAAS Accuracy Models*. Proceedings of the Institute of Navigation ION GPS-2000, Salt Lake City, UT, September 19-22, 2000.

[29] P. Misra, P. Enge (2006). *GLOBAL POSITIONING SYSTEM. Signals, Measurements, and Performance*. 2nd edition, Ganga-Jamuna Press, Lincoln, Massachusetts.

[30] A.P. Mowlam, P.A: Collier (2004). *Fast Ambiguity Resolution Performance using Partially-Fixed Multi-GNSS Phase Observations*. The 2004 International Symposium of GNSS/GPS, Sydney, Australia, 6-8 December 2004.

[31] B.W. Parkinson, P.A. Axelrad (1987). *Basis for the Development of Operational Algorithms for Simplified GPS Integrity Checking*. Proceedings of the Satellite Division First Technical Meeting, The Institute of Navigation, Colorado Springs, CO, 1887, pp. 269-276.

[32] B. Pervan, F.C. Chan (2001). *System concepts for cycle ambiguity resolution and verification for aircraft carrier landings*. Proceedings of the 14th International Technical Meeting of the Satellite Division of the ION GPS 2001, Salt Lake City, UT, Sept. 2001.

[33] B. Pervan, F.C. Chan, D. Gebre-Egziabher, S. Pullen, P. Enge (2003). *Performance Analysis of Carrier-Phase DGPS Navigation for Shipboard Landing of Airplane*. Journal of the Institute of Navigation, vol. 50, no. 3, July 2003.

[34] B. Pervan, C.E. Cohen, D.G. Lawrence, H.S. Cobb, J.D. Powell, B.W. Parkinson (1995). *High Integrity GPS-Based Precision Landing Using Integrity Beacon Pseudolites*. ISPA 95, Braunschweig, February 21-24, 1995.

[35] B.W. Remondi (2004). *Computing satellite velocity using broadcast ephemeris*. GPS Solutions 8, Springer-Verlag, pp. 181-183.

[36] RTCA Special Committee 159 (2001). *Minimum operational standards for global positioning system/wide area augmentation system airborne equipment*. RTCA document number DO-229C, Washington, November 28, 2001.

[37] S. Schlötzer (2004). *Three Carrier Ambiguity Resolution (TCAR) – A Study of Applicability*. Diploma Thesis, Berufsakademie Ravensburg, Friedrichshafen.

[38] M.A. Sturza (1988). *Navigation System Integrity Monitoring Using Redundant Measurements*. NAVIGATION, Journal of the Institute of Navigation, vol. 35, no. 4, winter 1988-89, pp. 69-87.

[39] P.J.G. Teunissen (1993). *Least-squares estimation of the integer GPS ambiguities*. IAG General Meeting 1993, Invited Lecture, Beijing, China.

[40] P.J.G. Teunissen (1997). *On the GPS widelane and its decorrelating property*. Journal of Geodesy, Springer-Verlag, pp. 577-587.

[41] P.J.G. Teunissen (2001). *Integer estimation in presence of biases*. Journal of Geodesy, vol. 75, no. 7-8, pp. 339-407.

[42] P.J.G. Teunissen, P. Joosten, D. Odijk (1999). *The Reliability of GPS Ambiguity Resolution*. GPS Solutions, vol. 2, no. 3, John Wiley & Sons, pp. 63-69.

[43] P.J.G. Teunissen (2005). *Integer aperture bootstrapping: a new GNSS ambiguity estimator with controllable fail-rate*. Journal of Geodesy, vol. 79, Springer-Verlag, pp. 389-397.

[44] P.J.G. Teunissen, A. Kleusberg (1998). *GPS for Geodesy*. 2nd edition, Springer-Verlag, Berlin, Heidelberg, New York.

[45] C.L. Thornton (1976). *Triangular Covariance Factorizations for Kalman Filtering*. Ph.D. Thesis, University of California, Los Angeles, School of Engineering.

[46] D. Titterton, J. Weston (2004). *Strapdown Inertial Navigation Technology*. 2nd edition, IEE Radar, Sonar and Navigation series 17, The Institution of Electrical Engineers, Stevenage.

[47] S. Verhagen (2004). *The GNSS integer ambiguities: estimation and validation*. Dissertation, Delft Institute of Earth Observation and Space Systems, Delft University of Technology, Delft.

[48] S. Verhagen, D. Odijk, F. Boon, J.M. López Almansa (2007). *Reliable Multi-Carrier Ambiguity Resolution in the Presence of Multipath*. ION GNSS 20th International Technical Meeting of the Satellite Division, Fort Worth, Texas, September 2007, pp. 339-350.

[49] D. Walsh, P. Daly, T. Rowe (1995). *An Analysis of Using Carrier Phase to Fulfill Cat III Required Navigation Performance*. Proceedings of the ION GPS-95, Palm Springs, CA, Sep. 12-15, 1995, pp. 1985-1993.

[50] T. Walter, P. Enge (1995). *Weighted RAIM for Precision Approach*. Proceedings of the 8th International Technical Meeting of the Satellite Division, Institute of Navigation ION GPS 1995, Palm Springs, CA, September 12-15, 1995, pp. 1195-2004.

[51] L. Wanninger (1994). *Der Einfluß der Ionosphäre auf die Positionierung mit GPS*. Wissenschaftliche Arbeiten der Fachrichtung Vermessungswesen der Universität Hannover, Nr. 201, Hannover.

[52] J. Wendel (2007). *Integrierte Navigationssysteme. Sensordatenfusion, GPS und Inertiale Navigation*. Oldenburg Verlag, München, Wien.

[53] G. Wübbena (1991). *Zur Modellierung von GPS-Beobachtungen für die hochgenaue Positionsbestimmung*. Wissenschaftliche Arbeiten der Fachrichtung Vermessungswesen der Universität Hannover, Nr. 168, Hannover.

[54] G. Xu (2003). *GPS. Theory, Algorithms and Applications*. Springer-Verlag, Berlin, Heidelberg, New York.

[55] Y. Yun, H. Yun, D. Kim, C. Kee (2008). *A Gaussian Sum Filter Approach for DGNSS Integrity Monitoring*. The Journal of Navigation 2008, The Royal Institute of Navigation, UK.

[56] A. Zappavigna (2002). *Galileo Phase B2C. UERE Budget Results*. Doc.no. GB2C/SE/TNO/0001, issue 6, Space Engineering S.p.A.

[57] W. Zhang, M.E. Cannon, O. Julien, P. Alves (2003). *Investigations of Combined GPS/GALILEO Cascading Ambiguity Resolution Schemes*. Proceedings of ION GPS/GNSS 2003, Portland, USA, pp. 2599-2610.